

On the finite element realization, boundary conditions and parameters identification of the relaxed micromorphic model

Von der Fakultät für Ingenieurwissenschaften,
Abteilung Bauwissenschaften
der Universität Duisburg-Essen
zur Erlangung des akademischen Grades
Doktor-Ingenieur
genehmigte Dissertation

von

Mohammad Sarhil, M.Sc.

Hauptberichter: Prof. Dr.-Ing. habil. J. Schröder
Korreferenten: Prof. Dr. rer. nat. habil. P. Neff
Jun.-Prof. Dr.-Ing. L. Scheunemann
Prof. Dr. Matti Schneider

Tag der Einreichung: 14. Mai 2024
Tag der mündlichen Prüfung: 14. Oktober 2024

Fakultät für Ingenieurwissenschaften,
Abteilung Bauwissenschaften
der Universität Duisburg-Essen
Institut für Mechanik
Prof. Dr.-Ing. habil. J. Schröder

Berichte des Instituts für Mechanik, Universität Duisburg-Essen

Nr. 32

Herausgeber:

Prof. Dr.-Ing. habil. J. Schröder

Organisation und Verwaltung:

Prof. Dr.-Ing. habil. J. Schröder
Institut für Mechanik
Fakultät für Ingenieurwissenschaften
Abteilung Bauwissenschaften
Universität Duisburg-Essen
Universitätsstraße 15
45141 Essen
Tel.: 0201 / 183 - 2682
Fax.: 0201 / 183 - 2680

© Mohammad Sarhil
Institut für Mechanik
Abteilung Bauwissenschaften
Fakultät für Ingenieurwissenschaften
Universität Duisburg-Essen
Universitätsstraße 15
45141 Essen

Alle Rechte, insbesondere das der Übersetzung in fremde Sprachen, vorbehalten. Ohne Genehmigung des Autors ist es nicht gestattet, dieses Heft ganz oder teilweise auf fotomechanischem Wege (Fotokopie, Mikrokopie), elektronischem oder sonstigen Wegen zu vervielfältigen.

ISBN: 978-3-9821811-8-9

Für Sally, Daniel und Leon

DuEPublico

Duisburg-Essen Publications online

UNIVERSITÄT
DUISBURG
ESSEN

Offen im Denken

ub | universitäts
bibliothek

Diese Dissertation wird via DuEPublico, dem Dokumenten- und Publikationsserver der Universität Duisburg-Essen, zur Verfügung gestellt und liegt auch als Print-Version vor.

DOI: 10.17185/duepublico/82783

URN: urn:nbn:de:hbz:465-20250106-135045-4

Alle Rechte vorbehalten.

Preface

This dissertation was written during my stay as a research assistant at the Institute of Mechanics, Department of Civil Engineering, Faculty of Engineering at the University of Duisburg-Essen. My position was funded by the Deutsche Forschungsgemeinschaft (DFG, German Research Foundation) – Project number 440935806 (SCHR 570/39, SCHE 2134/1, NE 902/10) within the DFG priority program 2256. I thank the German Research Foundation for their financial support.

I would like to express my sincere appreciation to Professor Jörg Schröder for giving me the opportunity to complete my dissertation under his supervision and for his support throughout the past few years. I am also greatly grateful to Professor Patrizio Neff for his intensive supervision, support and immediate help. I was able to obtain his scientific feedback at any time, even on weekends. Our insightful discussions and his thoughtful remarks have broadened my horizons. I am also thankful to Professor Lisa Scheunemann for her continuous support and help throughout my Master's studies and during the writing of this dissertation. I thank Prof. Matti Schneider for taking the time to review this dissertation. Besides, I would like to thank Professor Joachim Bluhm for his exceptional teaching style during my Master's studies.

I would like to extend my heartfelt thanks to my current and former colleagues Maximilian Vorwerk, Philipp Hartwig, Marvin Köbler, Paulo S. B. Nigro, Xiaodong Xia, Sonja Hellebrand, Marcos Margalho de Barros, Julia Sunten, Dominik Brands, Markus von Hoegen, Maximilian Scheunemann, Simon Kugai, Matthias Labusch, Simon Maike, Rainer Niekamp, Carina Schwarz, Yasemin von Hoegen, Mangesh Pise, Sabine Ressel, Serdar Serdas, Alexander Schwarz, Dominik-Oliver Clodit and Cinthia Garcia Sousa for the wonderful years of collaboration and friendship.

Last, I thank my parents, Salwa Fayad and Mahmoud Sarhil, for their love, care, sacrifices and support. I would like to express my most profound appreciation to my life partner through this adventure, my beloved wife Sally, who made numerous sacrifices to allow me to pursue my dreams. I cannot find the words to describe my gratitude to her. I also want to thank my children, Daniel and Leon, for the precious time I stole from them to dedicate to write this dissertation.

Essen, October 2024

Mohammad Sarhil

Abstract

Metamaterials are attracting much attention due to their remarkable mechanical properties. They can be tailored to fulfill a specific functionality. However, they usually exhibit size-effects phenomena, indicating that their mechanical behaviors vary when their size changes. To model them as a homogeneous medium, enriched continua theories that capture size-effects are the preferred choice. The relaxed micromorphic model is a generalized continuum that differs from the classical micromorphic theory by using the Curl of a micro-distortion field instead of the full gradient, however, leading to many advantages such as the notably reduced number of parameters and well-posedness for the symmetric force stress case. The most important advantage is the unique behavior as a macroscopic-microscopic two-scale linear elasticity model, which other generalized continua do not offer. In this work, we use the relaxed micromorphic continuum to model metamaterials. First, conforming $H^1(\mathcal{B}) \times H(\text{Curl}, \mathcal{B})$ finite elements are presented and tested in several numerical examples. We systematically investigate the boundary conditions of the micro-distortion field, proving the necessity of the consistent coupling boundary condition. We identify the microscopic elasticity tensor employing the stiffest response concept under affine and non-affine boundary conditions. Finally, we develop an optimization procedure to define all the unknown parameters through direct energy fitting.

Zusammenfassung

Metamaterialien gewinnen aufgrund ihrer bemerkenswerten mechanischen Eigenschaften immer mehr an Aufmerksamkeit. Sie können auf eine bestimmte Funktionalität zugeschnitten werden. Sie weisen jedoch in der Regel Größeneffekte auf, was bedeutet, dass sich ihr mechanisches Verhalten ändert, wenn sich ihre Größe ändert. Um sie als homogenisiertes Medium zu modellieren, sind erweiterte Kontinuumstheorien, die Größeneffekte erfassen, die bevorzugte Wahl. Das Relaxed Micromorphic Model ist so ein erweiterte Kontinuum, das sich von der klassischen mikromorphen Theorie dadurch unterscheidet, dass es der Curl eines Mikroverzerrungsfeldes anstelle des vollen Gradienten verwendet, was jedoch zu vielen Vorteilen führt, wie z. B. der deutlich reduzierten Anzahl von Parametern und der Wohlgestelltheit für den Fall symmetrischer Kraftspannung. Der wichtigste Vorteil ist das einzigartige Verhalten als makroskopisch-mikroskopisches Zwei-Skalen lineares Modell, das keine anderen erweiterte Kontinua bieten. In dieser Arbeit verwenden wir das Relaxed Micromorphic Model, um Metamaterialien zu modellieren. Zunächst werden konforme $H^1(\mathcal{B}) \times H(\text{Curl}, \mathcal{B})$ Finite Elemente vorgestellt und in mehreren numerischen Beispielen getestet. Wir untersuchen systematisch die Randbedingungen des Mikro-Verzerrungsfeldes und beweisen die Notwendigkeit der konsistenten Kopplungsrandbedingung. Wir identifizieren den mikroskopischen Elastizitätstensor unter Verwendung des Stiffest-Response-Konzepts mit affinen und nicht-affinen Randbedingungen. Schließlich entwickeln wir ein Optimierungsverfahren, um alle unbekannt Parameter durch direkte Energieanpassung zu bestimmen.

Contents

1	Introduction and Motivation	1
1.1	Outline	6
1.2	Publications	7
2	Fundamentals of continuum mechanics and enriched continua	9
2.1	Kinematics, deformation measures and time derivatives	9
2.2	Concept of stress	13
2.3	Balance equations	14
2.3.1	Balance of mass	14
2.3.2	Balance of linear momentum	15
2.3.3	Balance of angular momentum	15
2.3.4	Balance of energy	16
2.3.5	Entropy inequality	17
2.4	Material modeling: isotropy and anisotropy	18
2.5	Variational formulation for linear elasticity	20
2.6	Enriched continua	20
2.6.1	Kinematics	21
2.6.2	The micromorphic theory by Mindlin-Eringen	22
2.6.3	The Cosserat model	23
2.6.4	The relaxed micromorphic model by Neff	24
2.6.5	Some other generalized continua in a nutshell	25
3	The relaxed micromorphic model (RMM)	27
3.1	Hilbert spaces and related norms	27
3.2	Model description	29
3.3	Variational formulation	30
3.4	Limiting case $L_c \rightarrow 0$	32
3.5	Limiting case $L_c \rightarrow \infty$	33
3.6	Characteristics of the RMM: a two-scale elasticity model	34
4	Finite Element Method	37
4.1	Linearization of the weak forms	37
4.2	Finite element discretization	39
4.3	Conforming finite element approximations	40
4.3.1	$H^1(\mathcal{B})$ -conforming finite element formulation	41

4.3.2	$H(\text{curl}, \mathcal{B})$ -conforming finite element formulation	43
4.4	Implemented finite elements	47
4.5	Discretization of the linearized weak forms	48
4.5.1	$H^1(\mathcal{B}) \times H^1(\mathcal{B})$ finite elements	48
4.5.2	$H^1(\mathcal{B}) \times H(\text{curl}, \mathcal{B})$ finite elements	50
4.6	Numerical integration	52
4.7	Assembling procedure for the boundary value problem	52
4.8	Numerical examples	53
4.8.1	Patch-test	53
4.8.2	Discontinuous solution: convergence study	57
4.8.3	Characteristic length analysis: pure shear problem	64
4.9	Discussions	68
5	Modeling metamaterial beams under pure bending via RMM	71
5.1	Reference study: full discretization of metamaterial specimens	72
5.2	Parameter identification for the relaxed micromorphic continuum	76
5.2.1	Identification of the macroscopic elasticity tensor $\mathbb{C}_{\text{macro}}$	76
5.2.2	Identification of the microscopic elasticity tensor $\mathbb{C}_{\text{micro}}$ via affine deformations	77
5.2.3	Identification of the microscopic elasticity tensor $\mathbb{C}_{\text{micro}}$ via non-affine deformations	80
5.2.4	Identification of \mathbb{C}_e	82
5.3	The boundary conditions of the micro-distortion field	82
5.3.1	Symmetric force stress case	83
5.3.2	Non-symmetric force stress case	84
5.3.3	Cosserat limit, skew-symmetric micro-distortion field	84
5.4	Scaling of the curvature	88
5.5	Calibration of the curvature in RMM with the fully resolved solution	88
5.6	Validation: further numerical examples	92
5.6.1	Simple shearing	92
5.6.2	Cantilever under traction load	95
5.7	Discussions	97
6	Computational approach to identify the material parameters	99
6.1	The unit-cell and the material parameters	100
6.2	Motivation and consistency check for linear elasticity	101

6.2.1	Affine Dirichlet boundary condition	101
6.2.2	Periodic boundary condition	103
6.3	Computational approach to identify the material parameters for RMM . .	107
6.3.1	Skew-symmetric micro-distortion field instead of the full one	116
6.3.2	Full gradient of the micro-distortion field instead of its Curl	120
6.4	Comparisons and validation	124
7	Conclusions and outlook	129
	Appendix	131
A	Nédélec shape functions	131
A	Second-order triangular element NT2	131
B	First-order quadrilateral element NQ1	132
C	Second-order quadrilateral element NQ2	133
B	Voigt notation	137
	List of Figures/Tables	139
	References	145

1 Introduction and Motivation

To deal with various societal challenges, such as the lack of resources, sustainability, climate change, and the need for substitutes for critical materials like those used in batteries, new fundamental insights from mechanics and mathematics are required to develop new materials and efficient computational methods focusing on reducing the computational cost and the associated energy consumption. In various high-tech fields such as the electric automotive industry, lightweight aircraft industry, biomedical research and others, there is an increasing need for new solid materials with specific properties to provide optimal solutions. **Metamaterials**, artificially created structures, are a promising solution. The Greek term “meta” in metamaterials, meaning “beyond”, symbolizes that metamaterials have properties beyond those of traditional bulk materials, FISCHER ET AL. [2020]. They can be tailored to fit a specific functionality, and therefore, they are gaining much attention in both academia and industry. Figure 1.1 illustrates the number of annual peer-reviewed articles with the keyword “metamaterial” on Scopus published over the last 20 years, reflecting a rapidly growing interest. The first metamaterials can be tracked back to electromagnetism, where the direction of the electromagnetic radiation can be controlled, which enabled the development of many devices such as biosensors, absorbers, antennas, optical filters, and others (ABDULLAH ET AL. [2021], IYER ET AL. [2020], KUMAR ET AL. [2022]).

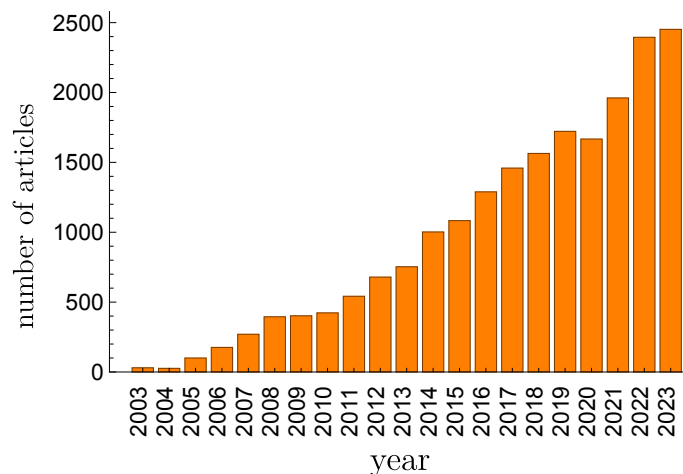


Figure 1.1: Annual number of peer-reviewed publications with the keyword “metamaterial” in Scopus (www.scopus.com) in the last 20 years.

The term “mechanical metamaterials” is more recent and refers to metamaterials with mechanical applications. The advances in additive manufacturing (AM), notably 3D printing, have revolutionized the production of mechanical metamaterials. These technologies have allowed the production of complex materials with intricate architectures across various length scales, see for example JIANG AND LI [2018], LEI ET AL. [2019], MONTGOMERY ET AL. [2020], PLOCHER AND PANESAR [2019]. Over the course of human history, the range of available materials has continued to expand to meet new demands. However, certain limitations have restricted the mechanical properties of classic bulk materials. For example, there is a relation between the density and strength of materials, where a high-strength material also has a high density and vice versa. Mechanical metamaterials are a new generation of materials that can break the previous limitations. An example of achieving an extremely high strength-to-density ratio through the engineering of the

microstructure is the metamaterial shown in SCHAEGLER ET AL. [2011], which consists of more than 99% air and is made of hollow tubes of nickel. Mechanical metamaterials also exhibit some unusual mechanical properties inherited from the topology of specifically designed unit-cells rather than their constituent materials' mechanical properties. Such mechanical properties are negative Poisson's ratio, negative compressibility, negative thermal expansion and ultra-large elastic deformations FISCHER ET AL. [2020], LEE ET AL. [2012], YU ET AL. [2018]. However, the most crucial aspect of mechanical metamaterials under static loading is the ability to tailor their mechanical properties, such as having a relatively large stiffness in some modes of deformation, whereas they could be significantly compliant in other modes, i.e. programmable stiffness, see for example LU ET AL. [2022].

Mechanical metamaterials can manipulate acoustic and elastic waves, see e.g. ELMADH ET AL. [2021], as they exhibit the band-gap property where a certain targeted frequency range cannot propagate within the metamaterial which can be of great importance in many fields. The band-gap property of metamaterials can drive innovations in the design of lightweight vehicles, with the focus on absorbing external shocks and dynamic loads. Furthermore, buildings and infrastructures built nearby sources of vibrations and noises, such as tramways, train stations, metro lines, highways, windmills and others, would benefit from these metamaterials to improve their enjoyment, safety and usability. Earthquake-proof structures can be designed using metamaterials to withstand earthquakes with specific frequency ranges. Many noise- and vibration-damping tools and applications based on these metamaterials could be easily and cheaply manufactured at a large scale JIMÉNEZ ET AL. [2016], MADEO ET AL. [2016b; 2018]. Countless unusual and novel applications, which we cannot even imagine or think of at this point, could suddenly come to light as soon as such metamaterials become readily available, especially with new generations of 3D printers capable of printing traditional metallic materials with high accuracy. Reviews about the applications of mechanical metamaterials can be found in BARCHIESI ET AL. [2019], KADIC ET AL. [2019], QI ET AL. [2022], SURJADI ET AL. [2019], WU ET AL. [2019], ZADPOOR [2016].

To facilitate the design procedures of new metamaterials, appropriate and effective computational methods are required to investigate their effective mechanical properties. One obvious option is modeling metamaterials by fully discretizing the underlying complex structure (full-scale resolution). This is typically infeasible for typical engineering problems due to the associated substantial computational costs. Homogenization approaches towards homogeneous continua are a practical choice that could simplify the design process drastically ZOHDİ [2004], ZOHDİ AND WRIGGERS [2005]. However, mechanical metamaterials typically reveal size-effect phenomena, meaning that their effective properties change when varying the material size for the case when scale-separation does not hold. Generally, size-effects can indicate both increasing and decreasing stiffness while reducing the size KIRCHHOF ET AL. [2023], WHEEL ET AL. [2015]. In this work, we consider only the case that smaller is relatively stiffer. The classical Cauchy-Boltzmann theory and first-order homogenization methods are incapable of describing materials with size-effects (or band-gaps) because of the absence of an internal length, which characterizes the underlying microstructure, from the energy functional and constitutive equations. **Generalized continua** are enhanced continua that can model these size-effects as a homogeneous continuum without accounting for the detailed microstructure. The first possibility of enhancement is achieved by accounting for higher-grade differential operators in the energy functional. Gradient elasticity (or strain/stress gradient) theories provide

extensions of the classical elasticity equations by adding different types of higher-order spatial derivatives of strains and stresses to account for the size-effects. Moreover, classical elastic singularities, e.g. due to point loads, dislocation lines and crack tips, can be eliminated, c.f. AIFANTIS [1992], ALTAN AND AIFANTIS [1992], LAZAR ET AL. [2006], by these higher-order gradients. The gradient elasticity theory was developed first in the early 1960s by MINDLIN [1964; 1965], MINDLIN AND ESHEL [1968]. Various formats of gradient elasticity were developed with different differential operators and different numbers of constitutive parameters, e.g. AIFANTIS [2011], ASKES ET AL. [2008], EREMEYEV ET AL. [2021], ERINGEN [1972; 1983], FISCHER ET AL. [2011], FOREST [2020], FOREST AND SAB [2012], GODA AND GANGHOFFER [2016], LAZAR [2014], SHEKARCHIZADEH ET AL. [2022], YANG ET AL. [2021]. A general review of the theories of gradient elasticity can be found in ALTAN AND AIFANTIS [1997], ASKES AND AIFANTIS [2011]. Gradient elasticity theories require continuity of the higher-order fields, which seems to be a non-physical assumption since microstructures often have perturbations that imply possible discontinuities in the higher-order gradient of the displacement. Moreover, it has been shown that gradient elasticity theories are inadequate for describing dynamic phenomena such as band-gap response in metamaterials since the microstructure has its own vibrational modes independently of the unit-cell’s macromotion. Alternatively, it is logical to introduce a new class of generalized continua by expanding the kinematics to contain additional degrees of freedom independent of the classical translational degrees of freedom. In this regard, we refer to the Cosserat and micromorphic theories. A classification of generalized continua is available in ALAVI ET AL. [2023], NEFF ET AL. [2014a].

The Cosserat (or micropolar) theory was initially introduced by the brothers Eugène Cosserat and François Cosserat, who defined an elastic continuum with kinematically independent translational and rotational degrees of freedom COSSERAT AND COSSERAT [1909]. In the framework of the Cosserat media, each point of the medium can be represented as an infinitesimal rigid body which moves and rotates ALAVI ET AL. [2022b], BLESSEN AND NEFF [2023], GHIBA AND NEFF [2023], GHIBA ET AL. [2023], NEFF [2006], NEFF ET AL. [2010b], SAEM ET AL. [2023], TROVALUSCI AND PAU [2014]. Cosserat theory can be used to model liquid crystals LEE AND ERINGEN [2003], granular materials MOHAN ET AL. [1999], MÜHLHAUS [1986], foam-like structures (like bones) ASCENZI ET AL. [1994], chiral metamaterials ALAVI ET AL. [2021b], cellular materials ONCK [2002] and masonry BESDO [1991], GODIO ET AL. [2017]. However, the Cosserat continuum is unable to model deformable microstructures such as metamaterials. The “full” micromorphic theory is the most general framework for a continuum which assumes a two-scale continuum model where the kinematics of each material point is expressed by a macroscopic continuous deformation and an independent internal microscopic deformation ERINGEN [1968], ERINGEN AND SUHUBI [1964], JU ET AL. [2021], NEFF AND FOREST [2007], SUHUBI AND ERINGEN [1964]. Generally, the energy function is governed by the macroscopic deformation gradient and the gradient of a second-order tensor called the micro-distortion. However, micromorphic models are excessively complex with many undefined constitutive parameters associated with higher-order tensors (e.g. gradient of the micro-distortion), making it challenging to convince engineers to consider them seriously.

This work adopts **the relaxed micromorphic model** introduced in GHIBA ET AL. [2015], NEFF ET AL. [2014a]. Being a micromorphic model, it features the classical translational degrees of freedom as well as a non-symmetric micro-distortion field. However, it employs a relaxed curvature, where the Curl of the micro-distortion field is utilized instead

of the full gradient. Using only the Curl has some decisive advantages. The assumed strain energy is drastically simplified where the curvature part is only incorporated through the Curl of the micro-distortion field. As a result, the number of constitutive parameters that need to be determined is reduced compared to the conventional micromorphic approach. The Curl of the micro-distortion field remains a second-order tensor, thus circumventing the need for constitutive relations involving sixth-order tensors that are associated with the gradient of the micro-distortion in the classical theory. The relaxed micromorphic model generates “bounded stiffness” NEFF ET AL. [2010a], RIZZI ET AL. [2021a;b;c; 2022b] for large values of the characteristic length (arbitrary small samples), in opposition to all strain gradient, Cosserat-micropolar or classical micromorphic approaches. As it turns out, the relaxed micromorphic model interpolates between two well-defined scales: the classical continuum scale of macroscopic elasticity, whose stiffness is given by a macroscopic elasticity tensor known uniquely from periodic homogenization and a microscopic scale, whose stiffness is given by a microscopic elasticity tensor. The role of the characteristic length is then to scale correctly with the size of the specimen and to describe the interaction between the two scales. The tangential continuity is sufficient as a regularity condition for the micro-distortion (same as the deformation gradient), and it is enough to control the tangential projection of the micro-distortion field on the boundary instead of the full field, GHIBA ET AL. [2021]. As we show later, the consistent coupling boundary condition enforces that the tangential projections of the gradient of the displacement field and the micro-distortion field on the boundary are the same D’AGOSTINO ET AL. [2022b], RIZZI ET AL. [2021a;b]. The consistent coupling boundary condition is a necessary component for modeling that allows the relaxed micromorphic model to reach the intended upper microscopic bound which permits a physical-based identification of the unknown material parameters associated with the microscopic scale. The relaxed micromorphic model recovers a symmetric force stress tensor while maintaining the well-posedness when setting the rotational (Cosserat) couple modulus to zero, which has been proven using new generalized Korn’s inequality GMEINER ET AL. [2023; 2024], LEWINTAN AND NEFF [2021], LEWINTAN ET AL. [2021]. Moreover, the relaxed micromorphic model has successfully captured the band gaps for many periodic metamaterials, see for example AIVALIOTIS ET AL. [2020], BARBAGALLO ET AL. [2019], D’AGOSTINO ET AL. [2020], DEMORE ET AL. [2022], MADEO ET AL. [2015; 2016a;b; 2017], RIZZI ET AL. [2022a;c;d]. The well-posedness for the static and dynamic problems has been proved in NEFF ET AL. [2015], OWCZAREK ET AL. [2019]. In KNEES ET AL. [2023; 2024], the global and local regularities of the relaxed micromorphic model were investigated.

Identifying the material parameters of generalized continua models poses an active open research topic and generally remains unsolved. In this regard, we refer to the discussions and challenges listed in SARHIL ET AL. [2023b;c; 2024]. Different schemes were introduced for the homogenization of heterogeneous fully discretized microstructures into the Cosserat continuum in ALAVI ET AL. [2022b], FOREST AND SAB [1998], HÜTTER [2019], REDA ET AL. [2021], different variants of the gradient elasticity continuum in ABALI AND BARCHIESI [2021], ABALI ET AL. [2019], BACIGALUPO ET AL. [2018], KHAKALO AND NIIRANEN [2020], LAHBAZI ET AL. [2022], SARAR ET AL. [2023], SCHMIDT ET AL. [2022], SKRZAT AND EREMEYEV [2020], WEEGER [2021], YANG AND MÜLLER [2021], YANG ET AL. [2020; 2022] and the classical Eringen-Mindlin micromorphic continuum (curvature based on full-gradient) in ALAVI ET AL. [2021a], BISWAS AND POH [2017], FOREST [2002], HÜTTER [2017], ROKOŠ ET AL. [2019; 2020a;b], ZHI ET AL. [2022]. How-

ever, too many major questions remain unanswered, and each researcher tailors its own approach without reaching a universally accepted solution. Two approaches are widely utilized in the scientific community to determine material parameters associated with the higher-order homogenized properties, which are asymptotic expansion methods, see e.g. BACIGALUPO AND GAMBAROTTA [2010a], BOUTIN [1996] (can be combined with fast Fourier transform methods, see LI AND ZHANG [2013], TRAN ET AL. [2012]) and heuristic approaches based on customized definitions of higher-order modified non-homogeneous Dirichlet boundary conditions (up to quartic) on the unit-cell BERKACHE ET AL. [2017], FOREST AND TRINH [2011], GODA AND GANGHOFFER [2016]. Among the heuristic approaches, quadratic boundary conditions have been investigated widely, see e.g. AUFRAY ET AL. [2010], FOREST [2002; 2016], FOREST AND TRINH [2011], KOUZNETSOVA ET AL. [2002; 2004], TRINH ET AL. [2012], in the field of homogenization into second gradient continua and classical full micromorphic continua. However, several challenging issues are described in the literature for this option. First, this approach does not yield vanishing effective higher-order moduli when a homogeneous material is tested. Second, when scale-separation holds (many unit-cells), and the classical first-order homogenization theory is applicable, Cauchy theory with the known macroscopic elasticity tensor is also not automatically regenerated, cf. ALAVI ET AL. [2021a]. Alternatively, additional body forces have been added to the microstructure with higher-order Dirichlet boundary conditions MONCHIET ET AL. [2020], YVONNET ET AL. [2020]. The obtained results agree well with the ones from asymptotic homogenization, but there remain artifacts for the specific case of a unit-cell made of soft inclusions and hard matrix, for which the higher-order moduli differ. A novel procedure has been introduced in HÜTTER [2019] by averaging only over micro-heterogeneities. TRINH ET AL. [2012] shows that fourth-order kinematic boundary conditions should be used to fully determine the higher-order moduli in a micromorphic theory. In HÜTTER [2022], a harmonic decomposition of a micromorphic theory is introduced to the governing equations and employed to porous materials. A variational approach is introduced for the homogenization from a Cauchy continuum on the micro-scale towards a second gradient or micromorphic continuum on the macro level in GANGHOFFER AND REDA [2021] and ALAVI ET AL. [2021a], respectively, where the microscopic displacement is decomposed into a homogeneous and a fluctuation part, as in classical first-order homogenization theory, but the homogeneous part of the deformation arises here from a variational approach. Based on the Hill–Mandel condition, WEEGER [2021] introduced a homogenization approach for periodic lattice structures and metamaterials into a second gradient linear elastic model on the macro-scale. Similar to FOREST AND TRINH [2011], zero energy modes are noticed for some of the higher-order moduli. In SCHMIDT ET AL. [2022], a homogenization scheme for higher-order continua is demonstrated based on Isogeometric Analysis. Further developments in the context of multiphysical applications are discussed by WASEEM ET AL. [2020]. In the field of asymptotic expansion homogenization, metamaterials are investigated in ABALI AND BARCHIESI [2021], ABALI ET AL. [2022], YANG AND MÜLLER [2021] with a focus on size-effects. A direct computational scheme is shown by ABALI ET AL. [2019] for determining the effective moduli through comparison with microstructure simulations for selected higher-order modes. The crucial rules of the wedge and double traction forces are analyzed in YANG ET AL. [2021].

The main goal of this work is to bridge the gap between the mathematical theory of the relaxed micromorphic model and its practical application in the engineering context.

The relaxed micromorphic model offers many potentials for modeling materials with size-effects, specifically metamaterials. Moreover, we are not interested in band-gap phenomena and therefore no dynamic effects are considered.

The finite element implementation and the numerical examples in this work are performed within **AceGen** and **AceFEM** programs, which are developed and maintained by Jože Korelc (University of Ljubljana). The interested reader is referred to KORELC [1997], KORELC AND WRIGGERS [2016].

1.1 Outline

In **Chapter 2**, we delve into the fundamental aspects of continuum mechanics, including kinematics, stress concept, and balance equations. We broaden the framework to incorporate enriched continua in general. Then, we narrow it down to the specific cases of the Cosserat, the Mindlin-Eringen micromorphic, and the relaxed micromorphic theories. After that, we demonstrate the connections between the kinematics and energy functionals of most known generalized continua.

Chapter 3 presents the relaxed micromorphic model, starting with the relevant Hilbert spaces and associated norms. We derive the variational formulation that leads to the strong and weak forms with the related boundary conditions. Then, we discuss the limiting cases when the characteristic length parameter approaches zero and infinity, which results in the unique behavior of the relaxed micromorphic model as a two-scale linear elasticity model.

In **Chapter 4**, we introduce the basics of the finite element method, focusing on conforming approximation spaces for the relaxed micromorphic model. We then demonstrate the unique properties of the implemented finite elements and the distinct behavior of the relaxed micromorphic model components including the different stress measures through numerical examples for a varying characteristic length parameter.

In **Chapter 5**, we model metamaterial beams subjected to bending with the relaxed micromorphic continuum. After obtaining the solution of fully resolved beams, we identify the material parameters of the relaxed micromorphic continuum. To obtain the microscopic elasticity tensor, we introduce two approaches based on affine and non-affine boundary conditions. We investigate the boundary conditions of the micro-distortion field for both symmetric and non-symmetric force stress cases. Finally, we calibrate the characteristic length parameter to fit the results of fully resolved beams.

In **Chapter 6**, we determine the material parameters in the relaxed micromorphic model for a given periodic microstructure through a least squares fitting of the total energy of the relaxed micromorphic homogeneous continuum to the total energy of the fully resolved heterogeneous microstructure. We check the consistency of our approach for linear elasticity subjected to periodic and affine Dirichlet boundary conditions. Then, we expand the approach to the relaxed micromorphic model, which involves considering an adequate number of quadratic deformation modes and different specimen sizes. Finally, we compare the least squares fitting results of the relaxed micromorphic model, the Cosserat-micropolar model, and the classical micromorphic model with two different curvature formulations.

Chapter 7 concludes the dissertation and gives an outlook to possible future investiga-

tions on homogenization into the relaxed micromorphic model.

1.2 Publications

During writing this dissertation, the following articles were published. Contents from these publications are used in this work. Drafts were uploaded on arXiv.

J. Schröder, M. Sarhil, L. Scheunemann and P. Neff. Lagrange and $H^1(\mathcal{B}) \times H(\text{curl}, \mathcal{B})$ based finite element formulations for the relaxed micromorphic model. *Computational Mechanics*, 70, 1309–1333, 2022. doi:10.1007/s00466-022-02198-3

M. Sarhil, L. Scheunemann, J. Schröder and P. Neff. On a tangential-conforming finite element formulation for the relaxed micromorphic model in 2D. *Proceedings in Applied Mathematics and Mechanics*, 21, e202100187, 2021. doi:10.1002/pamm.202100187

M. Sarhil, L. Scheunemann, J. Schröder and P. Neff. Size-effects of metamaterial beams subjected to pure bending: on boundary conditions and parameter identification in the relaxed micromorphic model. *Computational Mechanics*, 72, 1091–1113, 2023. doi:10.1007/s00466-023-02332-9.

M. Sarhil, L. Scheunemann, J. Schröder and P. Neff. On the identification of material parameters in the relaxed micromorphic continuum. *Proceedings in Applied Mathematics and Mechanics*, 23, e202300056, 2023. doi:10.1002/pamm.202300056.

M. Sarhil, L. Scheunemann, J. Schröder and P. Neff, Modeling the size-effect of metamaterial beams under bending via the relaxed micromorphic continuum. *Proceedings in Applied Mathematics and Mechanics*, 22, e202200033, 2023. doi:10.1002/pamm.202200033.

M. Sarhil, L. Scheunemann, P. Lewintan, J. Schröder, and P. Neff. A computational approach to identify the material parameters of the relaxed micromorphic model. *Computer Methods in Applied Mechanics and Engineering*, 425, 116944, 2024. doi:10.1016/j.cma.2024.116944

2 Fundamentals of continuum mechanics and enriched continua

All matter is discontinuous, as it is composed of molecules, which, in turn, comprise atoms consisting of nuclei and electrons. Most engineering applications involve materials at large length and time scales. This is the case when the considered material is at a length scale much larger than the atomic spacing, and the studied phenomenon is acting on a time scale longer than the atomic vibration period. Therefore, it is possible to ignore the discrete nature of the matter without making significant errors.

In this Chapter, we introduce an overview of the fundamental concepts of continuum mechanics of solids presented in ERINGEN [1967], SCHRÖDER ET AL. [2013], TRUESDELL AND NOLL [1965], TRUESDELL AND TOUPIN [1960a], and used in BALZANI [2006], BRANDS [2012], BRINKHUES [2012], HOEGEN [2019], IGELBÜSCHER [2021], KEIP [2012], LABUSCH [2018], SCHEUNEMANN [2017], VIEBAHN [2019]. The origins of the classical theory of continuum mechanics can be traced back to the pioneering works of the French scientist Augustin-Louis Cauchy. Therefore, this theory is commonly referred to as the Cauchy continuum DRAPACA AND SIVALOGANATHAN [2019], TRUESDELL [1992]. We then extend the framework to include more sophisticated enriched continua.

2.1 Kinematics, deformation measures and time derivatives

In continuum mechanics, the body under focus is analyzed as a continuous matter, and the underlying microscopic structure is not explicitly considered. The microstructure role is taken into account in the material's laws (constitutive relations). We assume a body that consists of a continuous set of material points in the three-dimensional Euclidean space \mathbb{R}^3 . To analyze deformations, we introduce two distinct states of the body. We consider an undeformed reference configuration \mathcal{B}_0 at time $t = t_0$, known as well as the material, initial or Lagrangian configuration, where the position of each material point is defined by a material position vector \mathbf{X} . The body undergoes a deformation to the deformed current configuration \mathcal{B} at time $t > t_0$, known as well as actual, spatial or Eulerian configuration, which is characterized by a spatial position vector \mathbf{x} . The position vectors \mathbf{X} and \mathbf{x} are defined by the orthonormal (cartesian) basis vectors $\{\mathbf{E}_I\}$ and $\{\mathbf{e}_i\}$ in the reference and actual configurations, respectively, as

$$\mathbf{X} = X^I \mathbf{E}_I, \quad \text{and} \quad \mathbf{x} = x^i \mathbf{e}_i, \quad \text{with} \quad i, I = 1, 2, 3. \quad (2.1)$$

The motion (deformation) of the body from the reference configuration \mathcal{B}_0 to the current configuration \mathcal{B} is defined by a continuous unique one-to-one mapping function, depicted in Figure 2.1,

$$\varphi(\mathbf{X}, t) : \mathcal{B}_0 \rightarrow \mathcal{B}, \quad (2.2)$$

where each material point in the reference configuration is mapped to precisely one point in the current configuration. The deformation mapping is an injective one-to-one function. Therefore it excludes any deformations that involve tearing and interpenetration of the body's matter. As a result, the inverse of deformation mapping must exist and is well defined

$$\mathbf{x} = \varphi(\mathbf{X}, t) \quad \text{and} \quad \mathbf{X} = \varphi^{-1}(\mathbf{x}, t). \quad (2.3)$$

We define the displacement as the difference between the position in the reference and

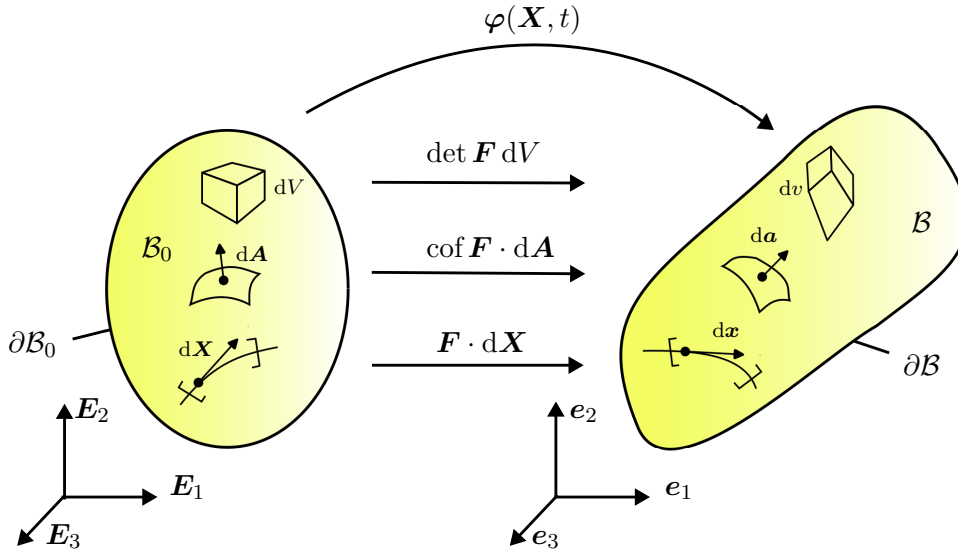


Figure 2.1: The body in reference (material) configuration on the left and current (spatial) configuration on the right.

current configuration

$$\mathbf{u}(\mathbf{X}, t) = \boldsymbol{\varphi}(\mathbf{X}, t) - \mathbf{X} = \mathbf{x} - \mathbf{X}. \quad (2.4)$$

The deformation gradient \mathbf{F} is a fundamental kinematic quantity on which every deformation and strain measure is based since it provides information on the alteration of the relative positions of the material points. It serves as a primary measure of deformation which is defined as the partial derivative of the spatial position \mathbf{x} with respect to the material position \mathbf{X}

$$\mathbf{F}(\mathbf{X}, t) = \frac{\partial \mathbf{x}}{\partial \mathbf{X}} = \text{Grad } \mathbf{x} = \nabla \mathbf{x}, \quad (2.5)$$

which can be rewritten in an alternative representation as

$$\mathbf{F} = \nabla(\mathbf{X} + \mathbf{u}) = \mathbf{I} + \nabla \mathbf{u}, \quad (2.6)$$

with the identity tensor \mathbf{I} and the gradient-operator $\text{Grad}(\bullet) = \nabla(\bullet)$ with respect to the material position \mathbf{X} . The deformation gradient is a linear operator which maps an infinitesimal line element from the reference undeformed configuration $d\mathbf{X}$ to the current deformed configuration $d\mathbf{x}$ as

$$d\mathbf{x} = \mathbf{F}(\mathbf{X}, t) \cdot d\mathbf{X} \quad \text{and} \quad d\mathbf{X} = \mathbf{F}^{-1}(\mathbf{x}, t) \cdot d\mathbf{x}, \quad (2.7)$$

where the inverse of the deformation gradient is defined as

$$\mathbf{F}^{-1}(\mathbf{x}, t) = \frac{\partial \mathbf{X}}{\partial \mathbf{x}} = \text{grad } \mathbf{X} = \nabla_{\mathbf{x}} \mathbf{X} = \mathbf{I} - \nabla_{\mathbf{x}} \mathbf{u}, \quad (2.8)$$

with $\text{grad}(\bullet) = \nabla_{\mathbf{x}}(\bullet)$ is the gradient operator with respect to the spatial position \mathbf{x} .

An infinitesimal material area element $d\mathbf{A} = \mathbf{N} dA$, with the material unit outward normal vector \mathbf{N} , is mapped into the actual configuration $d\mathbf{a} = \mathbf{n} da$, with the spatial unit outward normal vector \mathbf{n} , through the transformation

$$d\mathbf{a} = \det[\mathbf{F}] \mathbf{F}^{-T} \cdot d\mathbf{A} = \text{cof } \mathbf{F} \cdot d\mathbf{A}, \quad (2.9)$$

with $\text{cof } \mathbf{F} := \det[\mathbf{F}] \mathbf{F}^{-T}$ is the cofactor of \mathbf{F} . We transform an infinitesimal volume element from the reference configuration dV to the current configuration dv as

$$dv = \det \mathbf{F} dV . \quad (2.10)$$

To ensure the existence of a unique (one-to-one) transformation map, it is necessary to confirm the existence of the inverse mapping φ^{-1} . Consequently, the deformation gradient cannot be singular, and its inverse must exist, i.e. $\det \mathbf{F} \neq 0$. To prevent self-penetration of the body and the occurrence of negative volume elements, we enforce as a necessary condition that the determinant of the deformation gradient, referred to as the Jacobian, must be strictly positive $J := \det \mathbf{F} > 0$.

The deformation gradient \mathbf{F} describes the total deformation of the body, which can be decomposed multiplicatively (polar decomposition, see NEFF ET AL. [2014b]) into the stretch (straining) part and the rigid body rotation

$$\mathbf{F} = \mathbf{R} \cdot \mathbf{U} = \mathbf{V} \cdot \mathbf{R} , \quad (2.11)$$

with \mathbf{R} as the rotation tensor, and \mathbf{U} and \mathbf{V} are the right (material) stretch tensor and the left (spatial) stretch tensor, respectively. The rotation tensor is a proper orthogonal tensor that satisfies $\mathbf{R}^T = \mathbf{R}^{-1}$, $\mathbf{R}^T \cdot \mathbf{R} = \mathbf{I}$ and $\det \mathbf{R} = 1$. The deformation gradient provides all the information about the local deformation of a material point. However, it is not the most suitable method for accurately describing shape alterations because it includes the effects of rigid body rotations. We introduce the right (material) and left (spatial) Cauchy-Green deformation tensors as suitable deformation measures

$$\mathbf{C} = \mathbf{F}^T \cdot \mathbf{F} = \mathbf{U}^T \cdot \mathbf{U} \quad \text{and} \quad \mathbf{B} = \mathbf{F} \cdot \mathbf{F}^T = \mathbf{V} \cdot \mathbf{V}^T , \quad (2.12)$$

which are symmetric and free of rigid body rotations. They carry only information about the stretch of the body. Further, a key (relative) deformation measure is defined as half of the difference between the square norm of an infinitesimal line element in the reference configuration ($d\mathbf{X}$) and the square norm of the same line element after mapping into the actual configuration ($d\mathbf{x}$)

$$\begin{aligned} \frac{1}{2}(d\mathbf{x} \cdot d\mathbf{x} - d\mathbf{X} \cdot d\mathbf{X}) &= \frac{1}{2}(d\mathbf{X} \cdot \mathbf{F}^T \cdot \mathbf{F} \cdot d\mathbf{X} - d\mathbf{X} \cdot \mathbf{I} \cdot d\mathbf{X}) \\ &= d\mathbf{X} \cdot \frac{1}{2}(\mathbf{F}^T \cdot \mathbf{F} - \mathbf{I}) \cdot d\mathbf{X} \\ &= d\mathbf{X} \cdot \underbrace{\frac{1}{2}(\mathbf{C} - \mathbf{I})}_{:= \mathbf{E}} \cdot d\mathbf{X} . \end{aligned} \quad (2.13)$$

The Green-Lagrange strain tensor \mathbf{E} is symmetric and defined in the reference configuration. It vanishes for undeformed bodies and is independent of rigid body motions and rotations. It can be rewritten considering Equations (2.6) and (2.12) as

$$\mathbf{E} = \frac{1}{2} (\nabla \mathbf{u} + (\nabla \mathbf{u})^T + (\nabla \mathbf{u})^T \cdot \nabla \mathbf{u}) . \quad (2.14)$$

Alternatively, we rewrite Equation (2.13) as the following

$$\begin{aligned}
\frac{1}{2}(\mathrm{d}\mathbf{x} \cdot \mathrm{d}\mathbf{x} - \mathrm{d}\mathbf{X} \cdot \mathrm{d}\mathbf{X}) &= \frac{1}{2}(\mathrm{d}\mathbf{x} \cdot \mathbf{I} \cdot \mathrm{d}\mathbf{x} - \mathrm{d}\mathbf{x} \cdot \mathbf{F}^{-T} \cdot \mathbf{F}^{-1} \cdot \mathrm{d}\mathbf{x}) \\
&= \mathrm{d}\mathbf{x} \cdot \frac{1}{2}(\mathbf{I} - \mathbf{F}^{-T} \cdot \mathbf{F}^{-1}) \cdot \mathrm{d}\mathbf{x} \\
&= \mathrm{d}\mathbf{x} \cdot \underbrace{\frac{1}{2}(\mathbf{I} - \mathbf{B}^{-1})}_{:=\mathbf{e}} \cdot \mathrm{d}\mathbf{x}.
\end{aligned} \tag{2.15}$$

The Almansi strain tensor \mathbf{e} is symmetric and defined in the actual configuration. It vanishes for undeformed bodies and is independent of rigid body motions and rotations. It can be rewritten considering Equations (2.8) and (2.12) as

$$\mathbf{e} = \frac{1}{2} (\nabla_{\mathbf{x}}\mathbf{u} + (\nabla_{\mathbf{x}}\mathbf{u})^T - (\nabla_{\mathbf{x}}\mathbf{u})^T \cdot \nabla_{\mathbf{x}}\mathbf{u}). \tag{2.16}$$

The derivatives of the kinematic quantities in time and space are required to find the partial differential equations that govern the motion and deformation of the body. In the following, we introduce the time derivative of quantities we need later. The material velocity and material acceleration are obtained as the first and the second time derivatives of the motion function $\varphi(\mathbf{X}, t)$, receptively, characterized in the Lagrangian reference system ($\partial\mathbf{X}/\partial t = \mathbf{0}$)

$$\begin{aligned}
\dot{\mathbf{x}}(\mathbf{X}, t) &= \frac{\mathrm{d}\mathbf{x}(\mathbf{X}, t)}{\mathrm{d}t} = \frac{\partial\varphi(\mathbf{X}, t)}{\partial t}, \\
\ddot{\mathbf{x}}(\mathbf{X}, t) &= \frac{\mathrm{d}\dot{\mathbf{x}}(\mathbf{X}, t)}{\mathrm{d}t} = \frac{\partial^2\varphi(\mathbf{X}, t)}{\partial t^2}.
\end{aligned} \tag{2.17}$$

The material time derivative of the deformation gradient, which is referred to as the material velocity gradient, reads

$$\dot{\mathbf{F}} = \frac{\mathrm{d}}{\mathrm{d}t} \left(\frac{\partial\mathbf{x}}{\partial\mathbf{X}} \right) = \frac{\partial\dot{\mathbf{x}}}{\partial\mathbf{X}} = \text{Grad } \dot{\mathbf{x}} = \frac{\partial\dot{\mathbf{x}}}{\partial\mathbf{x}} \cdot \frac{\partial\mathbf{x}}{\partial\mathbf{X}} = \mathbf{L} \cdot \mathbf{F}, \tag{2.18}$$

with \mathbf{L} is the spatial velocity gradient which is given as

$$\mathbf{L} := \frac{\partial\dot{\mathbf{x}}}{\partial\mathbf{x}} = \text{grad } \dot{\mathbf{x}} = \frac{\partial\dot{\mathbf{x}}}{\partial\mathbf{X}} \cdot \frac{\partial\mathbf{X}}{\partial\mathbf{x}} = \dot{\mathbf{F}} \cdot \mathbf{F}^{-1}. \tag{2.19}$$

Finally, we calculate the material time derivative of the Jacobian

$$j = \frac{\partial \det \mathbf{F}}{\partial t} = \frac{\partial \det \mathbf{F}}{\partial \mathbf{F}} : \frac{\partial \mathbf{F}}{\partial t} = \det[\mathbf{F}] \mathbf{F}^{-T} : \dot{\mathbf{F}} = \underbrace{J \mathbf{F}^{-T} : (\mathbf{L} \cdot \mathbf{F})}_{\text{tr } \mathbf{L}} = J \text{div } \dot{\mathbf{x}}. \tag{2.20}$$

In this work, we consider only bodies undergoing small deformations and rotations which leads to the assumption that the components of the displacement gradient tensor are very small, i.e. $|\frac{\partial u_i}{\partial x_j}| \ll 1$ with $i, j = 1, 2, 3$. We neglect higher-order terms seen in Equations (2.14) and (2.16), leading to the linear strain tensor $\boldsymbol{\varepsilon}$ defined as

$$\boldsymbol{\varepsilon} = \frac{1}{2} (\nabla \mathbf{u} + (\nabla \mathbf{u})^T) = \text{sym}[\nabla \mathbf{u}], \quad (2.21)$$

which will be used to describe the deformations. Note that, within the assumption of small deformations and rotations, the space gradient can be considered the same in both material and spatial coordinates ($\nabla \bullet \approx \nabla_{\mathbf{x}} \bullet$).

2.2 Concept of stress

Consider a deformable continuum body subjected to external effects such as mechanical loads, gravity forces, heating or others. The internal forces that arise on infinitesimal surfaces within the body as a reaction to the external effects are referred to as stress. This stress can be visualized by a cut through the body with the normal vector \mathbf{n} acting on the cutting plane, see Figure 2.2.

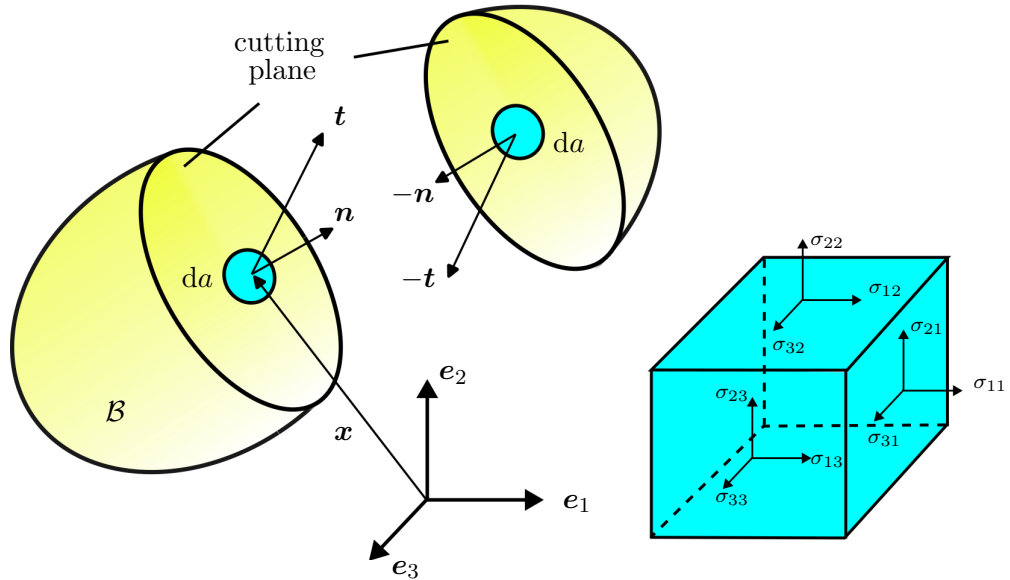


Figure 2.2: Illustration of a body detached into two parts to show the traction vector. The state of the stress can be expressed by the components of the traction vectors on three cutting planes with the normal vectors \mathbf{e}_1 , \mathbf{e}_2 , and \mathbf{e}_3 .

The forces are transmitted through the cutting surface from one segment to another, resulting in a force vector $\Delta \mathbf{f}$ distribution on a small area Δa which is belonging to the cutting plane. For an infinitesimally small area, i.e. $\Delta a \rightarrow 0$, we introduce the traction vector \mathbf{t} as

$$\mathbf{t}(\mathbf{x}, t, \mathbf{n}) := \lim_{\Delta a \rightarrow 0} \frac{\Delta \mathbf{f}}{\Delta a} = \frac{d\mathbf{f}}{da}. \quad (2.22)$$

The Cauchy theorem states that a symmetric second-order tensor field $\boldsymbol{\sigma}(\mathbf{x}, t)$ exists, which is independent of the orientation of \mathbf{n} and satisfies

$$\mathbf{t}(\mathbf{x}, t, \mathbf{n}) = \boldsymbol{\sigma}(\mathbf{x}, t) \cdot \mathbf{n}. \quad (2.23)$$

The Cauchy stress tensor $\boldsymbol{\sigma}$ represents the true stress in the current configuration because it relates the current force in the cutting plane to the current area element. The Cauchy

stress tensor can be expressed by three traction vectors associated to three cutting planes in the actual configuration defined by three linearly independent (perpendicular) normal vectors. An obvious choice is, of course, the traction vectors $\mathbf{t}_{\mathbf{e}_1}$, $\mathbf{t}_{\mathbf{e}_2}$ and $\mathbf{t}_{\mathbf{e}_3}$ defined on the cutting planes with the normal vectors \mathbf{e}_1 , \mathbf{e}_2 and \mathbf{e}_3 , respectively, representing the orthonormal basis vectors

$$\boldsymbol{\sigma}(\mathbf{x}, t) = \mathbf{t}_{\mathbf{e}_i} \otimes \mathbf{n}_j = t_{\mathbf{e}_i} \mathbf{e}_i \otimes n_j \mathbf{e}_j = \begin{pmatrix} \sigma_{11} & \sigma_{12} & \sigma_{13} \\ \sigma_{21} & \sigma_{22} & \sigma_{33} \\ \sigma_{31} & \sigma_{32} & \sigma_{33} \end{pmatrix} \mathbf{e}_i \otimes \mathbf{e}_j. \quad (2.24)$$

The index i of the stress tensor components σ_{ij} indicates the direction in which the traction component is pointing, and the index j defines the direction of the normal of the cutting surface. The present dissertation consider only bodies subjected to small deformations, and therefore, further stress quantities are not described.

2.3 Balance equations

In the following discussion, we explore the fundamental principles of continuum mechanics, which are material-independent and grounded on axioms that govern every natural phenomenon, i.e. they are based on observations and cannot be deduced from other laws. These principles serve as the essential basics for developing material modeling in computational mechanics. Below, we introduce the balance of mass, the balance of linear momentum, the balance of angular momentum, the balance of energy and the entropy inequality.

2.3.1 Balance of mass

The conservation law of mass states that “the total mass remains constant during the motion or deformation, provided it does not exchange mass with its surroundings, i.e. mass flux is zero”. In other words, mass cannot be created or destroyed. The total mass m reads

$$m = \int_{\mathcal{B}} \rho(\mathbf{x}, t) dv = \text{const}, \quad (2.25)$$

where ρ is the actual density. The material time derivative of the total mass is obtained, taking into consideration $dv = J dV$ and Equations (2.20) and (2.25), which has to vanish

$$\dot{m} = \frac{dm}{dt} = \frac{d}{dt} \int_{\mathcal{B}} \rho dv = \int_{\mathcal{B}} (\rho \operatorname{div} \dot{\mathbf{x}} + \dot{\rho}) dv = 0, \quad (2.26)$$

and the local form of the balance of mass reads

$$\rho \operatorname{div} \dot{\mathbf{x}} + \dot{\rho} = 0 \quad \forall \mathbf{x} \in \mathcal{B}, \quad (2.27)$$

with $\dot{\rho} = \frac{\partial \rho}{\partial t}$ is the material time derivative of the actual density. However, for small deformations, the difference between the actual and reference configurations is negligible and it is valid to assume $J \approx 1$ and $\dot{\rho} \approx 0$.

2.3.2 Balance of linear momentum

The axiom of balance of linear momentum, also known as Newton's second law of motion, postulates that "the material time derivative of the linear momentum is equal to the sum of all external surface and volume forces acting on the body". Thus, we have

$$\frac{d}{dt} \int_B \rho \dot{\mathbf{x}} dv = \int_B \bar{\mathbf{f}} dv + \int_{\partial B} \mathbf{t} da. \quad (2.28)$$

Here, $\bar{\mathbf{f}}$ is the body force per unit volume, and the traction vector \mathbf{t} acts on the boundary ∂B . With the help of the balance of mass in Equation (2.27), we get

$$\frac{d}{dt} \int_B \rho \dot{\mathbf{x}} dv = \int_B \rho \ddot{\mathbf{x}} dv. \quad (2.29)$$

By making use of Cauchy theorem in Equation (2.23) and the divergence theorem, i.e. $\int_{\partial B} \boldsymbol{\sigma} \cdot \mathbf{n} da = \int_B \operatorname{div} \boldsymbol{\sigma} dv$, the balance of linear momentum becomes

$$\int_B (\operatorname{div} \boldsymbol{\sigma} + \bar{\mathbf{f}} - \rho \ddot{\mathbf{x}}) dv = \mathbf{0}, \quad (2.30)$$

and the local statement of balance of linear momentum reads

$$\operatorname{div} \boldsymbol{\sigma} + \bar{\mathbf{f}} - \rho \ddot{\mathbf{x}} = \mathbf{0} \quad \forall \mathbf{x} \in \mathcal{B}. \quad (2.31)$$

2.3.3 Balance of angular momentum

The balance of angular momentum states that "the material time derivative of the angular momentum, also referred to as the moment of momentum, with respect to a fixed reference point $\bar{\mathbf{x}}$ is equal to the resultant moment of all external forces and moments acting on the body, with respect to the same reference point $\bar{\mathbf{x}}$ ". Thus, we get

$$\frac{d}{dt} \int_B \rho (\mathbf{x} - \bar{\mathbf{x}}) \times \dot{\mathbf{x}} dv = \int_B (\mathbf{x} - \bar{\mathbf{x}}) \times \bar{\mathbf{f}} dv + \int_{\partial B} (\mathbf{x} - \bar{\mathbf{x}}) \times \mathbf{t} da. \quad (2.32)$$

Seeking simplicity and without loss of generality, we consider $\bar{\mathbf{x}} = \mathbf{0}$. The left-hand side in Equation (2.32) becomes with the use of the balance of mass in Equation (2.27)

$$\frac{d}{dt} \int_B \rho \mathbf{x} \times \dot{\mathbf{x}} dv = \int_B \rho \mathbf{x} \times \ddot{\mathbf{x}} dv. \quad (2.33)$$

The traction part in Equation (2.32) can be reformulated by taking into consideration the divergence theorem and introducing the third-order permutation tensor \mathcal{E} as

$$\int_{\partial B} \mathbf{x} \times \mathbf{t} da = \int_{\partial B} \mathbf{x} \times \boldsymbol{\sigma} \cdot \mathbf{n} da = \int_B \mathbf{x} \times \operatorname{div} \boldsymbol{\sigma} + \mathcal{E} : \boldsymbol{\sigma}^T dv. \quad (2.34)$$

The third-order permutation tensor \mathcal{E} is defined by

$$\begin{aligned}
\mathcal{E}_{ijk} &= +1, & \text{when } (i, j, k) & \text{ is } (1, 2, 3), (2, 3, 1) \text{ or } (3, 1, 2) \\
\mathcal{E}_{ijk} &= -1, & \text{when } (i, j, k) & \text{ is } (3, 2, 1), (2, 1, 3) \text{ or } (1, 3, 2) \\
\mathcal{E}_{ijk} &= 0, & & \text{otherwise.}
\end{aligned} \tag{2.35}$$

Substituting Equations (2.33) and (2.34) into Equation (2.32) and considering the linear momentum balance in Equation (2.31), we obtain

$$\int_B \rho \mathbf{x} \times \underbrace{(\operatorname{div} \boldsymbol{\sigma} + \bar{\mathbf{f}} - \rho \ddot{\mathbf{x}})}_{=0} + \mathcal{E} : \boldsymbol{\sigma}^T dv = \mathbf{0}, \tag{2.36}$$

which leads to

$$\int_B \mathcal{E} : \boldsymbol{\sigma}^T dv = \mathbf{0}, \quad \text{and} \quad \mathcal{E} : \boldsymbol{\sigma}^T = \mathbf{0} \quad \forall \mathbf{x} \in \mathcal{B}. \tag{2.37}$$

The corresponding local form can be rewritten with the definition in Equation (2.35)

$$\mathcal{E} : \boldsymbol{\sigma}^T = \mathcal{E}_{ijk} : \sigma_{kj} \mathbf{e}_i = \begin{pmatrix} \sigma_{32} - \sigma_{23} \\ \sigma_{13} - \sigma_{31} \\ \sigma_{21} - \sigma_{12} \end{pmatrix} = \mathbf{0} \quad \forall \mathbf{x} \in \mathcal{B}, \tag{2.38}$$

and the Cauchy stress has to be symmetric, i.e.

$$\boldsymbol{\sigma} = \boldsymbol{\sigma}^T \quad \forall \mathbf{x} \in \mathcal{B}. \tag{2.39}$$

2.3.4 Balance of energy

The balance of energy, also known as the first law of thermodynamics, states that “the material time derivative of the total energy of a physical body, split into internal and kinetic energy, is equal to the sum of the power resulting from all external loads acting on the body”. We will, however, restrict ourselves to mechanical isothermal processes (constant temperature and no heat source or flux). Thus, we obtain

$$\frac{d}{dt} \left[\underbrace{\int_B \rho e dv}_{\text{internal energy}} + \underbrace{\int_B \frac{1}{2} \rho \dot{\mathbf{x}} \cdot \dot{\mathbf{x}} dv}_{\text{kinetic energy}} \right] = \underbrace{\int_B \dot{\mathbf{x}} \cdot \bar{\mathbf{f}} dv + \int_{\partial B} \dot{\mathbf{x}} \cdot \mathbf{t} da}_{\text{mechanical power}}, \tag{2.40}$$

where e denotes the specific internal energy defined per unit mass. The individual terms used above are reformulated with the assumption of small deformations to

$$\frac{d}{dt} \int_B \rho e dv = \int_B \rho \dot{e} dv, \tag{2.41}$$

$$\frac{d}{dt} \int_B \frac{1}{2} \rho \dot{\mathbf{x}} \cdot \dot{\mathbf{x}} dv = \int_B \rho \dot{\mathbf{x}} \cdot \ddot{\mathbf{x}} dv, \tag{2.42}$$

$$\int_{\partial B} \dot{\mathbf{x}} \cdot \mathbf{t} \, da = \int_B \dot{\mathbf{x}} \cdot \operatorname{div} \boldsymbol{\sigma} + \boldsymbol{\sigma} : \nabla \dot{\mathbf{x}} \, dv = \int_B \dot{\mathbf{x}} \cdot \operatorname{div} \boldsymbol{\sigma} + \boldsymbol{\sigma} : \dot{\boldsymbol{\varepsilon}} \, dv, \quad (2.43)$$

and by substituting into Equation (2.40), we obtain the expression

$$\int_B \rho \dot{e} - \boldsymbol{\sigma} : \dot{\boldsymbol{\varepsilon}} - \dot{\mathbf{x}} \cdot \underbrace{[\operatorname{div} \boldsymbol{\sigma} + \bar{\mathbf{f}} - \rho \ddot{\mathbf{x}}]}_{=0} \, dv = \int_B \rho \dot{e} - \boldsymbol{\sigma} : \dot{\boldsymbol{\varepsilon}} \, dv = 0. \quad (2.44)$$

Thus, the local statement of the balance of energy reads

$$\rho \dot{e} - \boldsymbol{\sigma} : \dot{\boldsymbol{\varepsilon}} = 0 \quad \forall \mathbf{x} \in \mathcal{B}. \quad (2.45)$$

2.3.5 Entropy inequality

A mathematical model is said to be thermodynamically consistent when it satisfies the entropy inequality, which every natural phenomenon obeys, as the disorder only increases. The entropy inequality, also known as the second law of thermodynamics, cannot be interpreted as a classical balance equation. It gives information about the direction in which an observed phenomenon should proceed. It is given in the form of an inequality where “the entropy change in a closed system must be zero for reversible processes and positive for irreversible processes”. The entropy \mathcal{S} of a body \mathcal{B} is introduced in terms of a specific entropy density function η defined per unit mass as

$$\mathcal{S} = \int_{\mathcal{B}} \rho \eta \, dv. \quad (2.46)$$

The entropy inequality for thermal independent processes with using the local statement of the balance of mass in Equation (2.27) reads

$$\dot{\mathcal{S}} = \frac{d}{dt} \int_{\mathcal{B}} \rho \eta \, dv = \int_{\mathcal{B}} \rho \dot{\eta} \, dv \geq 0. \quad (2.47)$$

Taking into consideration Helmholtz free energy per unit mass $\tilde{\psi} = e - \theta \eta$, and since we assume only isothermal processes, i.e. the temperature is constant $\theta = \operatorname{const} > 0$, we get the following local form with the help of the balance of energy in Equation (2.45)

$$\rho (\dot{e} - \dot{\tilde{\psi}}) = \boldsymbol{\sigma} : \dot{\boldsymbol{\varepsilon}} - \rho \dot{\tilde{\psi}} \geq 0 \quad \forall \mathbf{x} \in \mathcal{B}, \quad (2.48)$$

and with the introduction of the volume-specific Helmholtz free energy $\psi = \rho \tilde{\psi}$, the local form of the entropy inequality for small deformations can be reformulated to read

$$\boldsymbol{\sigma} : \dot{\boldsymbol{\varepsilon}} - \dot{\psi} \geq 0 \quad \forall \mathbf{x} \in \mathcal{B}. \quad (2.49)$$

With the assumption that the volume-specific free energy is a function of the linear strain, i.e. $\psi = \psi(\boldsymbol{\varepsilon})$, we can modify the entropy inequality to

$$\boldsymbol{\sigma} : \dot{\boldsymbol{\varepsilon}} - \frac{\partial \psi}{\partial \boldsymbol{\varepsilon}} : \dot{\boldsymbol{\varepsilon}} = \left(\boldsymbol{\sigma} - \frac{\partial \psi}{\partial \boldsymbol{\varepsilon}} \right) : \dot{\boldsymbol{\varepsilon}} \geq 0 \quad \forall \mathbf{x} \in \mathcal{B}, \quad (2.50)$$

and the constitutive relation for the stress tensor reads

$$\boldsymbol{\sigma} = \frac{\partial \psi}{\partial \boldsymbol{\varepsilon}}. \quad (2.51)$$

The previous stress-strain relation describes a hyperelastic material. The stress of a hyperelastic material can be derived from an assumed strain energy function. No entropy is produced (no plastic deformation, no damage, etc.), and the process is reversible. The corresponding standard elasticity tensor is obtained then as

$$\mathbb{C} = \frac{\partial \boldsymbol{\sigma}}{\partial \boldsymbol{\varepsilon}} = \frac{\partial^2 \psi}{\partial \boldsymbol{\varepsilon}^2} \quad \text{with} \quad \boldsymbol{\sigma} = \mathbb{C} : \boldsymbol{\varepsilon}. \quad (2.52)$$

For linear isotropic materials, the strain energy function takes the form

$$\psi = \mu \boldsymbol{\varepsilon} : \boldsymbol{\varepsilon} + \frac{1}{2} \lambda (\text{tr } \boldsymbol{\varepsilon})^2, \quad (2.53)$$

and the corresponding stress and elasticity tensors are

$$\boldsymbol{\sigma} = 2\mu \boldsymbol{\varepsilon} + \lambda (\text{tr } \boldsymbol{\varepsilon}) \mathbf{I} \quad \text{and} \quad \mathbb{C} = 2\mu \mathbb{I} + \lambda \mathbf{I} \otimes \mathbf{I}, \quad (2.54)$$

with $\mathbb{I}_{ijkl} = \frac{1}{2} [\delta_{ik} \delta_{jl} + \delta_{il} \delta_{jk}]$.

2.4 Material modeling: isotropy and anisotropy

When considering materials with specific microstructures like metamaterials, crystals, composites, and biological tissues, the behavior of the material can be directionally dependent, leading to what is termed as anisotropic behavior. On the other hand, materials exhibiting directionally independent behavior are termed isotropic. In order to formulate physically meaningful constitutive laws, the principles of material frame indifference and material symmetry need to be fulfilled, see e.g. BRANDS [2012], D'AGOSTINO ET AL. [2024], LABUSCH [2018], TRUESDELL [1969], TRUESDELL AND NOLL [1965], TRUESDELL AND TOUPIN [1960b], VIEBAHN [2019].

The principle of material frame indifference (objectivity) postulates that “the material response does not differ by changing the position of the observer”. In other words, it requires the invariance of the constitutive equations under superimposed rigid body motion. Let us assume a scalar-valued function $\hat{f}(\mathbf{v}_i, \mathbf{V}_i)$, a vector-valued function $\hat{\mathbf{f}}(\mathbf{v}_i, \mathbf{V}_i)$ and a tensor-valued function $\hat{\mathbf{F}}(\mathbf{v}_i, \mathbf{V}_i)$ depending on the vector-valued arguments \mathbf{v}_i and tensor-valued arguments \mathbf{V}_i . The functions \hat{f} , $\hat{\mathbf{f}}$ and $\hat{\mathbf{F}}$ satisfy the principle of material frame indifference when

$$\left. \begin{aligned} \hat{f}(\mathbf{v}_i, \mathbf{V}_i) &= \hat{f}(\mathbf{Q} \cdot \mathbf{v}_i, \mathbf{Q} \cdot \mathbf{V}_i \cdot \mathbf{Q}^T) \\ \mathbf{Q} \cdot \hat{\mathbf{f}}(\mathbf{v}_i, \mathbf{V}_i) &= \hat{\mathbf{f}}(\mathbf{Q} \cdot \mathbf{v}_i, \mathbf{Q} \cdot \mathbf{V}_i \cdot \mathbf{Q}^T) \\ \mathbf{Q} \cdot \hat{\mathbf{F}}(\mathbf{v}_i, \mathbf{V}_i) \cdot \mathbf{Q}^T &= \hat{\mathbf{F}}(\mathbf{Q} \cdot \mathbf{v}_i, \mathbf{Q} \cdot \mathbf{V}_i \cdot \mathbf{Q}^T) \end{aligned} \right\} \quad \forall \mathbf{Q} \in \text{SO}(3), \quad (2.55)$$

where the special orthogonal group $SO(3)$ represents an arbitrary rigid body rotation, i.e. the transformation $\mathbf{Q} \in SO(3)$ satisfies $\det \mathbf{Q} = 1$ and $\mathbf{Q}^T = -\mathbf{Q}$. The tensor functions \hat{f} , $\hat{\mathbf{f}}$ and $\hat{\mathbf{F}}$ are then termed as isotropic tensor functions.

The description of the material behavior must satisfy the principle of material symmetry as well, which states that “the constitutive response of a body must be independent of a transformation \mathbf{Q} belonging to its symmetry group \mathcal{G}_k ”, see D’AGOSTINO ET AL. [2024]. The symmetry group \mathcal{G}_k incorporates information about material symmetry. Thus, for a material with a given constitutive relationship of the form $\boldsymbol{\sigma} := \hat{\boldsymbol{\sigma}}(\boldsymbol{\varepsilon})$ and a given free energy function of the form $\psi := \hat{\psi}(\boldsymbol{\varepsilon})$, we have

$$\left. \begin{aligned} \mathbf{Q} \cdot \hat{\boldsymbol{\sigma}}(\boldsymbol{\varepsilon}) \cdot \mathbf{Q}^T &= \hat{\boldsymbol{\sigma}}(\mathbf{Q} \cdot \boldsymbol{\varepsilon} \cdot \mathbf{Q}^T) \\ \hat{\psi}(\boldsymbol{\varepsilon}) &= \hat{\psi}(\mathbf{Q} \cdot \boldsymbol{\varepsilon} \cdot \mathbf{Q}^T) \end{aligned} \right\} \quad \forall \mathbf{Q} \in \mathcal{G}_k. \quad (2.56)$$

A material is said to be isotropic if it is independent of any transformation \mathbf{Q} where \mathcal{G}_k is the special orthogonal group $SO(3)$ for this case. An isotropic strain energy and stress functions depending on the strain satisfies

$$\left. \begin{aligned} \mathbf{Q} \cdot \hat{\boldsymbol{\sigma}}(\boldsymbol{\varepsilon}) \cdot \mathbf{Q}^T &= \hat{\boldsymbol{\sigma}}(\mathbf{Q} \cdot \boldsymbol{\varepsilon} \cdot \mathbf{Q}^T) \\ \hat{\psi}(\boldsymbol{\varepsilon}) &= \hat{\psi}(\mathbf{Q} \cdot \boldsymbol{\varepsilon} \cdot \mathbf{Q}^T) \end{aligned} \right\} \quad \forall \mathbf{Q} \in SO(3), \quad (2.57)$$

which satisfies the requirement of the material frame indifference in Equation (2.55). Otherwise, the material symmetry group \mathcal{G}_k is a subgroup of $SO(3)$, then the material is anisotropic. This means an arbitrary rotation of the material under the same unrotated loading leads to a different material response. In order to characterize the behavior of anisotropic materials, the concept of structural tensors is introduced. The structural tensors \mathbf{M}_i are defined as $\mathbf{M}_i = \mathbf{a}_i \otimes \mathbf{a}_i$, with \mathbf{a}_i being the preferred directions of unit length. The structural tensors preserve the material symmetry group

$$\mathbf{M}_i = \mathbf{Q} \cdot \mathbf{M}_i \cdot \mathbf{Q}^T \quad \forall \mathbf{Q} \in \mathcal{G}_k. \quad (2.58)$$

An anisotropic strain energy and stress functions depending on the strain have to satisfy the requirements of material symmetry for the considered material, which read

$$\left. \begin{aligned} \mathbf{Q} \cdot \hat{\boldsymbol{\sigma}}(\boldsymbol{\varepsilon}, \mathbf{M}_i) \cdot \mathbf{Q}^T &= \hat{\boldsymbol{\sigma}}(\mathbf{Q} \cdot \boldsymbol{\varepsilon} \cdot \mathbf{Q}^T, \mathbf{M}_i) \\ \hat{\psi}(\boldsymbol{\varepsilon}, \mathbf{M}_i) &= \hat{\psi}(\mathbf{Q} \cdot \boldsymbol{\varepsilon} \cdot \mathbf{Q}^T, \mathbf{M}_i) \end{aligned} \right\} \quad \forall \mathbf{Q} \in \mathcal{G}_k. \quad (2.59)$$

The above-given relations in Equation (2.59), which hold for a special symmetry group \mathcal{G}_k of the assumed material, will be transformed to isotropic functions that are valid for any rigid body rotation $\mathbf{Q} \in SO(3)$. To do so, we rotate the structural tensors as well

$$\left. \begin{aligned} \mathbf{Q} \cdot \hat{\boldsymbol{\sigma}}(\boldsymbol{\varepsilon}, \mathbf{M}_i) \cdot \mathbf{Q}^T &= \hat{\boldsymbol{\sigma}}(\mathbf{Q} \cdot \boldsymbol{\varepsilon} \cdot \mathbf{Q}^T, \mathbf{Q} \cdot \mathbf{M}_i \cdot \mathbf{Q}^T) \\ \hat{\psi}(\boldsymbol{\varepsilon}, \mathbf{M}_i) &= \hat{\psi}(\mathbf{Q} \cdot \boldsymbol{\varepsilon} \cdot \mathbf{Q}^T, \mathbf{Q} \cdot \mathbf{M}_i \cdot \mathbf{Q}^T) \end{aligned} \right\} \quad \forall \mathbf{Q} \in SO(3), \quad (2.60)$$

and the objectivity requirement in Equation (2.55) is fulfilled. Accordingly, we can find a defined number of invariants and the relevant tensor operators without violating the requirements of material symmetry.

2.5 Variational formulation for linear elasticity

To maintain coherence in this thesis, we introduce an alternative methodology to derive the balance equations, initially focusing on linear elasticity. This method is based on minimizing the total elastic energy, leading to the formulation of the balance equations. Subsequently, we extend this approach to address the balance equations for other generalized continua. In the theory of linearized elasticity, infinitesimal deformations and rotations are assumed, i.e. $\|\nabla \mathbf{u}\| \ll 1$, and the actual configuration coincides with the reference configuration. The total energy for linear elastic continuum for the static case reads

$$\Pi(\mathbf{u}) = \int_{\mathcal{B}} \psi(\nabla \mathbf{u}) - \bar{\mathbf{f}} \cdot \mathbf{u} \, dV - \int_{\partial \mathcal{B}_t} \mathbf{t} \cdot \mathbf{u} \, dA \rightarrow \min, \quad (2.61)$$

where the elastic energy density is defined as

$$\psi(\nabla \mathbf{u}) = \frac{1}{2} \text{sym } \nabla \mathbf{u} : \mathbb{C} : \text{sym } \nabla \mathbf{u}. \quad (2.62)$$

The variation of the total energy with respect to the displacement vector, i.e. $\delta_{\mathbf{u}} \Pi = 0$, with

$$\delta_{\mathbf{u}} \Pi = \int_{\mathcal{B}} \mathbb{C} : \text{sym } \nabla \mathbf{u} : \nabla \delta \mathbf{u} - \bar{\mathbf{f}} \cdot \delta \mathbf{u} \, dV - \int_{\partial \mathcal{B}_t} \mathbf{t} \cdot \delta \mathbf{u} \, dA, \quad (2.63)$$

leads after applying integration by parts and the divergence theorem to

$$\delta_{\mathbf{u}} \Pi = \int_{\mathcal{B}} \{\text{div}(\mathbb{C} : \text{sym } \nabla \mathbf{u}) + \bar{\mathbf{f}}\} \cdot \delta \mathbf{u} \, dV, \quad (2.64)$$

and the associated strong form with the associated boundary conditions reads

$$\begin{aligned} \text{div}(\mathbb{C} : \text{sym } \nabla \mathbf{u}) + \bar{\mathbf{f}} &= \mathbf{0} && \text{in } \mathcal{B}, \\ \mathbf{t} &= (\mathbb{C} : \text{sym } \nabla \mathbf{u}) \cdot \mathbf{n} && \text{on } \partial \mathcal{B}_t, \\ \mathbf{u} &= \bar{\mathbf{u}} && \text{on } \partial \mathcal{B}_u, \end{aligned} \quad (2.65)$$

satisfying $\partial \mathcal{B}_u \cap \partial \mathcal{B}_t = \emptyset$ and $\partial \mathcal{B}_u \cup \partial \mathcal{B}_t = \partial \mathcal{B}$. The strain and stress quantities, both symmetric, are defined as $\boldsymbol{\varepsilon} = \text{sym } \nabla \mathbf{u}$ and $\boldsymbol{\sigma} = \mathbb{C} : \text{sym } \nabla \mathbf{u} = \mathbb{C} : \boldsymbol{\varepsilon}$.

2.6 Enriched continua

The classical continuum theory of Cauchy, as discussed earlier, considers the material point to be infinitesimally small, i.e. strict mathematical points. The micromorphic theory expands the material point's scope to capture a small space, e.g. one grain in granular materials or a unit-cell in metamaterials. Thus, it intrinsically provides the homogeneous continuum description with an internal length scale. The current Section is dedicated to extending the Cauchy continuum theory to encompass enriched continua in the most comprehensive manner possible, and we briefly introduce then three enriched continua.

Seeking comparison, we generally follow the notation used by the publications of the relaxed micromorphic model, such as NEFF ET AL. [2014a].

2.6.1 Kinematics

For the generalized continua theory, the physical body of interest consists of a set of material points with embedded deformable microcontinua, see Figure 2.3. This body in the reference configuration \mathcal{B}^0 undergoes deformation to reach the actual configuration \mathcal{B} . Within each material point, the embedded microcontinuum (or particle) in the reference configuration, denoted as \mathcal{B}_M^0 , deforms into \mathcal{B}_M in the actual configuration.

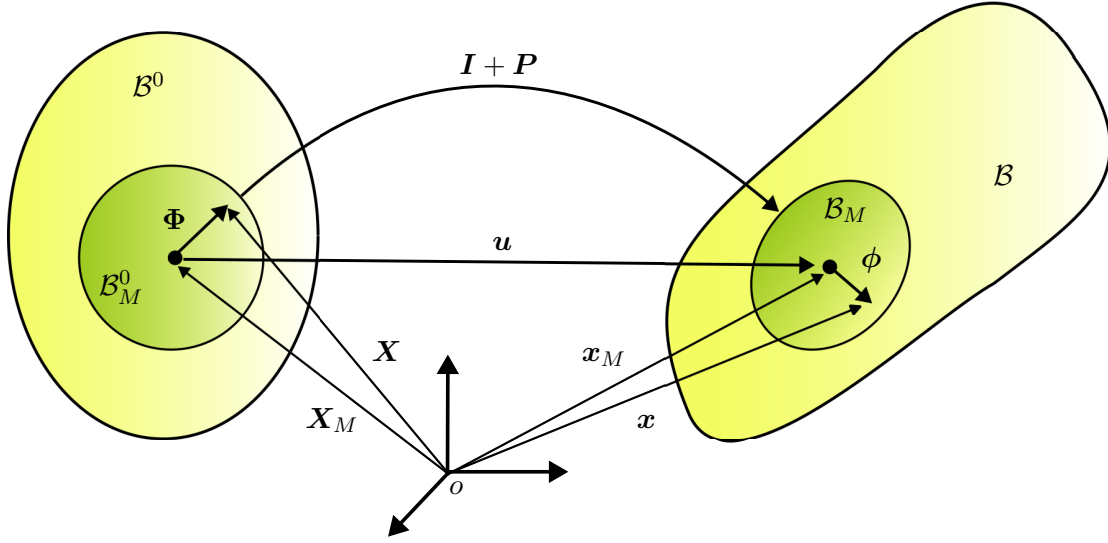


Figure 2.3: The micromorphic theory: the reference configuration on the left and current configuration on the right.

An appropriate mapping under an arbitrary deformation for the macro-micro system from the reference to the actual frame is achieved by combining both macro- and micromotion. The microcontinuum is characterized by its centroid. The macromotion carries this centroid from \mathbf{X}_M in the reference configuration to \mathbf{x}_M at the actual configuration as

$$\mathbf{x}_M(\mathbf{X}_M) = \mathbf{X}_M + \mathbf{u}(\mathbf{X}_M), \quad (2.66)$$

where \mathbf{u} is the macroscopic displacement vector. The micro deformation, accounting for the inner deformation of the particle, is assumed to be independent of the macroscopic deformation and homogeneous (first-order affine transformation). Consequently, a director vector Φ attached to the centroid of \mathcal{B}_M^0 is mapped to a director vector ϕ attached to the centroid of \mathcal{B}_M by

$$\phi = \mathbf{F}_M(\mathbf{X}_M) \cdot \Phi, \quad \text{with} \quad \mathbf{F}_M(\mathbf{X}_M) = \mathbf{I} + \mathbf{P}(\mathbf{X}_M), \quad (2.67)$$

where \mathbf{F}_M is the deformation gradient of the micromotion and \mathbf{P} is the micro-distortion field, see Equation (2.6). The micro-distortion is a macroscopic field which describes the microscopic deformation so the enriched continuum can capture the microscopic state explicitly. A point in the microcontinuum \mathcal{B}_M^0 with a position $\mathbf{X} = \mathbf{X}_M + \Phi$ in the reference configuration is mapped to a position \mathbf{x} at the actual configuration by

$$\mathbf{x}(\mathbf{X}_M, \Phi) = \mathbf{x}_m(\mathbf{X}_M) + \phi(\mathbf{X}_M, \Phi) = \mathbf{X}_M + \mathbf{u}(\mathbf{X}_M) + (\mathbf{I} + \mathbf{P}(\mathbf{X}_M)) \cdot \Phi, \quad (2.68)$$

and the motion of each point in the microcontinuum is uniquely defined by the pair $\{\mathbf{u}, \mathbf{P}\}$. In the most general case, the micro-distortion field \mathbf{P} is non-symmetric describing micro-shearing, micro-stretching and micro-rotation. The literature contains numerous models of enriched continua. These models differ mainly in the restrictions imposed on the micro-distortion field as well as the differential operator used for the curvature measure. In the following, we present the “full” micromorphic model by Mindlin-Eringen $(\mathbf{P}, \nabla \mathbf{P})$, The Cosserat micropolar model (skew \mathbf{P} , $\text{Curl } \mathbf{P}$) and the relaxed micromorphic model $(\mathbf{P}, \text{Curl } \mathbf{P})$. Our focus will remain solely on generalized continua within the framework of small deformations, so there will be no need to distinguish between reference and current configuration. The body of interest will be denoted by \mathcal{B} .

2.6.2 The micromorphic theory by Mindlin-Eringen

The micromorphic theory was developed first by R. D. Mindlin and A. C. Eringen in the 1960s, see for examples ERINGEN [1968], ERINGEN AND SUHUBI [1964], MINDLIN [1964; 1965], MINDLIN AND ESHEL [1968], SUHUBI AND ERINGEN [1964]. The full gradient of a second-order non-symmetric micro-distortion field is employed for the curvature measurement. The displacement vector $\mathbf{u}: \mathcal{B} \subseteq \mathbb{R}^3 \rightarrow \mathbb{R}^3$ and a non-symmetric micro-distortion field $\mathbf{P}: \mathcal{B} \subseteq \mathbb{R}^3 \rightarrow \mathbb{R}^{3 \times 3}$ are defined by the minimization of the total energy

$$\Pi(\mathbf{u}, \mathbf{P}) = \int_{\mathcal{B}} \psi(\nabla \mathbf{u}, \mathbf{P}, \nabla \mathbf{P}) \, dV \longrightarrow \min, \quad (2.69)$$

where no body forces or moments are considered presently seeking simplicity. The elastic energy density reads

$$\begin{aligned} \psi(\nabla \mathbf{u}, \mathbf{P}, \nabla \mathbf{P}) = \frac{1}{2} & \left((\nabla \mathbf{u} - \mathbf{P}) : \mathbb{C}_e : (\nabla \mathbf{u} - \mathbf{P}) + \text{sym } \mathbf{P} : \mathbb{C}_P : \text{sym } \mathbf{P} \right. \\ & \left. + \mu L_c^2 \nabla \mathbf{P} : \mathbb{L} : \nabla \mathbf{P} + 2(\nabla \mathbf{u} - \mathbf{P}) : \mathbb{C}_{e_P} : \text{sym } \mathbf{P} \right). \end{aligned} \quad (2.70)$$

Here, the fourth-order tensor $\mathbb{C}_e : \mathbb{R}^{3 \times 3} \rightarrow \mathbb{R}^{3 \times 3}$ acting on $\nabla \mathbf{u} - \mathbf{P}$ has at most 45 independent coefficients. The fourth-order tensor $\mathbb{C}_P : \text{Sym}(3) \rightarrow \text{Sym}(3)$ acting on $\text{sym } \mathbf{P}$ has the classical 21 independent coefficients. The sixth-order tensor \mathbb{L} is associated with curvature and has at most 378 coefficients while the fourth-order tensor \mathbb{C}_{e_P} has 54 independent coefficients. The parameter $L_c > 0$ is the characteristic length, and $\mu > 0$ is added for dimensional consistency, while \mathbb{L} is dimensionless. Note that this formulation here with $45 + 21 + 378 + 54 = 498$ independent coefficients is even simpler than the more general formulation in MINDLIN [1964], which contains two additional mixed terms, i.e. $(\nabla \mathbf{P}, \nabla \mathbf{u} - \mathbf{P})$ and $(\nabla \mathbf{P}, \text{Sym } \mathbf{P})$, with two associated fifth-order tensors with a total 903 independent coefficients. The specific appearance of $\text{sym } \mathbf{P}$ in the energy function is dictated by infinitesimal Galilean invariance, see e.g. RIZZI ET AL. [2024]. The strong form of the balance equations of the Mindlin-Eringen micromorphic continuum reads NEFF ET AL. [2014a]

$$\begin{aligned} \operatorname{div} \left(\underbrace{\mathbb{C}_e : (\nabla \mathbf{u} - \mathbf{P}) + \mathbb{C}_{e-P} : \operatorname{sym} \mathbf{P}}_{\Sigma} \right) &= \mathbf{0}, \\ \operatorname{div} \left(\underbrace{\mu L_c^2 \check{\mathbb{L}} : \nabla \mathbf{P}}_{\mathcal{M}} \right) - \underbrace{\left(\mathbb{C}_P : \operatorname{sym} \mathbf{P} + \mathbb{C}_{e-P}^T : (\nabla \mathbf{u} - \mathbf{P}) \right)}_{\mathbf{S}} + \Sigma &= \mathbf{0}, \end{aligned} \quad (2.71)$$

where Σ and \mathbf{S} are second-order non-symmetric force and micro-stress tensors, respectively, and \mathcal{M} is a third-order moment stress tensor. The balance equations (2.71) represent generalized balances of linear and angular momentum, respectively.

A significant challenge in employing the micromorphic theory for modeling the mechanical behavior of material lies in the difficulty of determining the numerous unknown coefficients. This not only presents a technical issue but also a challenge in physically interpreting the material parameters themselves, since some are size-dependent while others are size-independent, BARBAGALLO ET AL. [2017], CHEN AND LEE [2003a;b]. Finally, for the case $\mathbb{C}_e \rightarrow \infty$ and if no mixed terms are considered, we obtain $\mathbf{P} = \nabla \mathbf{u}$ and, consequently, we have

$$\psi(\nabla \mathbf{u}, \nabla(\nabla \mathbf{u})) = \frac{1}{2} \left(\operatorname{sym} \nabla \mathbf{u} : \mathbb{C}_P : \operatorname{sym} \nabla \mathbf{u} + \mu L_c^2 \nabla(\nabla \mathbf{u}) : \check{\mathbb{L}} : \nabla(\nabla \mathbf{u}) \right), \quad (2.72)$$

and the gradient elasticity model is recovered in which \mathbb{C}_P must coincide with the classical periodic homogenization.

2.6.3 The Cosserat model

The first enriched continuum is traced back to the works of the Cosserat brothers COSSERAT AND COSSERAT [1909]. They assume that each material point is rigid but can rotate. Therefore, a skew-symmetric micro-distortion field is considered by setting $\mathbf{A} := \operatorname{skew} \mathbf{P} \in \mathfrak{so}(3)$ with three additional rotational degrees of freedom instead of the full nine degrees of freedom in the Mindlin-Eringen micromorphic theory, BARBAGALLO [2017], GHIBA ET AL. [2023]. The displacement vector \mathbf{u} and the skew-symmetric micro-distortion field \mathbf{A} are defined through the following energy minimization

$$\Pi(\mathbf{u}, \mathbf{A}) = \int_{\mathcal{B}} \psi(\nabla \mathbf{u}, \mathbf{A}, \nabla(\operatorname{axl} \mathbf{A})) \, dV \longrightarrow \min, \quad (2.73)$$

and the energy density reads

$$\begin{aligned} \psi(\nabla \mathbf{u}, \mathbf{A}, \nabla \operatorname{axl} \mathbf{A}) &= \frac{1}{2} \left(\operatorname{sym} \nabla \mathbf{u} : \mathbb{C}_e : \operatorname{sym} \nabla \mathbf{u} \right. \\ &\quad + (\operatorname{skew} \nabla \mathbf{u} - \mathbf{A}) : \mathbb{C}_A : (\operatorname{skew} \nabla \mathbf{u} - \mathbf{A}) \\ &\quad \left. + \mu L_c^2 \nabla(\operatorname{axl} \mathbf{A}) : \bar{\mathbb{L}} : \nabla(\operatorname{axl} \mathbf{A}) \right), \end{aligned} \quad (2.74)$$

with

$$\mathbf{A} = \begin{pmatrix} 0 & A_{12} & A_{13} \\ -A_{12} & 0 & A_{23} \\ -A_{13} & -A_{23} & 0 \end{pmatrix}, \quad \text{and} \quad \text{axl } \mathbf{A} = (-A_{23}, A_{13}, -A_{12})^T. \quad (2.75)$$

Here, \mathbb{C}_ε is a standard elasticity tensor acting on $\text{sym } \nabla \mathbf{u}$. The tensor \mathbb{C}_A is a fourth-order tensor acting on $\text{skew } \nabla \mathbf{u} - \mathbf{A}$ and $\bar{\mathbb{L}}$ is a fourth-order tensor acting on $\nabla(\text{axl } \mathbf{A})$. The curvature in the Cosserat theory can be expressed using the Curl operator rather than the gradient with the help of Nye's formula since \mathbf{A} is skew-symmetric, see D'AGOSTINO ET AL. [2022a], NYE [1953],

$$\nabla(\text{axl } \mathbf{A}) = \frac{1}{2} \text{tr} [(\text{Curl } \mathbf{A})^T] \mathbf{I} - (\text{Curl } \mathbf{A})^T. \quad (2.76)$$

Therefore, an alternative formulation of the energy can be introduced with the help of the Curl operator acting on the skew-symmetric tensor \mathbf{A} . This formulation is isomorphic to the formulation in Equation (2.74) BARBAGALLO ET AL. [2017]

$$\begin{aligned} \psi(\nabla \mathbf{u}, \mathbf{A}, \text{Curl } \mathbf{A}) &= \frac{1}{2} (\text{sym } \nabla \mathbf{u} : \mathbb{C}_\varepsilon : \text{sym } \nabla \mathbf{u} \\ &\quad + (\text{skew } \nabla \mathbf{u} - \mathbf{A}) : \mathbb{C}_A : (\text{skew } \nabla \mathbf{u} - \mathbf{A}) \\ &\quad + \mu L_c^2 \text{Curl } \mathbf{A} : \bar{\mathbb{L}} : \text{Curl } \mathbf{A}). \end{aligned} \quad (2.77)$$

The strong form of the balance equations of the Cosserat model reads

$$\begin{aligned} \text{div} \left(\underbrace{\mathbb{C}_\varepsilon : \text{sym } \nabla \mathbf{u} + \mathbb{C}_A : (\text{skew } \nabla \mathbf{u} - \mathbf{A})}_{\boldsymbol{\Sigma}} \right) &= \mathbf{0}, \\ \text{skew Curl} \left(\underbrace{\mu L_c^2 \bar{\mathbb{L}} : \text{Curl } \mathbf{A}}_{\mathbf{m}} \right) - \underbrace{\mathbb{C}_A : (\text{skew } \nabla \mathbf{u} - \mathbf{A})}_{\text{skew } \boldsymbol{\Sigma}} &= \mathbf{0}, \end{aligned} \quad (2.78)$$

representing a generalized balance of linear and angular momentum, respectively. Here, $\boldsymbol{\Sigma}$ is a non-symmetric force stress tensor and \mathbf{m} is the second-order couple stress tensor.

A broad spectrum of materials, including granular materials MOHAN ET AL. [1999], MÜHLHAUS [1986], foam-like structures, bones ASCENZI ET AL. [1994], LAKES [1995], PARK AND LAKES [1986], and chiral metamaterials ALAVI ET AL. [2021b], aligns with the assumption of a rigid microstructure. However, the simplicity of the model restricts its effectiveness in modeling more complex materials such as metamaterials.

2.6.4 The relaxed micromorphic model by Neff

The relaxed micromorphic model balances the intricacies of the micromorphic continuum and the simplicity of the Cosserat model. It significantly reduces the number of unknown parameters compared to the Mindlin-Eringen micromorphic theory while still employing its kinematic (full micro-distortion field). Nonetheless, it incorporates only the Curl of the micro-distortion for the curvature as in the Cosserat theory. It provides an efficient solution for modeling materials that exhibit size-effects or/and band gaps.

Similar to the micromorphic theory, the kinematics of each material point in the relaxed micromorphic model are described by a displacement vector \mathbf{u} and a non-symmetric micro-distortion field \mathbf{P} . The elastic energy density is formulated as

$$\begin{aligned} \psi(\nabla\mathbf{u}, \mathbf{P}, \text{Curl}\mathbf{P}) = & \frac{1}{2}(\text{sym}[\nabla\mathbf{u} - \mathbf{P}] : \mathbb{C}_e : \text{sym}[\nabla\mathbf{u} - \mathbf{P}] \\ & + \text{sym}\mathbf{P} : \mathbb{C}_{\text{micro}} : \text{sym}\mathbf{P} \\ & + \text{skew}[\nabla\mathbf{u} - \mathbf{P}] : \mathbb{C}_c : \text{skew}[\nabla\mathbf{u} - \mathbf{P}] \\ & + \mu L_c^2 \text{Curl}\mathbf{P} : \mathbb{L} : \text{Curl}\mathbf{P}), \end{aligned} \quad (2.79)$$

where the Curl of the micro-distortion field is utilized instead of the full gradient for the curvature measurement, c.f. Equation (2.70). Chapter 3 is devoted to describing the components and the characteristics of the relaxed micromorphic model comprehensively. For the limit case $\mathbb{C}_{\text{micro}} \rightarrow \infty$, the micro-distortion field must be skew-symmetric $\mathbf{P} = \mathbf{A}$ and the Cosserat model is recovered with the corresponding strain energy density given in Equation (2.77). Furthermore, letting $\mathbb{C}_c \rightarrow \infty$ leads to $\mathbf{A} = \text{skew}\nabla\mathbf{u}$ and we obtain the couple stress model, see e.g. NEFF ET AL. [2016], with the following strain energy density

$$\begin{aligned} \psi(\nabla\mathbf{u}, \text{Curl}\text{skew}\nabla\mathbf{u}) = & \frac{1}{2}(\text{sym}\nabla\mathbf{u} : \mathbb{C}_e : \text{sym}\nabla\mathbf{u} \\ & + \mu L_c^2 \text{Curl}\text{skew}\nabla\mathbf{u} : \mathbb{L} : \text{Curl}\text{skew}\nabla\mathbf{u}). \end{aligned} \quad (2.80)$$

2.6.5 Some other generalized continua in a nutshell

Generalized continua encompass numerous models in the literature, and their notation is not unified. Reviews discussing the classes and relations between generalized continua can be found in FOREST [2013], NEFF ET AL. [2014a]. In Figure 2.4, we present a genealogy tree outlining various well-known generalized continuum models. This figure depicts their kinematics, energy dependencies, and interactions between these different models.

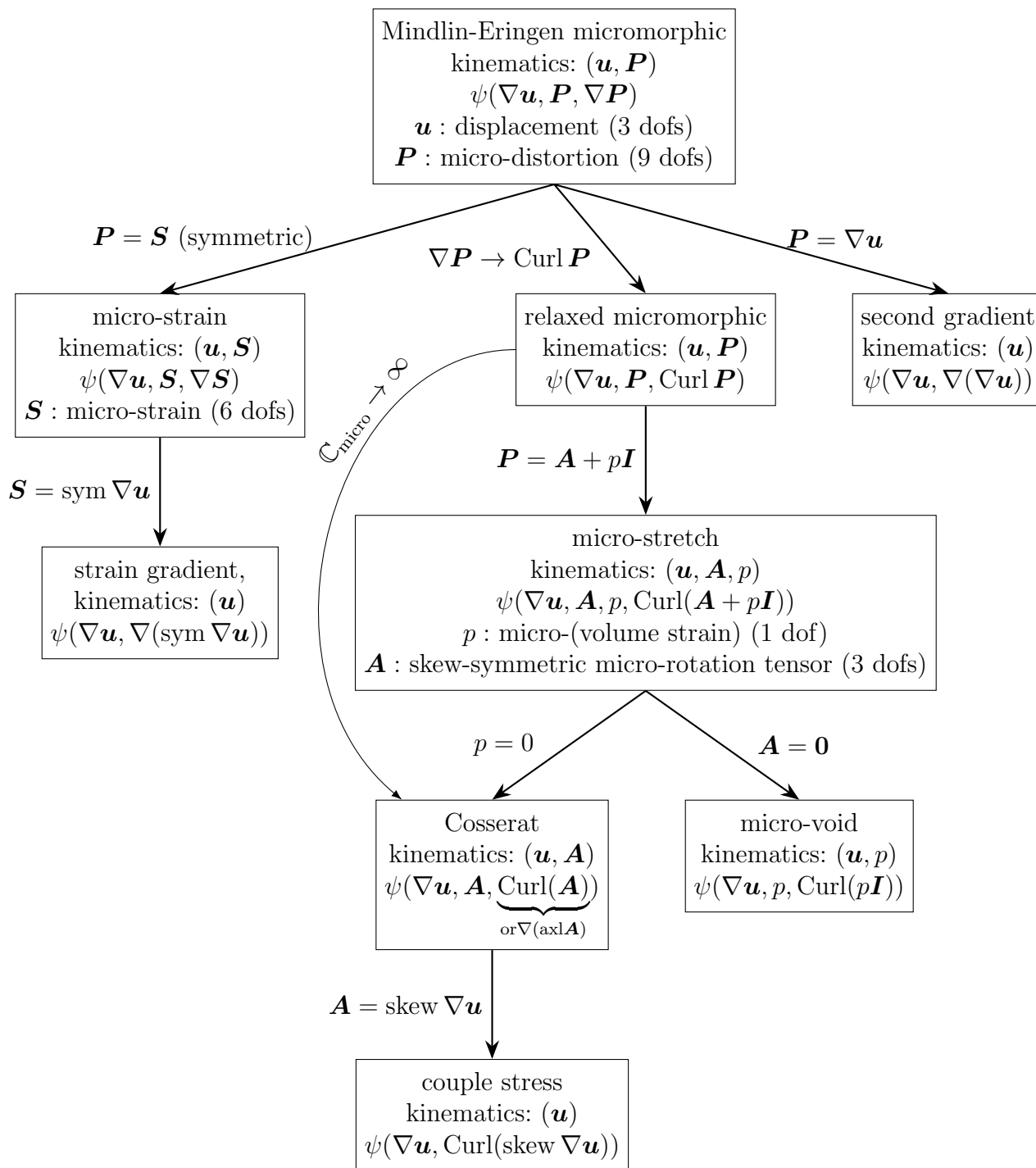


Figure 2.4: Genealogy tree of some generalized continua.

3 The relaxed micromorphic model (RMM)

The relaxed micromorphic model (RMM) is a generalized continuum description that simplifies the form of the assumed strain energy compared to the classical Mindlin-Eringen micromorphic theory by employing a relaxed curvature in terms of the Curl of a micro-distortion field rather than its full gradient DEMORE ET AL. [2022], MADEO ET AL. [2016b], NEFF ET AL. [2014a].

Utilizing only the Curl of the micro-distortion field offers several advantages. First, it achieves relative simplicity compared to the classical Eringen-Mindlin micromorphic theory, as reflected in the notably reduced number of material parameters. For instance, the relaxed micromorphic model characterizes a two-dimensional metamaterial consisting of a periodic cubic unit-cell with only eight parameters (three of them are uniquely defined by first-order classical homogenization). The simplicity is further highlighted by eliminating the fifth- and sixth-order tensors found in classical Mindlin-Eringen micromorphic theory. Second, the model demonstrates well-posedness for the important case of symmetric force stress, as proven using a new generalized Korn's inequality GMEINER ET AL. [2023; 2024], LEWINTAN AND NEFF [2021], LEWINTAN ET AL. [2021]. This property is not demonstrated in the Cosserat model since $\mu_c = 0$ leads to no coupling. The most notable advantage of the RMM is the bounded stiffness for small sizes, where the stiffness of the RMM is bounded from below and above. This allows the material parameters to be related to two well-defined scales GOURGIOTIS ET AL. [2024], SARHIL ET AL. [2023c], SCHRÖDER ET AL. [2022], which is not possible for classical micromorphic or gradient elasticity theories that exhibit unbounded stiffness for large values of the characteristic length parameter (a zoom in the microstructure).

In this Chapter, we provide a comprehensive description of the relaxed micromorphic model. We begin by introducing the relevant Hilbert spaces and norms in Section 3.1. Section 3.2 presents the energy function, offering a detailed explanation of the associated material parameters. The variational problem is derived in Section 3.3, leading to the weak and strong forms along with their respective boundary conditions. Analytical solutions for the limiting cases of $L_c \rightarrow 0$ and $L_c \rightarrow \infty$ are derived. The distinctive behavior of the relaxed micromorphic model as a two-scale elasticity model is highlighted in Section 3.6.

3.1 Hilbert spaces and related norms

In this Section, some common and well-known function spaces are introduced, BRENNER AND SCOTT [2008], BREZZI AND FORTIN [1991], ISELBÜSCHER [2021], VIEBAHN [2019], in order to define suitable function spaces for the unknown field variables. First, we introduce the Lebesgue space $L^p(\mathcal{B})$, which is characterized by p -integrable functions on the domain \mathcal{B} . A function a belongs to the Lebesgue space $L^p(\mathcal{B})$ if the p -th power of the function is bounded

$$L^p(\mathcal{B}) := \{a \mid \|a\|_{L^p} < \infty\} \quad \text{for } 1 \leq p < \infty, \quad (3.1)$$

with the associated norm

$$\|a\|_{L^p} := \left(\int_{\mathcal{B}} |a|^p dV \right)^{1/p}. \quad (3.2)$$

The space of square-integrable functions $L^2(\mathcal{B})$ is defined as

$$L^2(\mathcal{B}) := \{a \mid \|a\|_{L^2} < \infty, \quad \|a\|_{L^2}^2 = \int_{\mathcal{B}} a^2 dV\}, \quad (3.3)$$

and the Lebesgue norms of a generic vector-valued function \mathbf{a} and a generic second-order tensor function \mathbf{A} read

$$\|\mathbf{a}\|_{L^2}^2 := \sum_{i=1}^3 \|a_i\|_{L^2}^2, \quad \|\mathbf{A}\|_{L^2}^2 := \sum_{i=1}^3 \sum_{j=1}^3 \|A_{ij}\|_{L^2}^2. \quad (3.4)$$

The definition of Lebesgue spaces focuses solely on the function itself and does not involve statements regarding its derivatives. In contrast, Hilbert spaces include restrictions on the derivatives of the function, making them particularly interesting when continuity, or even higher-order continuity, is required. We introduce the Hilbert spaces $H^q(\mathcal{B})$, $H(\operatorname{div}, \mathcal{B})$ and $H(\operatorname{curl}, \mathcal{B})$ for a vector-valued function \mathbf{a} as

$$\begin{aligned} H^q(\mathcal{B}) &:= \{\mathbf{a} \in L^2(\mathcal{B}) \mid \nabla^q \mathbf{a} \in L^2(\mathcal{B})\}, \\ H(\operatorname{div}, \mathcal{B}) &:= \{\mathbf{a} \in L^2(\mathcal{B}) \mid \operatorname{div} \mathbf{a} \in L^2(\mathcal{B})\}, \\ H(\operatorname{curl}, \mathcal{B}) &:= \{\mathbf{a} \in L^2(\mathcal{B}) \mid \operatorname{curl} \mathbf{a} \in L^2(\mathcal{B})\}, \end{aligned} \quad (3.5)$$

with ∇^q as the q -th differential operator and the associated norms read

$$\begin{aligned} \|\mathbf{a}\|_{H^q(\mathcal{B})}^2 &:= \|\mathbf{a}\|_{L^2}^2 + \sum_{s=1}^q \|\nabla^s \mathbf{a}\|_{L^2}^2, \\ \|\mathbf{a}\|_{H(\operatorname{div}, \mathcal{B})}^2 &:= \|\mathbf{a}\|_{L^2}^2 + \|\operatorname{div} \mathbf{a}\|_{L^2}^2, \\ \|\mathbf{a}\|_{H(\operatorname{curl}, \mathcal{B})}^2 &:= \|\mathbf{a}\|_{L^2}^2 + \|\operatorname{curl} \mathbf{a}\|_{L^2}^2. \end{aligned} \quad (3.6)$$

The solution of the relaxed micromorphic model, as we will show later, is to be found in the space $(\mathbf{u}, \mathbf{P}) \in H^1(\mathcal{B}) \times H(\operatorname{curl}, \mathcal{B})$. The Hilbert space $H^1(\mathcal{B})$ is defined for the displacement vector \mathbf{u} as

$$H^1(\mathcal{B}) = \{\mathbf{u} \in L^2(\mathcal{B}) \mid \nabla \mathbf{u} \in L^2(\mathcal{B})\}, \quad (3.7)$$

with the norm

$$\|\mathbf{u}\|_{H^1(\mathcal{B})}^2 = \|\mathbf{u}\|_{L^2}^2 + \|\nabla \mathbf{u}\|_{L^2}^2. \quad (3.8)$$

The space $H(\operatorname{curl}, \mathcal{B})$ is defined for the micro-distortion field \mathbf{P} as

$$H(\operatorname{curl}, \mathcal{B}) = \{\mathbf{P}^i \in L^2(\mathcal{B}) \mid \operatorname{curl} \mathbf{P}^i \in L^2(\mathcal{B}), \quad \text{for } i = 1, 2, 3\}, \quad (3.9)$$

where \mathbf{P}^i are the row-vectors of \mathbf{P} , see Equations (3.16) and (3.17), and the associated norm reads

$$\|\mathbf{P}\|_{H(\operatorname{curl}, \mathcal{B})}^2 = \|\mathbf{P}\|_{L^2}^2 + \|\operatorname{Curl} \mathbf{P}\|_{L^2}^2. \quad (3.10)$$

The total norm of the space $H^1(\mathcal{B}) \times H(\operatorname{curl}, \mathcal{B})$ is defined as

$$\|(\mathbf{u}, \mathbf{P})\|_{H^1(\mathcal{B}) \times H(\operatorname{curl}, \mathcal{B})}^2 = \|\mathbf{u}\|_{H^1(\mathcal{B})}^2 + \|\mathbf{P}\|_{H(\operatorname{curl}, \mathcal{B})}^2. \quad (3.11)$$

We refer to SCHRÖDER ET AL. [2022], SKY [2022], SKY ET AL. [2022] for further details.

3.2 Model description

The relaxed micromorphic model is a continuum model that describes the kinematics of a material point using a displacement vector $\mathbf{u} : \mathcal{B} \subseteq \mathbb{R}^3 \rightarrow \mathbb{R}^3$ and a non-symmetric micro-distortion field $\mathbf{P} : \mathcal{B} \subseteq \mathbb{R}^3 \rightarrow \mathbb{R}^{3 \times 3}$. Both are defined for the static case by minimizing the potential

$$\Pi(\mathbf{u}, \mathbf{P}) = \int_{\mathcal{B}} \psi(\nabla \mathbf{u}, \mathbf{P}, \text{Curl } \mathbf{P}) - \bar{\mathbf{f}} \cdot \mathbf{u} - \bar{\mathbf{M}} : \mathbf{P} \, dV - \int_{\partial \mathcal{B}_t} \bar{\mathbf{t}} \cdot \mathbf{u} \, dA \longrightarrow \min, \quad (3.12)$$

with $(\mathbf{u}, \mathbf{P}) \in H^1(\mathcal{B}) \times H(\text{curl}, \mathcal{B})$. The vector $\bar{\mathbf{f}}$ and tensor $\bar{\mathbf{M}}$ describe the given body force and body moment, respectively, while $\bar{\mathbf{t}}$ is the traction vector acting on the boundary $\partial \mathcal{B}_t \subset \partial \mathcal{B}$. The elastic energy density ψ reads

$$\begin{aligned} \psi(\nabla \mathbf{u}, \mathbf{P}, \text{Curl } \mathbf{P}) = & \frac{1}{2} \left(\text{sym}[\nabla \mathbf{u} - \mathbf{P}] : \mathbb{C}_e : \text{sym}[\nabla \mathbf{u} - \mathbf{P}] \right. \\ & + \text{sym } \mathbf{P} : \mathbb{C}_{\text{micro}} : \text{sym } \mathbf{P} \\ & + \text{skew}[\nabla \mathbf{u} - \mathbf{P}] : \mathbb{C}_c : \text{skew}[\nabla \mathbf{u} - \mathbf{P}] \\ & \left. + \mu L_c^2 \text{Curl } \mathbf{P} : \mathbb{L} : \text{Curl } \mathbf{P} \right). \end{aligned} \quad (3.13)$$

Here, $\mathbb{C}_{\text{micro}}$ and \mathbb{C}_e are fourth-order positive definite standard elasticity tensors, \mathbb{C}_c is a fourth-order positive semi-definite rotational coupling tensor, \mathbb{L} is a fourth-order tensor acting on non-symmetric arguments, L_c is a non-negative parameter describing the characteristic length scale, and μ is a typical shear modulus which is added for dimensional consistency. The characteristic length parameter plays a significant role in the relaxed micromorphic model. This parameter is related to the size of the microstructure and determines its influence on the macroscopic mechanical behavior. The characteristic length allows scaling the number of considered unit-cells, keeping all remaining parameters of the model scale-independent, where the macro-scale with $\mathbb{C}_{\text{macro}}$ and the micro-scale with $\mathbb{C}_{\text{micro}}$ are retrieved for $L_c \rightarrow 0$ and $L_c \rightarrow \infty$, respectively, if suitable boundary conditions are applied, see NEFF ET AL. [2020], SARHIL ET AL. [2021], SCHRÖDER ET AL. [2022]. The characteristic length parameter accounts for non-localities in the considered metamaterial, where the deformation of each unit-cell is influenced by deformations and motions of the neighboring cells. The macroscopic elasticity tensor $\mathbb{C}_{\text{macro}}$ associated with $L_c \rightarrow 0$ can be defined by the standard first-order periodic homogenization (scale-separation holds), while the microscopic elasticity tensor $\mathbb{C}_{\text{micro}}$ associated with $L_c \rightarrow \infty$ represents the stiffest extrapolated response (zooming in the microstructure). The constitutive coefficients are assumed constant with the following symmetries

$$\begin{aligned} (\mathbb{C}_{\text{micro}})_{ijkl} &= (\mathbb{C}_{\text{micro}})klij = (\mathbb{C}_{\text{micro}})jikl, & (\mathbb{C}_c)_{ijkl} &= (\mathbb{C}_c)klij = -(\mathbb{C}_c)jikl, \\ (\mathbb{C}_e)_{ijkl} &= (\mathbb{C}_e)klij = (\mathbb{C}_e)jikl, & (\mathbb{L})_{ijkl} &= (\mathbb{L})klij, \end{aligned} \quad (3.14)$$

where $\mathbb{C}_{\text{micro}}$ and \mathbb{C}_e are connected to $\mathbb{C}_{\text{macro}}$ through a Reuss-like homogenization relation BARBAGALLO ET AL. [2017] (equivalent stiffness of springs in series)

$$\mathbb{C}_{\text{macro}}^{-1} = \mathbb{C}_{\text{micro}}^{-1} + \mathbb{C}_e^{-1} \quad \Rightarrow \quad \mathbb{C}_e = \mathbb{C}_{\text{micro}} : (\mathbb{C}_{\text{micro}} - \mathbb{C}_{\text{macro}})^{-1} : \mathbb{C}_{\text{macro}}. \quad (3.15)$$

The energy functional of the model does not explicitly feature the macroscopic elasticity tensor $\mathbb{C}_{\text{macro}}$. However, the previous relation involving $\mathbb{C}_{\text{micro}}$ and \mathbb{C}_e , which must be

explicitly contained in the energy functional, assures that linear elasticity with $\mathbb{C}_{\text{macro}}$ is recovered as L_c tends towards zero. Note that the shear modulus μ appears for dimensional reasons and is a priori not related to the shear moduli appearing in $\mathbb{C}_{\text{macro}}$ or $\mathbb{C}_{\text{micro}}$.

The micro-distortion field has the following general form for the three-dimensional case

$$\mathbf{P} = \begin{bmatrix} (\mathbf{P}^1)^T \\ (\mathbf{P}^2)^T \\ (\mathbf{P}^3)^T \end{bmatrix} = \begin{bmatrix} P_{11} & P_{12} & P_{13} \\ P_{21} & P_{22} & P_{23} \\ P_{31} & P_{32} & P_{33} \end{bmatrix} \quad \text{with} \quad \mathbf{P}^i = \begin{bmatrix} P_{i1} \\ P_{i2} \\ P_{i3} \end{bmatrix}, \quad i = 1, 2, 3, \quad (3.16)$$

where \mathbf{P}^i denotes the row vectors of \mathbf{P} . We let the Curl operator act on the row vectors of the micro-distortion field \mathbf{P} , i.e.

$$\text{Curl } \mathbf{P} = \begin{bmatrix} (\text{curl } \mathbf{P}^1)^T \\ (\text{curl } \mathbf{P}^2)^T \\ (\text{curl } \mathbf{P}^3)^T \end{bmatrix} = \begin{bmatrix} P_{13,2} - P_{12,3} & P_{11,3} - P_{13,1} & P_{12,1} - P_{11,2} \\ P_{23,2} - P_{22,3} & P_{21,3} - P_{23,1} & P_{22,1} - P_{21,2} \\ P_{33,2} - P_{32,3} & P_{31,3} - P_{33,1} & P_{32,1} - P_{31,2} \end{bmatrix}. \quad (3.17)$$

For the two-dimensional case, the micro-distortion field and its Curl operator are reduced to

$$\mathbf{P} = \begin{bmatrix} (\mathbf{P}^1)^T \\ (\mathbf{P}^2)^T \\ \mathbf{0}^T \end{bmatrix} = \begin{bmatrix} P_{11} & P_{12} & 0 \\ P_{21} & P_{22} & 0 \\ 0 & 0 & 0 \end{bmatrix} \quad \text{and} \quad \text{Curl } \mathbf{P} = \begin{bmatrix} 0 & 0 & P_{12,1} - P_{11,2} \\ 0 & 0 & P_{22,1} - P_{21,2} \\ 0 & 0 & 0 \end{bmatrix}. \quad (3.18)$$

3.3 Variational formulation

The variation of the potential with respect to the displacement field, i.e. $\delta_{\mathbf{u}}\Pi = 0$, with

$$\begin{aligned} \delta_{\mathbf{u}}\Pi &= \int_{\mathcal{B}} \underbrace{\{\mathbb{C}_e : \text{sym}[\nabla \mathbf{u} - \mathbf{P}] + \mathbb{C}_c : \text{skew}[\nabla \mathbf{u} - \mathbf{P}]\}}_{=: \boldsymbol{\sigma}} : \nabla \delta \mathbf{u} - \bar{\mathbf{f}} \cdot \delta \mathbf{u} \, dV \\ &\quad - \int_{\partial \mathcal{B}_t} \bar{\mathbf{t}} \cdot \delta \mathbf{u} \, dA, \end{aligned} \quad (3.19)$$

leads, after integration by parts and using the divergence theorem, to the weak form

$$\delta_{\mathbf{u}}\Pi = \int_{\mathcal{B}} \{\text{div } \boldsymbol{\sigma} + \bar{\mathbf{f}}\} \cdot \delta \mathbf{u} \, dV = 0, \quad (3.20)$$

where $\boldsymbol{\sigma}$ stands for the non-symmetric force stress tensor. The associated strong form with the related boundary conditions reads

$$\text{div } \boldsymbol{\sigma} + \bar{\mathbf{f}} = \mathbf{0} \quad \text{with} \quad \mathbf{u} = \bar{\mathbf{u}} \quad \text{on} \quad \partial \mathcal{B}_u \quad \text{and} \quad \bar{\mathbf{t}} = \boldsymbol{\sigma} \cdot \mathbf{n} \quad \text{on} \quad \partial \mathcal{B}_t, \quad (3.21)$$

satisfying $\partial \mathcal{B}_u \cap \partial \mathcal{B}_t = \emptyset$ and $\partial \mathcal{B}_u \cup \partial \mathcal{B}_t = \partial \mathcal{B}$ and \mathbf{n} is the outward normal on the boundary. Similarly, the variation of the potential with respect to the micro-distortion field, i.e. $\delta_{\mathbf{P}}\Pi = 0$, with

$$\delta_{\mathbf{P}}\Pi = \int_{\mathcal{B}} \underbrace{\{\boldsymbol{\sigma} - \mathbb{C}_{\text{micro}} : \text{sym } \mathbf{P} + \bar{\mathbf{M}}\}}_{=: \boldsymbol{\sigma}_{\text{micro}}} : \delta \mathbf{P} - \underbrace{\mu L_c^2 (\mathbb{L} : \text{Curl } \mathbf{P})}_{=: \mathbf{m}} : \text{Curl } \delta \mathbf{P} \, dV, \quad (3.22)$$

yields after using integration by parts and applying Stokes' theorem

$$\begin{aligned} \delta_{\mathbf{P}}\Pi &= \int_{\mathcal{B}} \{ \boldsymbol{\sigma} - \boldsymbol{\sigma}_{\text{micro}} - \text{Curl } \mathbf{m} + \overline{\mathbf{M}} \} : \delta \mathbf{P} \, dV \\ &+ \int_{\partial \mathcal{B}} \left\{ \sum_{i=1}^3 (\mathbf{m}^i \times \delta \mathbf{P}^i) \cdot \mathbf{n} \right\} \, dA = 0, \end{aligned} \quad (3.23)$$

where $\boldsymbol{\sigma}_{\text{micro}}$ and \mathbf{m} are the micro- and moment stresses, respectively, and \mathbf{m}^i and $\delta \mathbf{P}^i$ denote row vectors of the associated second-order tensors. Here, we have employed the relation

$$\int_{\mathcal{B}} \mathbf{m} : \text{Curl } \delta \mathbf{P} \, dV = \int_{\mathcal{B}} \text{Curl } \mathbf{m} : \delta \mathbf{P} \, dV - \int_{\partial \mathcal{B}} \left\{ \sum_{i=1}^3 (\mathbf{m}^i \times \delta \mathbf{P}^i) \cdot \mathbf{n} \right\} \, dA. \quad (3.24)$$

Using the identity of the scalar triple vector product

$$(\mathbf{a} \times \mathbf{b}) \cdot \mathbf{c} = (\mathbf{c} \times \mathbf{a}) \cdot \mathbf{b} = (\mathbf{b} \times \mathbf{c}) \cdot \mathbf{a}, \quad (3.25)$$

leads for the reformulation

$$\begin{aligned} \int_{\partial \mathcal{B}} \left\{ \sum_{i=1}^3 (\mathbf{m}^i \times \delta \mathbf{P}^i) \cdot \mathbf{n} \right\} \, dA &= \\ \int_{\partial \mathcal{B}_P} \left\{ \sum_{i=1}^3 (\delta \mathbf{P}^i \times \mathbf{n}) \cdot \mathbf{m}^i \right\} \, dA &- \int_{\partial \mathcal{B}_m} \left\{ \sum_{i=1}^3 (\mathbf{m}^i \times \mathbf{n}) \cdot \delta \mathbf{P}^i \right\} \, dA. \end{aligned} \quad (3.26)$$

The associated strong form reads

$$\text{Curl } \mathbf{m} = \boldsymbol{\sigma} - \boldsymbol{\sigma}_{\text{micro}} + \overline{\mathbf{M}}, \quad (3.27)$$

with related boundary conditions, formulated in terms of the row vectors \mathbf{P}^i and \mathbf{m}^i of the associated second-order tensors,

$$\sum_{i=1}^3 \mathbf{P}^i \times \mathbf{n} = \bar{\mathbf{t}}_p \quad \text{on } \partial \mathcal{B}_P \quad \text{and by definition} \quad \sum_{i=1}^3 \mathbf{m}^i \times \mathbf{n} = \mathbf{0} \quad \text{on } \partial \mathcal{B}_m, \quad (3.28)$$

where $\partial \mathcal{B}_P \cap \partial \mathcal{B}_m = \emptyset$ and $\partial \mathcal{B}_P \cup \partial \mathcal{B}_m = \partial \mathcal{B}$.

The first strong form in Equation (3.21) represents a generalized balance of linear momentum (force balance), while the second strong form in Equation (3.27) outlines a generalized balance of angular momentum (moment balance). The generalized moment balance invokes the Cosserat theory with the Curl Curl operator rising from the matrix Curl operator of the second-order moment stress \mathbf{m} . In comparison to the classical micromorphic model, see ERINGEN [1968], NEFF ET AL. [2014a], the relaxed micromorphic model uses the same kinematical measures but employs a curvature measure from the Cosserat micropolar theory, see NEFF ET AL. [2010b]. The strong form of the relaxed micromorphic model, along with the associated boundary conditions, can be summarized as follows:

$$\begin{aligned}
\operatorname{div} \boldsymbol{\sigma} + \bar{\mathbf{f}} &= \mathbf{0} && \text{on } \mathcal{B}, \\
\mathbf{u} &= \bar{\mathbf{u}} && \text{on } \partial\mathcal{B}_u, \\
\bar{\mathbf{t}} &= \boldsymbol{\sigma} \cdot \mathbf{n} && \text{on } \partial\mathcal{B}_t, \\
\boldsymbol{\sigma} - \boldsymbol{\sigma}_{\text{micro}} - \operatorname{Curl} \mathbf{m} + \bar{\mathbf{M}} &= \mathbf{0} && \text{on } \mathcal{B}, \\
\sum_{i=1}^3 \mathbf{P}^i \times \mathbf{n} &= \bar{\mathbf{t}}_P && \text{on } \partial\mathcal{B}_P, \\
\sum_{i=1}^3 \mathbf{m}^i \times \mathbf{n} &= \mathbf{0} && \text{on } \partial\mathcal{B}_m,
\end{aligned} \tag{3.29}$$

where $\partial\mathcal{B}_P \cap \partial\mathcal{B}_m = \partial\mathcal{B}_u \cap \partial\mathcal{B}_t = \emptyset$ and $\partial\mathcal{B}_P \cup \partial\mathcal{B}_m = \partial\mathcal{B}_u \cup \partial\mathcal{B}_t = \partial\mathcal{B}$. By substituting the generalized balance of angular momentum into the generalized balance of linear momentum, a resulting (but not independent) balance equation reads

$$\operatorname{div} \boldsymbol{\sigma}_{\text{micro}} + \bar{\mathbf{f}} = \mathbf{0} \quad \text{on } \mathcal{B}, \tag{3.30}$$

which does not appear in the Eringen-Mindlin micromorphic theory or the Cosserat micropolar model. A dependency between the displacement field and the micro-distortion field on the boundary was introduced by NEFF ET AL. [2020] and subsequently considered in D'AGOSTINO ET AL. [2022b], RIZZI ET AL. [2021a;b], SKY ET AL. [2021]. This so-called **consistent coupling boundary condition** relates the projection of the displacement gradient on the tangential plane of the boundary to the respective parts of the micro-distortion, i.e.

$$\mathbf{P} \cdot \boldsymbol{\tau} = \nabla \mathbf{u} \cdot \boldsymbol{\tau} \Leftrightarrow \mathbf{P}^i \times \mathbf{n} = \nabla \mathbf{u}^i \times \mathbf{n} \quad \text{for } i = 1, 2, 3 \quad \text{on } \partial\mathcal{B}_P = \partial\mathcal{B}_u, \tag{3.31}$$

where $\boldsymbol{\tau}$ is a tangential vector on the Dirichlet boundary and $\nabla \mathbf{u}^i$ are the row vectors of $\nabla \mathbf{u}$. This boundary condition can be enforced explicitly on the displacement's Dirichlet boundary because the displacement gradient's tangential projection is known. However, we can extend this relative boundary condition to parts of $\partial\mathcal{B}_m$ by enforcing the consistent coupling condition on $\partial\mathcal{B}_{\widehat{m}} \subseteq \partial\mathcal{B}_m$ via a penalty approach as

$$\Pi \Leftarrow \Pi + \int_{\partial\mathcal{B}_{\widehat{m}}} \frac{\kappa_1}{2} \sum_{i=1}^3 \|(\mathbf{P}^i - \nabla \mathbf{u}^i) \times \mathbf{n}\|^2 dA, \tag{3.32}$$

where κ_1 is the penalty parameter.

3.4 Limiting case $L_c \rightarrow 0$

For the limit $L_c \rightarrow 0$, the generalized balance of angular momentum in Equation (3.29) turns with $L_c = 0$ into

$$\boldsymbol{\sigma} - \boldsymbol{\sigma}_{\text{micro}} + \bar{\mathbf{M}} = \mathbf{0}. \tag{3.33}$$

Alternatively, it can be rewritten as the following

$$\mathbb{C}_e : \text{sym}[\nabla \mathbf{u} - \mathbf{P}] + \mathbb{C}_c : \text{skew}[\nabla \mathbf{u} - \mathbf{P}] - \mathbb{C}_{\text{micro}} : \text{sym} \mathbf{P} + \overline{\mathbf{M}} = \mathbf{0}. \quad (3.34)$$

The micro-distortion field \mathbf{P} can be calculated after some algebraic manipulations as

$$\begin{aligned} \text{sym} \mathbf{P} &= (\mathbb{C}_e + \mathbb{C}_{\text{micro}})^{-1} : (\mathbb{C}_e : \text{sym} \nabla \mathbf{u} + \text{sym} \overline{\mathbf{M}}), \\ \text{skew} \mathbf{P} &= \mathbb{C}_c^{-1} : \text{skew} \overline{\mathbf{M}} + \text{skew} \nabla \mathbf{u} \end{aligned} \quad (3.35)$$

which leads, with the assumption $\overline{\mathbf{M}} = \mathbf{0}$, to

$$\begin{aligned} \text{sym} \mathbf{P} &= (\mathbb{C}_e + \mathbb{C}_{\text{micro}})^{-1} : \mathbb{C}_e : \text{sym} \nabla \mathbf{u}, \\ \text{skew}[\nabla \mathbf{u} - \mathbf{P}] &= \mathbf{0} \end{aligned} \quad (3.36)$$

and by substituting in Equation (3.34), we obtain

$$\mathbb{C}_e : \text{sym}[\nabla \mathbf{u} - \mathbf{P}] = \mathbb{C}_{\text{micro}} : (\mathbb{C}_e + \mathbb{C}_{\text{micro}})^{-1} : \mathbb{C}_e : \text{sym} \nabla \mathbf{u}. \quad (3.37)$$

The generalized balance of linear momentum in Equation (3.29) taking into consideration Equations (3.36) and (3.37) becomes

$$\text{div} \left[\underbrace{(\mathbb{C}_{\text{micro}} : (\mathbb{C}_e + \mathbb{C}_{\text{micro}})^{-1} : \mathbb{C}_e)}_{=:\mathbb{C}_{\text{macro}}} : \text{sym} \nabla \mathbf{u} \right] + \overline{\mathbf{f}} = \mathbf{0}, \quad (3.38)$$

and we obtain the classical balance of linear momentum for the linear elastic Cauchy continuum. The definition of the macroscopic elasticity tensor $\mathbb{C}_{\text{macro}} = \mathbb{C}_{\text{micro}} : (\mathbb{C}_e + \mathbb{C}_{\text{micro}})^{-1} : \mathbb{C}_e = (\mathbb{C}_e^{-1} + \mathbb{C}_{\text{micro}}^{-1})^{-1}$, which has been introduced before in Equation (3.15), is a series sum of \mathbb{C}_e and $\mathbb{C}_{\text{micro}}$ (Reuss-like homogenization). Therefore, $\mathbb{C}_{\text{macro}}$ is softer than both \mathbb{C}_e and $\mathbb{C}_{\text{micro}}$, BARBAGALLO ET AL. [2017]. The case $L_c \rightarrow 0$ corresponds to the lower limit of the relaxed micromorphic model. This limit is associated with the soft response of large specimens (many unit-cells), and the classical first-order homogenization procedures are valid to identify the elasticity tensor $\mathbb{C}_{\text{macro}}$.

3.5 Limiting case $L_c \rightarrow \infty$

For the limit $L_c \rightarrow \infty$, the term $\text{Curl} \mathbf{P}$ has to vanish, see Equations (3.12) and (3.13). This implies the reduction of the micro-distortion to a gradient field $\mathbf{P} = \nabla \mathbf{v}$ NEFF ET AL. [2020], SKY [2022]. The elastic energy density of the relaxed micromorphic model in Equation (3.13) becomes

$$\begin{aligned} \psi(\nabla \mathbf{u}, \nabla \mathbf{v}) &= \frac{1}{2} \left(\text{sym}[\nabla \mathbf{u} - \nabla \mathbf{v}] : \mathbb{C}_e : \text{sym}[\nabla \mathbf{u} - \nabla \mathbf{v}] \right. \\ &\quad \left. + \text{sym} \nabla \mathbf{v} : \mathbb{C}_{\text{micro}} : \text{sym} \nabla \mathbf{v} \right. \\ &\quad \left. + \text{skew}[\nabla \mathbf{u} - \nabla \mathbf{v}] : \mathbb{C}_c : \text{skew}[\nabla \mathbf{u} - \nabla \mathbf{v}] \right). \end{aligned} \quad (3.39)$$

The variation of the total energy with respect to the remaining fields \mathbf{u} and \mathbf{v} reads

$$\begin{aligned}
\delta_{\mathbf{u}}\Pi &= \int_{\mathcal{B}} \left\{ \mathbb{C}_e : \text{sym}[\nabla \mathbf{u} - \nabla \mathbf{v}] + \mathbb{C}_c : \text{skew}[\nabla \mathbf{u} - \nabla \mathbf{v}] \right\} : \nabla \delta \mathbf{u} - \bar{\mathbf{f}} \cdot \delta \mathbf{u} \, dV \\
&\quad - \int_{\partial \mathcal{B}_t} \bar{\mathbf{t}} \cdot \delta \mathbf{u} \, dA, \\
\delta_{\mathbf{v}}\Pi &= \int_{\mathcal{B}} \left\{ \mathbb{C}_e : \text{sym}[\nabla \mathbf{u} - \nabla \mathbf{v}] + \mathbb{C}_c : \text{skew}[\nabla \mathbf{u} - \nabla \mathbf{v}] \right. \\
&\quad \left. - \mathbb{C}_{\text{micro}} : \text{sym} \nabla \mathbf{v} + \bar{\mathbf{M}} \right\} : \nabla \delta \mathbf{v} \, dV,
\end{aligned} \tag{3.40}$$

and the associated strong forms are

$$\text{div}[\mathbb{C}_e : \text{sym}[\nabla \mathbf{u} - \nabla \mathbf{v}] + \mathbb{C}_c : \text{skew}[\nabla \mathbf{u} - \nabla \mathbf{v}]] + \bar{\mathbf{f}} = \mathbf{0} \tag{3.41a}$$

$$\text{div}[\mathbb{C}_e : \text{sym}[\nabla \mathbf{u} - \nabla \mathbf{v}] + \mathbb{C}_c : \text{skew}[\nabla \mathbf{u} - \nabla \mathbf{v}] - \mathbb{C}_{\text{micro}} : \text{sym} \nabla \mathbf{v} + \bar{\mathbf{M}}] = \mathbf{0}. \tag{3.41b}$$

We substitute Equation (3.41b) into (3.41a) and obtain

$$\text{div}[\mathbb{C}_{\text{micro}} : \text{sym} \nabla \mathbf{v}] = \text{div} \bar{\mathbf{M}} - \bar{\mathbf{f}}. \tag{3.42}$$

Enforcing the consistent coupling condition on the boundary, see Equation (3.31), with vanishing body force $\bar{\mathbf{f}}$ leads to the apparent solution $\nabla \mathbf{v} = \nabla \mathbf{u}$. The divergence of the body moment can be interpreted as a microscopic body force $\bar{\bar{\mathbf{f}}} = -\text{div} \bar{\mathbf{M}}$. The minimization problem can be reformulated as

$$\int_{\mathcal{B}} \frac{1}{2} \nabla \mathbf{u} : \mathbb{C}_{\text{micro}} : \nabla \mathbf{u} - \bar{\bar{\mathbf{f}}} \cdot \mathbf{u} \, dV \longrightarrow \min \tag{3.43}$$

with the balance equation

$$\text{div}[\mathbb{C}_{\text{micro}} : \text{sym} \nabla \mathbf{u}] + \bar{\bar{\mathbf{f}}} = \mathbf{0} \tag{3.44}$$

and a linear elastic Cauchy continuum with elasticity tensor $\mathbb{C}_{\text{micro}}$ is recovered. The case $L_c \rightarrow \infty$ corresponds to the upper limit of the relaxed micromorphic mode characterized by linear elasticity with elasticity tensor $\mathbb{C}_{\text{micro}}$. This limit must be associated with the stiffest response of the assumed material as we are zooming in the microstructure into one single unit-cell.

3.6 Characteristics of the RMM: a two-scale elasticity model

As we demonstrated in Sections 3.4 and 3.5, the relaxed micromorphic model recovers a “soft” linear elasticity model with an elasticity tensor $\mathbb{C}_{\text{macro}}$ as $L_c \rightarrow 0$ and a “stiff” linear elasticity model with an elasticity tensor $\mathbb{C}_{\text{micro}}$ as $L_c \rightarrow \infty$. Therefore, the relaxed micromorphic model interpolates between two well-defined scales: the microscopic scale, described by linear elasticity with a microscopic elasticity tensor representing the maximum stiffness exhibited by the assumed metamaterial, and the macroscopic scale, characterized by linear elasticity with a macroscopic elasticity tensor obtained using standard

periodic first-order homogenization methods when scale-separation holds. The critical role of the characteristic length parameter is to scale correctly with the specimen size and to control the transition between the micro- and macro-scales. Therein, large values of the characteristic length correspond to zooming into the “stiff” microstructure, for example, one unit-cell, while small values result in an effective “soft” classical homogeneous response for large structures. Figure 3.1 illustrates how this unique behavior distinguishes the relaxed micromorphic model from other generalized continua that exhibit unbounded stiffness for arbitrarily small specimens (i.e., large values of the characteristic length).

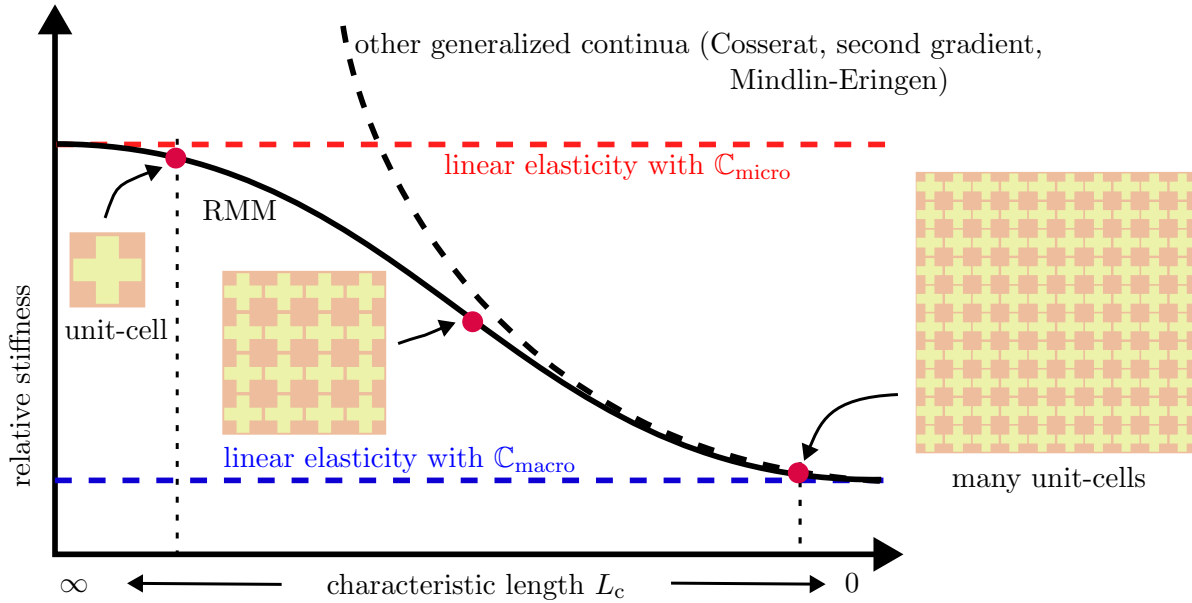


Figure 3.1: The stiffness of the relaxed micromorphic model (RMM) is bounded from above and below. Other generalized continua exhibit unbounded stiffness for small sizes. For large values of the characteristic length, linear elasticity with a microscopic elasticity tensor is recovered (one unit-cell) while linear elasticity with a macroscopic elasticity tensor is obtained for small values of the characteristic length (many unit-cells). Taken from SARHIL ET AL. [2024].

4 Finite Element Method

Within the last decades, the Finite Element Method (FEM) has been proven to be a well-established numerical approach for an approximate and effective solution of partial differential equations on complex finite geometries with different types of boundary conditions. The finite element method is based on approximating of the continuous problem into a discrete counterpart with a certain number of unknowns (degrees of freedom), which yields an equations system that can be solved employing suitable numerical methods and computer codes. For a general overview of the finite element method and the associated concepts, we refer to the standard books, e.g. BATHE [2006], WRIGGERS [2008], ZIENKIEWICZ ET AL. [2013].

In this Chapter, we introduce the fundamental concepts of the finite element realization of the relaxed micromorphic model with the needed $H^1(\mathcal{B})$ - and $H(\text{curl}, \mathcal{B})$ -conforming finite element approximation spaces. The proper finite element approximation of the micro-distortion field is the Nédélec space, which utilizes tangential-conforming vectorial shape functions. We provide a comprehensive description of the construction of $H^1(\mathcal{B}) \times H(\text{curl}, \mathcal{B})$ elements with Nédélec formulation of the first kind on triangular and quadrilateral meshes. Six finite elements are built, seeking comparison, which differ in the approximation space of the micro-distortion: two triangular elements with first- and second-order Nédélec formulation, two quadrilateral elements with first- and second-order Nédélec formulation, and two nodal triangular elements with standard first- and second-order Lagrangian formulation. Three numerical examples are introduced. The first numerical example is a patch-test to check the implementation. The second numerical example is designed to check the convergence behavior of the different finite elements when the solution is discontinuous in the micro-distortion field. We investigate the influence of the characteristic length in the last example, which covers the size-effect property.

Parts of this Chapter are published in:

J. Schröder, M. Sarhil, L. Scheunemann and P. Neff. Lagrange and $H^1(\mathcal{B}) \times H(\text{curl}, \mathcal{B})$ based finite element formulations for the relaxed micromorphic model. *Computational Mechanics*, 70, 1309–1333, 2022. doi:10.1007/s00466-022-02198-3

M. Sarhil, L. Scheunemann, J. Schröder and P. Neff. On a tangential-conforming finite element formulation for the relaxed micromorphic model in 2D. *Proceedings in Applied Mathematics and Mechanics*, 21, e202100187, 2021. doi:10.1002/pamm.202100187

4.1 Linearization of the weak forms

Since the solution of the variational problem in Section 3.3 can generally be nonlinear, the solution of boundary value problems requires an iterative procedure. The Newton-Raphson scheme is particularly efficient for solving nonlinear algebraic systems, converging quadratically in a sufficiently close neighborhood of the real solution. Therefore, linearizing the underlying coupled weak forms in Equations (3.19) and (3.22) becomes necessary. We revisited the weak forms, clarifying their physical interpretation by expanding them into expressions linked to virtual work. We rewrite the first weak form in Equation (3.19) as

$$\delta_{\mathbf{u}}\Pi = \underbrace{\int_{\mathcal{B}} \boldsymbol{\sigma} : \nabla \delta \mathbf{u} \, dV}_{=:\delta_{\mathbf{u}}\Pi^{int}} - \left(\underbrace{\int_{\mathcal{B}} \bar{\mathbf{f}} \cdot \delta \mathbf{u} \, dV + \int_{\partial \mathcal{B}_t} \bar{\mathbf{t}} \cdot \delta \mathbf{u} \, dA}_{=:\delta_{\mathbf{u}}\Pi^{ext}} \right), \quad (4.1)$$

where $\delta_{\mathbf{u}}\Pi^{int}$ and $\delta_{\mathbf{u}}\Pi^{ext}$ denote the virtual internal and external work associated with the displacement field. Similarly, we reform the second weak form in Equation (3.22) as

$$\delta_{\mathbf{P}}\Pi = \underbrace{\int_{\mathcal{B}} (\boldsymbol{\sigma}_{\text{micro}} - \boldsymbol{\sigma}) : \delta \mathbf{P} + \mathbf{m} : \text{Curl} \delta \mathbf{P} \, dV}_{=:\delta_{\mathbf{P}}\Pi^{int}} - \underbrace{\int_{\mathcal{B}} \bar{\mathbf{M}} : \delta \mathbf{P} \, dV}_{=:\delta_{\mathbf{P}}\Pi^{ext}}, \quad (4.2)$$

where $\delta_{\mathbf{P}}\Pi^{int}$ and $\delta_{\mathbf{P}}\Pi^{ext}$ denote the virtual internal and external work associated with the micro-distortion field. The linearization of previous weak forms with respect to a given point $\mathbf{u} = \check{\mathbf{u}}$ and $\mathbf{P} = \check{\mathbf{P}}$ reads

$$\begin{aligned} \text{Lin } \delta_{\mathbf{u}}\Pi(\check{\mathbf{u}}, \check{\mathbf{P}}, \delta \mathbf{u}, \Delta \mathbf{u}, \Delta \mathbf{P}) &= \delta_{\mathbf{u}}\Pi(\check{\mathbf{u}}, \check{\mathbf{P}}, \delta \mathbf{u}) + \Delta_{\mathbf{u}} \delta_{\mathbf{u}}\Pi(\check{\mathbf{u}}, \check{\mathbf{P}}, \delta \mathbf{u}, \Delta \mathbf{u}) \\ &\quad + \Delta_{\mathbf{P}} \delta_{\mathbf{u}}\Pi(\check{\mathbf{u}}, \check{\mathbf{P}}, \delta \mathbf{u}, \Delta \mathbf{P}), \\ \text{Lin } \delta_{\mathbf{P}}\Pi(\check{\mathbf{u}}, \check{\mathbf{P}}, \delta \mathbf{P}, \Delta \mathbf{u}, \Delta \mathbf{P}) &= \delta_{\mathbf{P}}\Pi(\check{\mathbf{u}}, \check{\mathbf{P}}, \delta \mathbf{P}) + \Delta_{\mathbf{u}} \delta_{\mathbf{P}}\Pi(\check{\mathbf{u}}, \check{\mathbf{P}}, \delta \mathbf{P}, \Delta \mathbf{u}) \\ &\quad + \Delta_{\mathbf{P}} \delta_{\mathbf{P}}\Pi(\check{\mathbf{u}}, \check{\mathbf{P}}, \delta \mathbf{P}, \Delta \mathbf{P}), \end{aligned} \quad (4.3)$$

where $\Delta \mathbf{u}$ and $\Delta \mathbf{P}$ are the incremental displacement and micro-distortion field, respectively. The incremental parts of the linearization are obtained through the (partial) directional derivatives with respect to the corresponding field quantity. The increment of the virtual work is obtained exemplarily as

$$\Delta_{\mathbf{u}} \delta_{\mathbf{u}}\Pi(\check{\mathbf{u}}, \check{\mathbf{P}}, \delta \mathbf{u}, \Delta \mathbf{u}) = \left. \frac{d}{d\epsilon} \delta_{\mathbf{u}}\Pi(\check{\mathbf{u}} + \epsilon \Delta \mathbf{u}, \check{\mathbf{P}}, \delta \mathbf{u}) \right|_{\epsilon=0} = D_{\mathbf{u}} \delta_{\mathbf{u}}\Pi(\check{\mathbf{u}}, \check{\mathbf{P}}, \delta \mathbf{u}) \cdot \Delta \mathbf{u}, \quad (4.4)$$

which applies analogously to the other terms. Moreover, we assume that the traction $\bar{\mathbf{t}}$, the body force $\bar{\mathbf{f}}$ and the body moment $\bar{\mathbf{M}}$ are conservative external loading so that their directional derivatives vanish, i.e. $\Delta \delta_{\mathbf{u}}\Pi^{ext} = 0$ and $\Delta \delta_{\mathbf{P}}\Pi^{ext} = 0$. Thus, we obtain the following linearization of the weak forms

$$\begin{aligned} \text{Lin } \delta_{\mathbf{u}}\Pi &= \int_{\mathcal{B}} \boldsymbol{\sigma} : \nabla \delta \mathbf{u} \, dV - \int_{\mathcal{B}} \bar{\mathbf{f}} \cdot \delta \mathbf{u} \, dV - \int_{\partial \mathcal{B}_t} \bar{\mathbf{t}} \cdot \delta \mathbf{u} \, dA \\ &\quad + \int_{\mathcal{B}} \nabla \delta \mathbf{u} : \partial_{\nabla \mathbf{u}} \boldsymbol{\sigma} : \nabla \Delta \mathbf{u} \, dV + \int_{\mathcal{B}} \nabla \delta \mathbf{u} : \partial_{\mathbf{P}} \boldsymbol{\sigma} : \Delta \mathbf{P} \, dV, \\ \text{Lin } \delta_{\mathbf{P}}\Pi &= \int_{\mathcal{B}} (\boldsymbol{\sigma}_{\text{micro}} - \boldsymbol{\sigma}) : \delta \mathbf{P} + \mathbf{m} : \text{Curl} \delta \mathbf{P} \, dV - \int_{\mathcal{B}} \bar{\mathbf{M}} : \delta \mathbf{P} \, dV \\ &\quad - \int_{\mathcal{B}} \delta \mathbf{P} : \partial_{\nabla \mathbf{u}} \boldsymbol{\sigma} : \nabla \Delta \mathbf{u} \, dV + \int_{\mathcal{B}} \delta \mathbf{P} : (\partial_{\mathbf{P}} \boldsymbol{\sigma}_{\text{micro}} - \partial_{\mathbf{P}} \boldsymbol{\sigma}) : \Delta \mathbf{P} \, dV \\ &\quad + \int_{\mathcal{B}} \text{Curl} \delta \mathbf{P} : \partial_{\text{Curl} \mathbf{P}} \mathbf{m} : \text{Curl} \Delta \mathbf{P} \, dV, \end{aligned} \quad (4.5)$$

with the following partial derivatives

$$\partial_{\nabla \mathbf{u}} \boldsymbol{\sigma} = \mathbb{C}_e + \mathbb{C}_c, \quad \partial_{\mathbf{P}} \boldsymbol{\sigma} = -(\mathbb{C}_e + \mathbb{C}_c), \quad \partial_{\mathbf{P}} \boldsymbol{\sigma}_{\text{micro}} = \mathbb{C}_{\text{micro}}, \quad \partial_{\text{Curl } \mathbf{P}} \mathbf{m} = \mu L_c^2 \mathbb{L}. \quad (4.6)$$

Note that the symmetry and anti-symmetry operators have been dropped because the definition of the tensors $\mathbb{C}_e, \mathbb{C}_{\text{micro}} : \mathbb{R}^{3 \times 3} \rightarrow \text{Sym}(3)$ and $\mathbb{C}_c : \mathbb{R}^{3 \times 3} \rightarrow \mathfrak{so}(3)$ implies these operators, see Equation (3.14), compare with SKY ET AL. [2022].

For the 2D case, the isotropic nature of the curvature arises because of the reduction of the Curl of micro-distortion field to a vector out of the plane $\text{Curl } \mathbf{P} := ((\text{Curl } \mathbf{P})_{13}, (\text{Curl } \mathbf{P})_{23})^T$, see Equation (3.18). This also applies to the moment stress $\mathbf{m} := (m_{13}, m_{23})^T$. Thus, the curvature is controlled solely by the characteristic length, assuming $\mathbb{L} = \mathbb{I}$, denoting the fourth-order identity tensor. The final form of the linearized weak forms for the 2D case reads

$$\begin{aligned} \text{Lin } \delta_{\mathbf{u}} \Pi &= \int_{\mathcal{B}} \boldsymbol{\sigma} : \nabla \delta \mathbf{u} \, dV - \int_{\mathcal{B}} \bar{\mathbf{f}} \cdot \delta \mathbf{u} \, dV - \int_{\partial \mathcal{B}_t} \bar{\mathbf{t}} \cdot \delta \mathbf{u} \, dA \\ &\quad + \int_{\mathcal{B}} \nabla \delta \mathbf{u} : (\mathbb{C}_e + \mathbb{C}_c) : \nabla \Delta \mathbf{u} \, dV - \int_{\mathcal{B}} \nabla \delta \mathbf{u} : (\mathbb{C}_e + \mathbb{C}_c) : \Delta \mathbf{P} \, dV, \\ \text{Lin } \delta_{\mathbf{P}} \Pi &= \int_{\mathcal{B}} (\boldsymbol{\sigma}_{\text{micro}} - \boldsymbol{\sigma}) : \delta \mathbf{P} + \mathbf{m} \cdot \text{Curl } \delta \mathbf{P} \, dV - \int_{\mathcal{B}} \bar{\mathbf{M}} : \delta \mathbf{P} \, dV \\ &\quad - \int_{\mathcal{B}} \delta \mathbf{P} : (\mathbb{C}_e + \mathbb{C}_c) : \nabla \Delta \mathbf{u} \, dV + \int_{\mathcal{B}} \delta \mathbf{P} : (\mathbb{C}_e + \mathbb{C}_c + \mathbb{C}_{\text{micro}}) : \Delta \mathbf{P} \, dV \\ &\quad + \int_{\mathcal{B}} \mu L_c^2 \text{Curl } \delta \mathbf{P} \cdot \text{Curl } \Delta \mathbf{P} \, dV. \end{aligned} \quad (4.7)$$

The coupled linearized forms are solved in each iteration step n with respect to the incremental quantities $\Delta \mathbf{u}_{n+1}$ and $\Delta \mathbf{P}_{n+1}$ under the assumptions that $\text{Lin } \delta_{\mathbf{u}} \Pi = 0$ and $\text{Lin } \delta_{\mathbf{P}} \Pi = 0$. The total displacement and micro-distortion fields are updated, i.e. $\mathbf{u}_{n+1} = \mathbf{u}_n + \Delta \mathbf{u}_{n+1}$ and $\mathbf{P}_{n+1} = \mathbf{P}_n + \Delta \mathbf{P}_{n+1}$ and this procedure continues iteratively until the incremental virtual works and the incremental displacement and micro-distortion field tend towards zero, i.e. less than a given tolerance.

4.2 Finite element discretization

The linearized equations have to be solved numerically with the FEM. The main concept of the FEM is to replace the real physical body \mathcal{B} with a finite number n_{ele} of non-overlapping finite elements \mathcal{B}_e resulting in a discrete counterpart \mathcal{B}_h , see Figure 4.1,

$$\mathcal{B} \approx \mathcal{B}_h = \bigcup_{e=1}^{n_{\text{ele}}} \mathcal{B}_e. \quad (4.8)$$

Each finite element approximates the primary variables, here the displacement and the micro-distortion field, via appropriate shape functions considering the values of the primary variables at specific locations (nodes and edges), and the continuous problem is transformed into a discrete problem with a finite number of values of the primary variables located at the Finite Element mesh.

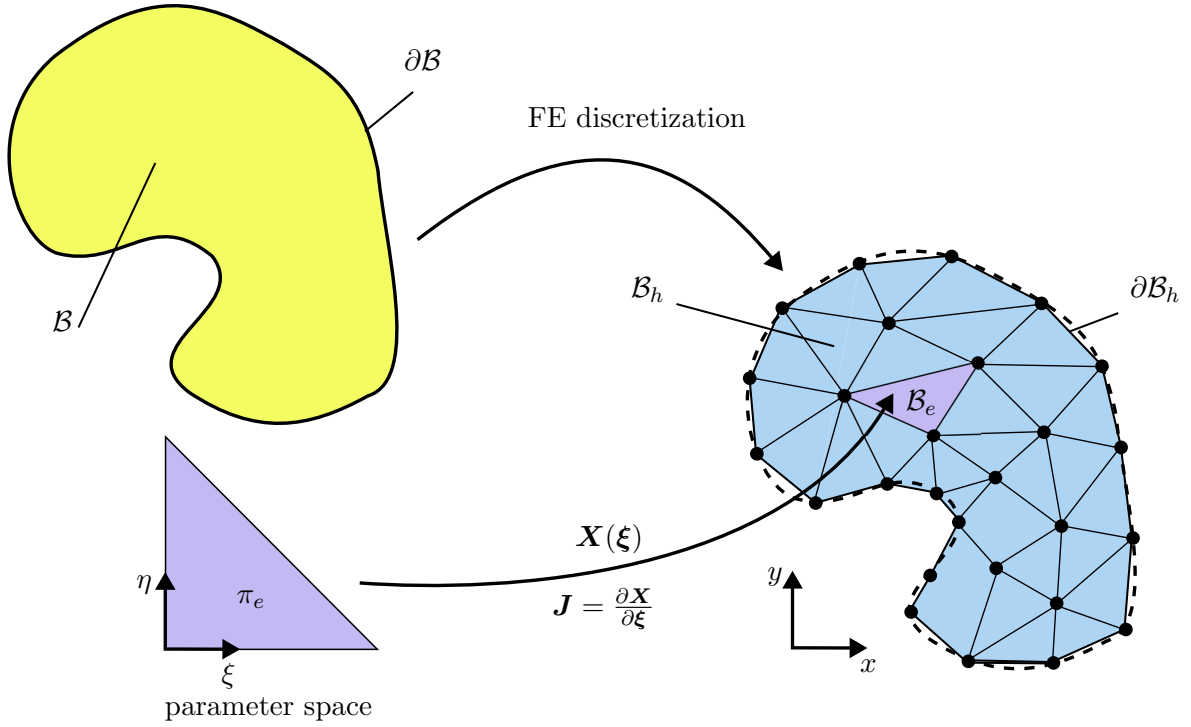


Figure 4.1: Discretization of the physical domain \mathcal{B} with the boundary $\partial\mathcal{B}$ resulting in an approximate domain \mathcal{B}_h with the boundary $\partial\mathcal{B}_h$ consisting of n_{ele} finite elements \mathcal{B}_e . Each finite element is formulated within the parameter space and subsequently mapped into the physical space.

The isoparametric concept is a commonly employed approach in the finite element method that has been adopted for this thesis. It involves introducing an isoparametric subspace called parameter space. Within this subspace, an isoparametric or unit element is defined in terms of natural coordinates $\boldsymbol{\xi} = \{\xi, \eta\}$ and subsequently mapped into the physical space $\mathbf{X} = \{x, y\}$. This mapping is established with respect to the transformation maps, which are determined by the Jacobian matrix.

4.3 Conforming finite element approximations

As a result of employing the matrix Curl operator of the micro-distortion field for the curvature measurement, the relaxed micromorphic model seeks the solution of the micro-distortion in $H(\text{curl}, \mathcal{B})$, while the displacement solution is still in $H^1(\mathcal{B})$. The appropriate finite elements of the relaxed micromorphic model must be conforming in $H^1(\mathcal{B}) \times H(\text{curl}, \mathcal{B})$ space. In the following, we present two approximation spaces for the relaxed micromorphic model for the purpose of comparison; nodal-edge $H^1(\mathcal{B}) \times H(\text{curl}, \mathcal{B})$ -conforming formulation and standard nodal formulation. Various $H^1(\mathcal{B}) \times H(\text{curl}, \mathcal{B})$ -conforming finite elements will be compared with standard $H^1(\mathcal{B}) \times H^1(\mathcal{B})$ -conforming finite elements of different shapes and orders in numerical examples.

4.3.1 $H^1(\mathcal{B})$ -conforming finite element formulation

A conforming $H^1(\mathcal{B})$ discretization employs the well-known Lagrange shape functions. They are widely used for the standard finite element formulations. The Lagrange interpolation functions are scalar-valued polynomials that are assigned to nodes. Details on the construction of Lagrange shape functions can be found in BATHE [2006], WRIGGERS [2008], ZIENKIEWICZ ET AL. [2013]. Lagrange shape functions have to satisfy two conditions. The first condition states that the shape function linked with node I denoted as N^I must be equal to one at that specific node and zero at all other nodes

$$N^I(\boldsymbol{\xi}_J) = \begin{cases} 1 & \text{if } I = J \\ 0 & \text{if } I \neq J \end{cases} . \quad (4.9)$$

The second condition, known as the partition of unity condition, asserts that the sum of the interpolation functions at each position of the element must equal one

$$\sum_I N^I(\boldsymbol{\xi}) = 1 . \quad (4.10)$$

We list in Table 4.1 the $H^1(\mathcal{B})$ -conforming finite element spaces that we will use later.

Discretization of the geometry and displacement field :

Assuming there are n^u nodes in each element for discretizing the displacement field \mathbf{u} . Both geometry and the displacement field are approximated using the same Lagrangian shape functions N_I^u (isoparametric concept), which are defined in the parameter space with natural coordinates $\boldsymbol{\xi} = \{\xi, \eta\}$,

$$\mathbf{X}_h = \sum_{I=1}^{n^u} N_I^u(\boldsymbol{\xi}) \mathbf{X}_I, \quad \mathbf{u}_h = \sum_{I=1}^{n^u} N_I^u(\boldsymbol{\xi}) \mathbf{d}_I^u, \quad (4.11)$$

where \mathbf{X}_I are the coordinates of displacement node I and \mathbf{d}_I^u are its displacement degrees of freedom. The deformation gradient is obtained in physical space by

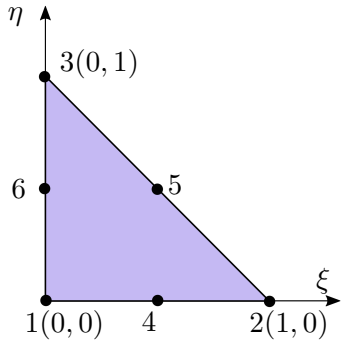
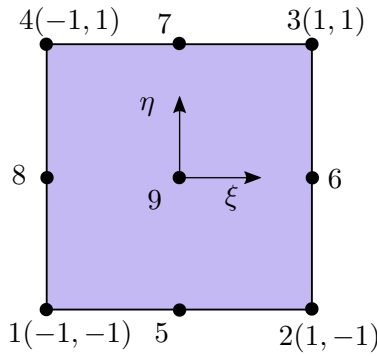
$$\nabla \mathbf{u}_h = \sum_{I=1}^{n^u} \mathbf{d}_I^u \otimes \nabla N_I^u(\boldsymbol{\xi}) \quad \text{with} \quad \nabla N_I^u(\boldsymbol{\xi}) = \mathbf{J}^{-T} \cdot \nabla_{\boldsymbol{\xi}} N_I^u, \quad (4.12)$$

where $\mathbf{J} = \frac{\partial \mathbf{X}}{\partial \boldsymbol{\xi}}$ is the mapping Jacobian, ∇ and $\nabla_{\boldsymbol{\xi}}$ denote gradient operators with respect to \mathbf{X} and $\boldsymbol{\xi}$, respectively.

Discretization of the micro-distortion field :

As previously mentioned, while the appropriate discretization for the micro-distortion field requires $H(\text{curl}, \mathcal{B})$ -conforming elements, we also introduce a standard Lagrange formulation for the micro-distortion field as well to facilitate comparison. Let us assume that n^P nodes are used to discretize the micro-distortion field \mathbf{P} . The micro-distortion

Table 4.1: The parametric $H^1(\mathcal{B})$ -conforming elements with the shape functions.

<p>linear T1 element 3 nodes</p> $N^1 = 1 - \xi - \eta$ $N^2 = \xi$ $N^3 = \eta$	<p>quadratic T2 element 6 nodes</p> $N^1 = (1 - \xi - \eta)(1 - 2\xi - 2\eta)$ $N^2 = \xi(2\xi - 1)$ $N^3 = \eta(2\eta - 1)$ $N^4 = 4\xi(1 - \xi - \eta)$ $N^5 = 4\xi\eta$ $N^6 = 4\eta(1 - \xi - \eta)$	
<p>linear Q1 element 4 nodes</p> $N^1 = \frac{1}{4}(1 - \xi)(1 - \eta)$ $N^2 = \frac{1}{4}(1 + \xi)(1 - \eta)$ $N^3 = \frac{1}{4}(1 + \xi)(1 + \eta)$ $N^4 = \frac{1}{4}(1 - \xi)(1 + \eta)$	<p>quadratic Q2 element 9 nodes</p> $N^1 = \frac{1}{4}(\xi^2 - \xi)(\eta^2 - \eta)$ $N^2 = \frac{1}{4}(\xi^2 + \xi)(\eta^2 - \eta)$ $N^3 = \frac{1}{4}(\xi^2 + \xi)(\eta^2 + \eta)$ $N^4 = \frac{1}{4}(\xi^2 - \xi)(\eta^2 + \eta)$ $N^5 = \frac{1}{2}(1 - \xi^2)(\eta^2 - \eta)$ $N^6 = \frac{1}{2}(\xi^2 + \xi)(1 - \eta^2)$ $N^7 = \frac{1}{2}(1 - \xi^2)(\eta^2 + \eta)$ $N^8 = \frac{1}{2}(\xi^2 - \xi)(1 - \eta^2)$ $N^9 = (1 - \xi^2)(1 - \eta^2)$	

field for the 2D case is approximated using the relevant scalar shape functions N_I^P

$$\mathbf{P}_h^1 = \begin{bmatrix} (P_h)_{11} \\ (P_h)_{12} \end{bmatrix} = \sum_{I=1}^{n^P} N_I^P(\boldsymbol{\xi}) \begin{bmatrix} (d_I^P)_{11} \\ (d_I^P)_{12} \end{bmatrix}, \quad (4.13)$$

$$\mathbf{P}_h^2 = \begin{bmatrix} (P_h)_{21} \\ (P_h)_{22} \end{bmatrix} = \sum_{I=1}^{n^P} N_I^P(\boldsymbol{\xi}) \begin{bmatrix} (d_I^P)_{21} \\ (d_I^P)_{22} \end{bmatrix},$$

where $(d_I^P)_{11}$, $(d_I^P)_{22}$, $(d_I^P)_{12}$ and $(d_I^P)_{21}$ are the degrees of freedom of the micro-distortion field at node I . In order to calculate the Curl of \mathbf{P} , the gradient of the row vectors in physical space can be calculated by

$$\nabla \mathbf{P}_h^i = \mathbf{J}^{-T} \cdot \nabla_{\boldsymbol{\xi}} \mathbf{P}_h^i \quad \text{for } i = 1, 2, \quad (4.14)$$

and the rotation of the vector \mathbf{P}_h^i reads

$$\text{curl}^{2D} \mathbf{P}_h^i = (P_h)_{i2,1} - (P_h)_{i1,2} \quad \text{for } i = 1, 2. \quad (4.15)$$

4.3.2 $H(\text{curl}, \mathcal{B})$ -conforming finite element formulation

Because of using the matrix Curl operator of the micro-distortion field for the curvature measurement, the relaxed micromorphic model seeks the solution of the micro-distortion field in $H(\text{curl}, \mathcal{B})$. The appropriate finite elements of such a case must be conforming in $H(\text{curl}, \mathcal{B})$ (tangentially conforming). The first formulation of conforming “edge” elements was introduced in RAVIART AND THOMAS [1977]. The name “edge” element was used because the degrees of freedom (dofs) are associated only with edges for a first-order approximation. $H(\text{curl}, \mathcal{B})$ -conforming finite elements of the first kind were presented in NÉDÉLEC [1980] and the second kind in NÉDÉLEC [1986], which are comparable with $H(\text{div}, \mathcal{B})$ -conforming elements of the first kind in RAVIART AND THOMAS [1977] and the second kind in BREZZI ET AL. [1985]. Employing covariant projections, an extension to elements with curved edges was developed by CROWLEY ET AL. [1988]. A general implementation of Nédélec elements of the first kind is presented in OLM ET AL. [2019], and a detailed review of $H(\text{div}, \mathcal{B})$ - and $H(\text{curl}, \mathcal{B})$ -conforming finite elements is available in KIRBY ET AL. [2012] and ROGNES ET AL. [2009]. Furthermore, hierarchical $H(\text{curl})$ -conforming finite elements are employed to solve Maxwell boundary and eigenvalue problems in SCHÖBERL AND ZAGLMAYR [2005]. Various finite element formulations of the relaxed micromorphic model were presented for the antiplane shear case in SKY ET AL. [2021], and the three-dimensional case in SKY ET AL. [2022; 2024a]. A conforming finite element formulation for a further relaxed curvature can be found in SKY ET AL. [2024b]. In this work, we choose the Nédélec space of the first kind. For more details, the reader is referred to BOFFI ET AL. [2014], KIRBY ET AL. [2012], MONK [1993], ROGNES ET AL. [2009]. Nédélec formulations use vectorial shape functions that satisfy tangential continuity at element interfaces. The lowest-order two-dimensional Nédélec elements are illustrated in Figure 4.2.

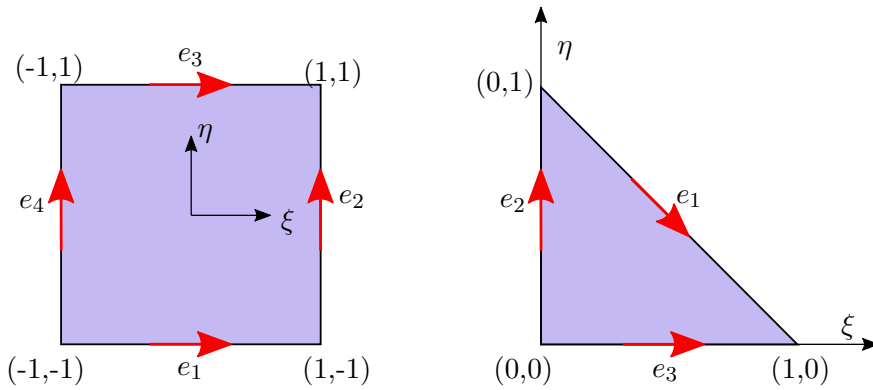


Figure 4.2: The lowest-order ($k = 1$) Nédélec elements: triangle $[\mathcal{ND}^\Delta]_1^2$ (right) and quadrilateral $[\mathcal{ND}^\square]_1^2$ (left). Definition of the individual edges e_i . The red arrows indicate the orientation of tangential flux. Taken from SCHRÖDER ET AL. [2022]

Triangular Nédélec elements of order k are based on the space

$$[\mathcal{ND}^\Delta]_k^2 = (\mathbb{P}_{k-1})^2 \oplus \mathbf{S}_k \quad \text{with} \quad \mathbf{S}_k = \{\mathbf{p} \in (\check{\mathbb{P}}_k)^2 \mid \mathbf{p} \cdot \boldsymbol{\xi} = 0\}, \quad (4.16)$$

where \mathbb{P}_{k-1} is the linear space of polynomials of degree $k - 1$ or less and $\check{\mathbb{P}}_k$ is the linear space of homogeneous polynomials of degree k . Equivalently, this space can be

characterized by

$$[\mathcal{ND}^\Delta]_k^2 = \langle \oplus \check{\mathbb{P}}_{k-1} \begin{bmatrix} -\eta \\ \xi \end{bmatrix} \rangle. \quad (4.17)$$

The dimension of this linear space is $\dim([\mathcal{ND}^\Delta]_k^2) = k(k+2)$. Quadrilateral Nédélec elements of order k are based on the linear space

$$[\mathcal{ND}^\square]_k^2 = \begin{bmatrix} Q_{k-1,k} \\ Q_{k,k-1} \end{bmatrix} \quad \text{where} \quad Q_{m,n} = \text{span}\{\xi^i \eta^j \mid i \leq m, j \leq n\}, \quad (4.18)$$

with $\dim([\mathcal{ND}^\square]_k^2) = 2k(k+1)$. The vectorial shape functions \mathbf{v}^k in parameter space are calculated by constructing a linear system of equations based on a set of inner and outer dofs. For the 2D case, the outer dofs of an edge e_i (see Figure 4.2) are determined by the integral

$$m_j^{e_i}(\mathbf{v}^k) = \int_{e_i} (\mathbf{v}^k \cdot \mathbf{t}_i) r_j \, ds, \quad \forall r_j \in \mathbb{P}_{k-1}(e_i), \quad (4.19)$$

where r_j is a polynomial \mathbb{P}_{k-1} along edge e_i and \mathbf{t}_i is the normalized tangential vector of edge e_i . The inner dofs are defined for triangular elements by

$$m_i^{\text{inner}}(\mathbf{v}^k) = \int_{\pi_e} \mathbf{v}^k \cdot \mathbf{q}_i \, da, \quad \forall \mathbf{q}_i \in (\mathbb{P}_{k-2}(\pi_e))^2, \quad (4.20)$$

while they are given for quadrilateral elements by

$$m_i^{\text{inner}}(\mathbf{v}^k) = \int_{\pi_e} \mathbf{v}^k \cdot \mathbf{q}_i \, da, \quad \forall \mathbf{q}_i \in \begin{bmatrix} Q_{k-1,k-2}(\pi_e) \\ Q_{k-2,k-1}(\pi_e) \end{bmatrix}. \quad (4.21)$$

The scalar-valued and vectorial functions r_j and \mathbf{q}_i are linearly independent polynomials that are chosen as Lagrange polynomials. For the lowest-order element ($k=1$), only outer dofs occur. For higher-order elements ($k \geq 2$), the number of outer dofs increases and additional inner dofs are introduced. E.g. for the $[\mathcal{ND}^\Delta]_2^2$ with a dimension 8, we have 6 outer dofs and 2 inner ones.

In the following, we illustrate the derivation of the vectorial Nédélec shape functions for the lowest-order triangular element NT1. The derivations of Nédélec's vectorial shape functions for the second-order triangular element and both first- and second-order quadrilateral elements are presented in Appendix A. A parametric triangular element is defined on a domain $\pi_e^\Delta = \{0 \leq \xi \leq 1, 0 \leq \eta \leq 1 - \xi\}$. The parametric lowest-order finite elements with the respective edge numbering are shown in Figure 4.2. The Nédélec space of a first-order triangular element (NT1) reads

$$[\mathcal{ND}^\Delta]_1^2 = \left\{ \begin{bmatrix} 1 \\ 0 \end{bmatrix}, \begin{bmatrix} 0 \\ 1 \end{bmatrix}, \begin{bmatrix} -\eta \\ \xi \end{bmatrix} \right\}, \quad (4.22)$$

and the general form of vectorial shape function is

$$\mathbf{v}^1 = \begin{bmatrix} a_1 - a_3 \eta \\ a_2 + a_3 \xi \end{bmatrix}, \quad (4.23)$$

where $a_i, i=1, 2, 3$ are coefficients yet to be defined based on the dofs. Starting from the definition in Equation (4.19), we set $r_j = 1$ for all edges. The tangential vectors of all edges, see Figure 4.2 (right), are given by

$$\mathbf{t}_1 = \frac{1}{\sqrt{2}} \begin{bmatrix} 1 \\ -1 \end{bmatrix}, \quad \mathbf{t}_2 = \begin{bmatrix} 0 \\ 1 \end{bmatrix}, \quad \mathbf{t}_3 = \begin{bmatrix} 1 \\ 0 \end{bmatrix}. \quad (4.24)$$

We calculate the dofs following Equation (4.19) using $\xi + \eta = 1$ on the first edge, $\xi = 0$ on the second edge and $\eta = 0$ on the third edge and obtain

$$m_1^{e_1} = a_1 - a_2 - a_3, \quad m_1^{e_2} = a_2, \quad m_1^{e_3} = a_1. \quad (4.25)$$

In order to obtain the vectorial shape functions $\mathbf{v}_1^1, \mathbf{v}_2^1$ and \mathbf{v}_3^1 from the general function in Equation (4.23), we have to compute three associated combinations for a_1, a_2 and a_3 . We derive the explicit expressions for the vectorial shape functions by enforcing

$$m_1^{e_i}(\mathbf{v}_j^k) = \delta_{ij}, \quad (4.26)$$

for shape vector \mathbf{v}_j^k associated with edge e_j . The evaluation of dofs for each edge, i.e.

$$\begin{aligned} \text{edge 1: } & m_1^{e_1} = 1, & m_1^{e_2} = 0, & m_1^{e_3} = 0 & \Rightarrow & a_1 = 0, & a_2 = 0, & a_3 = -1 \\ \text{edge 2: } & m_1^{e_1} = 0, & m_1^{e_2} = 1, & m_1^{e_3} = 0 & \Rightarrow & a_1 = 0, & a_2 = 1, & a_3 = -1 \\ \text{edge 3: } & m_1^{e_1} = 0, & m_1^{e_2} = 0, & m_1^{e_3} = 1 & \Rightarrow & a_1 = 1, & a_2 = 0, & a_3 = 1 \end{aligned} \quad (4.27)$$

leads to the shape vectors

$$\mathbf{v}_1^1 = \begin{pmatrix} \eta \\ -\xi \end{pmatrix}, \quad \mathbf{v}_2^1 = \begin{pmatrix} \eta \\ 1 - \xi \end{pmatrix}, \quad \mathbf{v}_3^1 = \begin{pmatrix} 1 - \eta \\ \xi \end{pmatrix}. \quad (4.28)$$

A visualization is depicted in Figure 4.3. Note that each vectorial shape function linked with a specific edge is perpendicular to the other edges, i.e. it has tangential projection only on its associated edge.

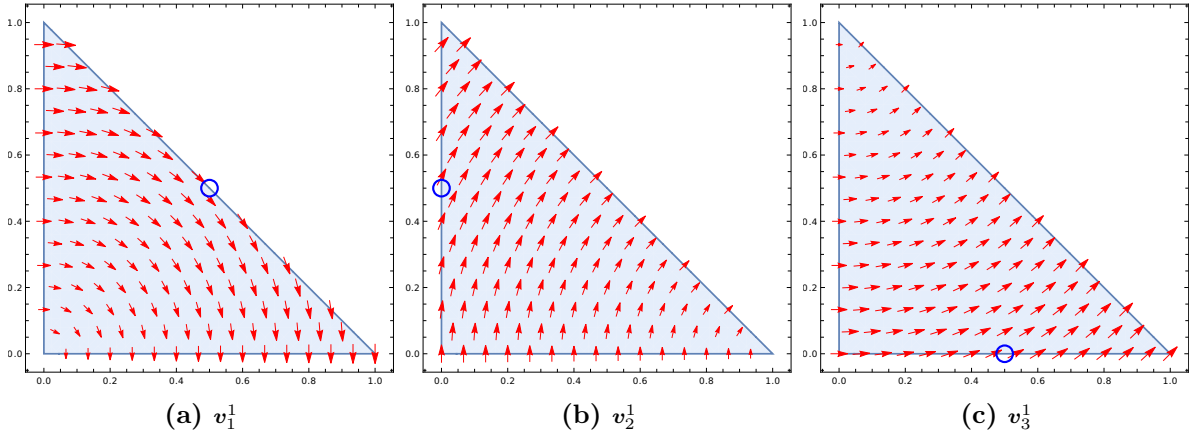


Figure 4.3: Tangential-conforming vectorial shape functions of NT1 element. Blue circles indicate the position where the dofs are defined. Taken from SCHRÖDER ET AL. [2022]

Mapping vectorial shape functions \mathbf{v}_I^k from the parameter space to $\check{\psi}_I^k$ in the physical space must conserve the tangential continuity property. This is guaranteed by using the covariant Piola transformation, see for example ROGNES ET AL. [2009], which reads

$$\check{\psi}_I^k = \mathbf{J}^{-T} \cdot \mathbf{v}_I^k \quad \text{and} \quad \text{curl } \check{\psi}_I^k = \frac{1}{\det \mathbf{J}} \mathbf{J} \cdot \text{curl}_\xi \mathbf{v}_I^k. \quad (4.29)$$

For our implementation of $H(\text{curl}, \mathcal{B})$ -conforming elements, we modify the mapping to enforce the required orientation of the degrees of freedom at inter-element boundaries

and to attach a direct physical interpretation to the Neumann-type boundary conditions. Hence, two additional parameters, α and β , appear for the vectorial shape functions associated with edge dofs

$$\boldsymbol{\psi}_I^k = \alpha_I \beta_I \check{\boldsymbol{\psi}}_I^k \quad \text{and} \quad \text{curl } \boldsymbol{\psi}_I^k = \alpha_I \beta_I \text{curl } \check{\boldsymbol{\psi}}_I^k, \quad (4.30)$$

where $\alpha_I = \pm 1$ is the orientation consistency function which ensures that on an edge, belonging to two neighboring finite elements, a positive tangential flux direction is defined. Therefore, this positive tangential direction is determined based on a positive x -coordinate. A tangential component pointing in negative x -direction is multiplied by a value $\alpha_I = -1$ to obtain an overall positive tangential flux on each edge. When the tangential direction has no projection on the x -axis, the same procedure is employed in y -direction. This can be summarized as

$$\alpha_I = \begin{cases} +1 & \text{if } \left. (\check{\boldsymbol{\psi}}_I^k)_1 \right|_{E_I} > 0, \\ -1 & \text{if } \left. (\check{\boldsymbol{\psi}}_I^k)_1 \right|_{E_I} < 0, \\ +1 & \text{if } \left. (\check{\boldsymbol{\psi}}_I^k)_1 \right|_{E_I} = 0 \quad \text{and} \quad \left. (\check{\boldsymbol{\psi}}_I^k)_2 \right|_{E_I} > 0, \\ -1 & \text{if } \left. (\check{\boldsymbol{\psi}}_I^k)_1 \right|_{E_I} = 0 \quad \text{and} \quad \left. (\check{\boldsymbol{\psi}}_I^k)_2 \right|_{E_I} < 0. \end{cases} \quad (4.31)$$

Figure 4.4 illustrates an example of calculating the orientation parameter values of two neighboring elements.

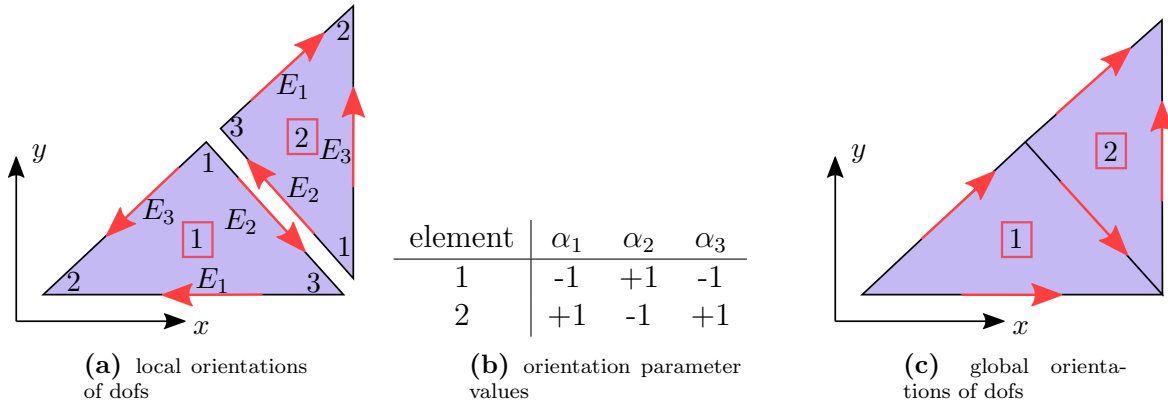


Figure 4.4: Example of assembling of two neighboring elements which satisfy the orientation consistency via the orientation parameter α_I . Taken from SCHRÖDER ET AL. [2022]

The normalization parameter β_I enforces that the sum of vectorial shape functions $\boldsymbol{\psi}_I^k$ at a shared edge scalar multiplied with the associated tangential vector must be equal to one in physical space. Furthermore, the sum of the shape functions belonging to one edge scalar multiplied by the tangential vector of the other edges must vanish. These conditions are reflected by

$$\boldsymbol{\tau}_I \cdot \sum_J \boldsymbol{\psi}_J^k \Big|_{E_I} \equiv \begin{cases} 1 & \text{if } I = J \\ 0 & \text{if } I \neq J \end{cases} \quad (4.32)$$

Here, $\sum_J \psi_J^k \Big|_{E_I}$ is the sum of shape vectors related to outer dofs of an edge E_J evaluated on edge E_I and $\boldsymbol{\tau}_I$ is the normalized tangential vector of an edge E_I where E denotes the edges in the physical space. Based on Equations (4.30) and (4.32), we compute straightforward the parameters β_I . In detail, we get for first- and second-order elements

$$\beta_I = L_I \quad \text{and} \quad \beta_I = \frac{L_I}{2}, \quad (4.33)$$

respectively, where L_I denotes the length of edge E_I in physical space. For the 2D case, the rotation of vectorial shape functions only has one active component out of the plane, which reads

$$\text{curl}^{2D} \boldsymbol{\psi}_I^k = \frac{\alpha_I \beta_I}{\det \mathbf{J}} \text{curl}_{\boldsymbol{\xi}}^{2D} \mathbf{v}_I^k. \quad (4.34)$$

The micro-distortion field \mathbf{P} is approximated by the vectorial dofs $\mathbf{d}_I^P = ((d_I^P)_1, (d_I^P)_2)^T$ representing its tangential projections at location $I = 1, \dots, n^P$. The micro-distortion field and its Curl are interpolated as

$$\mathbf{P}_h = \sum_{I=1}^{n^P} \mathbf{d}_I^P \otimes \boldsymbol{\psi}_I^k, \quad \text{Curl } \mathbf{P}_h = \sum_{I=1}^{n^P} \mathbf{d}_I^P \otimes \text{curl } \boldsymbol{\psi}_I^k. \quad (4.35)$$

The non-vanishing components of the Curl operator of the micro-distortion field for the 2D case are obtained by

$$\begin{bmatrix} \text{curl}^{2D} \mathbf{P}_h^1 \\ \text{curl}^{2D} \mathbf{P}_h^2 \end{bmatrix} = \sum_{I=1}^{n^P} \text{curl}^{2D} \boldsymbol{\psi}_I^k \mathbf{d}_I^P = \begin{bmatrix} \sum_{I=1}^{n^P} \text{curl}^{2D} \boldsymbol{\psi}_I^k (d_I^P)_1 \\ \sum_{I=1}^{n^P} \text{curl}^{2D} \boldsymbol{\psi}_I^k (d_I^P)_2 \end{bmatrix}. \quad (4.36)$$

4.4 Implemented finite elements

We introduce four nodal-edge $H^1(\mathcal{B}) \times H(\text{curl}, \mathcal{B})$ elements based on the formulation in Section 4.3.2 and two standard nodal $H^1(\mathcal{B}) \times H^1(\mathcal{B})$ elements based on Section 4.3.1. All implemented finite elements use scalar quadratic shape functions of Lagrange-type for the displacement field discretization with the notation T2 for triangles and Q2 for quadrilaterals. The micro-distortion field is discretized using different formulations presented in Sections 4.3.1 and 4.3.2. For the standard nodal elements, Lagrange-type ansatz functions are employed, leading to element types T2T1 (linear ansatz for \mathbf{P}) and T2T2 (quadratic ansatz for \mathbf{P}). Different nodal-edge elements are built using first- and second-order Nédélec formulations with tangential-conforming shape functions denoted as NT1 and NT2 for triangular elements and QT1 and QT2 for quadrilateral elements. The micro-distortion dofs in the standard nodal $H^1(\mathcal{B}) \times H^1(\mathcal{B})$ elements are tensorial with 2×2 entries, while the nodal-edge $H^1(\mathcal{B}) \times H(\text{curl}, \mathcal{B})$ elements use vectorial dofs for the micro-distortion field representing the tangential projections. The used finite elements are depicted in the parameter space in Figure 4.5.

The expected convergence rates of $H^1(\mathcal{B}) \times H(\text{curl}, \mathcal{B})$ elements for the relaxed micromorphic model were discussed for anti-plane shear and 3D cases in SKY ET AL. [2021; 2022]. In a similar way for an element with an $H^1(\mathcal{B})$ -conforming formulation of order k for the

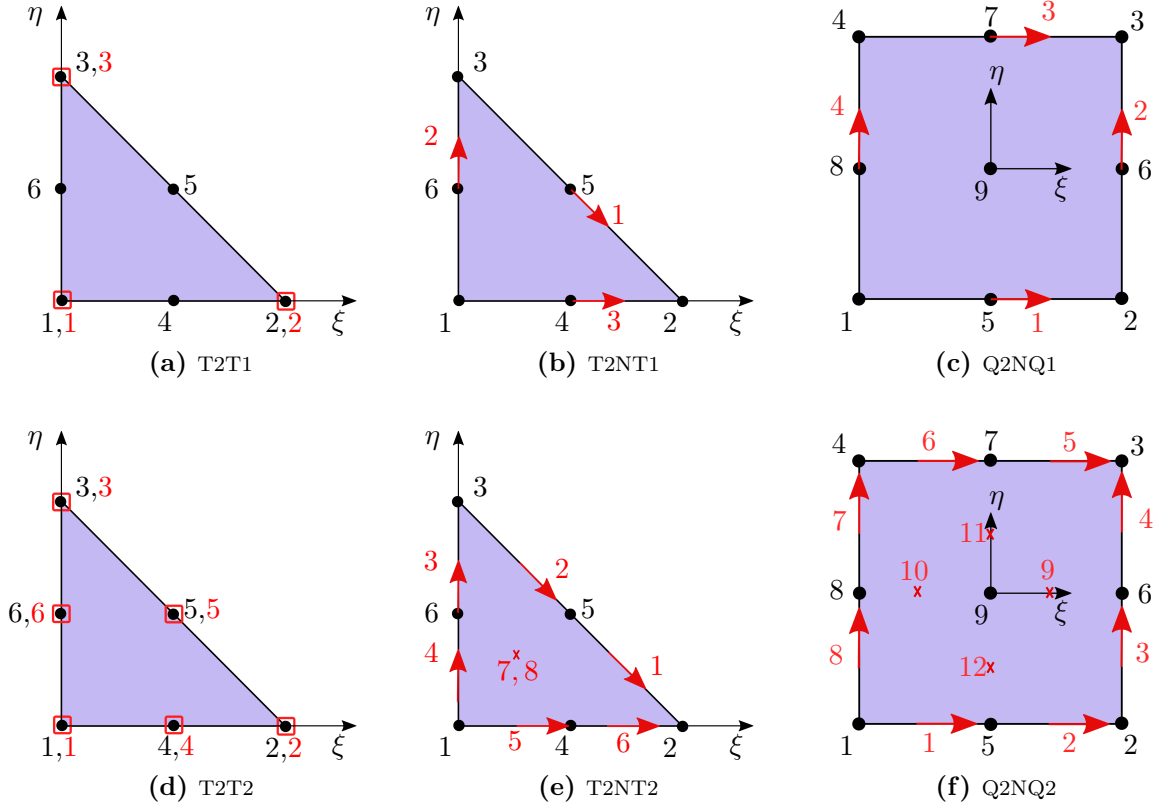


Figure 4.5: The implemented finite elements in the parameter space. Black dots represent the displacement nodes while red squares stand for micro-distortion field nodes associated with 2×2 tensorial dofs in Lagrange formulation. Red arrows and crosses indicate the edge and inner vectorial dofs, respectively, of the micro-distortion field used in Nédélec formulation. Taken from SCHRÖDER ET AL. [2022]

displacement approximation and a first type Nédélec formulation of order k for the micro-distortion approximation, the solution should converge with an optimal convergence rate k in $H^1(\mathcal{B}) \times H(\text{curl}, \mathcal{B})$ norm which is defined in Section 3.1. Therefore, we expect that the elements T2NT2 and Q2NQ2 achieve an optimal convergence rate of two.

4.5 Discretization of the linearized weak forms

In the following, we give the discretized formulations of the linearized weak forms shown in Equation (4.7) for the implemented finite element approximation spaces. Here, we use the Voigt notation, demonstrated in Appendix B, which stores the second-order tensors as vectors and the fourth-order tensors as matrices. Voigt notation provides an efficient representation of the discrete linearized weak forms (distinguished with wide hat $\widehat{\bullet}$).

4.5.1 $H^1(\mathcal{B}) \times H^1(\mathcal{B})$ finite elements

The approximation of the physical, virtual and incremental displacement field is given element-wise by means of

$$\mathbf{u}_h = \sum_{I=1}^{n^u} \mathbf{N}_I^u \mathbf{d}_I^u, \quad \delta \mathbf{u}_h = \sum_{I=1}^{n^u} \mathbf{N}_I^u \delta \mathbf{d}_I^u, \quad \Delta \mathbf{u}_h = \sum_{I=1}^{n^u} \mathbf{N}_I^u \Delta \mathbf{d}_I^u, \quad (4.37)$$

with the definition of the matrix \mathbf{N}_I^u as

$$\mathbf{N}_I^u = \begin{bmatrix} N_I^u & 0 \\ 0 & N_I^u \end{bmatrix}, \quad (4.38)$$

where $\mathbf{d}_I^u = ((d_I^u)_1, (d_I^u)_2)^T$ denotes the discrete nodal displacements at node I while $\delta \mathbf{d}_I^u$ and $\Delta \mathbf{d}_I^u$ are the virtual and incremental counterparts, respectively. The displacement gradient and the associated virtual and incremental counterparts are discretized as

$$\widehat{\nabla} \mathbf{u}_h = \sum_{I=1}^{n^u} \mathbf{B}_I^u \mathbf{d}_I^u, \quad \widehat{\nabla} \delta \mathbf{u}_h = \sum_{I=1}^{n^u} \mathbf{B}_I^u \delta \mathbf{d}_I^u, \quad \widehat{\nabla} \Delta \mathbf{u}_h = \sum_{I=1}^{n^u} \mathbf{B}_I^u \Delta \mathbf{d}_I^u, \quad (4.39)$$

with the following definition of the \mathbf{B}_I^u matrix which contains the spatial derivatives of the shape functions

$$\mathbf{B}_I^u = \begin{bmatrix} (N_I^u)_{,1} & 0 \\ 0 & (N_I^u)_{,2} \\ (N_I^u)_{,2} & 0 \\ 0 & (N_I^u)_{,1} \end{bmatrix}. \quad (4.40)$$

The approximation of the physical, virtual and incremental micro-distortion field is given element-wise for $H^1(\mathcal{B})$ -conforming element by means of

$$\widehat{\mathbf{P}}_h = \sum_{I=1}^{n^P} \mathbf{N}_I^P \mathbf{d}_I^P, \quad \widehat{\delta \mathbf{P}}_h = \sum_{I=1}^{n^P} \mathbf{N}_I^P \delta \mathbf{d}_I^P, \quad \widehat{\Delta \mathbf{P}}_h = \sum_{I=1}^{n^P} \mathbf{N}_I^P \Delta \mathbf{d}_I^P, \quad (4.41)$$

where the matrix \mathbf{N}_I^P is defined as:

$$\mathbf{N}_I^P = \begin{bmatrix} N_I^P & 0 & 0 & 0 \\ 0 & N_I^P & 0 & 0 \\ 0 & 0 & N_I^P & 0 \\ 0 & 0 & 0 & N_I^P \end{bmatrix}. \quad (4.42)$$

Here, $\mathbf{d}_I^P = ((d_I^P)_{11}, (d_I^P)_{22}, (d_I^P)_{12}, (d_I^P)_{21})^T$ represents the discrete nodal micro-distortion at node I , while $\delta \mathbf{d}_I^P$ and $\Delta \mathbf{d}_I^P$ stand for the virtual and incremental counterparts, respectively. The Curl of the micro-distortion field and its virtual and incremental counterparts are further discretized as

$$\text{Curl } \mathbf{P}_h = \sum_{I=1}^{n^P} \mathbf{B}_I^P \mathbf{d}_I^P, \quad \text{Curl } \delta \mathbf{P}_h = \sum_{I=1}^{n^P} \mathbf{B}_I^P \delta \mathbf{d}_I^P, \quad \text{Curl } \Delta \mathbf{P}_h = \sum_{I=1}^{n^P} \mathbf{B}_I^P \Delta \mathbf{d}_I^P, \quad (4.43)$$

with the matrix \mathbf{B}_I^P defined as

$$\mathbf{B}_I^P = \begin{bmatrix} -(N_I^P)_{,2} & 0 & (N_I^P)_{,1} & 0 \\ 0 & (N_I^P)_{,1} & 0 & -(N_I^P)_{,2} \end{bmatrix}. \quad (4.44)$$

Next, we substitute the discrete approximations into the linearized weak forms as presented in Equation (4.7). The discrete formulation of the linearized weak form of the generalized balance of linear momentum for one $H^1(\mathcal{B}) \times H^1(\mathcal{B})$ finite element is given by

$$\begin{aligned} (\text{Lin } \delta_{\mathbf{u}} \Pi)^e &= \sum_{I=1}^{n^u} (\delta \mathbf{d}_I^u)^T \underbrace{\left\{ \int_{\mathcal{B}_e} (\mathbf{B}_I^u)^T \widehat{\boldsymbol{\sigma}} \, dV - \int_{\mathcal{B}_e} \mathbf{N}_I^u \bar{\mathbf{f}} \, dV - \int_{(\partial \mathcal{B}_e)_t} \mathbf{N}_I^u \bar{\mathbf{t}} \, dA \right\}}_{r_I^u} \\ &+ \sum_{I=1}^{n^u} \sum_{J=1}^{n^u} (\delta \mathbf{d}_I^u)^T \underbrace{\left\{ \int_{\mathcal{B}_e} (\mathbf{B}_I^u)^T (\widehat{\mathbb{C}}_e + \widehat{\mathbb{C}}_c) \mathbf{B}_J^u \, dV \right\}}_{\mathbf{k}_{IJ}^{uu}} \Delta \mathbf{d}_J^u \\ &+ \sum_{I=1}^{n^u} \sum_{J=1}^{n^P} (\delta \mathbf{d}_I^u)^T \underbrace{\left\{ - \int_{\mathcal{B}_e} (\mathbf{B}_I^u)^T (\widehat{\mathbb{C}}_e + \widehat{\mathbb{C}}_c) \mathbf{N}_J^P \, dV \right\}}_{\mathbf{k}_{IJ}^{up}} \Delta \mathbf{d}_J^P. \end{aligned} \quad (4.45)$$

Analogously, the linearized weak form of the generalized balance of angular momentum for one $H^1(\mathcal{B}) \times H^1(\mathcal{B})$ finite element reads

$$\begin{aligned} (\text{Lin } \delta_{\mathbf{P}} \Pi)^e &= \sum_{I=1}^{n^P} (\delta \mathbf{d}_I^P)^T \underbrace{\left\{ \int_{\mathcal{B}_e} \mathbf{N}_I^P (\widehat{\boldsymbol{\sigma}}_{\text{micro}} - \widehat{\boldsymbol{\sigma}}) + (\mathbf{B}_I^P)^T \mathbf{m} \, dV - \int_{\mathcal{B}_e} \mathbf{N}_I^P \widehat{\mathbf{M}} \, dV \right\}}_{r_I^P} \\ &+ \sum_{I=1}^{n^P} \sum_{J=1}^{n^u} (\delta \mathbf{d}_I^P)^T \underbrace{\left\{ - \int_{\mathcal{B}_e} \mathbf{N}_I^P (\widehat{\mathbb{C}}_e + \widehat{\mathbb{C}}_c) \mathbf{B}_J^u \, dV \right\}}_{\mathbf{k}_{IJ}^{pu}} \Delta \mathbf{d}_J^u \\ &+ \sum_{I=1}^{n^P} \sum_{J=1}^{n^P} (\delta \mathbf{d}_I^P)^T \underbrace{\left\{ \int_{\mathcal{B}_e} \mathbf{N}_I^P (\widehat{\mathbb{C}}_e + \widehat{\mathbb{C}}_c + \widehat{\mathbb{C}}_{\text{micro}}) \mathbf{N}_J^P + \mu L_c^2 (\mathbf{B}_I^P)^T \mathbf{B}_J^P \, dV \right\}}_{\mathbf{k}_{IJ}^{pp}} \Delta \mathbf{d}_J^P. \end{aligned} \quad (4.46)$$

4.5.2 $H^1(\mathcal{B}) \times H(\text{curl}, \mathcal{B})$ finite elements

$H^1(\mathcal{B}) \times H(\text{curl}, \mathcal{B})$ elements differ from $H^1(\mathcal{B}) \times H^1(\mathcal{B})$ elements primarily in the approximation space used for the micro-distortion field and, consequently, its Curl. The discretization of the physical, virtual and incremental micro-distortion field \mathbf{P} is given by

$$\widehat{\mathbf{P}}_h = \sum_{I=1}^{n^P} \Psi_I^P \mathbf{d}_I^P, \quad \delta \widehat{\mathbf{P}}_h = \sum_{I=1}^{n^P} \Psi_I^P \delta \mathbf{d}_I^P, \quad \Delta \widehat{\mathbf{P}}_h = \sum_{I=1}^{n^P} \Psi_I^P \Delta \mathbf{d}_I^P, \quad (4.47)$$

with the matrix Ψ_I^P is defined as

$$\Psi_I^P = \begin{bmatrix} (\psi_I^k)_1 & 0 \\ 0 & (\psi_I^k)_2 \\ (\psi_I^k)_2 & 0 \\ 0 & (\psi_I^k)_1 \end{bmatrix}. \quad (4.48)$$

Here, $\mathbf{d}_I^P = [(d_I^P)_1, (d_I^P)_2]^T$ represents the discrete nodal tangential projection of the micro-distortion at node I while $\delta \mathbf{d}_I^P$ and $\Delta \mathbf{d}_I^P$ stand for the virtual and incremental counterparts, respectively. The Curl of micro-distortion field and its virtual and incremental counterparts are further discretized as

$$\begin{aligned} \text{Curl } \mathbf{P}_h &= \sum_{I=1}^{n^P} \text{curl}^{2D} \psi_I^k \mathbf{d}_I^P, \\ \text{Curl } \delta \mathbf{P}_h &= \sum_{I=1}^{n^P} \text{curl}^{2D} \psi_I^k \delta \mathbf{d}_I^P, \\ \text{Curl } \Delta \mathbf{P}_h &= \sum_{I=1}^{n^P} \text{curl}^{2D} \psi_I^k \Delta \mathbf{d}_I^P, \end{aligned} \quad (4.49)$$

Next, we substitute the discrete approximations into the linearized weak forms as presented in Equation (4.7). The discrete formulation of the linearized weak form of the generalized balance of linear momentum for one $H^1(\mathcal{B}) \times H(\text{curl}, \mathcal{B})$ finite element is given by

$$\begin{aligned} (\text{Lin } \delta_u \Pi)^e &= \sum_{I=1}^{n^u} (\delta \mathbf{d}_I^u)^T \underbrace{\left\{ \int_{\mathcal{B}_e} (\mathbf{B}_I^u)^T \widehat{\boldsymbol{\sigma}} \, dV - \int_{\mathcal{B}_e} \mathbf{N}_I^u \bar{\mathbf{f}} \, dV - \int_{(\partial \mathcal{B}_e)_t} \mathbf{N}_I^u \bar{\mathbf{t}} \, dA \right\}}_{\mathbf{r}_I^u} \\ &+ \sum_{I=1}^{n^u} \sum_{J=1}^{n^u} (\delta \mathbf{d}_I^u)^T \underbrace{\left\{ \int_{\mathcal{B}_e} (\mathbf{B}_I^u)^T (\widehat{\mathbf{C}}_e + \widehat{\mathbf{C}}_c) \mathbf{B}_J^u \, dV \right\}}_{\mathbf{k}_{IJ}^{uu}} \Delta \mathbf{d}_J^u \\ &+ \sum_{I=1}^{n^u} \sum_{J=1}^{n^P} (\delta \mathbf{d}_I^u)^T \underbrace{\left\{ - \int_{\mathcal{B}_e} (\mathbf{B}_I^u)^T (\widehat{\mathbf{C}}_e + \widehat{\mathbf{C}}_c) \Psi_J^P \, dV \right\}}_{\mathbf{k}_{IJ}^{up}} \Delta \mathbf{d}_J^P. \end{aligned} \quad (4.50)$$

Analogously, the linearized weak form of the generalized balance of linear momentum for one $H^1(\mathcal{B}) \times H(\text{curl}, \mathcal{B})$ finite element reads

$$\begin{aligned}
(Lin \delta_P \Pi)^e &= \sum_{I=1}^{n^P} (\delta \mathbf{d}_I^P)^T \underbrace{\left\{ \int_{\mathcal{B}_e} (\Psi_I^P)^T (\widehat{\boldsymbol{\sigma}}_{\text{micro}} - \widehat{\boldsymbol{\sigma}}) + (\text{curl}^{2D} \boldsymbol{\psi}_I^k) \mathbf{m} \, dV - \int_{\mathcal{B}_e} (\Psi_I^P)^T \widehat{\mathbf{M}} \, dV \right\}}_{\mathbf{r}_I^P} \\
&\quad + \sum_{I=1}^{n^P} \sum_{J=1}^{n^u} (\delta \mathbf{d}_I^P)^T \underbrace{\left\{ - \int_{\mathcal{B}_e} (\Psi_I^P)^T (\widehat{\mathbf{C}}_e + \widehat{\mathbf{C}}_c) \mathbf{B}_J^u \, dV \right\}}_{\mathbf{k}_{IJ}^{Pu}} \Delta \mathbf{d}_J^u \\
&\quad + \sum_{I=1}^{n^P} \sum_{J=1}^{n^P} (\delta \mathbf{d}_I^P)^T \underbrace{\left\{ \int_{\mathcal{B}_e} (\Psi_I^P)^T (\widehat{\mathbf{C}}_e + \widehat{\mathbf{C}}_c + \widehat{\mathbf{C}}_{\text{micro}}) \Psi_J^P + \mu L_c^2 (\text{curl}^{2D} \boldsymbol{\psi}_I^k) (\text{curl}^{2D} \boldsymbol{\psi}_J^k) \mathbf{I} \, dV \right\}}_{\mathbf{k}_{IJ}^{PP}} \Delta \mathbf{d}_J^P.
\end{aligned} \tag{4.51}$$

4.6 Numerical integration

To compute the stiffness matrix and residual vector for each finite element, obtained as integral quantities over an element domain \mathcal{B}_e , we utilize Gauss quadrature. This method entails evaluating the function at multiple integration points within the element domain, multiplying these values by corresponding Gauss weights w_{Gp} , and subsequently summing them up. Applying the isoparametric concept allows us to convert the integral of a function $f(\mathbf{X})$ over an element \mathcal{B}_e in physical space to the unit element π_e in the parameter space

$$\int_{\mathcal{B}_e} f(\mathbf{X}) \, dV = \int_{\pi_e} f(\boldsymbol{\xi}) \det \mathbf{J}(\boldsymbol{\xi}) \, d\pi. \tag{4.52}$$

The previous integral can be numerically evaluated using Gauss quadrature

$$\int_{\pi_e} f(\boldsymbol{\xi}) \det \mathbf{J}(\boldsymbol{\xi}) \, d\pi \approx \sum_{Gp=1}^{n_{Gp}} w_{Gp} f(\boldsymbol{\xi}_{Gp}) \det \mathbf{J}(\boldsymbol{\xi}_{Gp}). \tag{4.53}$$

Here, a sufficient number of Gaussian points n_{Gp} and appropriate integration positions need to be selected for accurate computation. For more details, we refer to BATHE [2006], WRIGGERS [2008], ZIENKIEWICZ ET AL. [2013] and the references within.

4.7 Assembling procedure for the boundary value problem

To obtain the solution for a boundary value problem within a domain \mathcal{B} , discretized by n_{ele} finite elements, we must assemble the global system of equations. We arrange the finite element vectors of virtual and incremental primary variables

$$\delta \mathbf{d}_e = \begin{bmatrix} \delta \mathbf{d}_e^u \\ \delta \mathbf{d}_e^p \end{bmatrix}, \quad \text{and} \quad \Delta \mathbf{d}_e = \begin{bmatrix} \Delta \mathbf{d}_e^u \\ \Delta \mathbf{d}_e^p \end{bmatrix}, \tag{4.54}$$

with $\delta \mathbf{d}_e^\bullet = [(\delta \mathbf{d}_1^\bullet)^T, (\delta \mathbf{d}_2^\bullet)^T, \dots, (\delta \mathbf{d}_{n^\bullet}^\bullet)^T]^T$ and $\Delta \mathbf{d}_e^\bullet = [(\Delta \mathbf{d}_1^\bullet)^T, (\Delta \mathbf{d}_2^\bullet)^T, \dots, (\Delta \mathbf{d}_{n^\bullet}^\bullet)^T]^T$. The element stiffness matrix and residual vector are given by

$$\mathbf{k}_e = \begin{bmatrix} \mathbf{k}_e^{uu} & \mathbf{k}_e^{up} \\ \mathbf{k}_e^{pu} & \mathbf{k}_e^{pp} \end{bmatrix}, \quad \text{and} \quad \mathbf{r}_e = \begin{bmatrix} \mathbf{r}_e^u \\ \mathbf{r}_e^p \end{bmatrix}, \quad (4.55)$$

where we have

$$\mathbf{k}_e^{\bullet\bullet} = \begin{bmatrix} \mathbf{k}_{11}^{\bullet\bullet} & \mathbf{k}_{12}^{\bullet\bullet} & \dots & \mathbf{k}_{1n^\bullet}^{\bullet\bullet} \\ \mathbf{k}_{21}^{\bullet\bullet} & \mathbf{k}_{22}^{\bullet\bullet} & \dots & \mathbf{k}_{2n^\bullet}^{\bullet\bullet} \\ \dots & \dots & \dots & \dots \\ \mathbf{k}_{n^\bullet 1}^{\bullet\bullet} & \mathbf{k}_{n^\bullet 2}^{\bullet\bullet} & \dots & \mathbf{k}_{n^\bullet n^\bullet}^{\bullet\bullet} \end{bmatrix}, \quad \text{and} \quad \mathbf{r}_e^\bullet = \begin{bmatrix} \mathbf{r}_1^\bullet \\ \mathbf{r}_2^\bullet \\ \dots \\ \mathbf{r}_{n^\bullet}^\bullet \end{bmatrix}. \quad (4.56)$$

In order to obtain the global stiffness matrix \mathbf{K} , the global solution vector $\Delta \mathbf{D}$ and the global residual vector \mathbf{R} , we assemble the element contributions over the whole domain

$$\mathbf{K} = \mathbf{A} \begin{matrix} n_{ele} \\ \mathbf{A} \\ e=1 \end{matrix} \mathbf{k}_e, \quad \Delta \mathbf{D} = \mathbf{A} \begin{matrix} n_{ele} \\ \mathbf{A} \\ e=1 \end{matrix} \Delta \mathbf{d}_e, \quad \mathbf{R} = \mathbf{A} \begin{matrix} n_{ele} \\ \mathbf{A} \\ e=1 \end{matrix} \mathbf{r}_e, \quad (4.57)$$

and the global system of equation reads

$$(\delta \mathbf{D})^T (\mathbf{K} \Delta \mathbf{D} + \mathbf{R}) = 0 \quad \forall \delta \mathbf{D} \neq \mathbf{0} \quad \Rightarrow \quad \Delta \mathbf{D} = -\mathbf{K}^{-1} \mathbf{R}. \quad (4.58)$$

Within a Newton-Raphson iterative scheme the global solution vector is updated $\mathbf{D} = \mathbf{D} + \Delta \mathbf{D}$ until the global residual vector \mathbf{R} falls below a given tolerance.

4.8 Numerical examples

For the numerical examples in this Section, we assume isotropic material behavior which can be described by the set of material parameters $\lambda_{\text{micro}}, \mu_{\text{micro}}, \lambda_e, \mu_e, \mu_c, \mu$ and L_c , where λ_* and μ_* denote the Lamé coefficients. Moreover, we consider the Cosserat modulus $\mu_c = 0$, cf. NEFF [2006], NEFF ET AL. [2015], leading to the symmetry of the force stress tensor, however, the model is still well-posed.

4.8.1 Patch-test

Patch-tests, introduced in the 1960s, are instructed for the following intentions: i) to inspect the performance of finite element formulations violating continuity conditions (convergence) ii) to find out simple programming mistakes iii) as an established tool to check the convergence order for any element type, see ZIENKIEWICZ AND TAYLOR [1997]. For finite elements that satisfy required continuity conditions, patch-tests checks the correct programming.

We prepare a patch-test for the relaxed micromorphic model. A domain $\mathcal{B} = [0, 1] \times [0, 1]$ is considered. The isotropic case of the relaxed micromorphic model is assumed with material parameters $\lambda_{\text{micro}} = \mu_{\text{micro}} = \lambda_e = \mu_e = \mu = 1$, $L_c = 1$ and $\mu_c = 0$. The solution is given a priori ($\bar{\mathbf{u}}$ and $\bar{\mathbf{P}} = \nabla \bar{\mathbf{u}}$), and the generated body moments and forces are defined by solving the strong forms. In our numerical setup, we apply the derived body moments

and forces with Dirichlet boundary conditions $\mathbf{u} = \bar{\mathbf{u}}$ and $\mathbf{P} \cdot \boldsymbol{\tau} = \bar{\mathbf{P}} \cdot \boldsymbol{\tau}$ on the whole boundary $\partial\mathcal{B}$. Irregular meshes consisting of four quadrilaterals or triangles are utilized, see Figure 4.6.

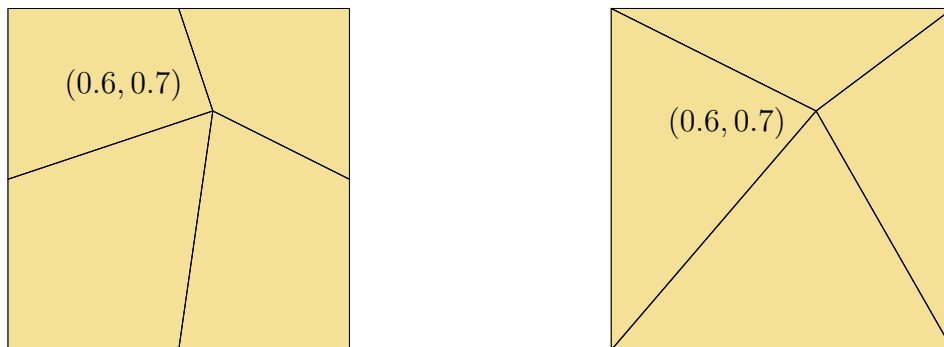


Figure 4.6: Patch-test discretization. Taken from SCHRÖDER ET AL. [2022]

Simple patch-test:

We test the case of a linear displacement and a constant micro-distortion field. The assumed solution with the related body-forces and body-moments reads

$$\bar{\mathbf{u}} = \begin{pmatrix} x \\ y \end{pmatrix}, \quad \bar{\mathbf{P}} = \begin{pmatrix} 1 & 0 \\ 0 & 1 \end{pmatrix}, \quad \bar{\mathbf{f}} = \mathbf{0}, \quad \bar{\mathbf{M}} = \begin{pmatrix} 4 & 0 \\ 0 & 4 \end{pmatrix}. \quad (4.59)$$

Due to the polynomial order of the shape functions, all elements must capture the solution precisely, which is what we obtain after testing, except for typical computational inaccuracies (machine precision).

Higher-order patch-test:

Next, we investigate the case of a quadratic displacement and a linear micro-distortion field. The given solution with the related body-forces and body-moments reads

$$\bar{\mathbf{u}} = \begin{pmatrix} x^2 \\ y^2 \end{pmatrix}, \quad \bar{\mathbf{P}} = \begin{pmatrix} 2x & 0 \\ 0 & 2y \end{pmatrix}, \quad \bar{\mathbf{f}} = \mathbf{0}, \quad \bar{\mathbf{M}} = \begin{pmatrix} 6x + 2y & 0 \\ 0 & 2x + 6y \end{pmatrix}. \quad (4.60)$$

Due to the polynomial order of the shape functions, the elements T2T1, T2T2, T2NT2 and Q2NQ2 can obtain the analytical solution (except for the typical computational inaccuracies). First-order Nédélec elements are unable to obtain the analytical solution without numerical errors because the element's spaces $[\mathcal{ND}^\Delta]_1^2$ and $[\mathcal{ND}^\square]_1^2$ do not contain the whole linear space $(\mathbb{P}_1)^2$. Therefore, we use this test to analyze the convergence behavior of first-order Nédélec elements T2NT1 and Q2NQ1. The used structured and unstructured meshes as well as the convergence behavior are displayed in Figures 4.7 and 4.8. The numerical solution converges to the analytical solution when refining the mesh.

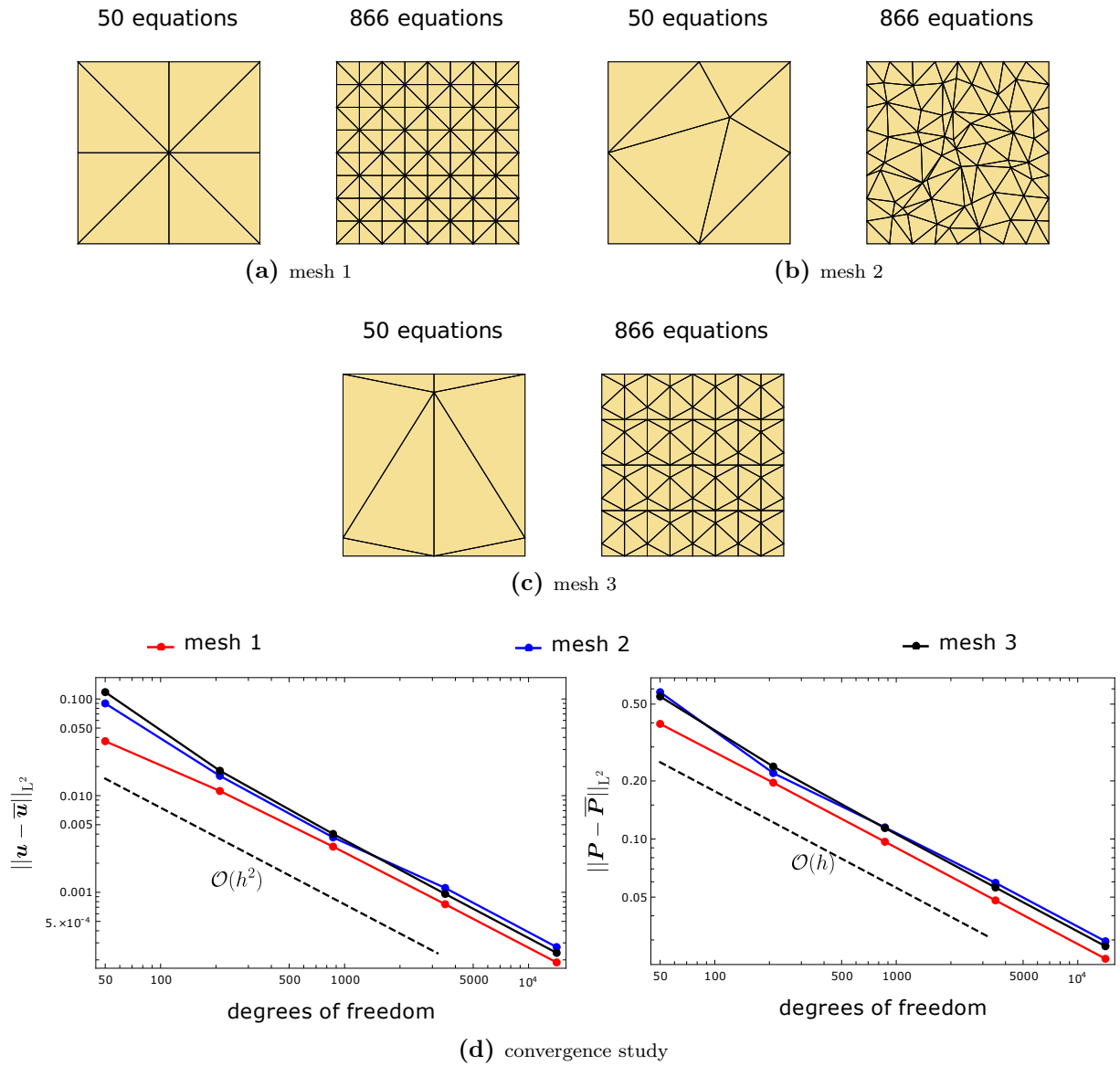


Figure 4.7: The error measurements $\|\mathbf{u} - \bar{\mathbf{u}}\|_{L^2}$ and $\|\mathbf{P} - \bar{\mathbf{P}}\|_{L^2}$ of the higher-order patch-test with quadratic displacement for element T2NT1 with varying number of equations in (d). Three different types of finite element meshing were chosen for the convergence study, see (a-c). Taken from SCHRÖDER ET AL. [2022]

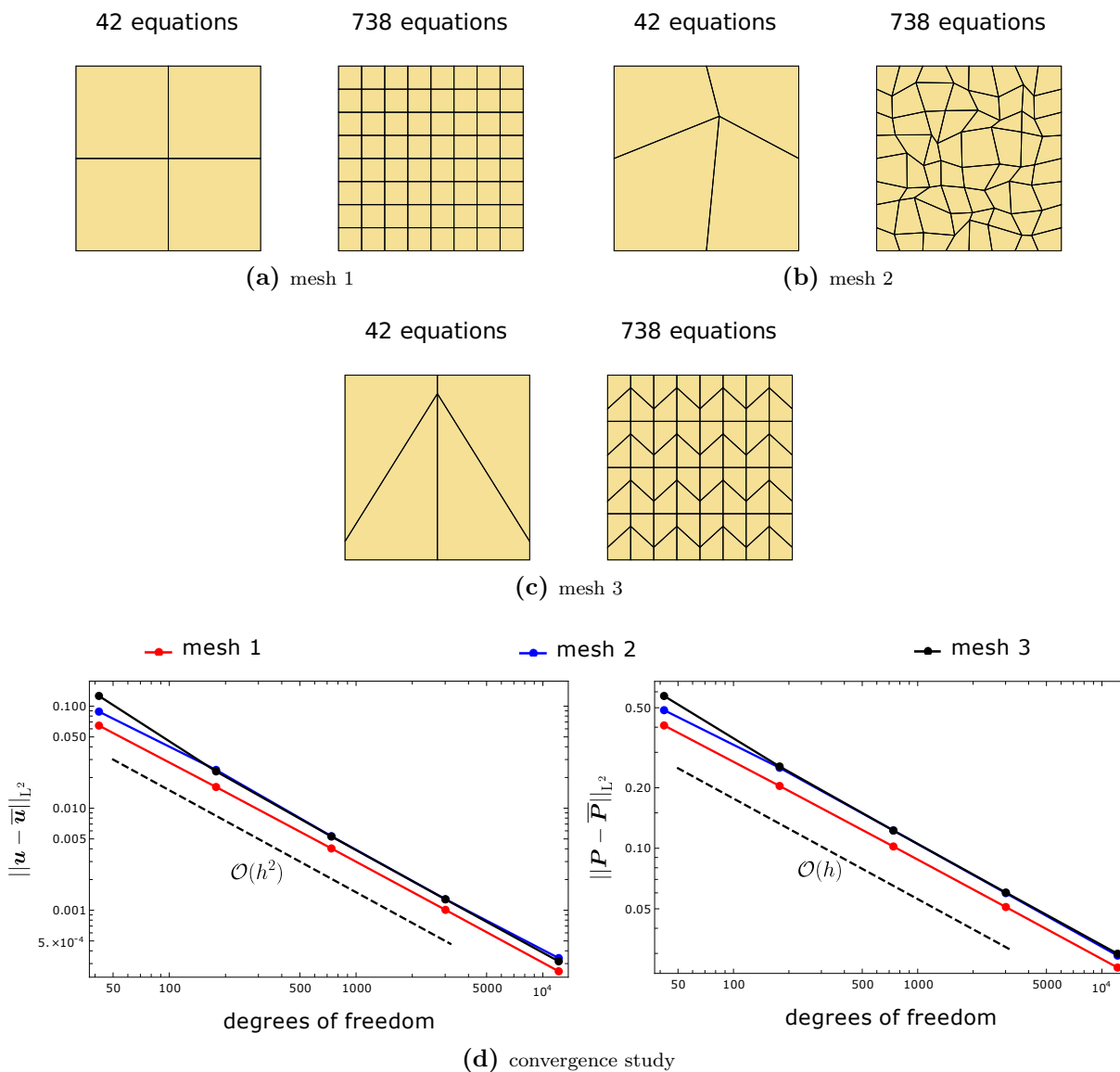


Figure 4.8: The error measurements $\|\mathbf{u} - \bar{\mathbf{u}}\|_{L^2}$ and $\|\mathbf{P} - \bar{\mathbf{P}}\|_{L^2}$ of the higher-order patch-test with quadratic displacement for element Q2NQ1 with varying number of equations in (d). Three different types of finite element meshing were chosen for the convergence study, see (a-c). Taken from SCHRÖDER ET AL. [2022]

4.8.2 Discontinuous solution: convergence study

For this boundary value problem, we assume a homogeneous rectangular domain \mathcal{B} with length $l = 2$ and height $h = 1$ shown in Figure 4.9. We consider the following displacement and micro-distortion field

$$\bar{\mathbf{u}} = \begin{cases} \begin{pmatrix} e^{y(1-x)} \\ e^{y^2(1-x)} \end{pmatrix} & \text{for } x \leq 1 \\ \begin{pmatrix} e^{y(x-1)} \\ e^{y^2(x-1)} \end{pmatrix} & \text{for } x > 1 \end{cases}, \quad (4.61)$$

$$\bar{\mathbf{P}} = \nabla \bar{\mathbf{u}} = \begin{cases} \begin{pmatrix} -ye^{y(1-x)} & (1-x)e^{y(1-x)} \\ -y^2e^{y^2(1-x)} & 2y(1-x)e^{y^2(1-x)} \end{pmatrix} & \text{for } x \leq 1 \\ \begin{pmatrix} ye^{y(x-1)} & (x-1)e^{y(x-1)} \\ y^2e^{y^2(x-1)} & 2y(x-1)e^{y^2(x-1)} \end{pmatrix} & \text{for } x > 1 \end{cases}, \quad (4.62)$$

where the displacement field and tangential components of the micro-distortion $\bar{\mathbf{P}} \cdot \mathbf{e}_2 = (\bar{P}_{12}, \bar{P}_{22})^T$ are continuous on an interface at $x = 1$ while the normal components $\bar{\mathbf{P}} \cdot \mathbf{e}_1 = (\bar{P}_{11}, \bar{P}_{21})^T$ show discontinuities. The isotropic case of the relaxed micromorphic model is assumed with the material parameters $\lambda_{\text{micro}} = \mu_{\text{micro}} = \lambda_e = \mu_e = \mu = 1$, $L_c = 1$ and $\mu_c = 0$. Solving the strong forms leads to vanishing body forces, while the body moments read

$$\bar{\mathbf{M}} = \begin{pmatrix} 3\bar{u}_{1,1} + \bar{u}_{2,2} & \bar{u}_{1,2} + \bar{u}_{2,1} \\ \bar{u}_{1,2} + \bar{u}_{2,1} & \bar{u}_{1,1} + 3\bar{u}_{2,2} \end{pmatrix}. \quad (4.63)$$

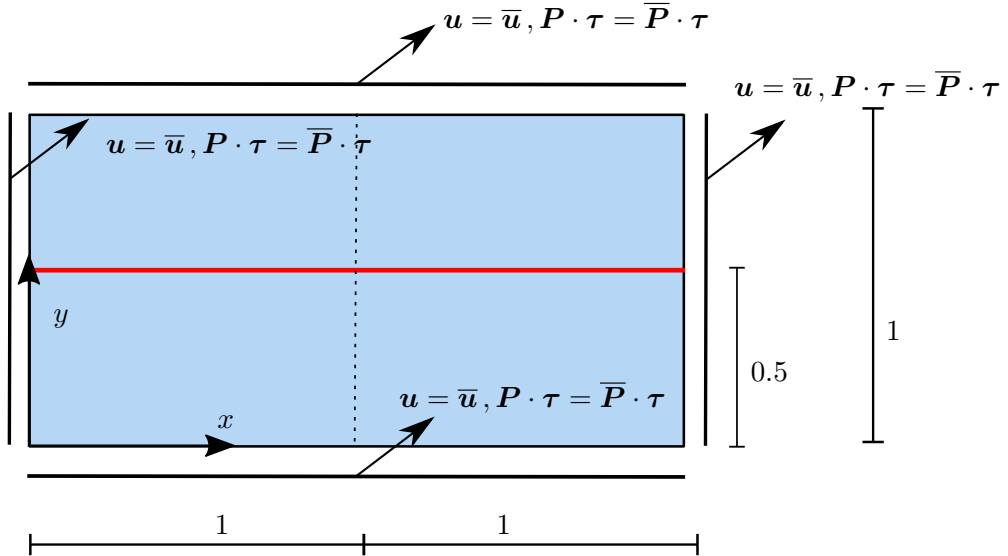


Figure 4.9: 2D homogeneous rectangular. The inspection line, used in Figures 4.11 and 4.12, can be seen in red color. Taken from SCHRÖDER ET AL. [2022]

For the numerical setup, the boundary conditions are enforced as

$$\mathbf{u} = \bar{\mathbf{u}} \quad \text{and} \quad \mathbf{P} \cdot \boldsymbol{\tau} = \bar{\mathbf{P}} \cdot \boldsymbol{\tau} = \nabla \bar{\mathbf{u}} \cdot \boldsymbol{\tau} \quad \text{on } \partial \mathcal{B}, \quad (4.64)$$

where the obtained body moments and different meshes are used. We display in Figure 4.10 the displacement and micro-distortion field obtained by 882 Q2NQ2 elements on a structured rectangular mesh (see Figure 4.13a). The tangential components of the micro-distortion are continuous on the interface, while the normal components exhibit a jump.

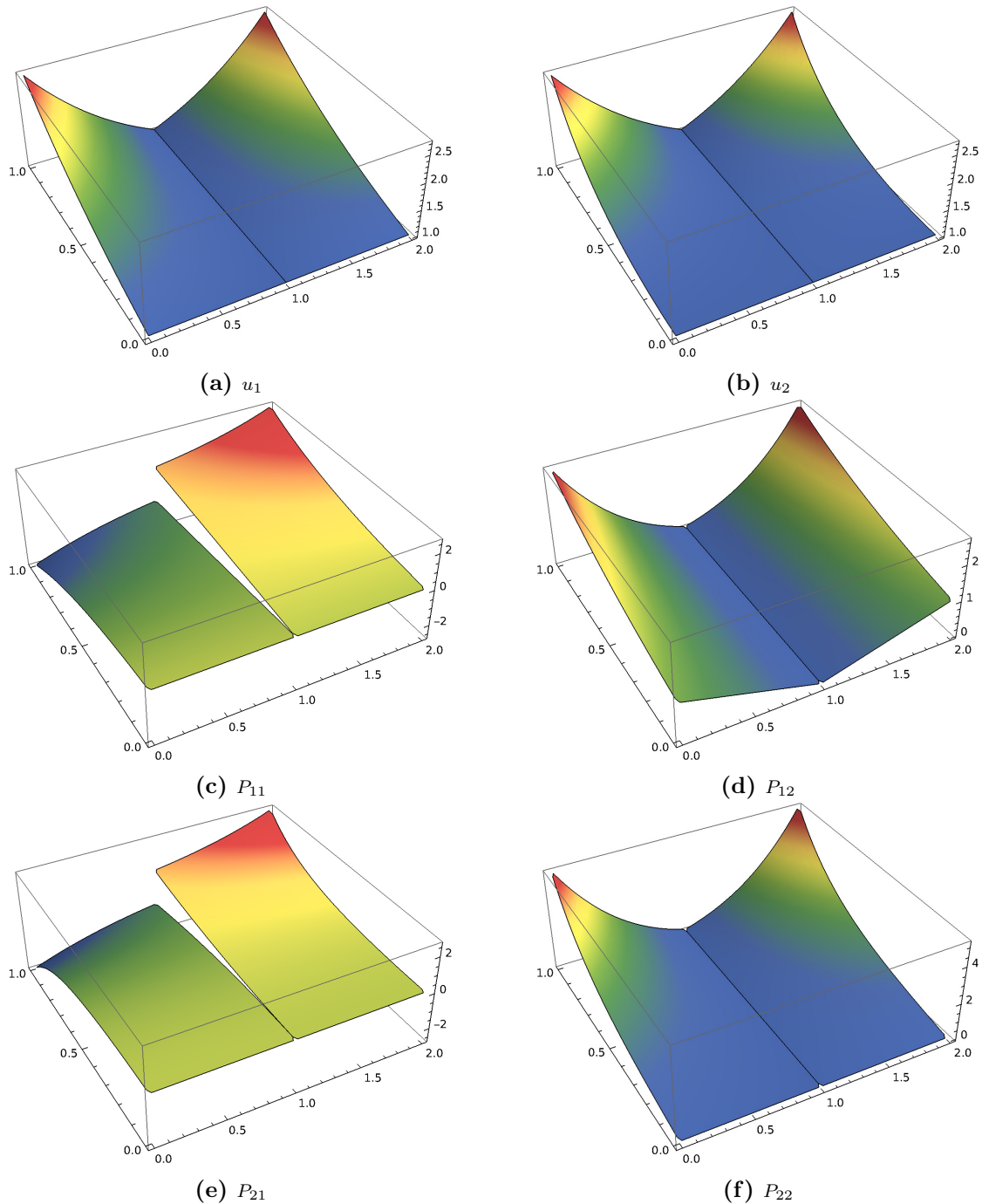


Figure 4.10: Displacement and micro-distortion field components. Taken from SCHRÖDER ET AL. [2022].

A convergence study of the component P_{11} along the inspection line $y = 0.5$ is plotted in Figures 4.11 and 4.12. $H^1(\mathcal{B}) \times H^1(\mathcal{B})$ elements, see Figure 4.11, lead to a continuous

solution that causes a transition zone at the interface which requires to be resolved by increasing the mesh density tremendously in order to resemble the discontinuous solution at the interface. Meanwhile, the discontinuous solution of P_{11} can be captured by $H^1(\mathcal{B}) \times H(\text{curl}, \mathcal{B})$ elements, see Figure 4.12. The second-order Nédélec formulations in T2NT2 and Q2NQ2 give a numerical solution close to the analytical solution, even with a coarse mesh. In contrast, first-order Nédélec formulations in T2NT1 and Q2NQ1 demand a denser mesh because they only illustrate a constant micro-distortion field in each element.

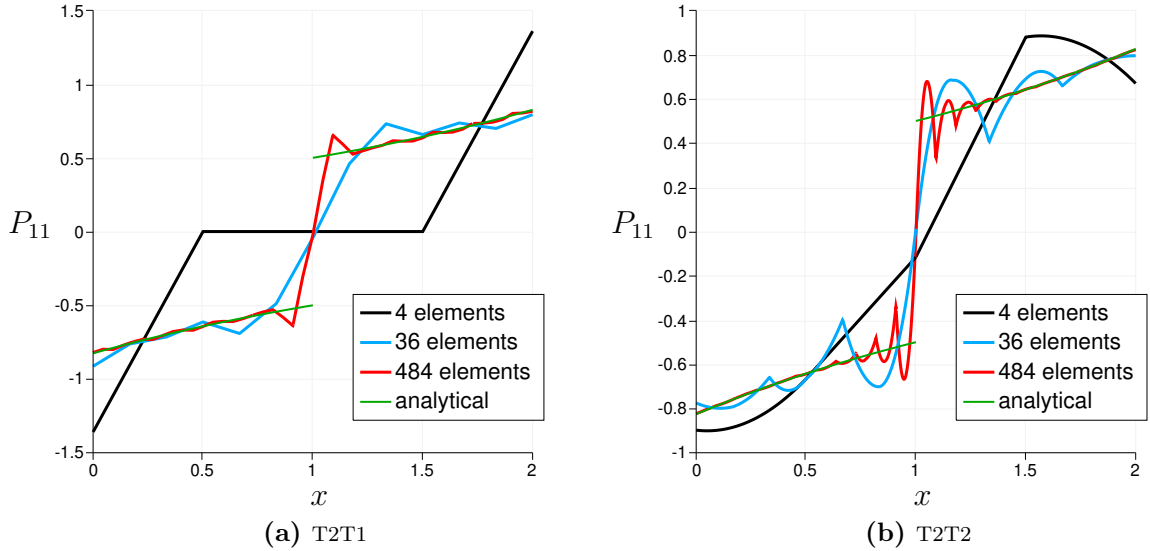


Figure 4.11: Illustration of P_{11} along the inspection line $y = 0.5$ using nodal elements with different mesh densities on regular structured meshes. Taken from SCHRÖDER ET AL. [2022].

We investigate the convergence rates of the implemented finite elements in this numerical example for three different meshes, see Figures 4.13, 4.14 and 4.15. The mesh schemes are refined similarly to Figures 4.7 and 4.8. Instead of plotting the L^2 -norm error of total space $\|\{\mathbf{u}, \mathbf{P}\} - \{\bar{\mathbf{u}}, \bar{\mathbf{P}}\}\|_{H^1(\mathcal{B}) \times H(\text{curl}, \mathcal{B})}^2$, see Section 3.1, we demonstrate its individual components. These are the L^2 -norms of the error of the displacement $\|\mathbf{u} - \bar{\mathbf{u}}\|_{L^2}$, its gradient $\|\nabla \mathbf{u} - \nabla \bar{\mathbf{u}}\|_{L^2}$, the micro-distortion $\|\mathbf{P} - \bar{\mathbf{P}}\|_{L^2}$ and its Curl field $\|\text{Curl } \mathbf{P} - \text{Curl } \bar{\mathbf{P}}\|_{L^2}$. The analysis of the individual error norms is more targeted-oriented from an engineering point of view since it deals with the different energy terms independently. Second-order Nédélec elements T2NT2 and Q2NQ2 lead to convergence rates of three in the L^2 -norm of the displacement error ($\|\mathbf{u} - \bar{\mathbf{u}}\|_{L^2}$), and a convergence rate of two in the remaining error norms. Thus, the second-order Nédélec elements T2NT2 and Q2NQ2 exhibit an optimal convergence rate of two in the space $H^1(\mathcal{B}) \times H(\text{curl}, \mathcal{B})$ norm, which meets the theoretical anticipations. First-order Nédélec elements T2NT1 and Q2NQ1 deliver one order of convergence less compared to second-order ones. The nodal elements T2T1 and T2T2 show a convergence rate of less than half in $H^1(\mathcal{B}) \times H(\text{curl}, \mathcal{B})$ norm.

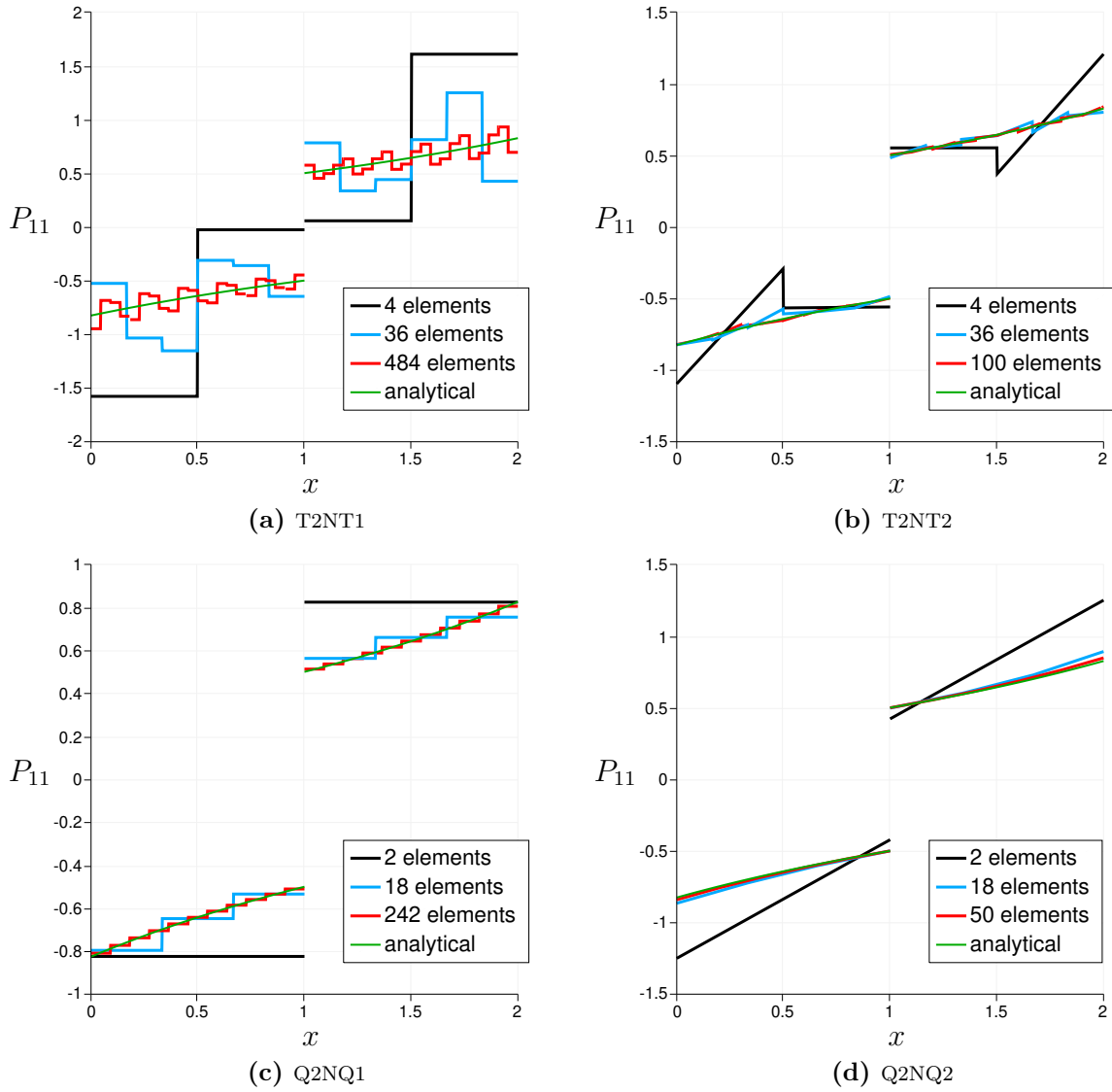


Figure 4.12: Illustration of P_{11} along the inspection line $y = 0.5$ using $H^1(\mathcal{B}) \times H(\text{curl}, \mathcal{B})$ elements with different mesh densities on regular structured meshes. Taken from SCHRÖDER ET AL. [2022].

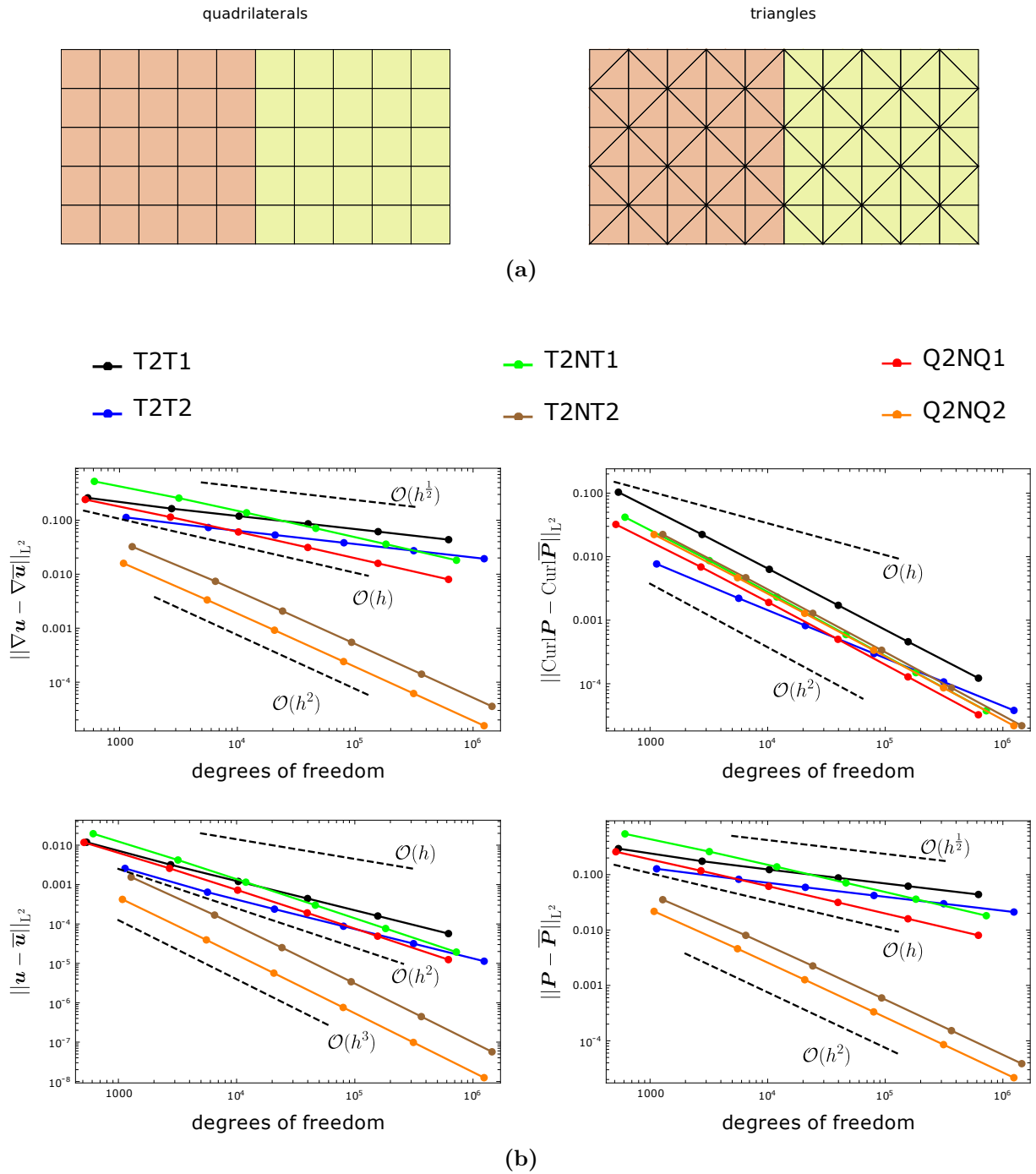


Figure 4.13: Computational convergence study (b) of first mesh depicted in (a). Taken from SCHRÖDER ET AL. [2022].

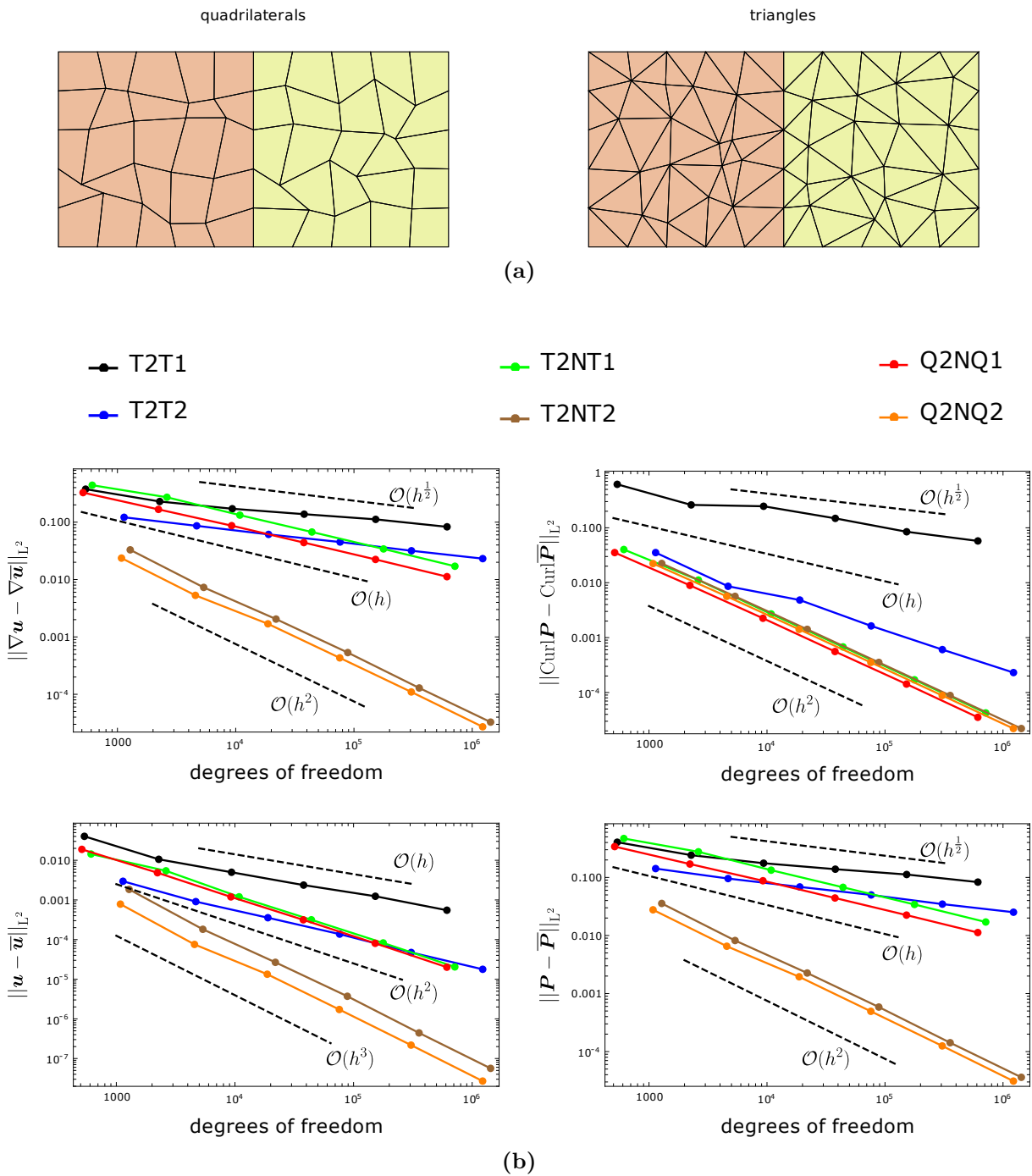


Figure 4.14: Computational convergence study (b) of second mesh depicted in (a). Taken from SCHRÖDER ET AL. [2022].

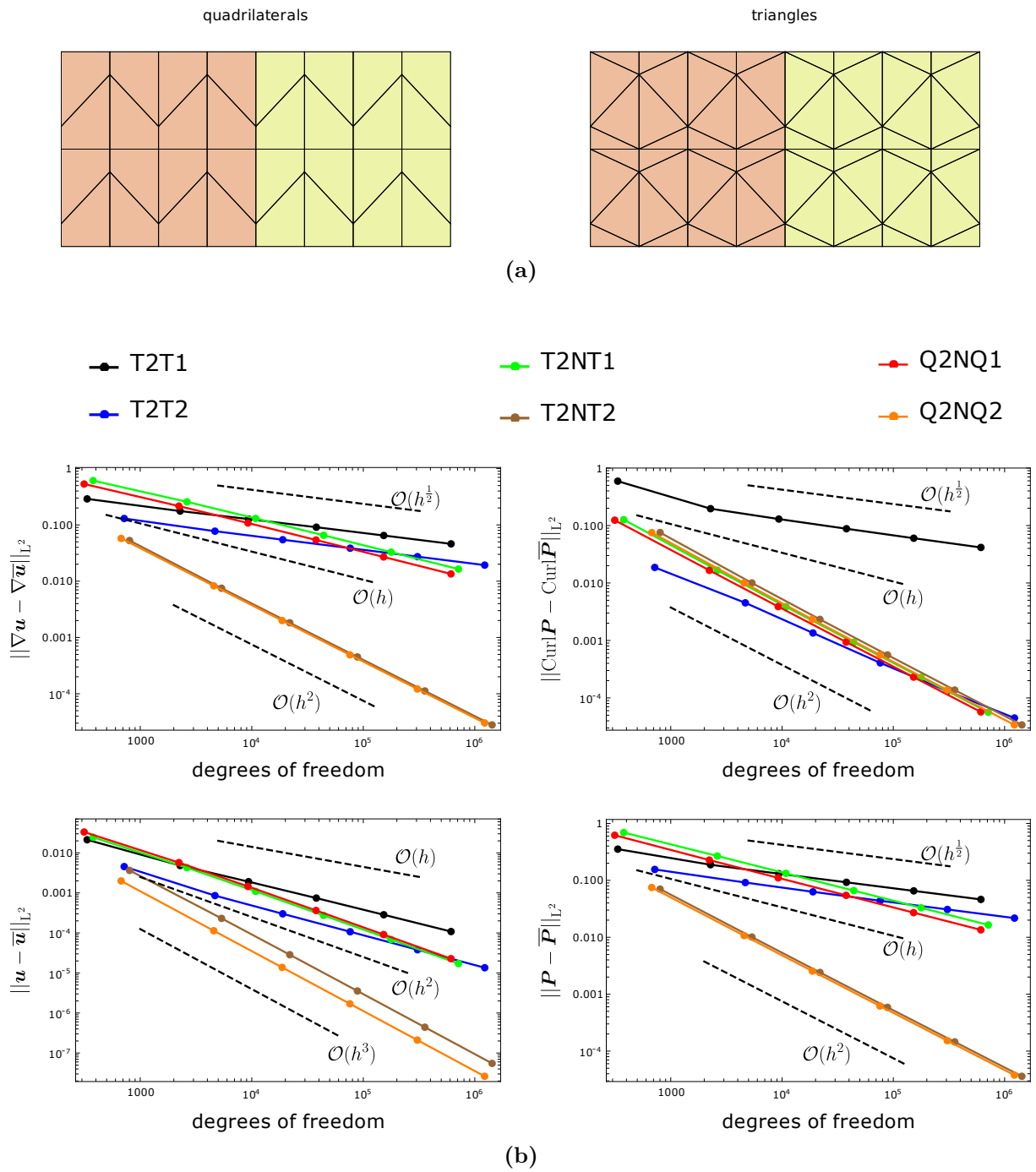


Figure 4.15: Computational convergence study (b) of third mesh depicted in (a). Taken from SCHRÖDER ET AL. [2022].

4.8.3 Characteristic length analysis: pure shear problem

We introduce a third boundary value problem shown in Figure 4.16, consisting of a circular domain \mathcal{B} with radius $r_o = 25$ and a circular hole at its center with radius $r_i = 2$. We consider no body forces or moments here. We clamp the displacement field $\bar{\mathbf{u}} = \mathbf{0}$ on the inner boundary $\partial\mathcal{B}_i$ and we rotate the outer boundary $\partial\mathcal{B}_o$ counter clockwise with $\bar{\mathbf{u}} = (-\frac{\Delta}{r_o}y, \frac{\Delta}{r_o}x)^T$ where $\Delta = 0.01$. For the micro-distortion field, we apply the consistent coupling boundary condition ($\mathbf{P} \cdot \boldsymbol{\tau} = \nabla \bar{\mathbf{u}} \cdot \boldsymbol{\tau}$) on all boundaries $\partial\mathcal{B} = \partial\mathcal{B}_i \cup \partial\mathcal{B}_o$. Two different cases are discussed here. A single material is considered for case (A), whereas two materials are assumed for case (B). The second material is located as a ring with an outer radius $r_m = 10$ and an inner radius $r_i = 2$. The material parameters are shown in Table 4.2. In this boundary value problem, we analyze the influence of a varying characteristic length parameter L_c .

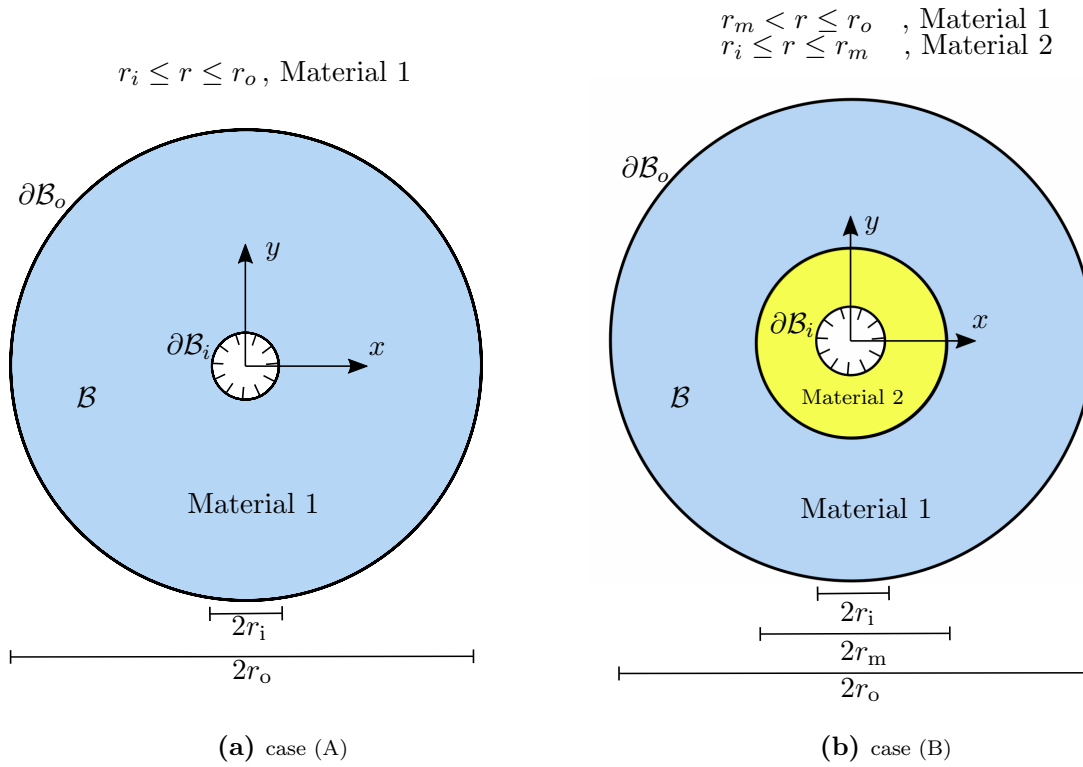


Figure 4.16: Boundary value problem: pure shear. Taken from SCHRÖDER ET AL. [2022].

Table 4.2: Material parameters of the third boundary problem, see Figure 4.16. Taken from SCHRÖDER ET AL. [2022]

Material 1	Material 2
$\lambda_{\text{micro}} = 555.55, \quad \mu_{\text{micro}} = 833.33$	$\lambda_{\text{micro}} = 2777.78, \quad \mu_{\text{micro}} = 4166.67$
$\lambda_e = 486.11, \quad \mu_e = 729.17$	$\lambda_e = 2430.555, \quad \mu_e = 3645.85$
$\mu_c = 0, \quad \mu = 833.33$	$\mu_c = 0, \quad \mu = 4166.67$
$\mathbb{L} = \mathbb{I}, \quad L_c \in \{0.001, 5, 1000\}$	$\mathbb{L} = \mathbb{I}, \quad L_c \in \{0.001, 5, 1000\}$

The problem results in a rotationally-symmetric solution where only the shear components ($u_{r,\theta}, u_{\theta,r}, P_{r\theta}, P_{\theta r} \neq 0$) are non-zero. Here, we show the solution in polar coordinates (polar

angle: θ , radius: r). The convergence behavior of the different elements is examined for case (B) and $L_c = 5$ using three different mesh densities (410, 3044 and 30620 triangular elements and 448, 3040 and 30256 quadrilateral elements). Since the micro-distortion field is in $H(\text{curl}, \mathcal{B})$, the tangential shear component $P_{r\theta}$ must be continuous while the radial shear component $P_{\theta r}$ shows a jump, see Figure 4.17, where Q2NQ2 elements are employed. Similar to the boundary value problem in Section 4.8.2, $H^1(\mathcal{B}) \times H^1(\mathcal{B})$ elements are unable to capture this discontinuity in $P_{\theta r}$, which is illustrated in Figure 4.18. The discontinuous solution of the micro-distortion field is demonstrated in Figure 4.19 using $H^1(\mathcal{B}) \times H(\text{curl}, \mathcal{B})$ elements. The higher-order Nédélec formulation in T2NT2 and Q2NQ2 elements already achieves satisfactory results with a coarse mesh.

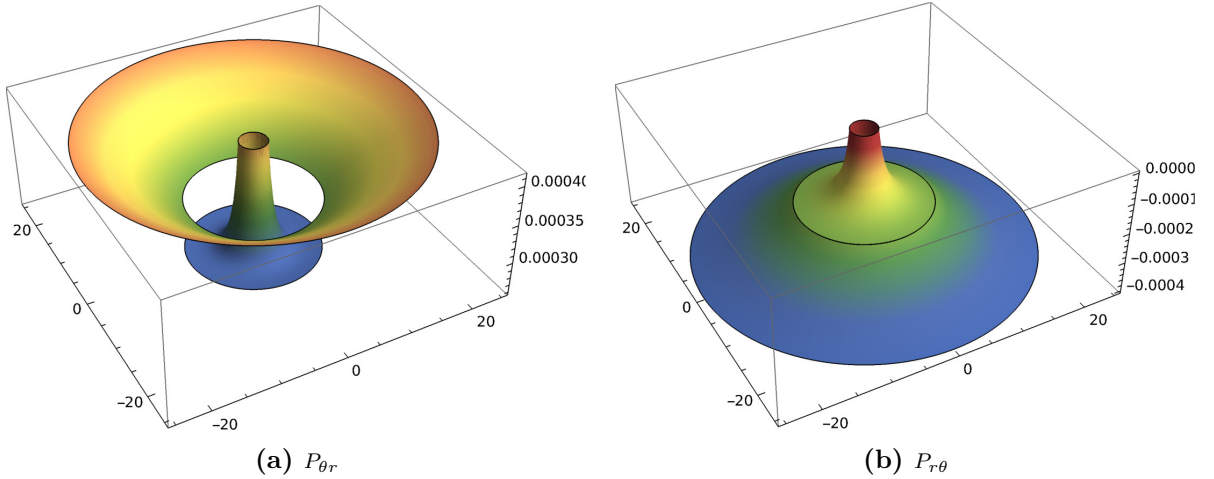


Figure 4.17: Non-vanishing micro-distortion components of the second boundary problem using 3040 Q2NQ2 elements for $L_c = 5$. Taken from SCHRÖDER ET AL. [2022].

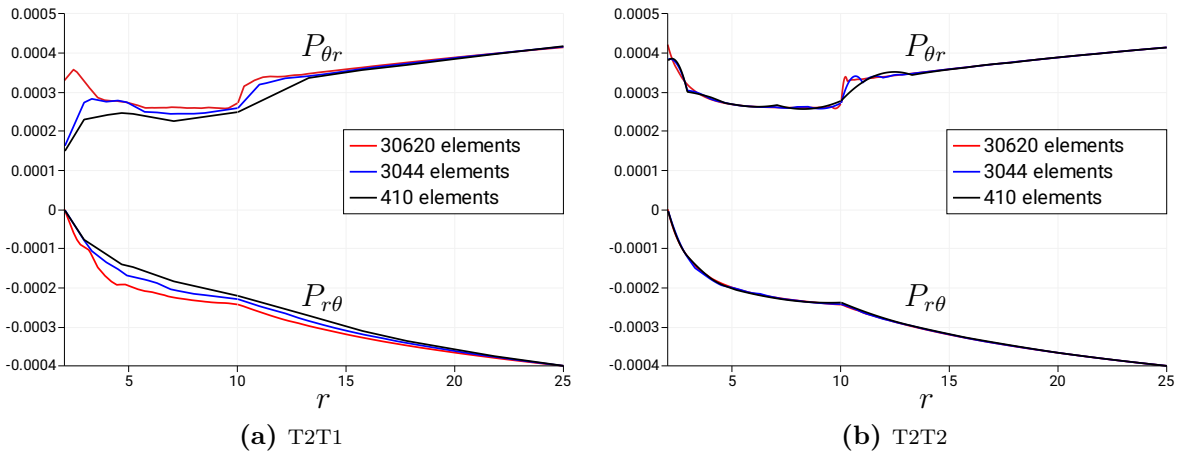


Figure 4.18: The non-vanishing components of \mathbf{P} along the radius for the $H^1(\mathcal{B}) \times H^1(\mathcal{B})$ elements using three mesh densities and $L_c = 5$. Taken from SCHRÖDER ET AL. [2022].

Next, we explore the influence of a variation of the length-scale parameter L_c on the response of the relaxed micromorphic model for case (A). The relation of the relaxed micromorphic model to the classical Cauchy theory has been discussed in detail in Chapter 3 for the limiting case $L_c \rightarrow 0$ and $L_c \rightarrow \infty$. $L_c \rightarrow 0$ relates to a macroscopic view of the material with microstructure, with the relaxed micromorphic model being equivalent to a

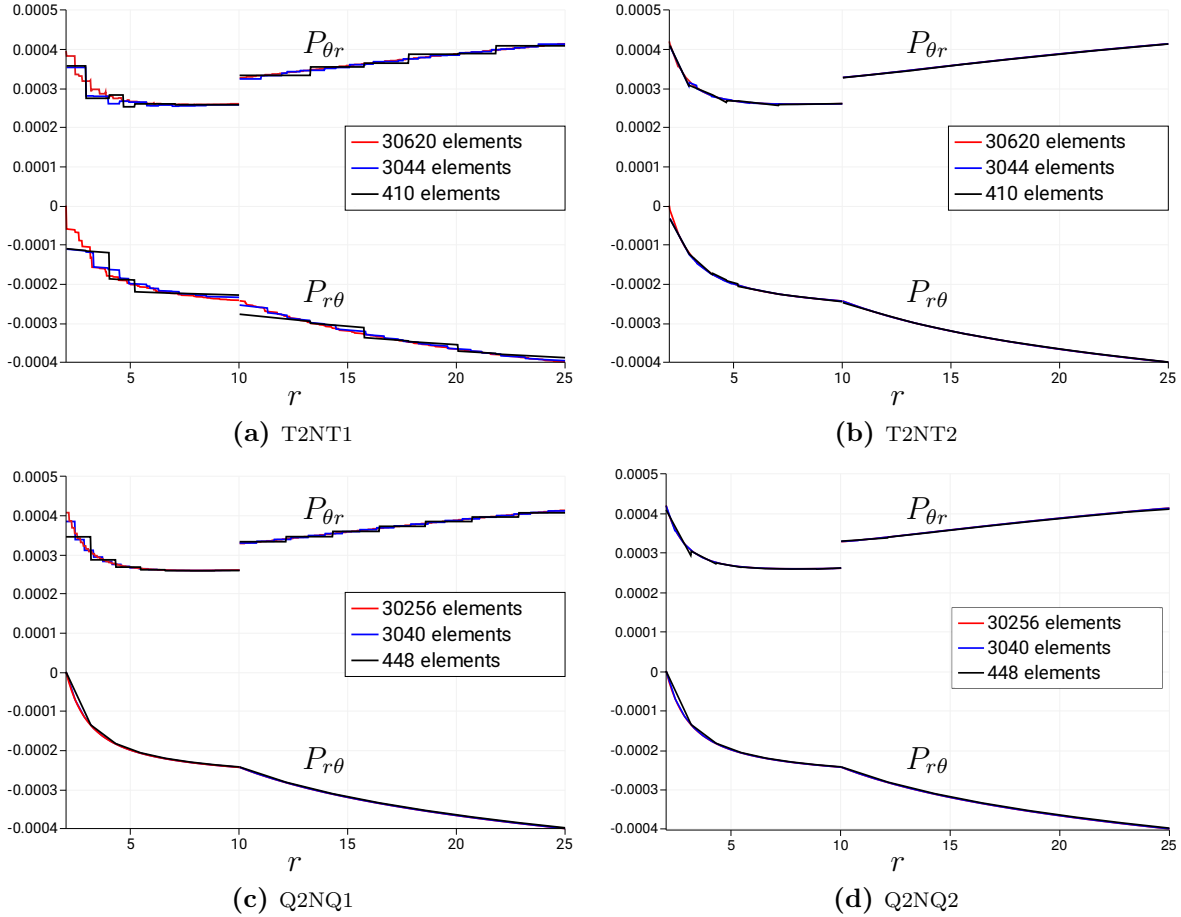


Figure 4.19: The non-vanishing components of \mathbf{P} along the radius for $H^1(\mathcal{B}) \times H(\text{curl}, \mathcal{B})$ elements using three mesh densities and $L_c = 5$. Taken from SCHRÖDER ET AL. [2022].

linear elasticity model with macroscopic stiffness tensor $\mathbb{C}_{\text{macro}}$ defined as the Reuss lower-bound of \mathbb{C}_e and $\mathbb{C}_{\text{micro}}$, i.e. $\mathbb{C}_{\text{macro}} := (\mathbb{C}_e^{-1} + \mathbb{C}_{\text{micro}}^{-1})^{-1}$, see Section 3.4. The case $L_c \rightarrow \infty$ corresponds to zooming into the microstructure, where an equivalence to linear elasticity with microscopic elasticity tensor $\mathbb{C}_{\text{micro}}$ can be reproduced, see Section 3.5. In the latter case, it can be shown that $\mathbf{P} = \nabla \mathbf{u}$ holds. In this investigation, we approximate the limiting cases by $L_c = 10^{-3}$ and $L_c = 10^3$, respectively. Figure 4.20 illustrates the elastic energy density along the radius, and Figure 4.21 shows the non-vanishing components of \mathbf{P} together with the respective displacement gradient components using 30624 Q2NQ2 elements. In Figure 4.22, we display the total potential of the relaxed micromorphic model while varying the characteristic length parameter L_c . The figures clearly show the behavior described above. The bounding behavior of the relaxed micromorphic model for small sizes is a significant advantage that most other generalized models miss. Nevertheless, the previous results do not hold for different boundary conditions of the micro-distortion field. Utilizing a different setting of Dirichlet boundary conditions (e.g. homogeneous Dirichlet boundary condition) will maintain the role of the characteristic length (increasing L_c makes the material stiffer) but the upper bound, when $L_c \rightarrow \infty$, will be reliant on the boundary value problem and the boundary conditions. Using the consistent coupling boundary condition allows the model to realize Cauchy linear elasticity with $\mathbb{C}_{\text{micro}}$ and $\mathbf{P} = \nabla \mathbf{u}$ for $L_c \rightarrow \infty$ regardless of the boundary value problem, see RIZZI ET AL. [2021a;b;c; 2022b]. For the consistent coupling boundary condition, $\mathbb{C}_{\text{micro}}$ can be related

to the stiffest response of the material on the smallest reasonable scale such as one unit-cell of a metamaterial as we will show later in Chapter 5. For the results of linear elasticity model, a standard T2 nodal element is implemented.

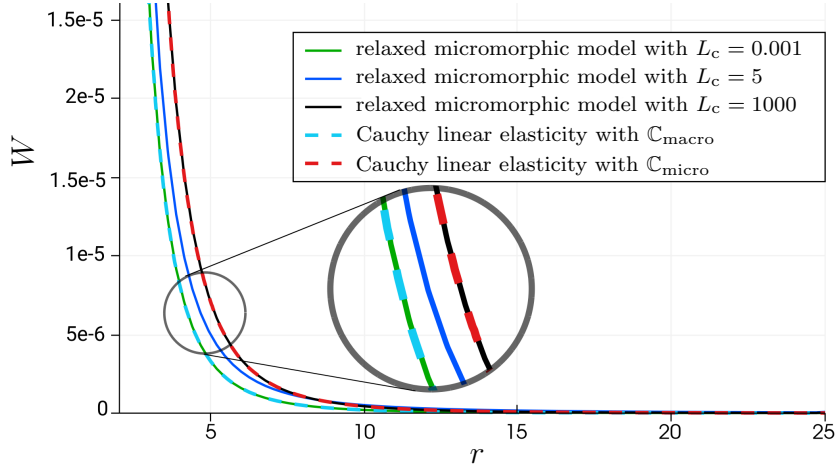


Figure 4.20: Elastic energy density along the radius. Taken from SCHRÖDER ET AL. [2022].

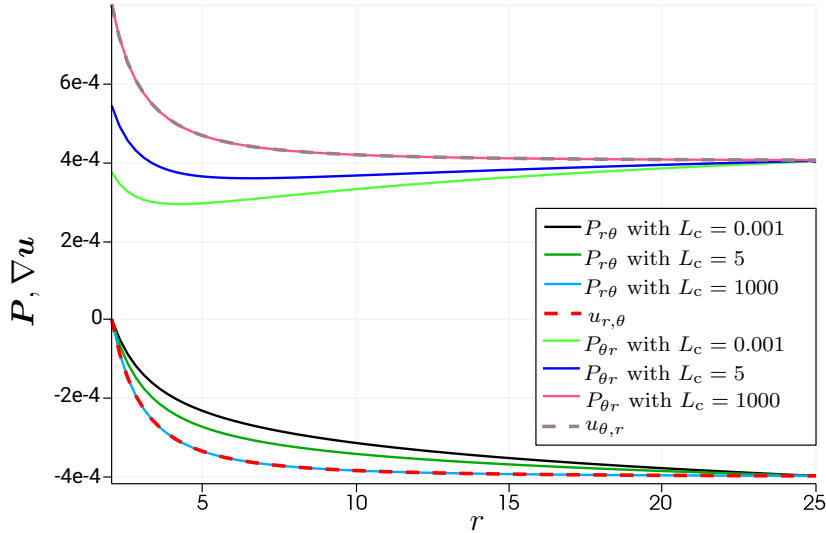


Figure 4.21: The non-vanishing components of \mathbf{P} and $\nabla \mathbf{u}$ along the radius. $\nabla \mathbf{u}$ is not influenced by the value of the characteristic length L_c . Taken from SCHRÖDER ET AL. [2022].

We analyze the behavior of the different stresses $\boldsymbol{\sigma}$, $\boldsymbol{\sigma}_{\text{micro}}$ and \mathbf{m} under a variation of L_c . The force stress tensor $\boldsymbol{\sigma}$ illustrated in Figure 4.23 vanishes for large values of the characteristic length, $L_c = 1000$. At the same time, it is bounded from above by the classical linear elasticity stress with elasticity tensor $\mathbb{C}_{\text{macro}}$ for $L_c = 0.001$. The only non-vanishing component of the moment stress m_{rz} is displayed in Figure 4.24 ($m_{\theta z} = 0$), which behaves opposite to the force stress when varying L_c . It is nearly zero for $L_c = 0.001$, and it increases for growing L_c . The micro-stress shown in Figure 4.25 is bounded between the linear elasticity stress with elasticity tensor $\mathbb{C}_{\text{micro}}$ from above and $\mathbb{C}_{\text{macro}}$ from below for large and small values of the characteristic length, respectively.

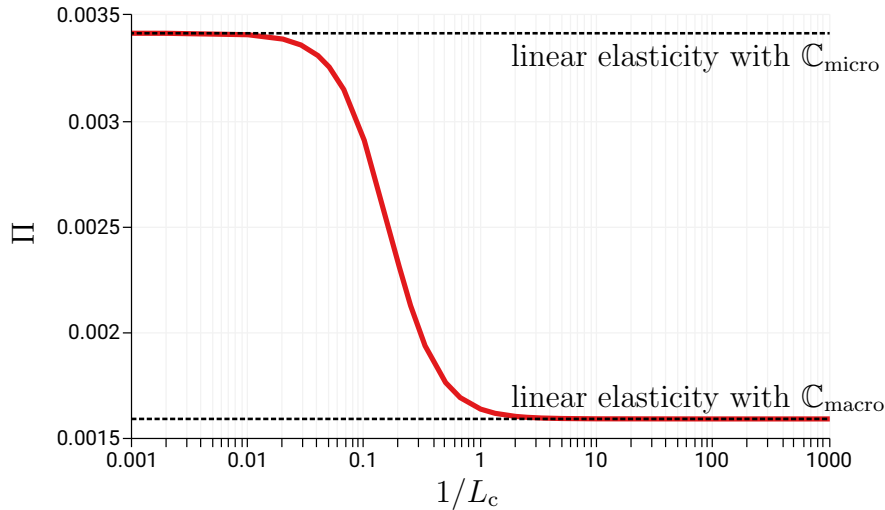


Figure 4.22: Total potential varying the characteristic length. Taken from SCHRÖDER ET AL. [2022].

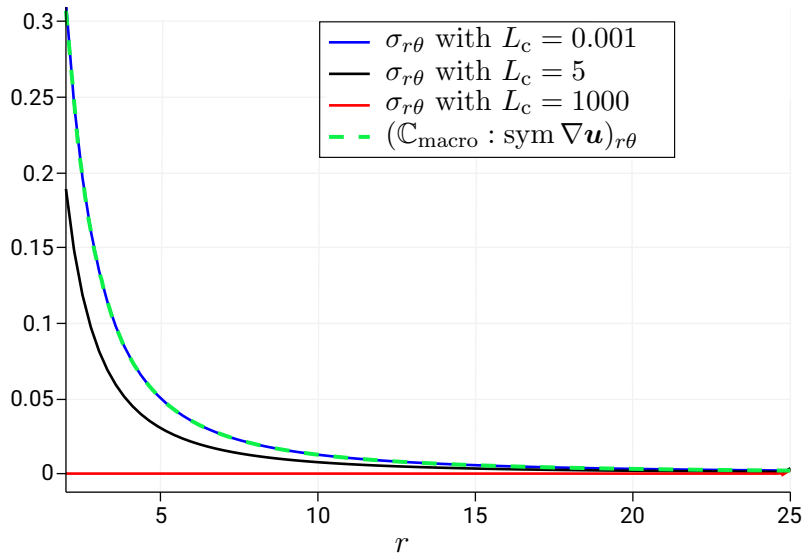


Figure 4.23: Force stress shear component $\sigma_{r\theta} = \sigma_{\theta r}$ plotted along the radius. Taken from SCHRÖDER ET AL. [2022].

4.9 Discussions

We put together the main components of standard nodal and nodal-edge finite element formulations of the relaxed micromorphic model. The standard nodal elements $H^1(\mathcal{B}) \times H^1(\mathcal{B})$ cannot achieve satisfactory results for a discontinuous solution. $H^1(\mathcal{B}) \times H(\text{curl}, \mathcal{B})$ elements capture the jumps of the normal components of the micro-distortion field. In contrast to the standard nodal elements, $H^1(\mathcal{B}) \times H(\text{curl}, \mathcal{B})$ elements lead to an efficient convergence in the sense of the error norm reduction with mesh refinement. We numerically investigated the role of the characteristic length that controls the scale-dependency property of the relaxed micromorphic model. For $L_c \rightarrow 0$, the model is equivalent to the standard Cauchy linear elasticity model with $\mathbb{C}_{\text{macro}}$ defined as the Reuss lower-limit of elasticity tensors \mathbb{C}_e and $\mathbb{C}_{\text{micro}}$, see Equation (3.15), while the model is corresponding to

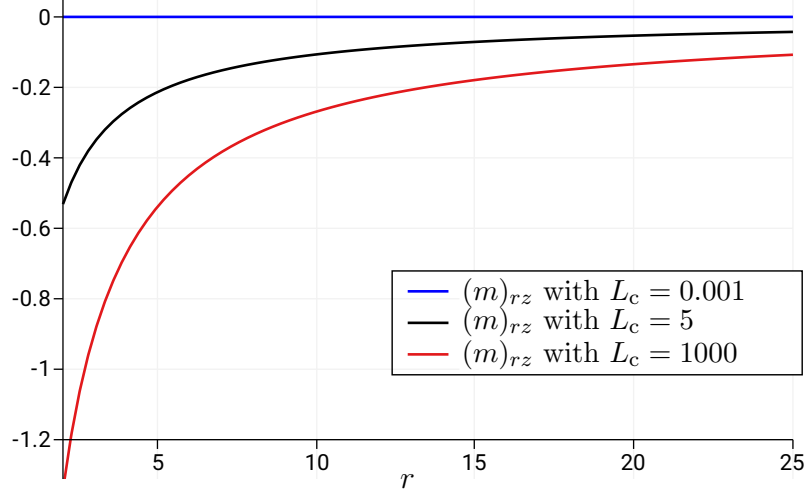


Figure 4.24: Non-zero component of moment stress m_{rz} plotted along the radius. Taken from SCHRÖDER ET AL. [2022].

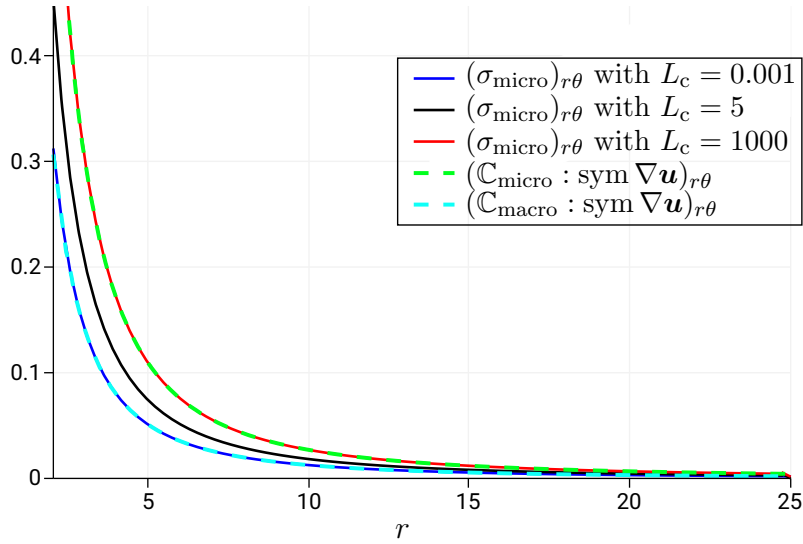


Figure 4.25: Micro-stress shear component $(\sigma_{\text{micro}})_{r\theta} = (\sigma_{\text{micro}})_{\theta r}$ plotted along the radius. Taken from SCHRÖDER ET AL. [2022].

a Cauchy linear elasticity model with $\mathbb{C}_{\text{micro}}$ with $\mathbf{P} = \nabla \mathbf{u}$ for $L_c \rightarrow \infty$. This aligns with the analytical results discussed in Sections 3.4 and 3.5.

We have shown the dependency of different stress measurements on the characteristic length. The force stress is at maximum for $L_c \rightarrow 0$ and vanishes for $L_c \rightarrow \infty$, but the moment stress behaves in the opposite way. The micro-stress varies between Cauchy linear elasticity stresses with $\mathbb{C}_{\text{micro}}$ and $\mathbb{C}_{\text{macro}}$ for $L_c \rightarrow \infty$ and $L_c \rightarrow 0$, respectively. For the remaining part of this thesis, we will use the Q2NQ2 element for numerical analysis.

5 Modeling metamaterial beams under pure bending via RMM

As we have shown analytically in Chapter 3 and numerically in Chapter 4, the relaxed micromorphic model interpolates between two well-defined scales: the classical continuum scale of macroscopic linear elasticity, whose stiffness is given by the elasticity tensor $\mathbb{C}_{\text{macro}}$ and a microscopic scale, which is linear elastic as well with stiffness $\mathbb{C}_{\text{micro}}$. The function of the characteristic length $L_c > 0$ is then to scale correctly with the size of the specimen and to describe the interaction between these two scales. For $L_c \rightarrow 0$, we get a macroscopic linear elasticity (complete scale-separation, stiffness $\mathbb{C}_{\text{macro}}$). For $L_c \rightarrow \infty$ (zooming into the microstructure), we recover a microscopic linear elasticity (stiffness $\mathbb{C}_{\text{micro}}$). The appearing length-scale independent elasticity tensors \mathbb{C}_e and $\mathbb{C}_{\text{micro}}$ are related by a Reuss-like formula in Equation (3.15) as a function of the uniquely known elasticity tensor $\mathbb{C}_{\text{macro}}$ from classical homogenization theory. Therefore, it remains to identify $\mathbb{C}_{\text{micro}}$, which happens to be the largest observable stiffness in the model. Such a definition for $\mathbb{C}_{\text{micro}}$ does not exist in the classical micromorphic model or other variants of it.

In this Chapter, we want to investigate the possibilities that this unique interpretation of the relaxed micromorphic model delivers. We consider metamaterial beams consisting of periodic unit-cell subjected to bending. The size-effects of bending was studied utilizing other generalized continua such as strain gradient, Cosserat-micropolar and other continua in ABALI ET AL. [2022], AL-BASYOUNI ET AL. [2015], HOSSEINI AND NIIRANEN [2022], KHAKALO AND NIIRANEN [2019; 2020], KHAKALO ET AL. [2018], LAKES [2022], LI ET AL. [2022], LIEBOLD AND MÜLLER [2016], YIN ET AL. [2021]. Modeling the mechanical behavior of many metamaterials was conducted for many applications using enriched continua in ABALI [2019], CARCATERRA ET AL. [2015], DEL VESCOVO AND GIORGIO [2014], EL DHABA [2020], GLAESENER ET AL. [2021], PLACIDI ET AL. [2017], RUEGER ET AL. [2019], SHEKARCHIZADEH ET AL. [2021], SHI ET AL. [2022], SRIDHAR ET AL. [2016; 2018]. Identifying $\mathbb{C}_{\text{macro}}$ is a standard procedure in periodic homogenization theory. The largest stiffness idea will drive the identification of $\mathbb{C}_{\text{micro}}$. First, we analyze the size-effects of metamaterial beams with fully discretized microstructure which we will use as a reference study. Afterward, we employ the relaxed micromorphic continuum to model the size-effects without accounting for the fully resolved microstructure. The material parameters and adequate boundary conditions of the micro-distortion field \mathbf{P} should be determined in order to establish a simplified fitting procedure on the reference metamaterial beams. The consistent coupling condition (applied on the Dirichlet boundary of \mathbf{u}) permits the relaxed micromorphic to operate on the whole range between $\mathbb{C}_{\text{macro}}$ and $\mathbb{C}_{\text{micro}}$, which is of key importance for correctly identifying the unknown material parameters, i.e. $\mathbb{C}_{\text{micro}}$. However, an alternative loading by a normal linear traction (applied moment), which delivers the same results for the fully resolved metamaterial, achieves consistent results for the relaxed micromorphic model when the consistent coupling condition is imposed via the penalty approach.

In a previous study NEFF ET AL. [2020], $\mathbb{C}_{\text{micro}}$ was supposed to be given by the Löwner matrix supremum $\mathbb{C}_{\text{micro}}^{\text{Löwner}}$ of elasticity tensors appearing under affine Dirichlet conditions on different choices of unit-cell, which is used to capture band-gaps successfully in D'AGOSTINO ET AL. [2020]. However, the results in the present Chapter inspires that $\mathbb{C}_{\text{micro}}^{\text{Löwner}}$ is too soft, when compared with the appearing stiffness in the bending regime. Here, we extend our understanding of $\mathbb{C}_{\text{micro}}$ towards all scenarios, notably including non-affine Dirichlet conditions.

The outline of this Chapter is as follows: the size-effects of the heterogeneous microstructured metamaterial beams are investigated in Section 5.1 for two loading cases that lead to the same results. In Section 5.2 we determine the material parameters of the relaxed micromorphic model. Section 5.3 analyzes the boundary conditions of the micro-distortion field for symmetric ($\mu_c = 0$) and non-symmetric ($\mu_c \neq 0$) force stresses. We then fit the relaxed micromorphic model solution to the microstructured metamaterial solution by calibrating the curvature in Section 5.5. In Section 5.6, the relaxed micromorphic model is shown to be capable of handling two loading scenarios in addition to pure bending. Finally, we discuss our findings of this Chapter in Section 5.7.

Parts of this Chapter have been published in:

M. Sarhil, L. Scheunemann, J. Schröder and P. Neff. Size-effects of metamaterial beams subjected to pure bending: on boundary conditions and parameter identification in the relaxed micromorphic model. *Computational Mechanics*, 72, 1091–1113, 2023. doi:10.1007/s00466-023-02332-9.

M. Sarhil, L. Scheunemann, J. Schröder and P. Neff. On the identification of material parameters in the relaxed micromorphic continuum. *Proceedings in Applied Mathematics and Mechanics*, 23, e202300056, 2023. doi:10.1002/pamm.202300056.

M. Sarhil, L. Scheunemann, J. Schröder and P. Neff, Modeling the size-effect of metamaterial beams under bending via the relaxed micromorphic continuum. *Proceedings in Applied Mathematics and Mechanics*, 22, e202200033, 2023. doi:10.1002/pamm.202200033.

5.1 Reference study: full discretization of metamaterial specimens

Here, we investigate the size-effect phenomena of metamaterial beams with a fully resolved microstructure consisting of periodic unit-cell. The size-effect phenomena will be analyzed via the effective bending stiffness of beams subjected to pure bending. According to the elementary beam theory of Euler–Bernoulli, the bending moment is linked to the “bending” curvature by

$$M(x) = D(x)\kappa(x), \quad (5.1)$$

where $D(x)$ and $\kappa(x)$ are the bending stiffness and the curvature at a position x along the beam. For a constant bending moment \overline{M} along the beam length, we assume an effective flexural rigidity \overline{D} and an effective curvature $\overline{\kappa}$ so that we obtain

$$\overline{D} = \frac{\overline{M}}{\overline{\kappa}}. \quad (5.2)$$

We design in the following two beam models subjected to a vanishing shear force and a constant moment along the length L , see Figure 5.1. A rotation $\theta = \kappa L$ is applied on the right end for the first loading case, while a moment load is enforced for the second loading case instead. An effective constant curvature can be determined with the help of an effective deflection $\overline{w}(x)$, which stands for the displacement of the beam in the y -direction at location x ,

$$\overline{\kappa} = \frac{d^2\overline{w}(x)}{dx^2}. \quad (5.3)$$

A deflection equation $\overline{w}(x)$, which will be fitted later to the fully resolved beams, featuring an effective constant curvature and satisfying the boundary conditions of the beam model, reads

$$\bar{w}(x) = \frac{\bar{\kappa}}{2}(x^2 - L^2) \quad \text{satisfying} \quad \bar{w}(L) = 0, \quad \text{and} \quad \frac{d\bar{w}(0)}{dx} = 0. \quad (5.4)$$

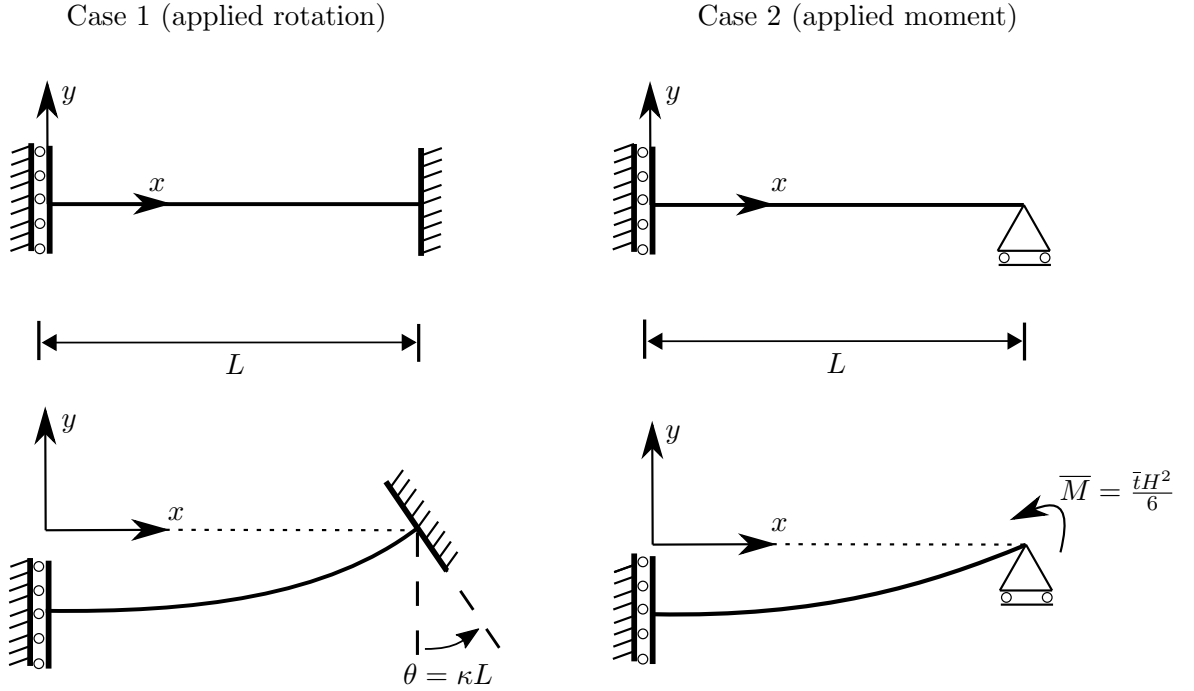


Figure 5.1: The beam models, compare Figure 5.3. Taken from SARHIL ET AL. [2023c].

A 2D metamaterial is considered with a periodic unit-cell consisting of a square with an edge length $l = 1.9 \cdot 10^{-2}$ m and a circular inclusion at its center with a diameter of $d = 1.2 \cdot 10^{-2}$ m, see Figure 5.2. Both matrix and inclusion are isotropic linear elastic with the material parameters shown in Table 5.1. The inclusion is 20 times softer than the matrix. A standard triangular finite element with quadratic shape functions (T2) is used for this analysis. The specimens are considered with dimensions $H \times L = nl \times 12nl$ so that the length of the beams is always twelve times the height where n is the number of unit-cells in the height direction, see Figure (5.2). The length of the beams is much larger than their height, so the Euler–Bernoulli beam theory is valid.

Table 5.1: Material parameters of the assumed metamaterial. Taken from SARHIL ET AL. [2023c].

	Young's modulus: E	Poisson's ratio: ν	λ	μ
Matrix	70 GPa	0.333	52.35 GPa	26.25 GPa
Inclusion	3.5 GPa	0.333	2.62 GPa	1.31 GPa

The boundary conditions of the beam models in Figure 5.1 are passed on to the 2D fully resolved metamaterial beams as shown in Figure 5.3. For the first loading case, we rotate the right edge in the plane through a given displacement in x -direction as a linear function of the height (y -coordinates). For the second loading case, a moment is applied on the right edge by means of a traction in x -direction as a linear function of y -coordinates. The left boundary for both loading cases is fixed in x -direction and free to move in y -direction. Furthermore, we fix the middle point on the right edge in y -direction. We intend

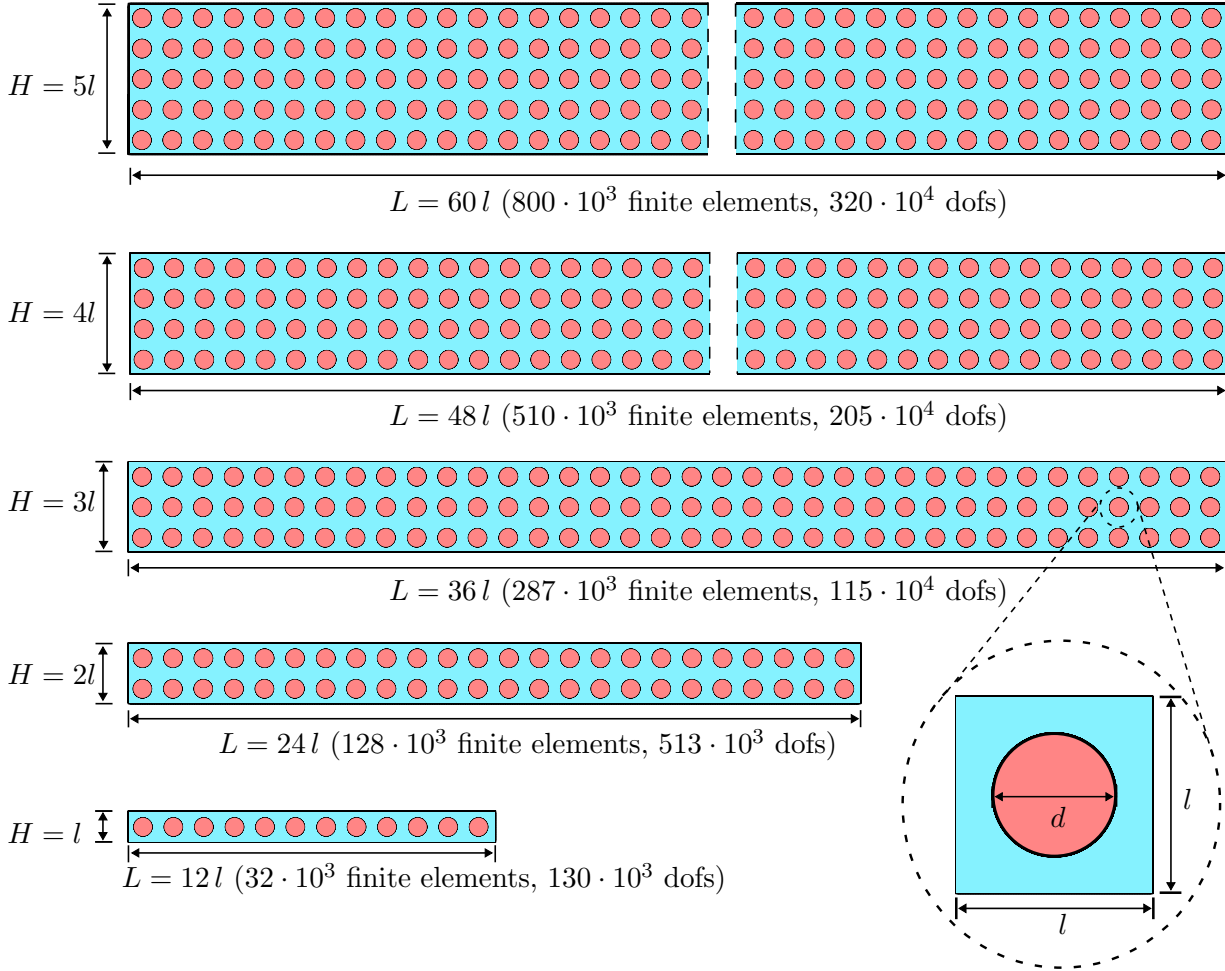


Figure 5.2: Illustration shows the geometry of the specimens for $n = 1, 2, 3, 4, 5$ with the assumed unit-cell. The number of finite elements with degrees of freedom (dofs) are shown in parentheses. Taken from SARHIL ET AL. [2023c].

by introducing these two loading cases to prove that they deliver identical results for the microstructured metamaterial beams. This equivalence of both loading cases should also be demonstrated by the relaxed micromorphic model when appropriate boundary conditions are set. However, dealing with traction is challenging for generalized continua because it implies defining unknown higher-order traction. Moreover, we assume $\kappa = 1$ and $\bar{t} = 10^9 \text{ N/m}$.

After solving the fully resolved microstructure, the effective curvature $\bar{\kappa}$ is obtained by the following least squares minimization over all the nodes n_{node} of the finite element mesh

$$\sum_I^{n_{\text{node}}} ((\mathbf{d}_I^u)_2 - \bar{w}(\mathbf{X}_I))^2 \rightarrow \min, \quad (5.5)$$

which leads, considering Equation (5.4), to

$$\bar{\kappa} = \frac{\sum_I^{n_{\text{node}}} (\mathbf{d}_I^u)_2 \frac{(\mathbf{X}_I)_1^2 - L^2}{2}}{\sum_I^{n_{\text{node}}} \left(\frac{(\mathbf{X}_I)_1^2 - L^2}{2} \right)^2}, \quad (5.6)$$

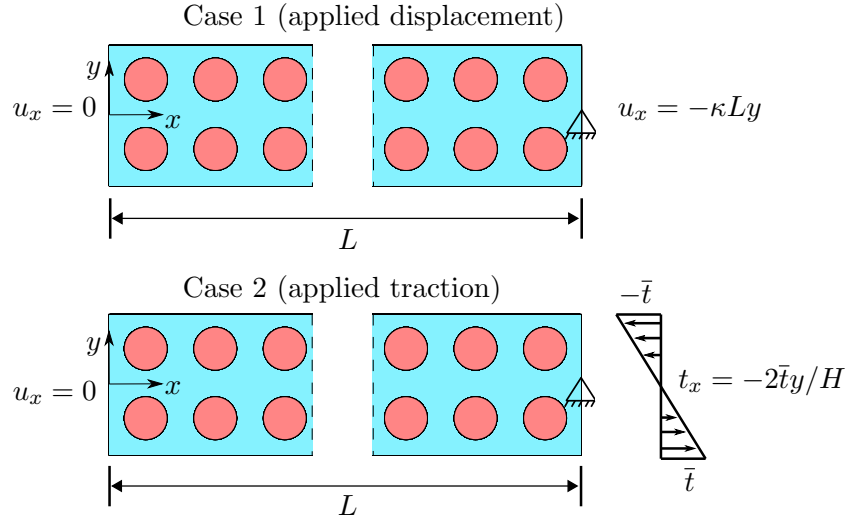


Figure 5.3: The boundary conditions of the fully resolved metamaterial shown exemplarily for $n = 2$ ($H \times L = 2l \times 24l$). Taken from SARHIL ET AL. [2023c].

where \mathbf{X}_I and \mathbf{d}_I^u are the coordinates and the displacement degrees of freedom at node I . The bending stiffness can be calculated following Equation (5.2), where the moment \bar{M} can be calculated using the reactions of nodes located at the left or right edges. Alternatively, the bending stiffness can be calculated by means of the maximum deflection at the left edge of the beam, i.e. $\bar{w}(0)$. This is because the fluctuation of the deflection of the heterogeneous solution is tiny compared to the maximum deflection on the left edge $\bar{w}(0)$. We obtain from Equations (5.2) and (5.4) substituting $x = 0$ and considering $\bar{w}(0) = w^{\text{FEM}}(0)$

$$\bar{D} = -\frac{\bar{M}L^2}{2w^{\text{FEM}}(0)}, \quad (5.7)$$

where $w^{\text{FEM}}(0)$ is the deflection of the FEM solution averaged over the left edge ($x = 0$). Calculating the bending stiffness using Equations (5.2) or (5.7) delivers the same result which we tested numerically.

The effective material properties of the large specimens can be obtained by the standard computational periodic first-order homogenization produced by a unit-cell with periodic boundary conditions, which is identified as $\mathbb{C}_{\text{macro}}$ in Section 5.2.1. As we will show later, the macroscopic elasticity tensor $\mathbb{C}_{\text{macro}}$ is not isotropic and shows cubic symmetry. The size-effects are shown via the so-called normalized bending stiffness \bar{D}/D_{macro} plotted in Figure 5.4, which relates the actual stiffness of the fully discretized metamaterial to the one obtained from homogenized linear elasticity with $\mathbb{C}_{\text{macro}}$ which reads analytically

$$D_{\text{macro}} = \frac{E_{\text{macro}} H^3}{12(1 - \nu_{\text{macro}}^2)}. \quad (5.8)$$

When we increase the specimen size, the normalized bending stiffness approaches value one. Applying a rotation (loading case 1) or a moment (loading case 2) leads to similar results.

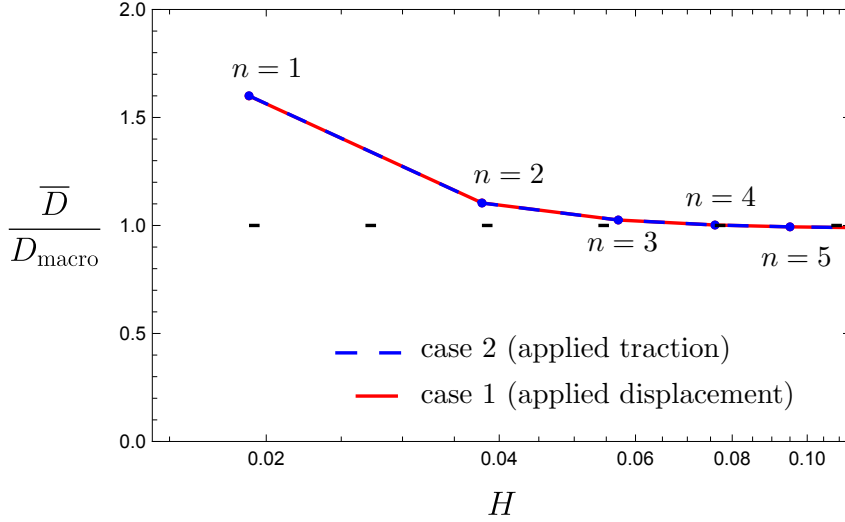


Figure 5.4: The normalized bending stiffness varying the beam size $H \times L = nl \times 12nl$. Taken from SARHIL ET AL. [2023c].

5.2 Parameter identification for the relaxed micromorphic continuum

The relaxed micromorphic model should reproduce the previous size-effects exhibited by the fully resolved heterogeneous metamaterial beams. However, the identification of the boundary conditions and material parameters is not obvious.

5.2.1 Identification of the macroscopic elasticity tensor $\mathbb{C}_{\text{macro}}$

Linear elasticity with the macroscopic elasticity tensor $\mathbb{C}_{\text{macro}}$ determines the lower bound of the relaxed micromorphic model, see Figure 3.1, associated with the case $L_c \rightarrow 0$. Thus, $\mathbb{C}_{\text{macro}}$ corresponds to large values of n where the macroscopic homogeneous response is expected, and the macroscopic problem is much larger than the microscopic problem. Thus, scale-separation holds and the classical homogenization theory can be applied. The standard analysis with a periodic unit-cell and periodic boundary conditions should be used, see for example ZOHDI AND WRIGGERS [2005]. The geometry of the unit-cell has no role in this analysis because of periodicity, e.g. every periodic unit-cell in Figure 5.5 delivers the same, c.f. NEFF ET AL. [2020].

Our analysis shows that $\mathbb{C}_{\text{macro}}$ has the cubic symmetry property for our assumed metamaterial, and it reads (Tilde stands for Voigt notation, see Appendix B)

$$\tilde{\mathbb{C}}_{\text{macro}} = \begin{pmatrix} 2\mu_{\text{macro}} + \lambda_{\text{macro}} & \lambda_{\text{macro}} & 0 \\ \lambda_{\text{macro}} & 2\mu_{\text{macro}} + \lambda_{\text{macro}} & 0 \\ 0 & 0 & \mu_{\text{macro}}^* \end{pmatrix}, \quad (5.9)$$

where three parameters need to be defined. We obtain by our standard numerical analysis

$$\tilde{\mathbb{C}}_{\text{macro}} = \begin{pmatrix} 47.86 & 17.61 & 0 \\ 17.61 & 47.86 & 0 \\ 0 & 0 & 9.98 \end{pmatrix} [\text{GPa}] \Rightarrow \begin{aligned} \lambda_{\text{macro}} &= 17.61 \text{ GPa} \\ \mu_{\text{macro}} &= 15.13 \text{ GPa} \\ \mu_{\text{macro}}^* &= 9.98 \text{ GPa} \end{aligned} . \quad (5.10)$$

5.2.2 Identification of the microscopic elasticity tensor $\mathbb{C}_{\text{micro}}$ via affine deformations

Linear elasticity with the microscopic elasticity tensor $\mathbb{C}_{\text{micro}}$ determines the upper bound of the relaxed micromorphic model, see Figure 3.1, associated with the case $L_c \rightarrow \infty$. Thus, $\mathbb{C}_{\text{micro}}$ is identified as the maximum stiffness on the micro-scale. Nevertheless, $\mathbb{C}_{\text{micro}}$ must exhibit the cubic symmetry similar to $\mathbb{C}_{\text{macro}}$ according to the extended Neumann's principle NEFF ET AL. [2020]. In order to achieve stiff estimates for $\mathbb{C}_{\text{micro}}$, we apply first affine Dirichlet boundary conditions, which must lead to a stiffer response than the periodic boundary conditions, i.e. $\mathbb{C}_{\text{macro}}$. There are infinite choices of the unit-cell available. However, we only have to choose unit-cells that preserve the cubic symmetry property under the applied Dirichlet boundary conditions. We investigate then different variants of unit-cell under the affine Dirichlet boundary conditions. We obtain the corresponding apparent stiffness tensor denoted as \mathbb{C}_i^{D} for each choice of a unit-cell $i = 1, \dots, r$ subjected to the affine Dirichlet boundary conditions. The positive definite microscopic elasticity tensor will be set as the least upper bound of the apparent stiffness of the microstructure measured in the energy norm following the Löwner matrix supremum problem, see for details NEFF ET AL. [2020].

For the assumed metamaterial, four different variants of the unit-cell are suitable, see Figure 5.5, which lead to the elasticity tensors $\mathbb{C}_i^{\text{D}}, i = 1, \dots, 4$ with the cubic symmetry property as intended. The results are summarized in Table 5.2.

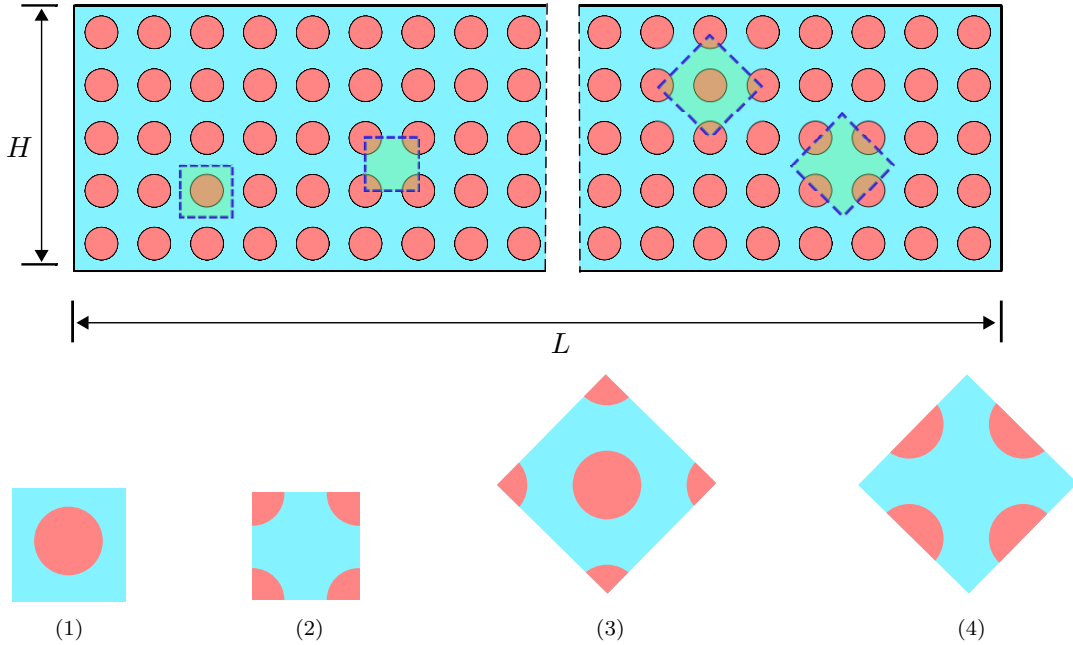


Figure 5.5: The possible choices of the unit-cell with cubic symmetry. The edge length of the unit-cell equals to l for (1) and (2) and $\sqrt{2}l$ for (3) and (4). Taken from SARHIL ET AL. [2023c].

The microscopic elasticity tensor $\mathbb{C}_{\text{micro}}^{\text{Löwner}}$ is defined then by the Löwner matrix supremum problem as

$$\boldsymbol{\varepsilon} : \mathbb{C}_{\text{micro}}^{\text{Löwner}} : \boldsymbol{\varepsilon} \geq \boldsymbol{\varepsilon} : \mathbb{C}_i^{\text{D}} : \boldsymbol{\varepsilon} \quad \text{where } i=1, \dots, 4 \quad , \quad \forall \boldsymbol{\varepsilon} \in \text{Sym}(3). \quad (5.11)$$

Table 5.2: The elasticity parameters of the unit-cells shown in Figure 5.5 under affine Dirichlet boundary conditions. The elasticity parameters define elasticity tensors which exhibit cubic symmetry similar to $\mathbb{C}_{\text{macro}}$. Taken from SARHIL ET AL. [2023c].

unit-cell	λ_i [GPa]	μ_i [GPa]	μ_i^* [GPa]
1	18.26	15.34	14.61
2	20.15	15.83	14.44
3	19.25	15.54	13.19
4	19.56	15.66	12.68

which turns for the cubic symmetry case to

$$\begin{aligned}
& \begin{pmatrix} \varepsilon_{11} \\ \varepsilon_{22} \\ 2\varepsilon_{12} \end{pmatrix} \begin{pmatrix} 2\mu_{\text{micro}}^{\text{Löwner}} + \lambda_{\text{micro}}^{\text{Löwner}} & \lambda_{\text{micro}}^{\text{Löwner}} & 0 \\ \lambda_{\text{micro}}^{\text{Löwner}} & 2\mu_{\text{micro}}^{\text{Löwner}} + \lambda_{\text{micro}}^{\text{Löwner}} & 0 \\ 0 & 0 & (\mu^*)_{\text{micro}}^{\text{Löwner}} \end{pmatrix} \begin{pmatrix} \varepsilon_{11} \\ \varepsilon_{22} \\ 2\varepsilon_{12} \end{pmatrix} \\
& \geq \begin{pmatrix} \varepsilon_{11} \\ \varepsilon_{22} \\ 2\varepsilon_{12} \end{pmatrix} \begin{pmatrix} 2\mu_i + \lambda_i & \lambda_i & 0 \\ \lambda_i & 2\mu_i + \lambda_i & 0 \\ 0 & 0 & \mu_i^* \end{pmatrix} \begin{pmatrix} \varepsilon_{11} \\ \varepsilon_{22} \\ 2\varepsilon_{12} \end{pmatrix}, \quad (5.12) \\
& \text{for } i=1,\dots,4, \quad \forall \begin{pmatrix} \varepsilon_{11} \\ \varepsilon_{22} \\ \varepsilon_{12} \end{pmatrix} \in \mathbb{R}^3.
\end{aligned}$$

The solution of the previous problem reads

$$\begin{aligned}
(\mu^*)_{\text{micro}}^{\text{Löwner}} &\geq \max_i \{\mu_i^*\}, & \mu_{\text{micro}}^{\text{Löwner}} &\geq \max_i \{\mu_i\}, \\
\lambda_{\text{micro}}^{\text{Löwner}} + \mu_{\text{micro}}^{\text{Löwner}} &\geq \max_i \{\mu_i + \lambda_i\},
\end{aligned} \quad (5.13)$$

for every unit-cell choice, i.e. $i = 1, \dots, 4$. We take therefore (see Table 5.2, the selected values are marked with bold font)

$$\begin{aligned}
(\mu^*)_{\text{micro}}^{\text{Löwner}} &:= \mu_1^* = 14.61 \text{ GPa}, & \mu_{\text{micro}}^{\text{Löwner}} &:= \mu_2 = 15.83 \text{ GPa}, \\
\lambda_{\text{micro}}^{\text{Löwner}} &:= \mu_2 + \lambda_2 - \mu_{\text{micro}}^{\text{Löwner}} = 20.15 \text{ GPa},
\end{aligned} \quad (5.14)$$

and thus

$$\tilde{\mathbb{C}}_{\text{micro}}^{\text{Löwner}} := \begin{pmatrix} 51.81 & 20.15 & 0 \\ 20.15 & 51.81 & 0 \\ 0 & 0 & 14.61 \end{pmatrix} [\text{GPa}]. \quad (5.15)$$

However, the previous estimate serves as a lower bound for $\mathbb{C}_{\text{micro}}$. In Figure 5.6, we show the size-effect of the fully resolved metamaterial beams and the linear elasticity solutions with the following elasticity tensors: I) $\mathbb{C}_{\text{macro}}$, II) $\mathbb{C}_{\text{micro}}^{\text{Löwner}}$, III) $\mathbb{C}_{\text{matrix}}$ of the homogeneous isotropic matrix, and IV) $\mathbb{C}_{\text{Voigt}}$ which is isotropic and obtained by the equal strain assumption $\mathbb{C}_{\text{Voigt}} = \phi_{\text{matrix}} \mathbb{C}_{\text{matrix}} + \phi_{\text{inclusion}} \mathbb{C}_{\text{inclusion}}$ where ϕ_{matrix} and $\phi_{\text{inclusion}}$ are the volume fractions of the matrix and inclusion, respectively, which leads to $\lambda_{\text{Voigt}} = 36.77$ GPa and $\mu_{\text{Voigt}} = 18.44$ GPa.

The obtained $\mathbb{C}_{\text{micro}}^{\text{Löwner}}$ in Equation (5.15) is too soft compared to the reference heterogeneous beams. Even linear elasticity with $\mathbb{C}_{\text{Voigt}}$ is softer than the solution of the fully

resolved metamaterial beam for $n = 1$. This can be explained by the fact that the typical bending mode cannot be mapped with affine Dirichlet Boundary conditions. Here, a ‘‘Voigt bound’’ for higher modes would be required, which does not exist for non-affine deformations. Note that the tensor $\mathbb{C}_{\text{micro}}$, although appearing in the relaxed micromorphic model and the classical micromorphic model, does not have the same meaning in the latter, which is related to the bounded stiffness property of the former.

We may relate $\mathbb{C}_{\text{micro}}$ to the matrix stiffness $\mathbb{C}_{\text{matrix}}$ since $\mathbb{C}_{\text{matrix}}$ represents the stiffest part of the assumed microstructure. Thus, introduce a scalar $\alpha \geq 1$ so that we have $\mathbb{C}_{\text{micro}} := \alpha \mathbb{C}_{\text{micro}}^{\text{L\"owner}}$. We define an upper limit for $\mathbb{C}_{\text{micro}}$ as

$$\boldsymbol{\varepsilon} : \mathbb{C}_{\text{matrix}} : \boldsymbol{\varepsilon} \geq \boldsymbol{\varepsilon} : \mathbb{C}_{\text{micro}} : \boldsymbol{\varepsilon} = \boldsymbol{\varepsilon} : \alpha \mathbb{C}_{\text{micro}}^{\text{L\"owner}} : \boldsymbol{\varepsilon}, \quad \forall \boldsymbol{\varepsilon} \in \text{Sym}(3). \quad (5.16)$$

By introducing Equation (5.16), we keep the anisotropic symmetry property of $\mathbb{C}_{\text{micro}}$ while the elasticity tensor $\mathbb{C}_{\text{matrix}}$ is isotropic. We obtain then

$$\begin{aligned} \mu_{\text{matrix}}^* = \mu_{\text{matrix}} &\geq \alpha (\mu^*)_{\text{micro}}^{\text{L\"owner}}, & \mu_{\text{matrix}} &\geq \alpha \mu_{\text{micro}}^{\text{L\"owner}}, \\ \lambda_{\text{matrix}} + \mu_{\text{matrix}} &\geq \alpha (\lambda_{\text{micro}}^{\text{L\"owner}} + \mu_{\text{micro}}^{\text{L\"owner}}), \end{aligned} \quad (5.17)$$

and the parameter α is defined by

$$\alpha \in [1, \min(\frac{\mu_{\text{matrix}}^*}{(\mu^*)_{\text{micro}}^{\text{L\"owner}}}, \frac{\mu_{\text{matrix}}}{\mu_{\text{micro}}^{\text{L\"owner}}}, \frac{\mu_{\text{matrix}} + \lambda_{\text{matrix}}}{\mu_{\text{micro}}^{\text{L\"owner}} + \lambda_{\text{micro}}^{\text{L\"owner}}})] = [1, 1.66]. \quad (5.18)$$

We illustrate in Figure 5.6 that linear elasticity with $\mathbb{C}_{\text{micro}} = 1.66 \mathbb{C}_{\text{micro}}^{\text{L\"owner}}$ is stiffer than the fully resolved metamaterial for $n = 1$ and therefore it is a valid choice. However, assuming $\mathbb{C}_{\text{micro}} = \mathbb{C}_{\text{matrix}}$ does not break the extended Neumann’s principle. We will investigate later numerically the consequences of the different choices for $\mathbb{C}_{\text{micro}}$.

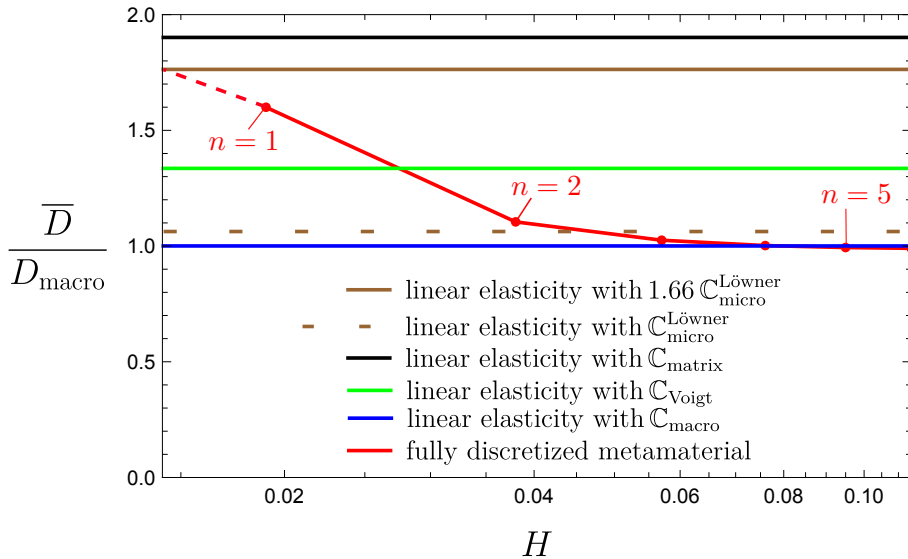


Figure 5.6: The normalized bending stiffness varying the beam size $H \times L = nl \times 12nl$ compared to the ones obtained by linear elasticity with different elasticity tensors shown in Section 5.2.2. Taken from SARHIL ET AL. [2023c].

5.2.3 Identification of the microscopic elasticity tensor $\mathbb{C}_{\text{micro}}$ via non-affine deformations

We determined in Section 5.2.2 the microscopic elasticity tensor $\mathbb{C}_{\text{micro}}$ as the Löwner matrix supremum. Nevertheless, the affine Dirichlet boundary conditions are too soft and unable to capture the size-effects of bending. In order to estimate the stiffness $\mathbb{C}_{\text{micro}}$ in the relaxed micromorphic model, we choose in the following approach the most simple ansatz

$$\mathbb{C}_{\text{micro}} = \beta^* \mathbb{C}_{\text{macro}} \quad \text{with} \quad \beta^* = \max\{\beta_i\} > 1 \quad \text{with} \quad i = 1, \dots, r. \quad (5.19)$$

The size dependency is a complex phenomenon in general and cannot be modeled by a single scalar β^* alone, of course. The parameters β_i are determined via the energy equivalence of a heterogeneous microstructured domain \mathcal{B}_i and an equivalent homogeneous domain $\mathcal{B}_i^{\text{macro}}$ with the same dimensions governed by linear elasticity with an elasticity tensor $\beta_i \mathbb{C}_{\text{macro}}$, see Figure 5.7. Here, we consider a higher-order deformation mode, which is the pure bending mode. The bending mode is enforced by applying non-affine Dirichlet boundary conditions on the whole boundary. They are derived from the analytical solution of the pure bending problem of the homogeneous problem in RIZZI ET AL. [2021b]

$$\mathbf{u} = \bar{\mathbf{u}} = \frac{\kappa}{2} \begin{pmatrix} -2xy \\ \frac{\lambda_{\text{macro}}}{2\mu_{\text{macro}} + \lambda_{\text{macro}}} y^2 + x^2 \end{pmatrix} \quad \text{on} \quad \partial\mathcal{B}, \quad (5.20)$$

which leads to a constant curvature κ for the homogeneous case with no shear strain and one active stress component σ_{11}

$$\bar{\boldsymbol{\varepsilon}} = \text{sym} \nabla \bar{\mathbf{u}} = \begin{pmatrix} -\kappa y & 0 \\ 0 & \frac{\lambda_{\text{macro}} \kappa y}{2\mu_{\text{macro}} + \lambda_{\text{macro}}} \end{pmatrix}, \quad (5.21)$$

$$\bar{\boldsymbol{\sigma}} = \begin{pmatrix} \frac{-4\mu_{\text{macro}}(\mu_{\text{macro}} + \lambda_{\text{macro}})\beta\kappa y}{2\mu_{\text{macro}} + \lambda_{\text{macro}}} & 0 \\ 0 & 0 \end{pmatrix}.$$

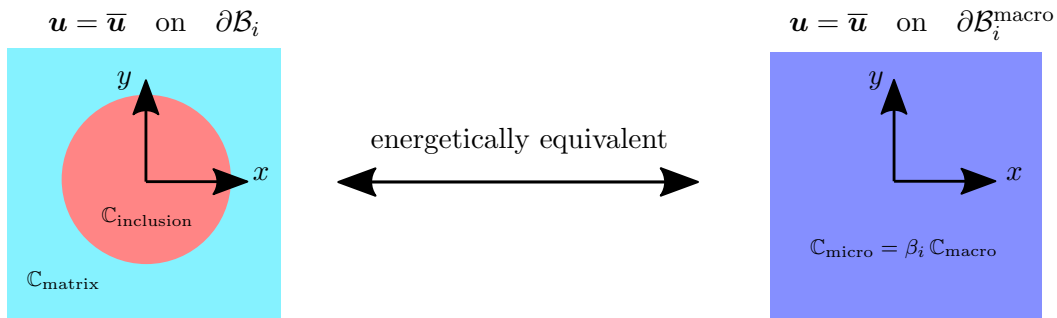


Figure 5.7: Illustration shows the procedure used to calculate β_i . Taken from SARHIL ET AL. [2023c].

We search for the stiffest possible component on the microstructure under flexural deformation mode by investigating different arrangements of unit-cells, which do not have to

exhibit cubic symmetry as in Section 5.2.2. Six different arrangements were considered, see Figure 5.8. The largest obtained value is $\beta^* = \beta_1 = 1.64$. Increasing the size of the arrangements of the unit-cells, considered in Figure 5.8, we retrieve the macroscopic property, where β_i converges to the value one as it should. This behavior is shown exemplarily for unit-cell (a) in Figure 5.9.

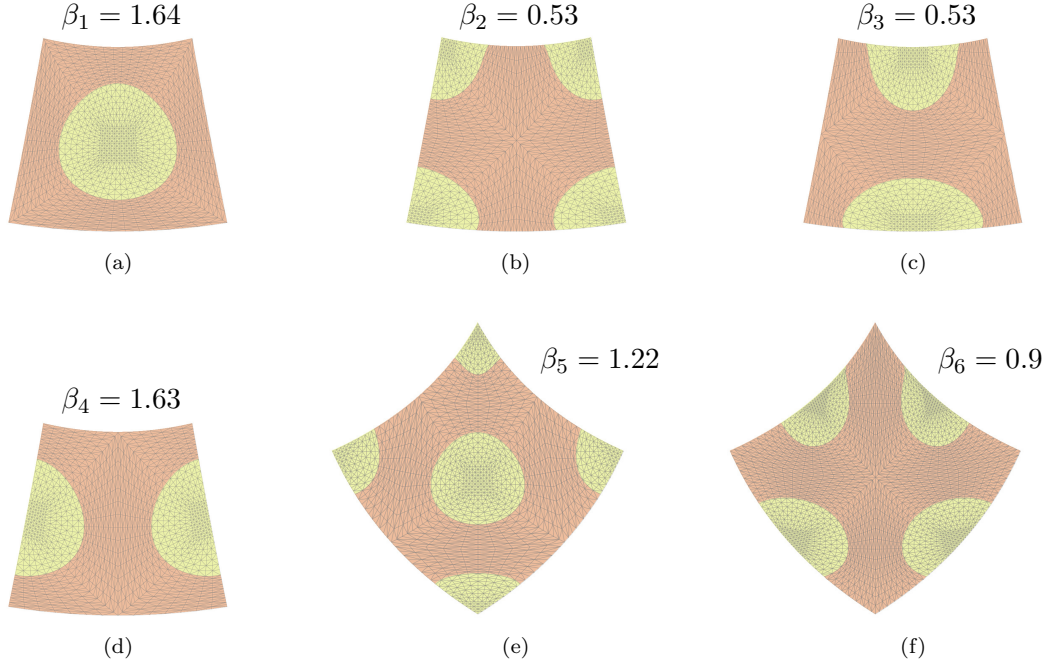


Figure 5.8: The values of the parameter β_i calculated for different unit-cells. Unit-cell (a) provides the stiffest flexural stiffness with $\beta^* = \beta_1 = 1.64$. Taken from SARHIL ET AL. [2023c].

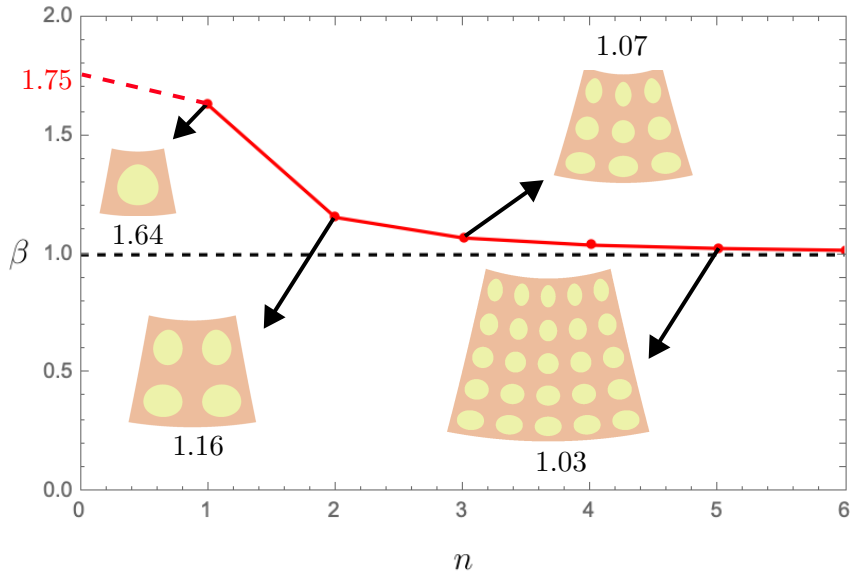


Figure 5.9: The parameter β converges to the value one when increasing the size of a cluster of unit cells ($n \times n$) shown exemplarily for type (a) in Figure 5.8. We also show the extrapolated value $\beta = 1.75$. Taken from SARHIL ET AL. [2023c].

We show in Figure 5.10 the size-effect of the fully resolved metamaterial beams and the linear elasticity solutions with elasticity tensors $\mathbb{C}_{\text{micro}} = 1.64 \mathbb{C}_{\text{macro}}$ and $\mathbb{C}_{\text{macro}}$. The

choice $\mathbb{C}_{\text{micro}} = 1.64\mathbb{C}_{\text{macro}}$ guarantees that a homogeneous continuum with elasticity tensor $\mathbb{C}_{\text{micro}} = 1.64\mathbb{C}_{\text{macro}}$ is stiffer than the fully discretized metamaterial. The upper limit $\mathbb{C}_{\text{micro}} = 1.64\mathbb{C}_{\text{macro}}$ is slightly stiffer than the relatively stiffest metamaterial beam ($n = 1$), which confirms its validity. However, we extrapolate $\mathbb{C}_{\text{micro}} = 1.75\mathbb{C}_{\text{macro}}$ as an improved upper bound to provide a better fitting.

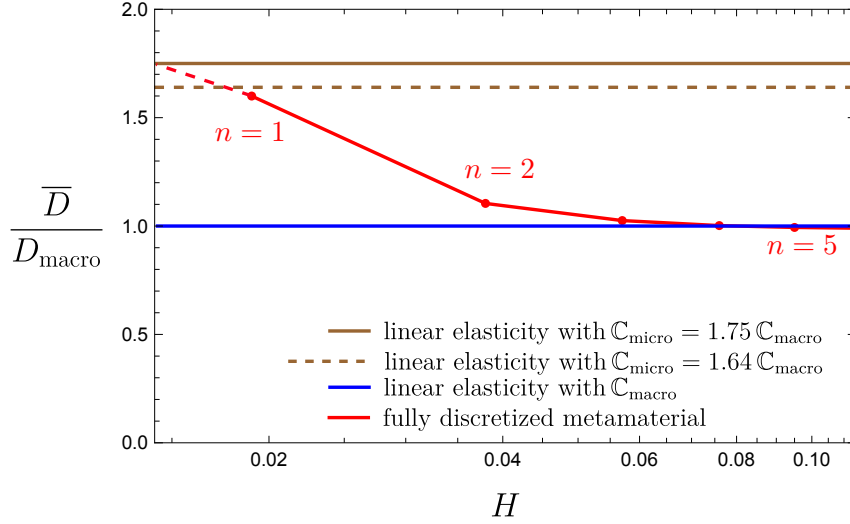


Figure 5.10: The normalized bending stiffness varying the beam size $H \times L = nl \times 12nl$ compared to the ones obtained by linear elasticity with different elasticity tensors shown in Section 5.2.3. Taken from SARHIL ET AL. [2023c].

5.2.4 Identification of \mathbb{C}_e

The elasticity tensor \mathbb{C}_e is calculated via the micro-macro Reuss-like homogenization formula in Equation (3.15). The obtained elasticity tensor \mathbb{C}_e is automatically positive definite since $\mathbb{C}_{\text{micro}} > \mathbb{C}_{\text{macro}}$ and has cubic symmetry property. However, no obvious physical interpretation can be assigned to the tensor \mathbb{C}_e .

5.3 The boundary conditions of the micro-distortion field

It is worth noting that there has been a lack of attention given to investigating boundary conditions (BCs) in the context of enriched continua in the literature. However, the importance of such conditions must be addressed, as they play a crucial role in identifying material parameters accurately. Without setting the correct BCs for the micro-distortion field, the behavior of enriched continua can change significantly, rendering the identification of material parameters meaningless.

In the context of the relaxed micromorphic model, the boundary conditions (BCs) of the micro-distortion field play especially a critical role. It is important to choose appropriate BCs that induce a curvature in the model, i.e. $\text{Curl } \mathbf{P} \neq \mathbf{0}$. This is because inadequate boundary conditions of the micro-distortion field can lead to unwanted behavior of the relaxed micromorphic model. Such behavior can manifest in the form of the model not exhibiting size-effects or failing to reach the intended upper limit (linear elasticity with $\mathbb{C}_{\text{micro}}$) for $L_c \rightarrow \infty$. Hence, selecting the right BCs is crucial for ensuring the accuracy and reliability of the relaxed micromorphic model.

5.3.1 Symmetric force stress case

We assume here $\mathbb{C}_c = \mathbf{0}$ ($\mu_c = 0$) which causes symmetric force stress $\boldsymbol{\sigma}$ and symmetric Curl \mathbf{m} because the balance of angular momentum in Equation (3.29d) becomes symmetric. We test the sufficiency of the boundary conditions by comparing the solution of the relaxed micromorphic model for varied values of the characteristic length parameter L_c with the solutions obtained by the standard linear elasticity with elasticity tensors $\mathbb{C}_{\text{micro}}$ and $\mathbb{C}_{\text{macro}}$. More specifically, the relaxed micromorphic model should reproduce linear elasticity with elasticity tensors $\mathbb{C}_{\text{micro}}$ and $\mathbb{C}_{\text{macro}}$ for $L_c \rightarrow \infty$ and $L_c \rightarrow 0$, respectively. To put it differently, the theoretical features of the RMM that are depicted in Figure 3.1 have been successfully retrieved.

In order to conduct a numerical test, we fixed the geometry of a beam to $H \times L = 2l \times 24l$. We assume $\mathbb{C}_{\text{micro}} = 1.75 \mathbb{C}_{\text{macro}}$ and set $\mu = \mu_{\text{macro}}$. The boundary conditions of the displacement field are taken similar to the ones applied on the fully resolved metamaterials in Figure 5.3. For the first case with applied rotation, the consistent coupling condition is applied on the right and left edges via a penalty approach, see Figure 5.11 and Equation (3.32). Indeed, enforcing the consistent coupling condition on the Dirichlet boundary of the displacement field is adequate to fulfill the theoretical limits of the relaxed micromorphic model, i.e. linear elasticity with elasticity tensors $\mathbb{C}_{\text{micro}}$ and $\mathbb{C}_{\text{macro}}$. Removing the consistent coupling condition on left or right edges leads to vanishing curvature, turning the relaxed micromorphic model into standard linear elasticity with $\mathbb{C}_{\text{macro}}$. The previous behavior is demonstrated in Figure 5.12. The exact same behavior is observed for the second loading case with applied traction if we apply the consistent coupling condition on the boundary corresponding to the first loading case, see Figure 5.11. Consequently, the relaxed micromorphic model leads to consistent results for both loading cases, see Figure 5.12.

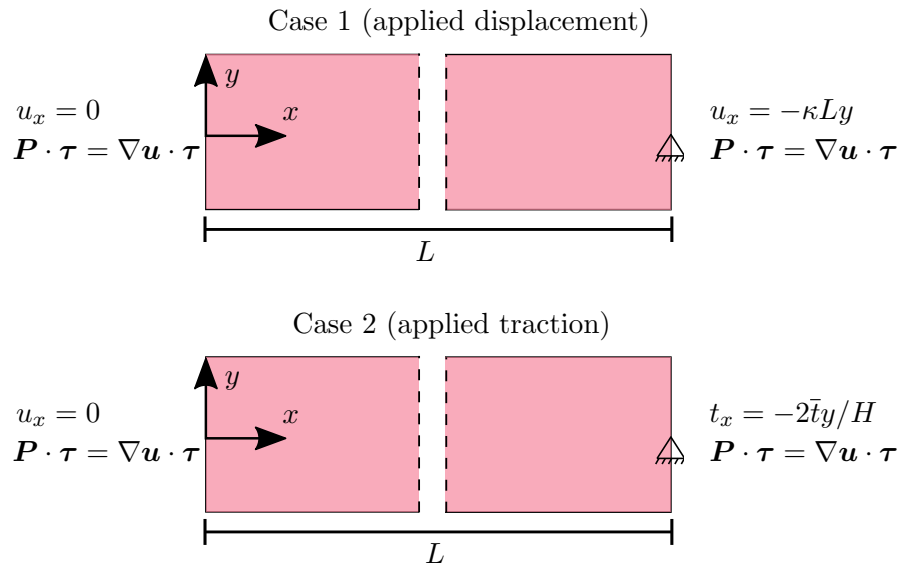


Figure 5.11: The boundary value problems of the homogeneous relaxed micromorphic model for both loading cases. These boundary value problems are equivalent to the two cases of the heterogeneous metamaterial shown in Figure 5.3. The upper and lower edges are traction-free. Taken from SARHIL ET AL. [2023c].

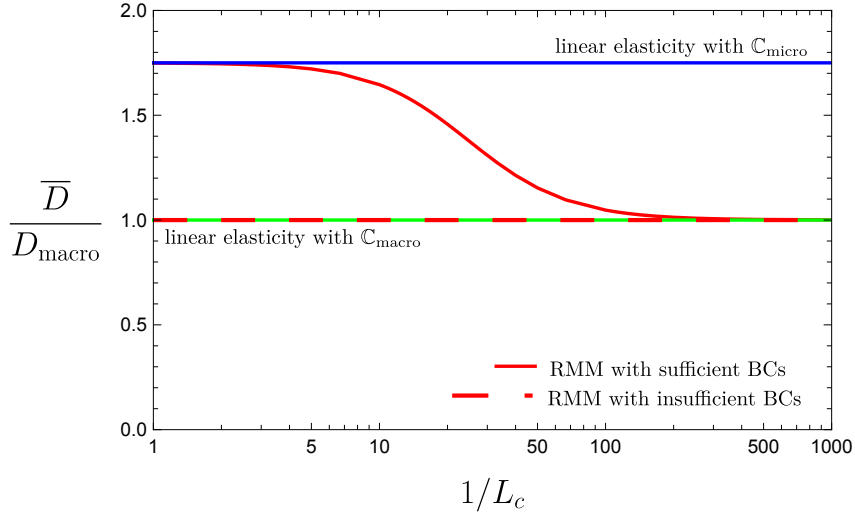


Figure 5.12: The normalized bending stiffness obtained by the relaxed micromorphic model for both loading cases for the symmetric force stress scenario $\mathbb{C}_c = \mathbf{0}$ while varying the characteristic length L_c . Sufficient BCs indicate applying the consistent coupling condition on the left and right edges, see Figure 5.11. Removing the consistent coupling condition on left or right edge is considered as insufficient and leads to no size-effect. Taken from SARHIL ET AL. [2023c].

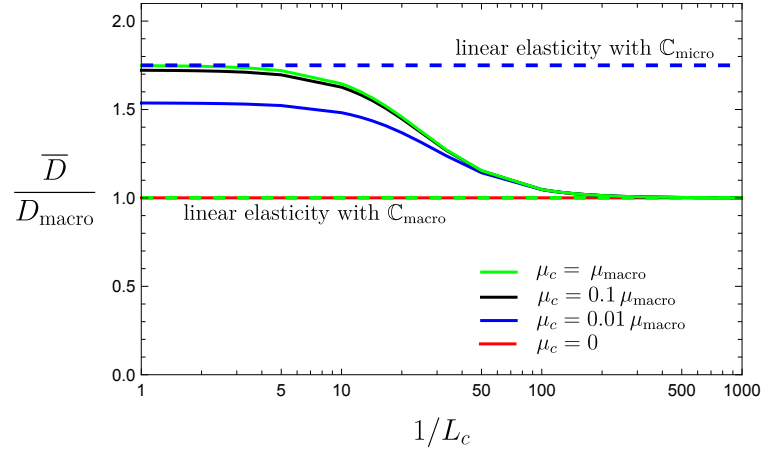
5.3.2 Non-symmetric force stress case

Next, we investigate the non-symmetric force stress case, i.e. the balance of angular momentum in Equation (3.29d) is non-symmetric. We assume $\mathbb{C}_c = 2\mu_c \mathbb{I}$ (2D case) where \mathbb{I} is the fourth-order identity tensor and μ_c is the Cosserat couple modulus acting as a spring constant between the skew-symmetric parts of $\nabla \mathbf{u}$ and \mathbf{P} . We study the influence of varying the Cosserat couple modulus $\mu_c \in [0, 0.01, 0.1, 1] * \mu_{\text{macro}}$ considering different scenarios of the boundary condition of \mathbf{P} . The geometry and the remaining material parameters are taken as for the symmetric case, see Section 5.3.1.

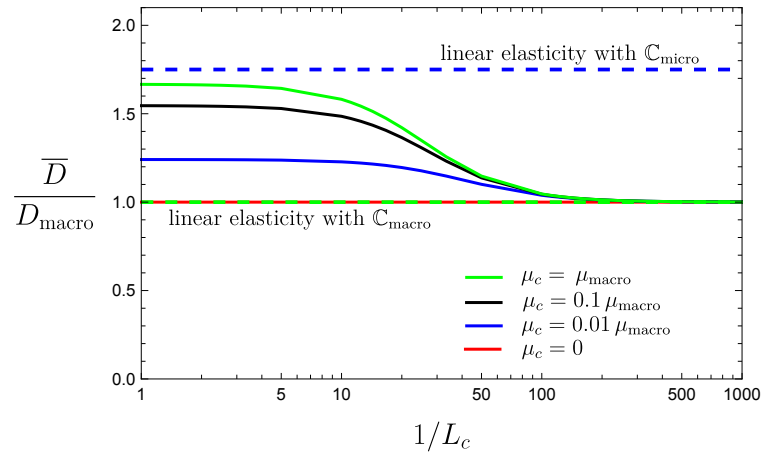
In Figure 5.13, we show the normalized bending stiffness for the cases (a) the consistent coupling condition is applied either on the left or right edge, (b) no consistent coupling boundary condition is considered and (c) the consistent coupling boundary condition is applied on both left and right edges. Size-effects are noticed even if the consistent coupling condition is not placed simultaneously on the right and left edges, which is not the case for the symmetric force stress ($\mu_c = 0$), c.f. Figure 5.12. Increasing the Cosserat couple modulus μ_c raises the stiffness of the relaxed micromorphic model closer to linear elasticity with $\mathbb{C}_{\text{micro}}$ for $L_c \rightarrow \infty$ and even reach it in Figure 5.13(a). However, it is not guaranteed that the relaxed micromorphic model achieves linear elasticity with $\mathbb{C}_{\text{micro}}$ for $L_c \rightarrow \infty$, see Figure 5.13(b). The results of enforcing the consistent coupling condition on both left and right edges are equivalent for the symmetric and non-symmetric cases in Figures 5.12 and 5.13(c), respectively, and the Cosserat couple modulus has no influence.

5.3.3 Cosserat limit, skew-symmetric micro-distortion field

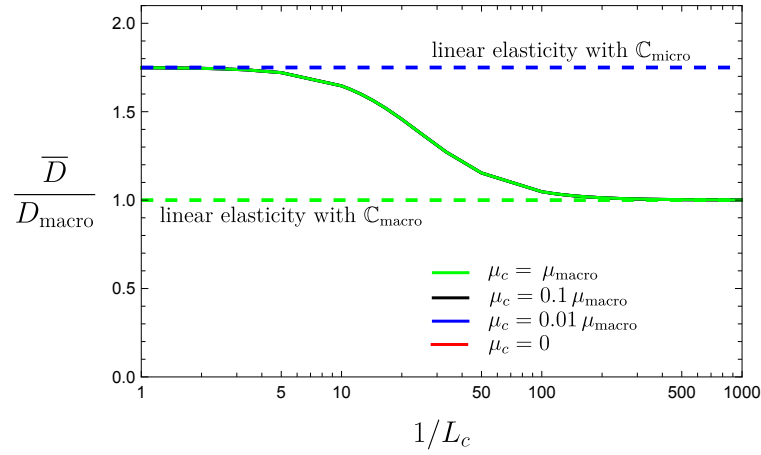
The micropolar Cosserat continuum in Section 2.6.3 is recovered for the case of $\mathbb{C}_{\text{micro}} \rightarrow \infty$. The micro-distortion field must be then skew-symmetric $\mathbf{A} = \text{skew } \mathbf{P}$, c.f. ALAVI ET AL. [2022a], BLESSEN AND NEFF [2023], GHIBA ET AL. [2023], KHAN ET AL.



(a) consistent coupling condition either on the left or right edge



(b) no consistent coupling condition



(c) consistent coupling condition on the left and right edges

Figure 5.13: The normalized bending stiffness obtained by the relaxed micromorphic model for both loading cases with non-symmetric force stress and with varying the characteristic length L_c . Different scenarios are investigated for the boundary conditions of the micro-distortion field. Enforcing the consistent coupling condition on both left and right edges (c) reproduces the results of the symmetric force stress case in Figure 5.11 and Cosserat modulus has no effect. Taken from SARHIL ET AL. [2023c].

[2022]. We investigate numerically the influence of different scenarios of the boundary conditions for the micro-distortion field \mathbf{P} similar to Section 5.3.2: (a) the consistent coupling condition is applied on either the left or right edge, (b) without enforcing the consistent boundary condition and (c) the consistent coupling condition is applied on both left and right edges for $\mathbb{C}_{\text{micro}} = 1000 \mathbb{C}_{\text{macro}}$. Different values of the Cosserat couple modulus μ_c are assumed for varied values of the characteristic length parameter L_c in Figure 5.15. We find that when the consistent coupling condition is not simultaneously applied at both right and left ends, large values of L_c result in a beam that does not bend, see Figure 5.14, causing an infinite nonphysical bending stiffness. This emphasizes the crucial role of the consistent coupling condition, not just in the relaxed micromorphic model, but also in the Cosserat case. Hence due to the bending stiffness issue, we have opted to show the normalized total energy Π/Π_{macro} for this analysis alternatively (instead of \bar{D}/D_{macro}).

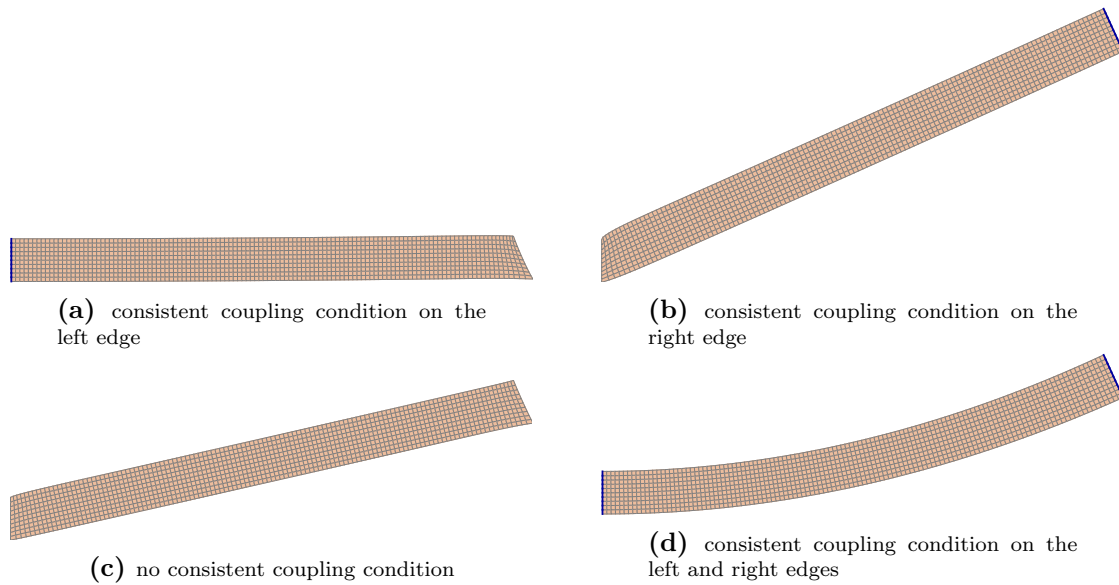
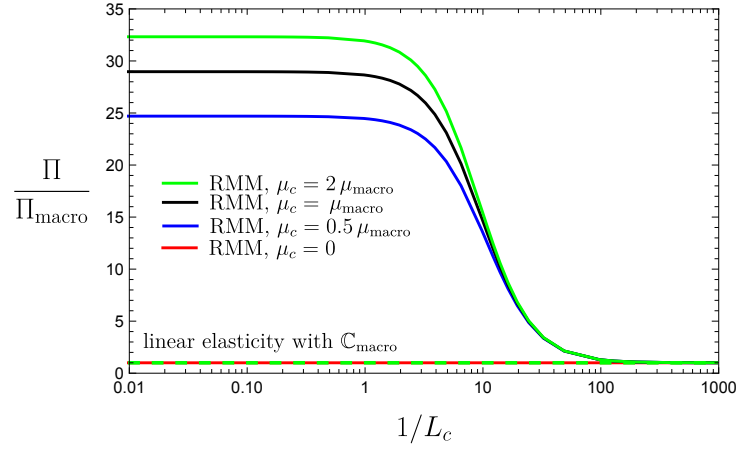
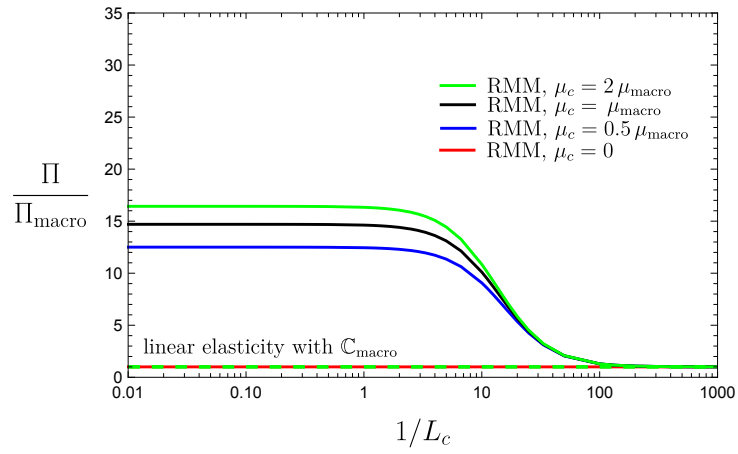


Figure 5.14: The deformed beams for the case $\mathbb{C}_{\text{micro}} = 1000 \mathbb{C}_{\text{macro}}$ "Cosserat type" with $L_c = 1000 \text{ m}$ and $\mu_c = 2 \mu_{\text{macro}}$. The classical bending deformation can only be induced when the consistent coupling condition is applied on both its left and right ends (d). Taken from SARHIL ET AL. [2023c].

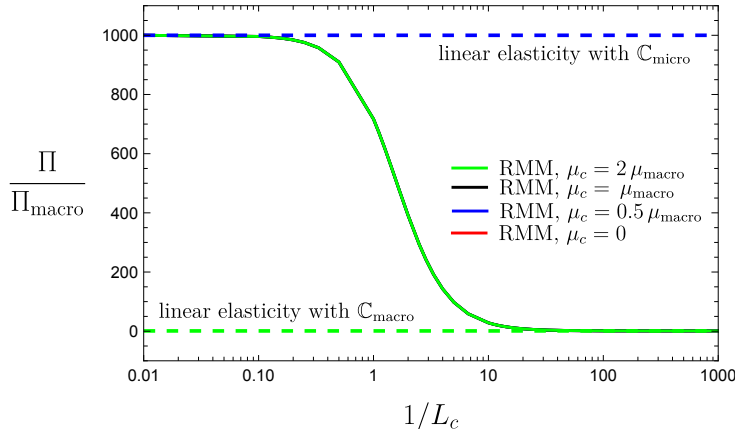
We notice that linear elasticity with elasticity tensor $\mathbb{C}_{\text{micro}} = 1000 \mathbb{C}_{\text{macro}}$ is recognized as an upper limit when the consistent coupling condition is enforced simultaneously on both left and right edges, see Figure 5.15(c). Nevertheless, less prominent size-effects are noticed when the consistent coupling condition is not enforced, Figure 5.15(a-b). While size-effects are prompted only for non-vanishing Cosserat couple modulus $\mu_c \neq 0$ for cases (a) and (b), enforcing the consistent coupling condition simultaneously on both left and right edges leads to size-effects with no influence of the Cosserat couple modulus μ_c which is well-known for the Cosserat model under pure bending. This can be explained by the fact that for pure bending the skew-symmetric part of the micro-distortion field is the same as the skew-symmetric part of the gradient of the displacement, see RIZZI ET AL. [2021b], which is the case for both the relaxed micromorphic continuum in Figure 5.13(c) and the Cosserat model in Figure 5.15(c).



(a) consistent coupling condition either on the left or right edge



(b) no consistent coupling condition



(c) consistent coupling condition on the left and right edges

Figure 5.15: The relative total energy obtained by the relaxed micromorphic model for both loading cases with non-symmetric force stress ($\mu_c \neq 0$) and with varying the characteristic length L_c . Here, we assume $\mathbb{C}_{\text{micro}} = 1000 \mathbb{C}_{\text{macro}}$ leading to a skew-symmetric micro-distortion field which retrieves the Cosserat model since the curvature expression is then equivalent with the Cosserat framework, see GHIBA ET AL. [2023]. Different scenarios are investigated for the boundary conditions of the micro-distortion field. Taken from SARHIL ET AL. [2023c].

5.4 Scaling of the curvature

The curvature for the 2D case is isotropic because $\text{Curl} \mathbf{P}$ is reduced to a vector, see Equation (3.18). Therefore, the curvature will be controlled by the quantity μL_c^2 , assuming $\mathbb{L} = \mathbb{I}$ is the fourth-order identity tensor. Since the parameters μ and L_c should be set constant independent of the specimen size, the curvature is modified by incorporating the size of the beams through the number n . Figure 5.4 shows that a stiffer response is observed for smaller values of the number n ($n = 1$ is the stiffest). The relaxed micromorphic model exhibits stiffer response for larger values of the characteristic length parameter L_c (inversely proportional to n), see for example Figure 5.12. Therefore, we replace the last term in Equation (3.13) by

$$\frac{1}{2} \mu \left(\frac{L_c}{n} \right)^2 \text{Curl} \mathbf{P} : \text{Curl} \mathbf{P}, \quad (5.22)$$

where n denotes the number of unit cells in the y-direction. Hence, for a constant L_c , smaller values are obtained for the term L_c/n by increasing the beam size (increasing n). This modification reproduces the intended size-effects (smaller is stiffer), which is not ad hoc, but follows from a rigorous scaling argument, c.f. NEFF ET AL. [2020] and applies to other continua as well such as higher-gradient or classical micromorphic continua.

5.5 Calibration of the curvature in RMM with the fully resolved solution

We provided in Section 5.2 an identification scheme for the scale-independent material parameters of the relaxed micromorphic model. The boundary conditions of the micro-distortion field were determined in Section 5.3 in order to guarantee the intended behavior of the relaxed micromorphic model and the influence of the characteristic length L_c for both loading cases, as illustrated in Figure 3.1. The quantities associated with the curvature are yet to be identified.

For this calibration, we assume symmetric force stress, i.e. $\mu_c = 0$. As we discussed in Sections 5.2.2, 5.2.3 and 5.3.3, different choices are made for $\mathbb{C}_{\text{micro}}$, e.g. $\mathbb{C}_{\text{micro}} = 1.66 \mathbb{C}_{\text{micro}}^{\text{L\"owner}}$ (affine BCs), $\mathbb{C}_{\text{micro}} = \mathbb{C}_{\text{matrix}}$, $\mathbb{C}_{\text{micro}} = 1.75 \mathbb{C}_{\text{macro}}$ (non-affine BCs) and $\mathbb{C}_{\text{micro}} = 1000 \mathbb{C}_{\text{macro}}$ (Cosserat). Considering $\mathbb{C}_{\text{micro}} = 10000 \mathbb{C}_{\text{macro}}$ yield similar results to $\mathbb{C}_{\text{micro}} = 1000 \mathbb{C}_{\text{macro}}$, as expected, which can be explained by the fact that we are operating in a range close to the lower bound $\mathbb{C}_{\text{macro}}$. For each choice of $\mathbb{C}_{\text{micro}}$, the curvature should be calibrated by means of L_c and μ . Without loss of generality, we can always assume the shear modulus $\mu = \mu_{\text{macro}}$ and then the characteristic length L_c should be chosen in order to fit the solution of the fully discretized metamaterial, Figure 5.16. Alternatively, the characteristic length L_c can be set in advance, e.g. $L_c = l$ (size of the unit-cell), and then the shear modulus μ should be calibrated, see Figure 5.17 and Equation (5.22). The decisive quantity is the product μL_c^2 . Since the Cosserat curvature coincides with the curvature expression of the relaxed micromorphic model GHIBA ET AL. [2023], one would expect that using similar values for μL_c^2 is a sensible choice. As Figures 5.16(d) and 5.17(d) show, this is not the case. For a rough Cosserat fit different orders of magnitude for μL_c^2 have to be taken which are getting arbitrary. Furthermore, the data points can be fitted also with a Cosserat type model but it should be remarked that the unbounded stiffness (beyond $n = 1$) leads to a sensitive identification of the parameters. The same

problem would appear by using other continua such as the second gradient or the classical micromorphic theories.

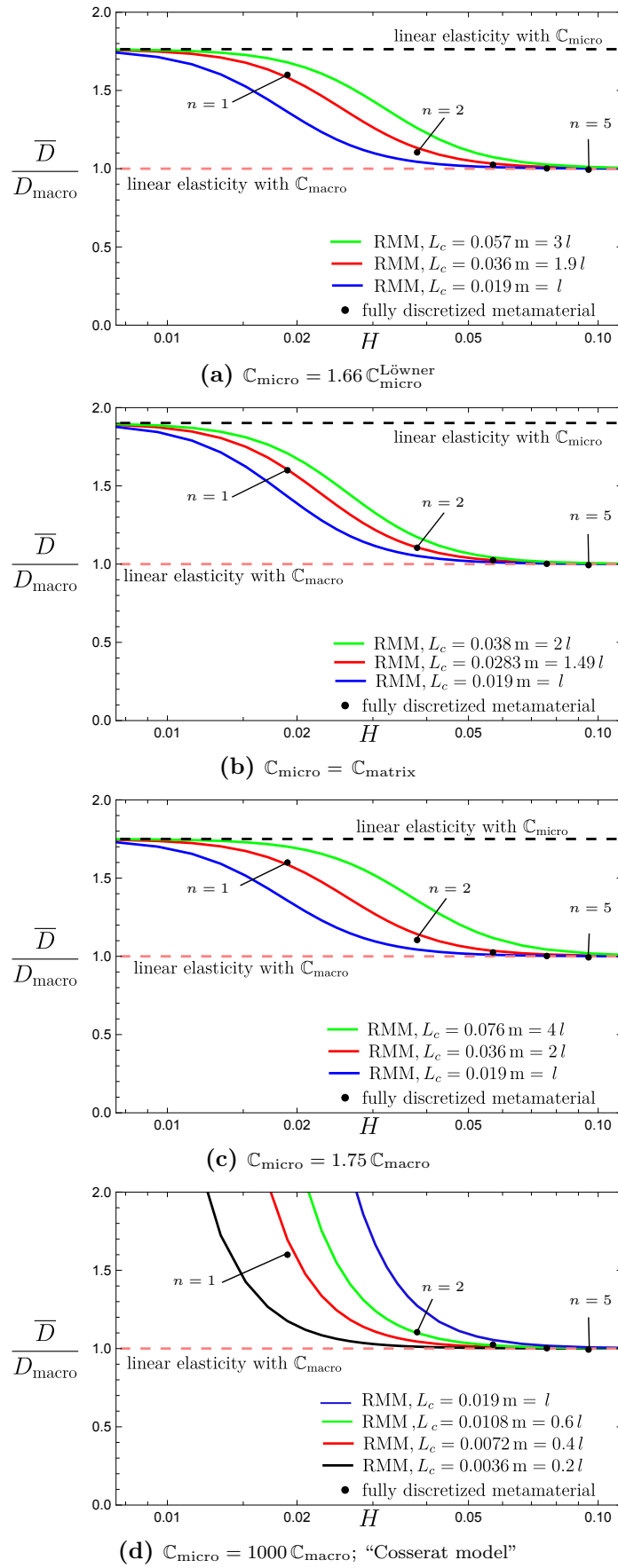


Figure 5.16: The normalized bending stiffness varying the beam size $H \times L = nl \times 12nl$ obtained by the fully discretized metamaterial and the relaxed micromorphic model. We analyze here different choices for C_{micro} with varying L_c and fixing $\mu = \mu_{\text{macro}}$. The results are equivalent for both loading cases. Taken from SARHIL ET AL. [2023c].

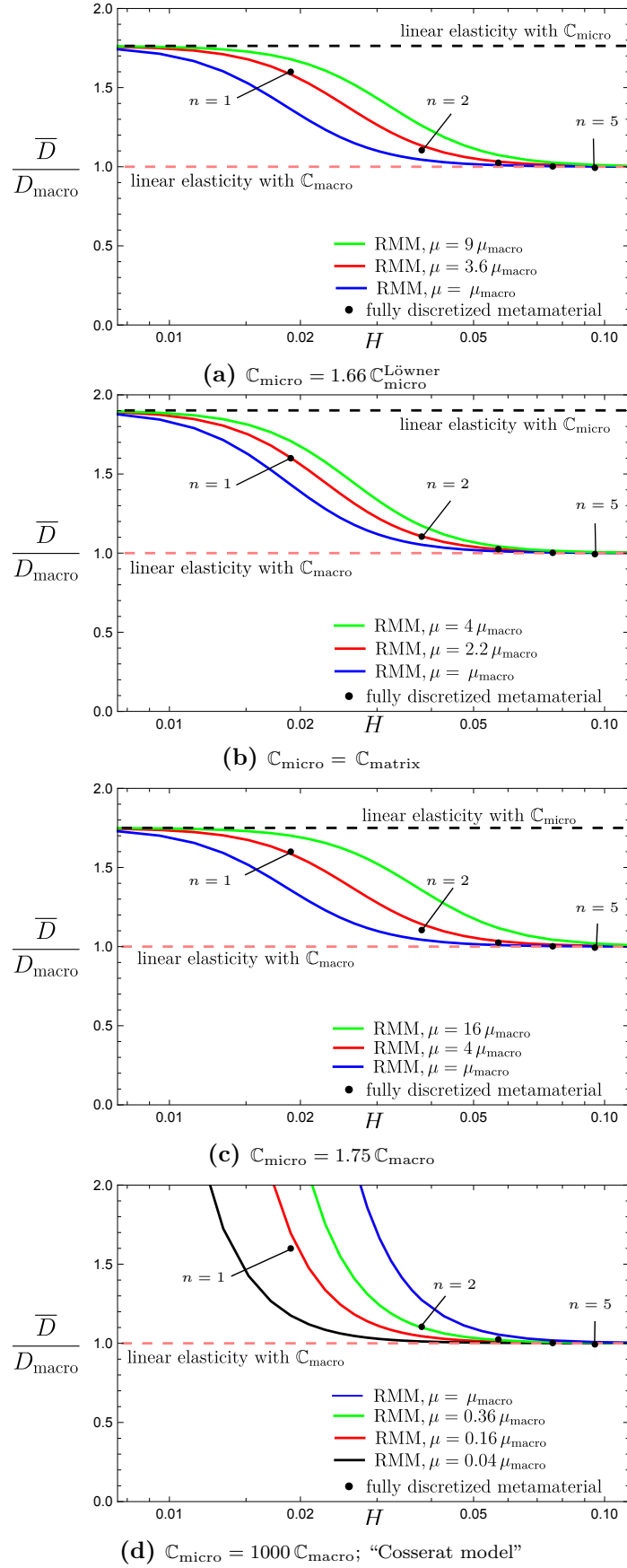


Figure 5.17: The normalized bending stiffness varying the beam size $H \times L = nl \times 12nl$ obtained by the fully discretized metamaterial and the relaxed micromorphic model. We analyze here different choices for C_{micro} with varying μ and fixing $L_c = l$. The results are equivalent for both loading cases. Taken from SARHIL ET AL. [2023c].

5.6 Validation: further numerical examples

This study assesses the obtained material parameters of the relaxed micromorphic model for two additional loading scenarios apart from pure bending. We consider the fully resolved metamaterial beams with the dimensions and material parameters outlined before in Section 5.1. In the relaxed micromorphic model, we consider the symmetric case where $\mu_c = 0$. The macroscopic elasticity tensor, $\mathbb{C}_{\text{macro}}$, is defined in Section 5.2.1 and the curvature is scaled to the specimen's size using Equation (5.22) under the assumption of $\mu = \mu_{\text{macro}}$. The microscopic elasticity tensor $\mathbb{C}_{\text{micro}}$ is determined using the same four different assumptions outlined in Section 5.5.

5.6.1 Simple shearing

The boundary conditions are derived from the solution of an infinite stripe under simple shear in RIZZI ET AL. [2021a]

$$\mathbf{u} = \bar{\mathbf{u}} = \begin{pmatrix} ay \\ 0 \end{pmatrix} \quad \text{on} \quad \partial\mathcal{B}, \quad (5.23)$$

which leads to the following strain and stress tensors for the homogeneous linear elasticity with macroscopic elasticity tensor $\mathbb{C}_{\text{macro}}$

$$\bar{\boldsymbol{\varepsilon}} = \begin{pmatrix} 0 & a/2 \\ a/2 & 0 \end{pmatrix}, \quad \bar{\boldsymbol{\sigma}} = \begin{pmatrix} 0 & a\mu_{\text{macro}}^* \\ a\mu_{\text{macro}}^* & 0 \end{pmatrix}. \quad (5.24)$$

The boundary value problems for the relaxed micromorphic model and the reference fully resolved metamaterial are depicted in Figure 5.18. Dirichlet boundary condition for the displacement field and the consistent coupling condition are enforced over the entire boundary.

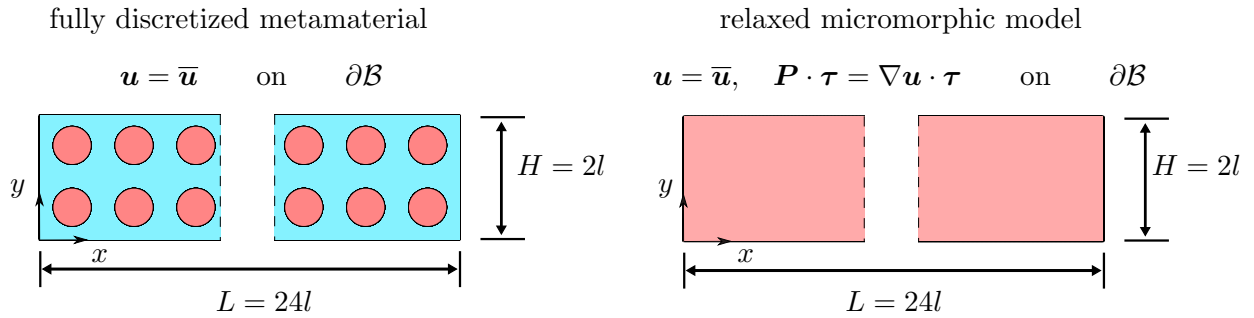


Figure 5.18: Boundary value problem: pure shear, shown exemplarily for $n = 2$, for the fully discretized metamaterial and the homogeneous relaxed micromorphic continuum. Taken from SARHIL ET AL. [2023c].

We analyze the size-effects via the normalized shear force $\frac{T}{T_{\text{macro}}}$, which is shown in Figure 5.19. Here, T is the actual shear force while the macroscopic shear force T_{macro} (associated with linear elasticity with $\mathbb{C}_{\text{macro}}$) is given by $T_{\text{macro}} = a\mu_{\text{macro}}^* L$. The size-effects associated with pure shear response are less pronounced than the size-effects associated with pure bending. We notice that the choices $\mathbb{C}_{\text{micro}} = 1.66 \mathbb{C}_{\text{micro}}^{\text{Löwner}}$ and $\mathbb{C}_{\text{micro}} = 1.75 \mathbb{C}_{\text{macro}}$ deliver close results for the bending in Figure 5.16 but different results for the simple shear in Figure 5.19 which can be explained by their different anisotropy properties. We

notice that the results for shear are less satisfactory than the results for bending since fitting was based on bending mode.

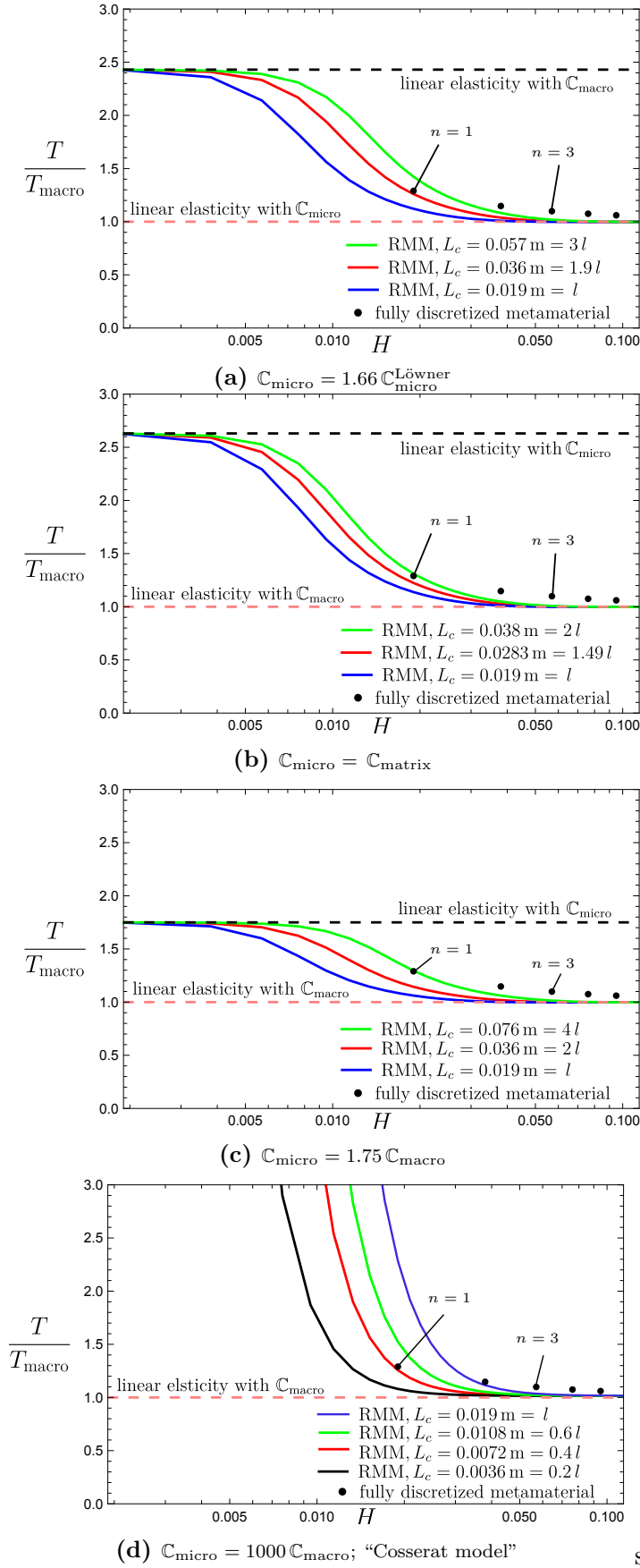


Figure 5.19: The normalized shear force varying the specimen’s size $H \times L$ for different choices of C_{micro} . Taken from SARHIL ET AL. [2023c].

5.6.2 Cantilever under traction load

We consider the classical cantilever problem in the following setup. We fix the right edge of the beam in both directions while a constant traction of $t_y = \bar{t}$ is applied in the y -direction on the left edge. The boundary value problems for both the fully discretized metamaterial and the relaxed micromorphic model are illustrated in Figure 5.20. The microscopic elasticity model can be recovered for large values of L_c when the consistent coupling condition is applied to the entire boundary. However, for small values of L_c , a boundary layer is built up at the upper and lower edges, requiring a fine mesh. This issue can be resolved by partially applying the consistent boundary condition, i.e. $(\mathbf{P} \cdot \boldsymbol{\tau})_y = (\nabla \mathbf{u} \cdot \boldsymbol{\tau})_y$.

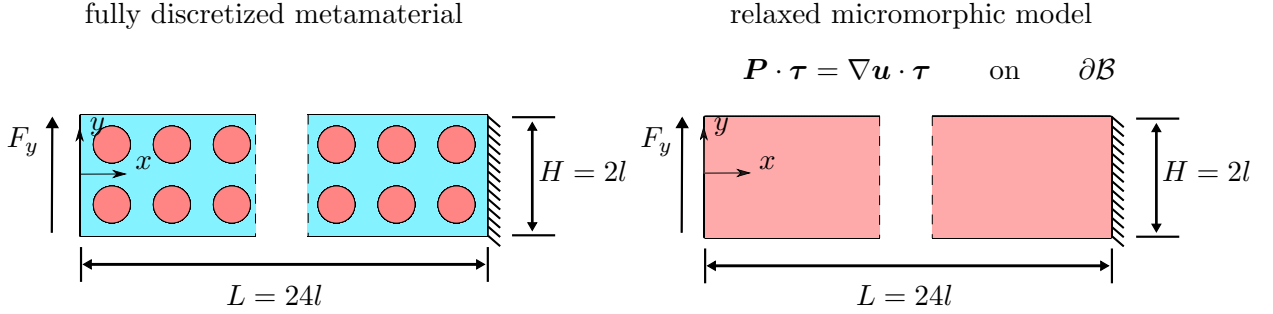


Figure 5.20: Boundary value problem: cantilever, shown exemplarily for $n = 2$, for the fully discretized metamaterial and the homogeneous relaxed micromorphic continuum. Taken from SARHIL ET AL. [2023c].

The equivalent beam model with the deformed shape (for $n = 2$) are displayed in Figure 5.21. The cantilever is subjected to a constant shear force $F_y = \bar{t} H$ and a linear moment that is zero on the left end and maximum on the right end $M = F_y x$.

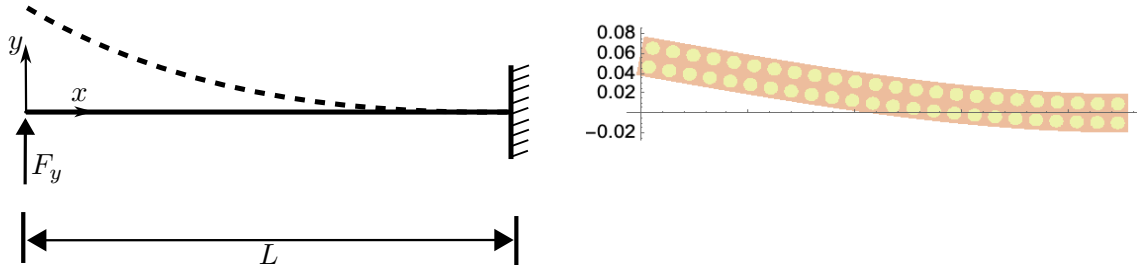


Figure 5.21: The beam model of the cantilever and the deformed shape for $n = 2$. Taken from SARHIL ET AL. [2023c].

We analyze the size-effects via the inverse of the normalized maximum displacement, expressed as $\frac{w_{\text{macro}}(0)}{w(0)}$, see Figure 5.22. Here, $w(0)$ is the actual displacement in y -direction, while the macroscopic displacement (associated with linear elasticity with $\mathbb{C}_{\text{macro}}$) is calculated via the elementary beam theory by the formula $w_{\text{macro}}(0) = \frac{4(1-\nu_{\text{macro}}^2)F_y L^3}{E_{\text{macro}} H^3}$. The results of both the fully discretized metamaterial and the relaxed micromorphic model show good agreement, as the dominant size-effect is bending. However, if consistent boundary conditions are not applied across the entire boundary, agreement is not achieved. This highlight again the importance of the consistent boundary condition and the flexibility of the relaxed micromorphic continuum to model any engineering problem.

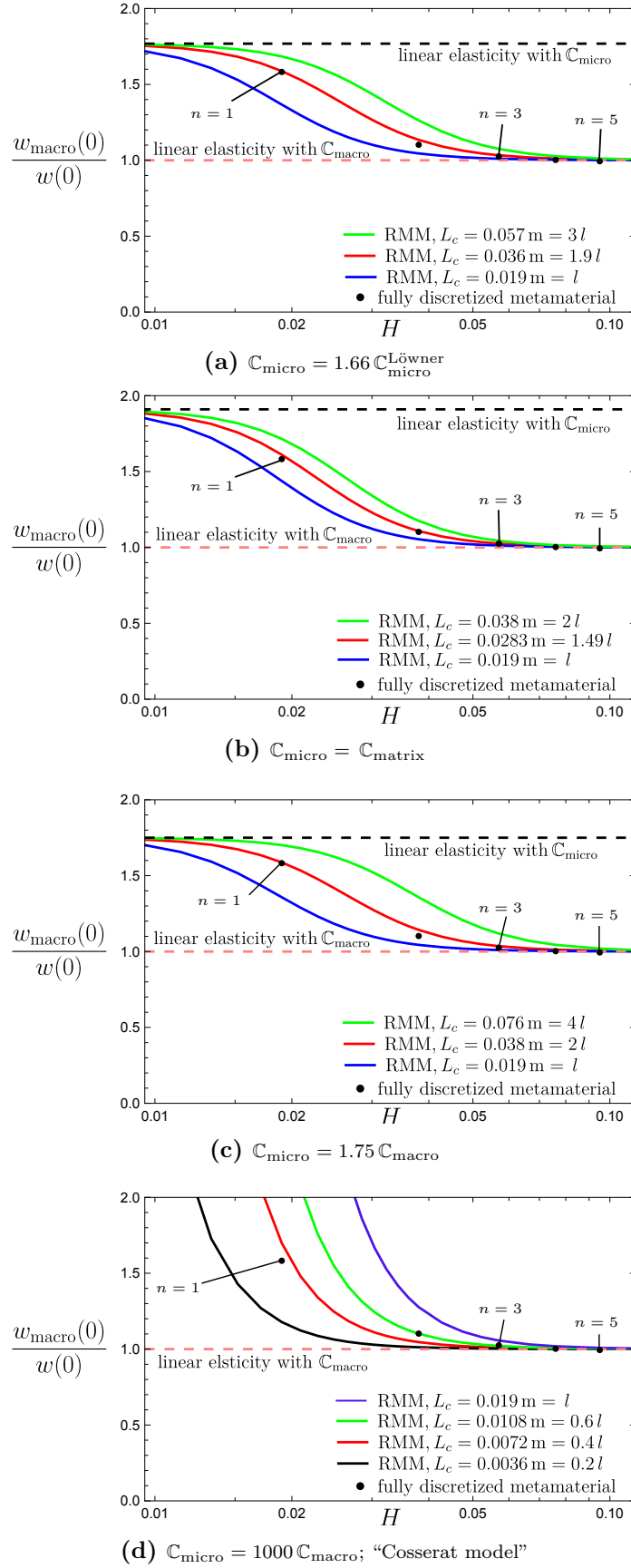


Figure 5.22: The inverse of the normalized deflection at the free end of the cantilever ($x = 0$) for varying the specimen’s size $H \times L$ for different choices of C_{micro} . Taken from SARHIL ET AL. [2023c].

5.7 Discussions

We analyzed the size-effects of fully resolved beams under pure bending. We have shown that applying a rotation (via a given displacement) or a moment (via an applied traction) on the fully discretized metamaterial beams leads to similar results, which we should also get when we model the beams via the relaxed micromorphic model.

We defined the macroscopic elasticity tensor $\mathbb{C}_{\text{macro}}$ using the standard first-order homogenization with periodic boundary conditions. However, the microscopic elasticity tensor $\mathbb{C}_{\text{micro}}$ is linked to the stiffest possible response of the assumed metamaterial. We introduced two approaches for the identification of $\mathbb{C}_{\text{micro}}$. The first approach is based on the least upper bound of the apparent stiffness of the microstructure measured in the energy norm following the Löwner matrix supremum problem in NEFF ET AL. [2020]. Therefore, different unit-cell variants are considered under the affine Dirichlet boundary conditions. However, the flexural deformation mode is not captured by affine Dirichlet boundary conditions, and the resulting $\mathbb{C}_{\text{micro}}$ is not stiff enough to reproduce the solution of fully resolved metamaterial beams subjected to bending. Therefore, we have to scale up the elasticity tensor obtained by Löwner matrix supremum. A second approach is built to identify the microscopic elasticity tensor by non-affine boundary conditions (bending deformation mode). Therefore, different unit-cells are bent to obtain the largest possible flexural rigidity.

Next, we thoroughly examined the boundary conditions for both loading cases (rotation or moment) for the symmetric and non-symmetric force stress scenarios. The consistent coupling boundary condition allows the model to work on the whole intended range bounded by linear elasticity with microscopic and macroscopic elasticity tensors from above and below, respectively. Thus, correctly identifying the parameters of the relaxed micromorphic model must be associated with the consistent coupling boundary condition. Otherwise, $\mathbb{C}_{\text{micro}}$ is not recognized as an upper bound.

A final fitting is conducted to decide the values of characteristic length and the shear modulus associated with the curvature measure in the relaxed micromorphic model. The relaxed micromorphic model reproduces successfully the size-effects in a consistent manner for both loading cases. Finally, the obtained parameters of the relaxed micromorphic model were examined for two loading scenarios apart from pure bending. Good agreement was obtained in general. However, the unique identification of the microscopic elasticity tensor $\mathbb{C}_{\text{micro}}$ remains yet to be done, but it must be stiffer than the apparent stiffness under the affine Dirichlet boundary conditions.

6 Computational approach to identify the material parameters

We defined the microscopic elasticity tensor as the stiffest response at the unit-cell level in Chapter 5. This was inspired by NEFF ET AL. [2020], where the microscopic elasticity tensor was determined by the Löwner matrix supremum of elasticity tensors under affine Dirichlet conditions. However, it was found too soft for size-effects in the bending regime SARHIL ET AL. [2023a]. This prompted an expansion of our understanding of the microscopic elasticity tensor, particularly by incorporating non-affine Dirichlet conditions SARHIL ET AL. [2023b;c], resulting in a microscopic elasticity tensor calibrated precisely for bending. However, a homogenization procedure for the identification of the unknown parameters, including the characteristic length, has not yet been established.

Various methods have been proposed for the homogenization of heterogeneous microstructures into the Cosserat continuum in FOREST AND SAB [1998], HÜTTER [2019], REDA ET AL. [2021], the gradient elasticity continuum in ABALI AND BARCHIESI [2021], ABALI ET AL. [2019], BACIGALUPO ET AL. [2018], KHAKALO AND NIIRANEN [2020], LAHBAZI ET AL. [2022], SARAR ET AL. [2023], SCHMIDT ET AL. [2022], SKRZAT AND EREMEYEV [2020], WEEGER [2021], YANG AND MÜLLER [2021], YANG ET AL. [2020; 2022], and the classical Eringen-Mindlin micromorphic continuum in ALAVI ET AL. [2021a], BISWAS AND POH [2017], FOREST [2002], HÜTTER [2017; 2022], ROKOŠ ET AL. [2019; 2020a;b], ZHI ET AL. [2022]. However, in the field of homogenization towards generalized continua, several important queries emerge that have mostly been explored and answered under the standard first-order homogenization theory GANGHOFFER ET AL. [2023], TRINH ET AL. [2012]. Homogenizing into higher-order continua is indeed a challenging task, with the definition of a representative volume element (RVE) and the choice of boundary conditions being the first apparent issues that one faces. The first-order homogenization theory postulates that the condition of continuity of the local fields at the interface of the RVE results in the periodicity requirement of the displacement fluctuation field. It is worth noting that the independence of the effective property on the selected RVE is ensured in first-order homogenization theory as long as we use periodic geometry accompanied by periodic boundary conditions. However, the periodicity requirement becomes less relevant in the absence of scale-separation and an overall strain gradient loading in the framework of higher-order homogenization, see BACIGALUPO AND GAMBAROTTA [2010b]. Consequently, the higher-order moduli are dependent on the choice of the RVE. Alternatively, the analysis can be done on a cluster of unit-cells and considering the converged behavior in the central unit-cell to get rid of boundary layer effects but zero-energy modes for some certain deformation modes are obtained FOREST AND TRINH [2011]. Another crucial issue is that the boundary conditions cannot strictly regulate the average second gradient, and usually, multiple modes are activated simultaneously. Consequently, selecting the relevant higher-order polynomial coefficients becomes very difficult. This can be revised by volumetric constraints JÄNICKE AND STEEB [2012].

In this Chapter, we aim to avoid the yet unanswered questions by utilizing a non-classical homogenization strategy to define the remaining unknown parameters of the relaxed micromorphic model. This optimization strategy is based on the least squares fitting of the energy of the homogeneous relaxed micromorphic continuum with the energy of the fully discretized specimens. It does not need the use of classical (or non-classical) micro-macro transition relations, which are unknown yet for the relaxed micromorphic model. By evaluating various deformation modes, whether random or not, and different specimen sizes, we

identify the unknown parameters of the relaxed micromorphic model. The presented approach circumvents the issues associated with conventional homogenization theory, which are strictly valid when scale-separation holds. Consequently, when size-effect phenomena appear and scale-separation is not well-defined, establishing a representative volume element (RVE) becomes inherently problematic and illogical. We specify the optimization to align with the assumed cubic unit-cell, which is not a limitation for the assumed algorithm, as we precisely know the anisotropy properties of the relaxed micromorphic model. A relevant methodology is outlined in ABALI ET AL. [2019], which selects n deformation modes to determine n unknowns and precisely solves the resulting n equations.

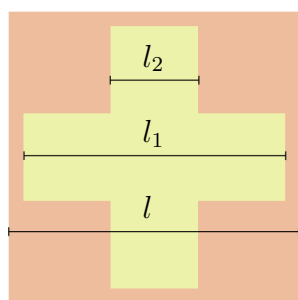
This Chapter follows the outline: In Section 6.1, we introduce the periodic uni-cell and its material parameters. Section 6.2 is devoted to presenting an algorithm that serves as a motivational example and conceptual validation. This algorithm determines the stiffness matrix of an equivalent homogeneous continuum for one unit-cell under both affine Dirichlet and periodic boundary conditions. The algorithm is then further expanded in Section 6.3 to encompass the case of an equivalent relaxed micromorphic homogeneous continuum. In Section 6.4, we conduct a comparison between the fitting results of the relaxed micromorphic model, the Cosserat model and the classical micromorphic model with a simplified curvature and an isotropic curvature. The results are discussed and validated in Section 6.4.

Parts of this Chapter are published in:

M. Sarhil, L. Scheunemann, P. Lewintan, J. Schröder, and P. Neff. A computational approach to identify the material parameters of the relaxed micromorphic model. *Computer Methods in Applied Mechanics and Engineering*, 425, 116944, 2024. doi:10.1016/j.cma.2024.116944

6.1 The unit-cell and the material parameters

We consider a unit-cell consisting of a stiff matrix (aluminum) and a swiss-cross shape ultra-soft inclusion where the Lamé parameters differ by a factor 10000. Both materials are isotropic linear elastic. The parameters and the geometry of the unit-cell are shown in Figure 6.1. We consider n unit-cells in each direction in the computation domain $\mathcal{B} = [-\frac{L}{2}, \frac{L}{2}] \times [-\frac{L}{2}, \frac{L}{2}] = [-\frac{nl}{2}, \frac{nl}{2}] \times [-\frac{nl}{2}, \frac{nl}{2}]$.



Lamé parameters	λ [kN/mm ²]	μ [kN/mm ²]
Matrix	51.08	26.32
Inclusion	$51.08 \cdot 10^{-4}$	$26.32 \cdot 10^{-4}$

l [mm]	l_1 [mm]	l_2 [mm]
$1/n$	$0.9l$	$0.3l$

Figure 6.1: Unit-cell with the material and geometrical parameters. Taken from SARHIL ET AL. [2024].

6.2 Motivation and consistency check for linear elasticity

In this Section, we present the fundamentals of an optimization procedure established on the concept of a least squares fitting of energies for determining the unknown parameters of the effective homogenized continuum. Note that linear elasticity model is assumed here on both microscopic and macroscopic scales.

6.2.1 Affine Dirichlet boundary condition

We employ this approach to first identify the elasticity tensor of an equivalent linear elastic homogeneous medium under affine boundary conditions, as shown in Figure 6.2. Although affine Dirichlet boundary conditions are not typically considered in classical homogenization theory, it is important to note that there exists a unique effective elasticity tensor $\mathbb{C}^{\text{affine}}$ which defines energy equivalence under all affine boundary conditions, however, for a certain unit-cell. It is worth mentioning that this tensor is stiffer than the effective elasticity tensor $\mathbb{C}^{\text{periodic}}$ obtained under periodic boundary conditions, as discussed in Chapter 5. To encompass both cases, we use the generalized notation \mathbb{C}^{hom} since the same algorithm is involved in determining both tensors.

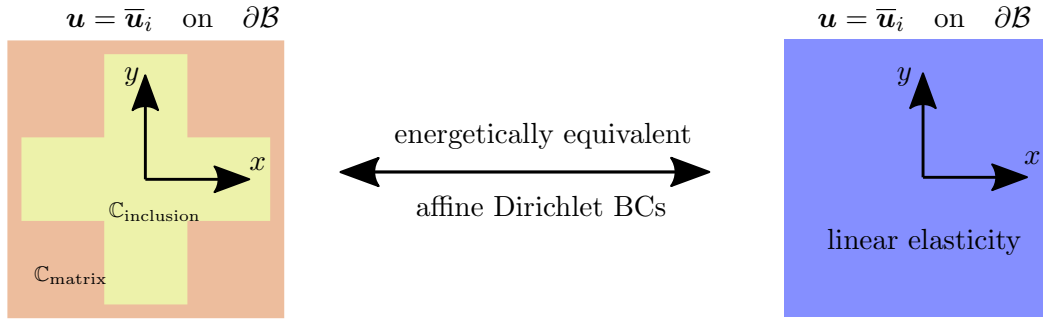


Figure 6.2: Illustration of the homogenization algorithm used to identify the parameters of an equivalent linear elastic medium under affine kinematic boundary condition. Taken from SARHIL ET AL. [2024].

The Hill-Mandel lemma postulates that the strain energies of the heterogeneous and equivalent homogeneous continua are equal. We have the following minimization problem

$$r^2 = \min_{\mathbb{C}^{\text{hom}}} \sum_{i=1}^{i_{\text{max}}} \|\Pi_i^{\text{het}}(\mathbf{u}, \mathbb{C}) - \Pi_i^{\text{hom}}(\mathbf{u}, \mathbb{C}^{\text{hom}})\|^2, \quad (6.1)$$

where i indicates different loading cases induced by affine Dirichlet boundary conditions enforced on the whole boundary ($\bar{\mathbf{u}}_i = \bar{\boldsymbol{\varepsilon}}_i \cdot \mathbf{x}$ on $\partial\mathcal{B}$ with $\bar{\boldsymbol{\varepsilon}}_i \in \text{Sym}(3)$). $\Pi_i^{\text{het}}(\mathbf{u}, \mathbb{C})$ is the total energy of the heterogeneous domain under loading case i while $\Pi_i^{\text{hom}}(\mathbf{u}, \mathbb{C}^{\text{hom}})$ is the total energy of an equivalent linear elastic homogeneous continuum under loading case i . They read

$$\Pi_i^{\text{het}}(\mathbf{u}, \mathbb{C}) = \frac{1}{2} \int_{\mathcal{B}} \boldsymbol{\varepsilon} : \mathbb{C}(\mathbf{x}) : \boldsymbol{\varepsilon} \, dV, \quad \Pi_i^{\text{hom}}(\mathbf{u}, \mathbb{C}^{\text{hom}}) = \frac{1}{2} \int_{\mathcal{B}} \boldsymbol{\varepsilon} : \mathbb{C}^{\text{hom}} : \boldsymbol{\varepsilon} \, dV. \quad (6.2)$$

The stiffness's anisotropy class must be specified in advance. This may require additional considerations and careful choosing of the suitable stiffness's anisotropy class to ensure

the accuracy of the results. We consider an equivalent continuum with a stiffness tensor that holds cubic anisotropy. This aligns with our preference for a cubic unit-cell in Figure 6.1. The stiffness matrix \mathbb{C}^{hom} in Voigt notation reads

$$\tilde{\mathbb{C}}^{\text{hom}} = \begin{bmatrix} 2\mu^{\text{hom}} + \lambda^{\text{hom}} & \lambda^{\text{hom}} & 0 \\ \lambda^{\text{hom}} & 2\mu^{\text{hom}} + \lambda^{\text{hom}} & 0 \\ 0 & 0 & \mu^{*\text{hom}} \end{bmatrix}, \quad (6.3)$$

which is characterized by three independent parameters. The total strain energy of the equivalent homogeneous continuum can be rewritten as

$$\begin{aligned} \Pi_i^{\text{hom}}(\mathbf{u}, \mathbb{C}^{\text{hom}}) &= \frac{1}{2} \int_{\mathcal{B}} \boldsymbol{\varepsilon} : \mathbb{C}^{\text{hom}} : \boldsymbol{\varepsilon} \, dV \\ &= \int_{\mathcal{B}} \mu^{\text{hom}} (\varepsilon_{11}^2 + \varepsilon_{22}^2) + \mu^{*\text{hom}} (2\varepsilon_{12}^2) + \frac{\lambda^{\text{hom}}}{2} (\varepsilon_{11} + \varepsilon_{22})^2 \, dV \\ &= \underbrace{\mu^{\text{hom}} \left(\int_{\mathcal{B}} (\varepsilon_{11}^2 + \varepsilon_{22}^2) \, dV \right)}_{\Pi_{i,\mu}^{\text{hom}}} + \underbrace{\mu^{*\text{hom}} \left(\int_{\mathcal{B}} 2\varepsilon_{12}^2 \, dV \right)}_{\Pi_{i,\mu^*}^{\text{hom}}} \\ &\quad + \underbrace{\lambda^{\text{hom}} \left(\int_{\mathcal{B}} \frac{1}{2} (\varepsilon_{11} + \varepsilon_{22})^2 \, dV \right)}_{\Pi_{i,\lambda}^{\text{hom}}} \\ &= \mu^{\text{hom}} \Pi_{i,\mu}^{\text{hom}} + \mu^{*\text{hom}} \Pi_{i,\mu^*}^{\text{hom}} + \lambda^{\text{hom}} \Pi_{i,\lambda}^{\text{hom}}. \end{aligned} \quad (6.4)$$

The goal of the assumed algorithm is to identify the parameters λ^{hom} , μ^{hom} , and $\mu^{*\text{hom}}$ by solving the minimization problem in Equation (6.1). However, initial values must be appointed to solve the n boundary value problems. Consequently, an iterative procedure is required after setting initial values for the unknown parameters. We then seek the increments $\Delta\lambda^{\text{hom}}$, $\Delta\mu^{\text{hom}}$, and $\Delta\mu^{*\text{hom}}$ such that:

$$\begin{aligned} \Pi_i^{\text{hom}}(\mathbf{u}, \mathbb{C}^{\text{hom}} + \Delta\mathbb{C}^{\text{hom}}) &= (\mu^{\text{hom}} + \Delta\mu^{\text{hom}}) \Pi_{i,\mu}^{\text{hom}} + (\mu^{*\text{hom}} + \Delta\mu^{*\text{hom}}) \Pi_{i,\mu^*}^{\text{hom}} \\ &\quad + (\lambda^{\text{hom}} + \Delta\lambda^{\text{hom}}) \Pi_{i,\lambda}^{\text{hom}} \\ &= \Pi_i^{\text{hom}}(\mathbf{u}, \mathbb{C}^{\text{hom}}) + \Delta\mu^{\text{hom}} \Pi_{i,\mu}^{\text{hom}} + \Delta\mu^{*\text{hom}} \Pi_{i,\mu^*}^{\text{hom}} \\ &\quad + \Delta\lambda^{\text{hom}} \Pi_{i,\lambda}^{\text{hom}}. \end{aligned} \quad (6.5)$$

The total strain energy of the equivalent homogeneous continuum can be written for i_{max} loading cases as

$$\begin{aligned}
\begin{bmatrix} \Pi_1^{\text{hom}}(\mathbf{u}, \mathbb{C}^{\text{hom}} + \Delta \mathbb{C}^{\text{hom}}) \\ \Pi_2^{\text{hom}}(\mathbf{u}, \mathbb{C}^{\text{hom}} + \Delta \mathbb{C}^{\text{hom}}) \\ \vdots \\ \Pi_{i_{\max}}^{\text{hom}}(\mathbf{u}, \mathbb{C}^{\text{hom}} + \Delta \mathbb{C}^{\text{hom}}) \end{bmatrix} &= \underbrace{\begin{bmatrix} \Pi_{1,\mu}^{\text{homo}} & \Pi_{1,\mu^*}^{\text{hom}} & \Pi_{1,\lambda}^{\text{hom}} \\ \Pi_{2,\mu}^{\text{hom}} & \Pi_{2,\mu^*}^{\text{hom}} & \Pi_{2,\lambda}^{\text{hom}} \\ \vdots & \vdots & \vdots \\ \Pi_{i_{\max},\mu}^{\text{hom}} & \Pi_{i_{\max},\mu^*}^{\text{hom}} & \Pi_{i_{\max},\lambda}^{\text{hom}} \end{bmatrix}}_{\mathbf{D}} \underbrace{\begin{bmatrix} \Delta \mu^{\text{hom}} \\ \Delta \mu^{*\text{hom}} \\ \Delta \lambda^{\text{hom}} \end{bmatrix}}_{\Delta \mathbb{C}^{\text{hom}}} \\
&+ \underbrace{\begin{bmatrix} \Pi_1^{\text{hom}}(\mathbf{u}, \mathbb{C}^{\text{hom}}) \\ \Pi_2^{\text{hom}}(\mathbf{u}, \mathbb{C}^{\text{hom}}) \\ \vdots \\ \Pi_{i_{\max}}^{\text{hom}}(\mathbf{u}, \mathbb{C}^{\text{hom}}) \end{bmatrix}}_{\mathbf{b}}.
\end{aligned} \tag{6.6}$$

The minimization problem in Equation (6.1) becomes

$$\begin{aligned}
r^2 &= \min_{\Delta \mathbb{C}^{\text{hom}}} \sum_{i=1}^{i_{\max}} \|\Pi_i^{\text{het}}(\mathbf{u}, \mathbb{C}) \\
&\quad - (\Pi_i^{\text{hom}}(\mathbf{u}, \mathbb{C}^{\text{hom}}) + \Delta \mu^{\text{hom}} \Pi_{i,\mu}^{\text{hom}} + \Delta \mu^{*\text{hom}} \Pi_{i,\mu^*}^{\text{hom}} + \Delta \lambda^{\text{hom}} \Pi_{i,\lambda}^{\text{hom}})\|^2,
\end{aligned} \tag{6.7}$$

and the solution of the least squares problem reads

$$\Delta \mathbb{C}^{\text{hom}} = (\mathbf{D}^T \mathbf{D})^{-1} \mathbf{D}^T (\mathbf{a} - \mathbf{b}) \quad \text{with} \quad a_i = \Pi_i^{\text{het}}(\mathbf{u}, \mathbb{C}), \tag{6.8}$$

where the parameters μ^{hom} , $\mu^{*\text{hom}}$ and λ^{hom} are updated in an iterative procedure until the error r^2 converges to a constant value, optimally zero. The algorithm is presented in Algorithm 1. For this algorithm, a standard T2 finite element with quadratic shape functions is used.

The implemented procedure leads for any $i_{\max} \geq 3$ and single unit-cell ($n = 1$) to the solution $\mu^{\text{hom}} = 6.251 \text{ kN/mm}^2$, $\mu^{*\text{hom}} = 8.337 \text{ kN/mm}^2$ and $\lambda^{\text{hom}} = 4.379 \text{ kN/mm}^2$, see Figure 6.3. This meets the solution of the classical homogenization theory, see NEFF ET AL. [2020], within one iteration, which is expected because the system is linear. The error vanishes, meaning the fitting delivers the unique solution, and the Hill-Mandel condition is precisely fulfilled. Note that choosing three deformation modes ($i_{\max} = 3$) is sufficient when these modes yield three independent equations, such as shearing, stretching along one of the axes and a third mode resulting in a third linearly independent equation.

6.2.2 Periodic boundary condition

In standard homogenization theory, periodic boundary conditions are the choice to define the effective properties. This is based on the scale-separation assumption due to the significant difference in length scales between the macroscopic and microscopic problems. The microscopic strain is decomposed into a constant macroscopic part $\bar{\boldsymbol{\varepsilon}}$ and a fluctuation part $\hat{\boldsymbol{\varepsilon}}$ as

```

begin
  production of the reference data (heterogeneous material)
  - inputs: the unit-cell geometry with the material parameters of the matrix
    and inclusion
  - define  $i_{\max}$  affine deformation modes  $\bar{\boldsymbol{\varepsilon}}_i$  for  $i = 1, \dots, i_{\max}$ 
  - if affine boundary conditions then  $\mathbf{u} = \bar{\mathbf{u}} = \bar{\boldsymbol{\varepsilon}}_i \cdot \mathbf{x}$  on  $\partial\mathcal{B}$ 
  - if periodic boundary conditions then  $\bar{\mathbf{u}} = \bar{\boldsymbol{\varepsilon}}_i \cdot \mathbf{x}$  on  $\mathcal{B}$ 
  - solve  $i_{\max}$  boundary value problems of the heterogeneous material
  - calculate the vector  $\mathbf{a}^T = [\Pi_1^{\text{het}}, \Pi_2^{\text{het}}, \dots, \Pi_{i_{\max}}^{\text{het}}]$ 

  defining the unknown (homogeneous material)
  - set initial values for the parameters  $\lambda^{\text{hom}}, \mu^{\text{hom}}, \mu^{*\text{hom}}$ 
  repeat
    - apply the deformation modes ( $\bar{\boldsymbol{\varepsilon}}_i$  for  $i = 1, \dots, i_{\max}$ )
    - if affine boundary conditions then  $\mathbf{u} = \bar{\mathbf{u}} = \bar{\boldsymbol{\varepsilon}}_i \cdot \mathbf{x}$  on  $\partial\mathcal{B}$ 
    - if periodic boundary conditions then  $\bar{\mathbf{u}} = \bar{\boldsymbol{\varepsilon}}_i \cdot \mathbf{x}$  on  $\mathcal{B}$ 
    - solve  $i_{\max}$  boundary value problems of the equivalent homogeneous
      medium (for affine BCs, we solve the total displacement field while for
      periodic BCs, we solve the fluctuation part)
    - calculate the vector  $\mathbf{b}^T = [\Pi_1^{\text{hom}}, \Pi_2^{\text{hom}}, \dots, \Pi_{i_{\max}}^{\text{hom}}]$ 
    - calculate the derivative matrix  $\mathbf{D}$ ; ( $\mathbf{D}_i$ : row vectors)

      
$$\mathbf{D}_i^T = [\Pi_{i,\mu}^{\text{hom}}, \Pi_{i,\mu^*}^{\text{hom}}, \Pi_{i,\lambda}^{\text{hom}}] \quad \text{for } i = 1, \dots, i_{\max}$$


    - solve:

      
$$[\Delta\mu^{\text{hom}}, \Delta\mu^{*\text{hom}}, \Delta\lambda^{\text{hom}}]^T = (\mathbf{D}^T \mathbf{D})^{-1} \mathbf{D}^T (\mathbf{a} - \mathbf{b})$$


    -update:

      
$$\begin{aligned} \mu^{\text{hom}} &\leftarrow \mu^{\text{hom}} + \Delta\mu^{\text{hom}}, \\ \mu^{*\text{hom}} &\leftarrow \mu^{*\text{hom}} + \Delta\mu^{*\text{hom}}, \\ \lambda^{\text{hom}} &\leftarrow \lambda^{\text{hom}} + \Delta\lambda^{\text{hom}} \end{aligned}$$


    - calculate the current error  $r^2$ 
  until  $r^2 < \text{tol}$ 
  - The parameters  $\mu^{\text{hom}}, \mu^{*\text{hom}}, \lambda^{\text{hom}}$  are known
end

```

Algorithm 1: Algorithm for the minimization problem for an equivalent homogeneous linear elastic continuum. Taken from SARHIL ET AL. [2024].

We consider four random modes $i_{\max} = 4$ applied on a unit-cell $n = 1$

$$\bar{\varepsilon}_1 = \begin{pmatrix} -0.02 & 0.03 \\ 0.03 & 0.01 \end{pmatrix}, \bar{\varepsilon}_2 = \begin{pmatrix} 0.03 & -0.01 \\ -0.01 & 0.05 \end{pmatrix},$$

$$\bar{\varepsilon}_3 = \begin{pmatrix} 0.01 & 0.01 \\ 0.01 & -0.01 \end{pmatrix}, \bar{\varepsilon}_4 = \begin{pmatrix} 0.01 & 0 \\ 0 & 0.02 \end{pmatrix}.$$

set initial values:

$$\mu^{\text{hom}} = 26.32 \text{ kN/mm}^2, \mu^{*\text{hom}} = 26.32 \text{ kN/mm}^2 \text{ and } \lambda^{\text{hom}} = 51.08 \text{ kN/mm}^2.$$

The algorithm delivers:

iteration	μ^{hom} [kN/mm ²]	$\mu^{*\text{hom}}$ [kN/mm ²]	λ^{hom} [kN/mm ²]	r^2 [(kN·mm) ²]
0	26.32	26.32	51.08	0.05198
1	6.251	8.337	4.379	$2.374 \cdot 10^{-26}$
2	6.251	8.337	4.379	$1.105 \cdot 10^{-28}$

final result:

$$\mu^{\text{hom}} = 6.251 \text{ kN/mm}^2, \mu^{*\text{hom}} = 8.337 \text{ kN/mm}^2 \text{ and } \lambda^{\text{hom}} = 4.379 \text{ kN/mm}^2.$$

Figure 6.3: Results of the parameter identification algorithm for an equivalent linear elasticity continuum under affine boundary conditions. Taken from SARHIL ET AL. [2024].

$$\boldsymbol{\varepsilon} = \bar{\boldsymbol{\varepsilon}} + \hat{\boldsymbol{\varepsilon}} \quad \text{and} \quad \mathbf{u} = \bar{\mathbf{u}} + \hat{\mathbf{u}} = \bar{\boldsymbol{\varepsilon}} \cdot \mathbf{x} + \hat{\mathbf{u}}. \quad (6.9)$$

The partial derivatives of the total energy of the homogeneous equivalent continuum with respect to the unknown material parameters are computed, taking into consideration that the integral of the fluctuation part of strain over the domain equals zero, i.e. $\int_B \hat{\boldsymbol{\varepsilon}} \, dV = \mathbf{0}$,

$$\begin{aligned} \Pi_{i,\mu}^{\text{hom}} &= \int_B (\varepsilon_{11}^2 + \varepsilon_{22}^2) \, dV \\ &= V_B (\bar{\varepsilon}_{11}^2 + \bar{\varepsilon}_{22}^2) + \underbrace{\int_B 2(\bar{\varepsilon}_{11}\hat{\varepsilon}_{11} + \bar{\varepsilon}_{22}\hat{\varepsilon}_{22}) \, dV}_{=0} + \int_B (\hat{\varepsilon}_{11}^2 + \hat{\varepsilon}_{22}^2) \, dV, \\ \Pi_{i,\mu^*}^{\text{hom}} &= \int_B 2\varepsilon_{12}^2 \, dV = 2V_B \bar{\varepsilon}_{12}^2 + \underbrace{\int_B 4\bar{\varepsilon}_{12}\hat{\varepsilon}_{12} \, dV}_{=0} + \int_B 2\hat{\varepsilon}_{12}^2 \, dV. \\ \Pi_{i,\lambda}^{\text{hom}} &= \int_B \frac{1}{2}(\varepsilon_{11} + \varepsilon_{22})^2 \, dV \\ &= \frac{V_B}{2}(\bar{\varepsilon}_{11} + \bar{\varepsilon}_{22})^2 + \underbrace{\int_B (\bar{\varepsilon}_{11} + \bar{\varepsilon}_{22})(\hat{\varepsilon}_{11} + \hat{\varepsilon}_{22}) \, dV}_{=0} + \int_B \frac{1}{2}(\hat{\varepsilon}_{11} + \hat{\varepsilon}_{22})^2 \, dV, \end{aligned} \quad (6.10)$$

The boundary $\partial\mathcal{B}$ is divided into two parts (“+”, “-”) which satisfies $\partial\mathcal{B} = \partial\mathcal{B}^+ \cup \partial\mathcal{B}^-$ with outward unit normals \mathbf{n}^- and \mathbf{n}^+ satisfying $\mathbf{n}^- = -\mathbf{n}^+$ and the periodicity condition is postulated as

$$\hat{\mathbf{u}}(\mathbf{x}^+) = \hat{\mathbf{u}}(\mathbf{x}^-), \quad (6.11)$$

which is depicted in Figure 6.4. The algorithm is identical to the one for affine Dirichlet boundary conditions shown in Algorithm 1, but the i_{max} deformation modes are enforced on the body, i.e. $\bar{\mathbf{u}} = \bar{\boldsymbol{\varepsilon}} \cdot \mathbf{x}$ on \mathcal{B} . For this, we implement a standard T2 finite element, which discretizes the fluctuation field.

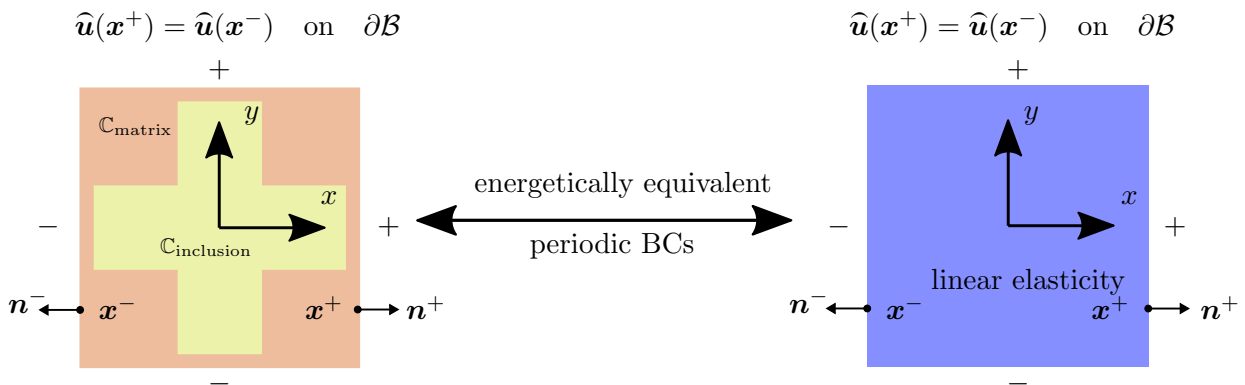


Figure 6.4: Periodicity condition of the fluctuation field is enforced on both heterogeneous and homogeneous equivalent continua. Taken from SARHIL ET AL. [2024].

The results of the implemented algorithm are shown in Figure 6.5. For any choice of three deformation modes or more $i_{\text{max}} \geq 3$, we get the exact solution in one it-

eration which reads $\mu^{\text{hom}} = 5.9 \text{ kN/mm}^2$, $\mu^{*\text{hom}} = 0.627 \text{ kN/mm}^2$ and $\lambda^{\text{hom}} = 1.748 \text{ kN/mm}^2$. This meets the solution of classical homogenization theory in NEFF ET AL. [2020], SARHIL ET AL. [2023b]. Like the case of affine boundary conditions, three deformation modes are sufficient when they deliver three linearly independent equations. The result of this analysis serves as the limit case for the relaxed micromorphic model for very large specimens $n \rightarrow \infty$, i.e. linear elasticity with elasticity tensor $\mathbb{C}_{\text{macro}}$. Enforcing vanishing fluctuations on the boundary restores the same results of the affine Dirichlet boundary condition.

We consider four random modes $i_{\text{max}} = 4$ applied on a unit-cell $n = 1$

$$\bar{\varepsilon}_1 = \begin{pmatrix} -0.02 & 0.03 \\ 0.03 & 0.01 \end{pmatrix}, \bar{\varepsilon}_2 = \begin{pmatrix} 0.03 & -0.01 \\ -0.01 & 0.05 \end{pmatrix},$$

$$\bar{\varepsilon}_3 = \begin{pmatrix} 0.01 & 0.01 \\ 0.01 & -0.01 \end{pmatrix}, \bar{\varepsilon}_4 = \begin{pmatrix} 0.01 & 0 \\ 0 & 0.02 \end{pmatrix}$$

set initial values:

$$\mu^{\text{hom}} = 26.32 \text{ kN/mm}^2, \mu^{*\text{hom}} = 26.32 \text{ kN/mm}^2 \text{ and } \lambda^{\text{hom}} = 51.08 \text{ kN/mm}^2.$$

The algorithm delivers:

iteration	μ^{hom} [kN/mm ²]	$\mu^{*\text{hom}}$ [kN/mm ²]	λ^{hom} [kN/mm ²]	r^2 [(kN·mm) ²]
0	26.32	26.32	51.08	0.05863
1	5.9	0.627	1.748	$1.275 \cdot 10^{-27}$
2	5.9	0.627	1.748	$2.353 \cdot 10^{-31}$

final result:

$$\mu^{\text{hom}} = 5.9 \text{ kN/mm}^2, \mu^{*\text{hom}} = 0.627 \text{ kN/mm}^2 \text{ and } \lambda^{\text{hom}} = 1.748 \text{ kN/mm}^2 .$$

Figure 6.5: Results of the parameter identification algorithm for an equivalent linear elasticity continuum under periodic boundary conditions. Taken from SARHIL ET AL. [2024].

6.3 Computational approach to identify the material parameters for RMM

In order to build a relation between the heterogeneous fully-detailed metamaterial and the homogeneous relaxed micromorphic continuum, we handle the size-effect by incorporating the number of considered unit-cells within the computational domain of the reference heterogeneous material with assuming $\mathbb{L} = \mathbb{II}$ (2D case), see Equation (5.22). Thus, the elastic energy density of the relaxed micromorphic in Equation (3.13) becomes

$$\begin{aligned}
\psi(\nabla \mathbf{u}, \mathbf{P}, \text{Curl } \mathbf{P}) = & \frac{1}{2}(\text{sym}[\nabla \mathbf{u} - \mathbf{P}] : \mathbb{C}_e : \text{sym}[\nabla \mathbf{u} - \mathbf{P}] \\
& + \text{sym } \mathbf{P} : \mathbb{C}_{\text{micro}} : \text{sym } \mathbf{P} \\
& + \text{skew}[\nabla \mathbf{u} - \mathbf{P}] : \mathbb{C}_c : \text{skew}[\nabla \mathbf{u} - \mathbf{P}] \\
& + \mu \left(\frac{L_c}{n}\right)^2 \text{Curl } \mathbf{P} : \text{Curl } \mathbf{P}).
\end{aligned} \tag{6.12}$$

The scalar n has been introduced representing the number of the unit-cells in the computational domain $\mathcal{B} = [-\frac{L}{2}, \frac{L}{2}] \times [-\frac{L}{2}, \frac{L}{2}] = [-\frac{nl}{2}, \frac{nl}{2}] \times [-\frac{nl}{2}, \frac{nl}{2}]$ as illustrated in Figure 6.6. The characteristic length parameter L_c is fixed then for any considered size.

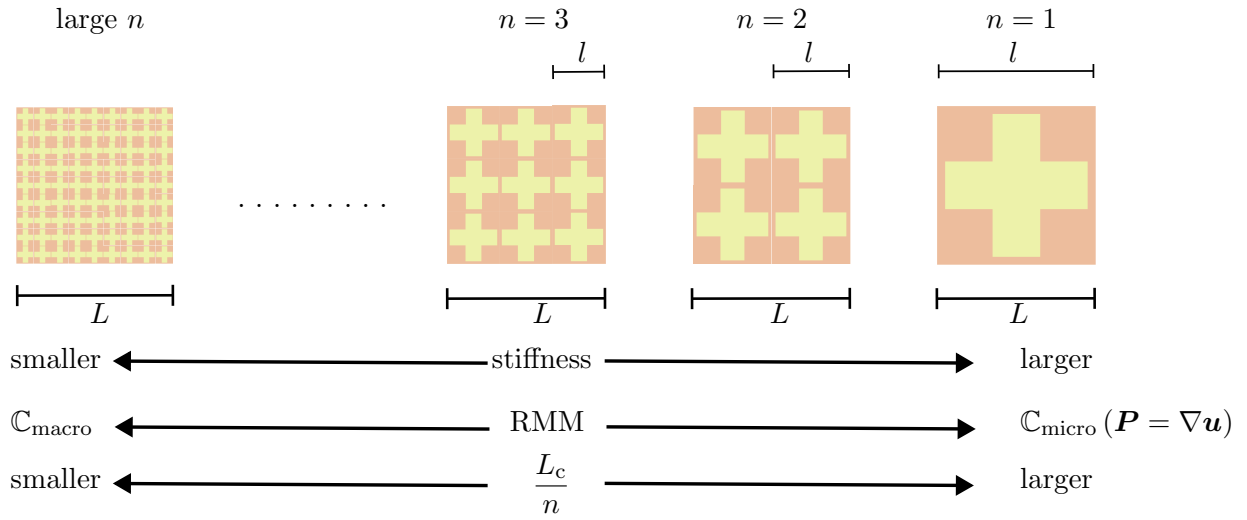


Figure 6.6: Illustration of the scaling L_c/n delivering the intended “smaller is stiffer” effect for computations on a domain of fixed size and constant L_c . Taken from SARHIL ET AL. [2024].

The macroscopic elasticity tensor $\mathbb{C}_{\text{macro}}$ corresponds to large specimens $n \rightarrow \infty$, where a unit-cell with periodic boundary conditions should be used as in our analysis in Section 6.2.2. The macroscopic elasticity tensor $\mathbb{C}_{\text{macro}}$ exhibits cubic symmetry with three independent parameters, and reads

$$\begin{aligned}
\tilde{\mathbb{C}}_{\text{macro}} = & \begin{bmatrix} 2\mu_{\text{macro}} + \lambda_{\text{macro}} & \lambda_{\text{macro}} & 0 \\ \lambda_{\text{macro}} & 2\mu_{\text{macro}} + \lambda_{\text{macro}} & 0 \\ 0 & 0 & \mu_{\text{macro}}^* \end{bmatrix}, \quad \text{with} \\
\lambda_{\text{macro}} = & 1.748 \text{ kN/mm}^2, \quad \mu_{\text{macro}} = 5.9 \text{ kN/mm}^2, \quad \mu_{\text{macro}}^* = 0.627 \text{ kN/mm}^2.
\end{aligned} \tag{6.13}$$

The stiffness tensors \mathbb{C}_e and $\mathbb{C}_{\text{micro}}$ should contain the maximal invariance group of the periodic microstructure (i.e. $\mathbb{C}_{\text{macro}}$) following the extended Neumann’s principle in NEFF ET AL. [2020]. Thus, we have

$$\begin{aligned}\tilde{\mathbb{C}}_{\text{micro}} &= \begin{bmatrix} 2\mu_{\text{micro}} + \lambda_{\text{micro}} & \lambda_{\text{micro}} & 0 \\ \lambda_{\text{micro}} & 2\mu_{\text{micro}} + \lambda_{\text{micro}} & 0 \\ 0 & 0 & \mu_{\text{micro}}^* \end{bmatrix}, \\ \tilde{\mathbb{C}}_{\text{e}} &= \begin{bmatrix} 2\mu_{\text{e}} + \lambda_{\text{e}} & \lambda_{\text{e}} & 0 \\ \lambda_{\text{e}} & 2\mu_{\text{e}} + \lambda_{\text{e}} & 0 \\ 0 & 0 & \mu_{\text{e}}^* \end{bmatrix},\end{aligned}\quad (6.14)$$

and the elastic energy density assuming symmetric force stress $\mathbb{C}_c = \mathbf{0}$ becomes

$$\begin{aligned}\psi(\nabla \mathbf{u}, \mathbf{P}, \text{Curl } \mathbf{P}) &= \mu_{\text{e}} \left((u_{1,1} - P_{11})^2 + (u_{2,2} - P_{22})^2 \right) \\ &\quad + \frac{\mu_{\text{e}}^*}{2} (u_{1,2} + u_{2,1} - P_{12} - P_{21})^2 \\ &\quad + \frac{\lambda_{\text{e}}}{2} (u_{1,1} + u_{2,2} - P_{11} - P_{22})^2 + \mu_{\text{micro}} (P_{11}^2 + P_{22}^2) \\ &\quad + \frac{\mu_{\text{micro}}^*}{2} (P_{12} + P_{21})^2 + \frac{\lambda_{\text{micro}}}{2} (P_{11} + P_{22})^2 \\ &\quad + \frac{\mu L_c^2}{2n^2} \left((\text{Curl } \mathbf{P})_{13}^2 + (\text{Curl } \mathbf{P})_{23}^2 \right).\end{aligned}\quad (6.15)$$

Note that assuming $\mathbb{C}_c = \mathbf{0}$ is a valid option, when the consistent boundary condition is used which we demonstrated in Chapter 5. The Reuss-like homogenization relation in Equation (3.15) taking into consideration the relations in Equation (6.14) leads to

$$\begin{aligned}\mu_{\text{e}} &= \frac{\mu_{\text{micro}} \mu_{\text{macro}}}{\mu_{\text{micro}} - \mu_{\text{macro}}}, & \mu_{\text{e}}^* &= \frac{\mu_{\text{micro}}^* \mu_{\text{macro}}^*}{\mu_{\text{micro}}^* - \mu_{\text{macro}}^*}, \\ \lambda_{\text{e}} + \mu_{\text{e}} &= \frac{(\lambda_{\text{micro}} + \mu_{\text{micro}})(\lambda_{\text{macro}} + \mu_{\text{macro}})}{(\lambda_{\text{micro}} + \mu_{\text{micro}}) - (\lambda_{\text{macro}} + \mu_{\text{macro}})}.\end{aligned}\quad (6.16)$$

The current problem depicted in Figure 6.7 can be expressed by least squares fitting of energies of the reference heterogeneous solution and the homogenous relaxed micromorphic model solution

$$r^2 = \min_{\mu_{\text{micro}}, \mu_{\text{micro}}^*, \lambda_{\text{micro}}, \mu L_c^2} \sum_{n=1}^{n_{\text{max}}} \sum_{i=1}^{i_{\text{max}}} \|\Pi_{i \times n}^{\text{het}}(\mathbf{u}) - \Pi_{i \times n}(\mathbf{u}, \mathbf{P})\|^2, \quad (6.17)$$

with $i = 1, \dots, i_{\text{max}}$ loading cases on $n \times n$ unit-cells for $n = 1, \dots, n_{\text{max}}$. Consequently, $j_{\text{max}} = i_{\text{max}} n_{\text{max}}$ reference solutions need to be obtained for the heterogeneous material.

To solve the minimization problem in Equation (6.17), we define the following derivatives

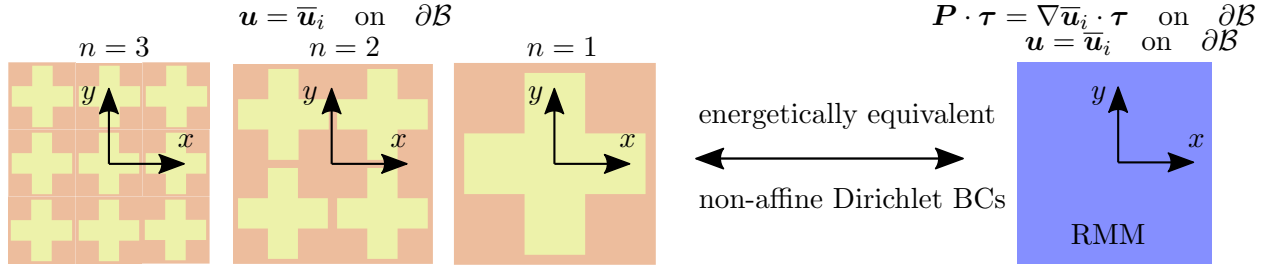


Figure 6.7: Illustration of the minimization problem to obtain the material parameters in the RMM. The consistent coupling condition is enforced on the whole boundary. Taken from SARHIL ET AL. [2024].

$$\begin{aligned}
 \Pi_{i \times n, \mu_{\text{micro}}} &= \frac{\partial \Pi_{i \times n}}{\partial \mu_{\text{micro}}} = \int_{\mathcal{B}} \frac{\partial \psi}{\partial \mu_{\text{micro}}} dV, \\
 \Pi_{i \times n, \mu_{\text{micro}}^*} &= \frac{\partial \Pi_{i \times n}}{\partial \mu_{\text{micro}}^*} = \int_{\mathcal{B}} \frac{\partial \psi}{\partial \mu_{\text{micro}}^*} dV, \\
 \Pi_{i \times n, \lambda_{\text{micro}}} &= \frac{\partial \Pi_{i \times n}}{\partial \lambda_{\text{micro}}} = \int_{\mathcal{B}} \frac{\partial \psi}{\partial \lambda_{\text{micro}}} dV, \\
 \Pi_{i \times n, \mu L_c^2} &= \frac{\partial \Pi_{i \times n}}{\partial \mu L_c^2} = \int_{\mathcal{B}} \frac{\partial \psi}{\partial \mu L_c^2} dV,
 \end{aligned} \tag{6.18}$$

which cannot be evaluated analytically. Therefore, they will be determined numerically by a finite difference scheme as

$$\frac{\partial \Pi}{\partial \bullet} = \frac{\Pi(\bullet + \epsilon) - \Pi(\bullet)}{\epsilon} \tag{6.19}$$

where the scalar ϵ has to be small. The minimization problem in Equation (6.17) can be expressed instead in terms of the increments of the unknown quantities and we get

$$\begin{aligned}
 r^2 = \min_{\Delta \mu_{\text{micro}}, \Delta \mu_{\text{micro}}^*, \Delta \lambda_{\text{micro}}, \Delta \mu L_c^2} & \sum_{n=1}^{n_{\text{max}}} \sum_{i=1}^{i_{\text{max}}} \left\| \Pi_{i \times n}^{\text{het}} - \left(\Pi_{i \times n} + \frac{\partial \Pi_{i \times n}}{\partial \mu_{\text{micro}}} \Delta \mu_{\text{micro}} \right. \right. \\
 & \left. \left. + \frac{\partial \Pi_{i \times n}}{\partial \mu_{\text{micro}}^*} \Delta \mu_{\text{micro}}^* + \frac{\partial \Pi_{i \times n}}{\partial \lambda_{\text{micro}}} \Delta \lambda_{\text{micro}} + \frac{\partial \Pi_{i \times n}}{\partial \mu L_c^2} \Delta \mu L_c^2 \right) \right\|^2.
 \end{aligned} \tag{6.20}$$

Hence, we obtain an optimization problem where the unknowns have to be updated in an iterative procedure. In the following, we execute a line search algorithm to ensure that the unknowns do not violate some constraints, which we introduce later. The solution of the minimization problem at the current position $(\mu_{\text{micro}}, \mu_{\text{micro}}^*, \lambda_{\text{micro}}, \mu L_c^2)$ leads to the following vector

$$\mathbf{\Lambda} = (\mathbf{D}^T \mathbf{D})^{-1} \mathbf{D}^T (\mathbf{a} - \mathbf{b}), \tag{6.21}$$

with

$$\mathbf{a} = \begin{bmatrix} \Pi_{1 \times 1}^{\text{het}} \\ \Pi_{1 \times 2}^{\text{het}} \\ \cdot \\ \cdot \\ \Pi_{i_{\max} \times n_{\max}}^{\text{het}} \end{bmatrix}, \quad \mathbf{b} = \begin{bmatrix} \Pi_{1 \times 1} \\ \Pi_{1 \times 2} \\ \cdot \\ \cdot \\ \Pi_{i_{\max} \times n_{\max}} \end{bmatrix}, \quad \mathbf{\Lambda} = \begin{bmatrix} \Delta \mu_{\text{micro}} \\ \Delta \mu_{\text{micro}}^* \\ \Delta \lambda_{\text{micro}} \\ \Delta \mu L_c^2 \end{bmatrix}, \quad (6.22)$$

and

$$\mathbf{D} = \begin{bmatrix} \mathbf{D}_{1 \times 1}^T \\ \mathbf{D}_{1 \times 2}^T \\ \cdot \\ \cdot \\ \mathbf{D}_{i_{\max} \times n_{\max}}^T \end{bmatrix} = \begin{bmatrix} \frac{\partial \Pi_{1 \times 1}}{\partial \mu_{\text{micro}}} & \frac{\partial \Pi_{1 \times 1}}{\partial \mu_{\text{micro}}^*} & \frac{\partial \Pi_{1 \times 1}}{\partial \lambda_{\text{micro}}} & \frac{\partial \Pi_{1 \times 1}}{\partial \mu L_c^2} \\ \frac{\partial \Pi_{1 \times 2}}{\partial \mu_{\text{micro}}} & \frac{\partial \Pi_{1 \times 2}}{\partial \mu_{\text{micro}}^*} & \frac{\partial \Pi_{1 \times 2}}{\partial \lambda_{\text{micro}}} & \frac{\partial \Pi_{1 \times 2}}{\partial \mu L_c^2} \\ \cdot & \cdot & \cdot & \cdot \\ \cdot & \cdot & \cdot & \cdot \\ \frac{\partial \Pi_{i_{\max} \times n_{\max}}}{\partial \mu_{\text{micro}}} & \frac{\partial \Pi_{i_{\max} \times n_{\max}}}{\partial \mu_{\text{micro}}^*} & \frac{\partial \Pi_{i_{\max} \times n_{\max}}}{\partial \lambda_{\text{micro}}} & \frac{\partial \Pi_{i_{\max} \times n_{\max}}}{\partial \mu L_c^2} \end{bmatrix}, \quad (6.23)$$

where the vector $\mathbf{\Lambda}$ represents a preferred direction at the current position. The new position has to be updated as

$$\begin{bmatrix} \mu_{\text{micro}} \\ \mu_{\text{micro}}^* \\ \lambda_{\text{micro}} \\ \mu L_c^2 \end{bmatrix}_{\text{new}} = \begin{bmatrix} \mu_{\text{micro}} \\ \mu_{\text{micro}}^* \\ \lambda_{\text{micro}} \\ \mu L_c^2 \end{bmatrix} + \beta \mathbf{\Lambda} \quad (6.24)$$

where β is the distance along the direction $\mathbf{\Lambda}$. An exact strategy can be implemented to optimize the identification of β with the criterion

$$r^2 = \min_{\beta} \sum_{n=1}^{n_{\max}} \sum_{i=1}^{i_{\max}} \left\| \Pi_{i \times n}^{\text{het}} - \Pi_{i \times n}(\mu_{\text{micro}} + \beta \Lambda_1, \mu_{\text{micro}}^* + \beta \Lambda_2, \lambda_{\text{micro}} + \beta \Lambda_3, \mu L_c^2 + \beta \Lambda_4) \right\|^2. \quad (6.25)$$

The quantity $\mathbb{C}_{\text{micro}} - \mathbb{C}_{\text{macro}}$ must be positive definite to keep \mathbb{C}_e positive definite, see Equation (3.15), and therefore $\mathbb{C}_{\text{micro}}$ must be stiffer than $\mathbb{C}_{\text{macro}}$. Moreover, L_c must be strictly positive which yields then a maximum distance β_{\max} along the preferred direction which satisfies

$$\begin{aligned} \mu_{\text{micro}} + \beta_{\max} \Lambda_1 &> \mu_{\text{macro}}, \\ \mu_{\text{micro}}^* + \beta_{\max} \Lambda_2 &> \mu_{\text{macro}}^*, \\ \lambda_{\text{micro}} + \beta_{\max} \Lambda_3 + \mu_{\text{micro}} + \beta_{\max} \Lambda_1 &> \lambda_{\text{macro}} + \mu_{\text{macro}}, \\ \mu L_c^2 + \beta_{\max} \Lambda_4 &> 0. \end{aligned} \quad (6.26)$$

For our implementation, inexact identification of β is implemented seeking simplicity by evaluating the function at multiple points in the domain $\beta \in [0, \min(1, \beta_{\max})]$ along the preferred direction $\mathbf{\Lambda}$ and we choose the one with the least error r^2 .

The selection of the boundary conditions plays an essential role in the homogenization theory. We choose Dirichlet boundary conditions that encompass both affine and non-affine parts on the entire boundary

$$\bar{\mathbf{u}}_i = \mathbf{B}_i \cdot \mathbf{x} + \mathbf{C}_i \cdot \mathbf{x} \otimes \mathbf{x} \quad \text{on} \quad \partial\mathcal{B} \quad (6.27)$$

with

$$\mathbf{B}_i = \begin{bmatrix} (B_i)_{11} & (B_i)_{12} \\ (B_i)_{21} & (B_i)_{22} \end{bmatrix} \quad \text{with} \quad (B_i)_{jk} = \text{random}[-0.05, 0.05] \quad (6.28)$$

and

$$\mathbf{C}_i \cdot \mathbf{x} \otimes \mathbf{x} = \begin{bmatrix} (C_i)_{111} & (C_i)_{112} & (C_i)_{122} \\ (C_i)_{211} & (C_i)_{212} & (C_i)_{222} \end{bmatrix} \begin{bmatrix} x^2 \\ xy \\ y^2 \end{bmatrix} \quad \text{with} \quad (C_i)_{jkl} = \text{random}[-0.05, 0.05]. \quad (6.29)$$

Incorporating non-affine boundary conditions is anticipated, in analogy to the theories of higher-order homogenization. Nevertheless, size-effects have been reported for both affine and non-affine loading. The implemented algorithm can be seen in Algorithm 2 which is searching for an optimized quantity μL_c^2 associated with the curvature. To represent the order of L_c with respect to the size of the unit-cell, we give a definition for the shear modulus μ by using the isotropic elastic moduli closest to the cubic macroscopic moduli $\mathbb{C}_{\text{macro}}$ for the log-Euclidean norm NORRIS [2006]. This definition is unique and independent of whether the difference in stiffness or compliance is considered. The isotropic equivalent shear modulus reads

$$\mu = \sqrt[5]{(\mu_{\text{macro}})^2 (\mu_{\text{macro}}^*)^3} = 1.537 \text{ kN/mm}^2. \quad (6.30)$$

The results of the implemented algorithm for the parameter identification of the RMM are shown in Figure 6.8. We employ 40 randomly generated deformation modes across three distinct sizes. Consequently, we solve 120 boundary value problems for the heterogeneous case before initiating the least squares optimization procedure.

The implemented optimization algorithm reaches the intended purpose, resulting in a final error much less than the error of the given initial values. However, μ_{micro}^* tends towards very large values which do not fit a classical shear modulus. Thus, we need to introduce the concept of the stiffest possible response: the microscopic elasticity tensor cannot yield a stiffer response than the homogeneous stiff matrix for any loading scenario. The stiffest possible response concept stems from the relaxed micromorphic model operating between two scales, both governed by linear elasticity with standard elasticity tensor.

The concept of the stiffest possible response ensures the preservation of the physical interpretation of the upper bound, which cannot be logically stiffer than the stiff matrix, at least from an engineering point of view. While the microscopic elasticity tensor $\mathbb{C}_{\text{micro}}$ also exists in the classical micromorphic models, it lacks an associated bound. Thus, the microscopic elasticity tensor in the classical micromorphic continuum is not reflected in a microscopic scale (linear elasticity with elasticity tensor $\mathbb{C}_{\text{micro}}$). Setting $\mathbb{C}_{\text{micro}}$ to infinity aligns with the assumption of an infinitely rigid microstructure that can only rotate (Cosserat model), which is a very unrealistic simplification. The goal of the stiffest response constraint, likely resulting in a poorer fit, is to preserve a physical interpretation of

begin

production of the reference data (*heterogeneous material*)

- define n_{\max} deformation modes ($i = 1, \dots, i_{\max}$) applied on the boundary

$$\bar{\mathbf{u}}_i = \mathbf{B}_i \cdot \mathbf{x} + \mathbf{C}_i \cdot \mathbf{x} \otimes \mathbf{x} \quad \text{on} \quad \partial\mathcal{B}$$

- define number of cluster sizes considered in analysis with $n \times n$ unit-cells;
 $n = 1, \dots, n_{\max}$
- solve $j_{\max} = i_{\max} n_{\max}$ boundary value problems of the heterogeneous material
- calculate the vector $\mathbf{a}^T = [\Pi_{1 \times 1}^{\text{het}}, \Pi_{1 \times 2}^{\text{het}}, \dots, \Pi_{i_{\max} \times n_{\max}}^{\text{het}}]$

defining the unknown (*homogeneous relaxed micromorphic continuum*)

- give initial values for the parameters $\mu_{\text{micro}}, \mu_{\text{micro}}^*, \lambda_{\text{micro}}, \mu L_c^2$

repeat

- apply the deformation modes on the boundary
($\bar{\mathbf{u}}_i = \mathbf{B}_i \cdot \mathbf{x} + \mathbf{C}_i \cdot \mathbf{x} \otimes \mathbf{x}$ on $\partial\mathcal{B}$)
- calculate the vector $\mathbf{b}^T = [\Pi_{1 \times 1}, \Pi_{1 \times 2}, \dots, \Pi_{i_{\max} \times n_{\max}}]$
- calculate the matrix \mathbf{D} ; row vectors read

$$\mathbf{D}_{i \times n}^T = \left[\frac{\partial \Pi_{i \times n}}{\partial \mu_{\text{micro}}}, \frac{\partial \Pi_{i \times n}}{\partial \mu_{\text{micro}}^*}, \frac{\partial \Pi_{i \times n}}{\partial \lambda_{\text{micro}}}, \frac{\partial \Pi_{i \times n}}{\partial \mu L_c^2} \right]$$

- solve:

$$\mathbf{\Lambda} = (\mathbf{D}^T \mathbf{D})^{-1} \mathbf{D}^T (\mathbf{a} - \mathbf{b})$$

- define $\beta_{\max} \leq 1$ which keeps \mathbb{C}_e positive definite and L_c positive
- try multiple values of $\beta = \left\{ \frac{1}{512}, \frac{1}{256}, \frac{1}{128}, \frac{1}{64}, \frac{1}{32}, \frac{1}{8}, \frac{1}{4}, \frac{1}{2}, 1 \right\} \beta_{\max}$
- choose β which delivers the least error r^2 along the direction $\mathbf{\Lambda}$
- update:

$$\mu_{\text{micro}} \leftarrow \mu_{\text{micro}} + \beta \Lambda_1, \quad \mu_{\text{micro}}^* \leftarrow \mu_{\text{micro}}^* + \beta \Lambda_2$$

$$\lambda_{\text{micro}} \leftarrow \lambda_{\text{micro}} + \beta \Lambda_3, \quad \mu L_c^2 \leftarrow \mu L_c^2 + \beta \Lambda_4$$

- calculate the current error r_{new}^2 to compare with the one from last iteration r_{old}^2

until $\frac{r_{\text{old}}^2 - r_{\text{new}}^2}{r_{\text{old}}^2} < \text{tol}$

- the parameters $\mu_{\text{micro}}, \mu_{\text{micro}}^*, \lambda_{\text{micro}}, \mu L_c^2$ are known

end

Algorithm 2: Algorithm for the optimization procedure of parameter identification of the relaxed micromorphic model. Taken from SARHIL ET AL. [2024].

We consider forty random modes $i_{\max} = 40$ applied on three sizes $n_{\max} = 3$

$$\bar{\mathbf{u}}_i = \mathbf{B}_i \cdot \mathbf{x} + \mathbf{C}_i \cdot \mathbf{x} \otimes \mathbf{x} \quad \text{on} \quad \partial\mathcal{B}$$

components of \mathbf{B}_i and \mathbf{C}_i are randomly generated, see Equations (6.28) and (6.29)

known from previous analysis in Equations (6.13) and (6.30):

$$\begin{aligned} \mu_{\text{macro}} &= 5.9 \text{ kN/mm}^2, & \mu_{\text{macro}}^* &= 0.627 \text{ kN/mm}^2, \\ \lambda_{\text{macro}} &= 1.748 \text{ kN/mm}^2, & \mu &= 1.537 \text{ kN/mm}^2 \end{aligned}$$

set initial values:

$$\begin{aligned} \mu_{\text{micro}} &= 26.32 \text{ kN/mm}^2, & \mu_{\text{micro}}^* &= 26.32 \text{ kN/mm}^2, \\ \lambda_{\text{micro}} &= 51.08 \text{ kN/mm}^2, & L_c &= 1 \text{ mm} \end{aligned}$$

The algorithm delivers:

iteration	μ_{micro} [kN/mm ²]	μ_{micro}^* [kN/mm ²]	λ_{micro} [kN/mm ²]	L_c [mm]	r^2 [(kN·mm) ²]
0	26.32	26.32	51.08	1	0.015237
1	19.66	50.85	38.46	0.788	0.00273407
2	15.38	143.12	27.98	0.697	0.0011551
:	:	:	:	:	:
6	10.18	344.45	11.29	0.883	0.000352264
7	10.19	358.87	11.3	0.882	0.000352236
:	:	:	:	:	:
10	10.19	354.77	11.3	0.882	0.000352234
11	10.19	354.88	11.3	0.882	0.000352234
12	10.19	354.87	11.3	0.882	0.000352234

final parameters set:

$$\begin{aligned} \mu_{\text{micro}} &= 10.19 \text{ kN/mm}^2, & \mu_{\text{micro}}^* &= 354.87 \text{ kN/mm}^2, \\ \lambda_{\text{micro}} &= 11.3 \text{ kN/mm}^2, & L_c &= 0.882 \text{ mm} = 0.882 L. \end{aligned}$$

Figure 6.8: Results of the parameter identification algorithm for the relaxed micromorphic model. We refer to the obtained final parameters set here as **parameter set 1**. Taken from SARHIL ET AL. [2024].

the microscopic scale appearing solely in the relaxed micromorphic model. Here, the coefficients of $\mathbb{C}_{\text{micro}}$ are expected to have a reasonable range, avoiding arbitrary magnitudes of the material parameters found in other generalized continua. However, the reasonability of this assumption remains an open question for future research. This bound on the stiffness will be expressed in terms of energy norms (Löwner order) as

$$\boldsymbol{\varepsilon} : \mathbb{C}_{\text{micro}} : \boldsymbol{\varepsilon} \leq \boldsymbol{\varepsilon} : \mathbb{C}_{\text{matrix}} : \boldsymbol{\varepsilon}, \quad \forall \boldsymbol{\varepsilon} \in \text{Sym}(3). \quad (6.31)$$

The latter condition can be rewritten as

$$\begin{aligned} \begin{bmatrix} \varepsilon_{12} \\ \varepsilon_{22} \\ 2\varepsilon_{12} \end{bmatrix}^T \begin{bmatrix} 2\mu_{\text{micro}} + \lambda_{\text{micro}} & \lambda_{\text{micro}} & 0 \\ \lambda_{\text{micro}} & 2\mu_{\text{micro}} + \lambda_{\text{micro}} & 0 \\ 0 & 0 & \mu_{\text{micro}}^* \end{bmatrix} \begin{bmatrix} \varepsilon_{12} \\ \varepsilon_{22} \\ 2\varepsilon_{12} \end{bmatrix} &\leq \\ \begin{bmatrix} \varepsilon_{12} \\ \varepsilon_{22} \\ 2\varepsilon_{12} \end{bmatrix}^T \begin{bmatrix} 2\mu_{\text{matrix}} + \lambda_{\text{matrix}} & \lambda_{\text{matrix}} & 0 \\ \lambda_{\text{matrix}} & 2\mu_{\text{matrix}} + \lambda_{\text{matrix}} & 0 \\ 0 & 0 & \mu_{\text{matrix}}^* \end{bmatrix} \begin{bmatrix} \varepsilon_{12} \\ \varepsilon_{22} \\ 2\varepsilon_{12} \end{bmatrix}, & \quad (6.32) \\ \forall \begin{bmatrix} \varepsilon_{12} \\ \varepsilon_{22} \\ \varepsilon_{12} \end{bmatrix} \in \mathbb{R}^3, & \end{aligned}$$

and the solution reads, see NEFF ET AL. [2020],

$$\begin{aligned} \mu_{\text{micro}}^* &\leq \mu_{\text{matrix}}, \\ \mu_{\text{micro}} &\leq \mu_{\text{matrix}}, \\ \mu_{\text{micro}} + \lambda_{\text{micro}} &\leq \mu_{\text{matrix}} + \lambda_{\text{matrix}}. \end{aligned} \quad (6.33)$$

The first optimization gives a shear modulus $\mu_{\text{micro}}^* = 354.87 \text{ kN/mm}^2$ which violate the criterion of the stiffest response in Equation (6.33) since $\mu_{\text{matrix}}^* = 26.32 \text{ kN/mm}^2$. Accordingly, we refine the optimization algorithm. In each iteration, if the new value(s) break the constraints in Equation (6.33), we project the parameter that violates the constraints back into the acceptable domain. We then repeat the current iteration, omitting this parameter. Regardless, in the next iteration, we include all parameters again. In our algorithm, only the parameter μ_{micro}^* attempts to break the upper limit constraint, leading to its projection back into the admissible domain in each iteration. The results of the revised algorithm are depicted in Figure 6.9. The obtained parameters from the optimization procedure with upper constraints lead to a larger error than when no constraints are considered. There is a concern, particularly with gradient-based algorithms, regarding whether they converge to a global minimum and the potential for a much more satisfactory solution. To investigate this, we calculated the error for 11^4 parameter sets, employing 10 divisions within the permitted domain for each parameter between the macroscopic and matrix parameters. The set exhibiting the least error was chosen as the algorithm's starting point. The algorithm consistently converges to the same solution shown in Figure 6.10 for any starting point (we have tried many other starting points). The advantageous behavior of the relaxed micromorphic model is acknowledged as a two-scale model. It is bounded by two limits, each with distinct physical interpretations, and all the unknown parameters have well-defined ranges. Therefore, employing a gradient-based optimization

procedure was demonstrated to be effective. Vice versa, utilizing a gradient-based optimization for the classical Eringen-Mindlin micromorphic theory, lacking an upper bound, does pose challenges due to the higher number of parameters and the uncertainty about the magnitude of these unknowns. We tried to enhance the fitting by introducing an additional skew-symmetric term in the energy, i.e. $\mu_c \|\text{skew}(\nabla \mathbf{u} - \mathbf{P})\|^2$, representing the micro-rotation coupling, where μ_c is the Cosserat modulus. However, the Cosserat couple modulus trended towards negative values and needed to be projected back to zero, delivering symmetric force stress $\boldsymbol{\sigma}$ as before. This highlights the importance of using the consistent coupling boundary condition and meets the results of our principle investigations in Chapter 5.

6.3.1 Skew-symmetric micro-distortion field instead of the full one

By setting $\mathbb{C}_{\text{micro}} \rightarrow \infty$, the relaxed micromorphic model retrieves the Cosserat model, see Section 2.6.3. The micro-distortion field \mathbf{P} must then be skew-symmetric, c.f. ALAVI ET AL. [2022a], BLESSEN AND NEFF [2023], GHIBA ET AL. [2023], JEONG AND NEFF [2010], JEONG ET AL. [2009], KHAN ET AL. [2022], NEFF AND JEONG [2009], NEFF ET AL. [2010a]. The energy function of the relaxed micromorphic model is modified then with setting $\mathbf{A} := \text{skew } \mathbf{P} \in \mathfrak{so}(3)$ to

$$\begin{aligned} \psi_{\text{Cosserat}}(\nabla \mathbf{u}, \mathbf{A}, \text{Curl } \mathbf{A}) = & \frac{1}{2} (\text{sym } \nabla \mathbf{u} : \mathbb{C}_{\text{macro}} : \text{sym } \nabla \mathbf{u} \\ & + (\text{skew } \nabla \mathbf{u} - \mathbf{A}) : \mathbb{C}_c : (\text{skew } \nabla \mathbf{u} - \mathbf{A}) \\ & + \mu L_c^2 \text{Curl } \mathbf{A} : \mathbb{L} : \text{Curl } \mathbf{A}). \end{aligned} \quad (6.34)$$

which turns out for the cubic anisotropic case into as

$$\begin{aligned} \psi_{\text{Cosserat}}(\nabla \mathbf{u}, \mathbf{A}, \text{Curl } \mathbf{A}) = & \mu_{\text{macro}} (u_{1,1}^2 + u_{2,2}^2) + \frac{\mu_{\text{macro}}^*}{2} (u_{1,2} + u_{2,1})^2 \\ & + \frac{\lambda_{\text{macro}}}{2} (u_{1,1} + u_{2,2})^2 + \frac{\mu_c}{2} (u_{1,2} - u_{2,1} - 2A_{12})^2 \\ & + \frac{\mu L_c^2}{2n^2} ((\text{Curl } \mathbf{A})_{13}^2 + (\text{Curl } \mathbf{A})_{23}^2). \end{aligned} \quad (6.35)$$

Here, μ_c must be strictly positive for the Cosserat model to be operative, otherwise the coupling of the fields (\mathbf{u}, \mathbf{A}) vanishes. We applied the optimization algorithm for the Cosserat model where only two unknown parameters (L_c and μ_c) must be identified. The results are demonstrated in Figure 6.11. We explored two boundary condition scenarios for the micro-distortion field: (I) consistent boundary conditions applied to the entire boundary, and (II) free boundary conditions. The results obtained with consistent boundary conditions delivered significantly better fitting. Consequently, the following analysis focuses on the results obtained under consistent boundary conditions.

We consider forty random modes $i_{\max} = 40$ applied on three sizes $n_{\max} = 3$

$$\bar{\mathbf{u}}_i = \mathbf{B}_i \cdot \mathbf{x} + \mathbf{C}_i \cdot \mathbf{x} \otimes \mathbf{x} \quad \text{on} \quad \partial\mathcal{B}$$

where components of \mathbf{B}_i and \mathbf{C}_i are randomly generated, see Equations (6.28) and (6.29)

known from previous analysis in Equations (6.13) and (6.30):

$$\begin{aligned} \mu_{\text{macro}} &= 5.9 \text{ kN/mm}^2, & \mu_{\text{macro}}^* &= 0.627 \text{ kN/mm}^2, \\ \lambda_{\text{macro}} &= 1.748 \text{ kN/mm}^2, & \mu &= 1.537 \text{ kN/mm}^2 \end{aligned}$$

set initial values:

$$\begin{aligned} \mu_{\text{micro}} &= 26.32 \text{ kN/mm}^2, & \mu_{\text{micro}}^* &= 26.32 \text{ kN/mm}^2, \\ \lambda_{\text{micro}} &= 51.08 \text{ kN/mm}^2, & L_c &= 1 \text{ mm} \end{aligned}$$

The algorithm delivers:

iteration	μ_{micro} [kN/mm ²]	μ_{micro}^* [kN/mm ²]	λ_{micro} [kN/mm ²]	L_c [mm]	r^2 [(kN·mm) ²]
0	26.32	26.32	51.08	1	0.015237
1	19.37	26.32	19.33	1.039	0.0048919
2	13.73	26.32	10.8	1.083	0.00124667
3	10.07	26.32	7.83	1.126	0.000695682
4	10.57	26.32	8.19	1.122	0.000674557
5	10.55	26.32	8.22	1.123	0.000674545
6	10.55	26.32	8.22	1.123	0.000674545
7	10.55	26.32	8.22	1.123	0.000674545

final parameters set:

$$\begin{aligned} \mu_{\text{micro}} &= 10.55 \text{ kN/mm}^2, & \mu_{\text{micro}}^* &= 26.32 \text{ kN/mm}^2, \\ \lambda_{\text{micro}} &= 8.22 \text{ kN/mm}^2, & L_c &= 1.123 \text{ mm} = 1.123 L \end{aligned}$$

Figure 6.9: Results of the parameter identification algorithm for the relaxed micromorphic model. Here, we impose a constraint on the microscopic elasticity tensor $\mathbb{C}_{\text{micro}}$ to ensure it is not stiffer than the stiff matrix. We refer to the obtained final parameters set here as **parameter set 2**. Taken from SARHIL ET AL. [2024].

We consider forty random modes $i_{\max} = 40$ applied on three sizes $n_{\max} = 3$

$$\bar{\mathbf{u}}_i = \mathbf{B}_i \cdot \mathbf{x} + \mathbf{C}_i \cdot \mathbf{x} \otimes \mathbf{x} \quad \text{on} \quad \partial\mathcal{B}$$

components of \mathbf{B}_i and \mathbf{C}_i are randomly generated, see Equations (6.28) and (6.29)

known from previous analysis in Equations (6.13) and (6.30):

$$\begin{aligned} \mu_{\text{macro}} &= 5.9 \text{ kN/mm}^2, & \mu_{\text{macro}}^* &= 0.627 \text{ kN/mm}^2, \\ \lambda_{\text{macro}} &= 1.748 \text{ kN/mm}^2, & \mu &= 1.537 \text{ kN/mm}^2 \end{aligned}$$

set initial values:

$$\begin{aligned} \mu_{\text{micro}} &= 10.03 \text{ kN/mm}^2, & \mu_{\text{micro}}^* &= 26.32 \text{ kN/mm}^2, \\ \lambda_{\text{micro}} &= 6.7 \text{ kN/mm}^2, & L_c &= 1.36 \text{ mm} \end{aligned}$$

The algorithm delivers:

iteration	μ_{micro} [kN/mm ²]	μ_{micro}^* [kN/mm ²]	λ_{micro} [kN/mm ²]	L_c [mm]	r^2 [(kN·mm) ²]
0	10.03	26.32	6.7	1.36	0.00153283
1	10.74	26.32	7.9	1.057	0.000785925
2	10.42	26.32	8.17	1.128	0.000674967
3	10.56	26.32	8.22	1.122	0.000674548
4	10.55	26.32	8.22	1.123	0.000674545
5	10.55	26.32	8.22	1.123	0.000674545

final parameters set:

$$\begin{aligned} \mu_{\text{micro}} &= 10.55 \text{ kN/mm}^2, & \mu_{\text{micro}}^* &= 26.32 \text{ kN/mm}^2, \\ \lambda_{\text{micro}} &= 8.22 \text{ kN/mm}^2, & L_c &= 1.123 \text{ mm} = 1.123 L \end{aligned}$$

Figure 6.10: Results of the parameter identification algorithm for the relaxed micromorphic model. Here, we impose a constraint on the microscopic elasticity tensor $\mathbb{C}_{\text{micro}}$ to ensure it is not stiffer than the stiff matrix. We start with different initial values and the algorithm delivers the same values as in Figure 6.9. Taken from SARHIL ET AL. [2024].

We consider forty random modes $i_{\max} = 40$ applied on three sizes $n_{\max} = 3$

$$\bar{\mathbf{u}}_i = \mathbf{B}_i \cdot \mathbf{x} + \mathbf{C}_i \cdot \mathbf{x} \otimes \mathbf{x} \quad \text{on} \quad \partial\mathcal{B}$$

components of \mathbf{B}_i and \mathbf{C}_i are randomly generated, see Equations (6.28) and (6.29)

known from previous analysis in Equations (6.13) and (6.30):

$$\begin{aligned} \mu_{\text{macro}} &= 5.9 \text{ kN/mm}^2, & \mu_{\text{macro}}^* &= 0.627 \text{ kN/mm}^2, \\ \lambda_{\text{macro}} &= 1.748 \text{ kN/mm}^2, & \mu &= 1.537 \text{ kN/mm}^2 \end{aligned}$$

further assumptions: ($\approx \mathbb{C}_{\text{micro}} \rightarrow \infty$)

$$\mu_{\text{micro}} = 10000 \mu_{\text{macro}}, \quad \mu_{\text{micro}}^* = 10000 \mu_{\text{macro}}^*, \quad \lambda_{\text{micro}} = 10000 \lambda_{\text{macro}}$$

set initial values:

$$\mu_c = 1 \text{ kN/mm}^2, \quad L_c = 1 \text{ mm}$$

The algorithm delivers:

with consistent boundary condition				without consistent boundary condition			
iteration	μ_c [kN/mm ²]	L_c [mm]	r^2 [(kN·mm) ²]	iteration	μ_c [kN/mm ²]	L_c [mm]	r^2 [(kN·mm) ²]
0	1	1	0.01967	0	1	1	0.0261827
1	4.04	0.615	0.00265	1	2.04	0.711	0.0258911
2	12.97	0.59	0.002517	2	14.51	0.51	0.0257639
:	:	:	:	:	:	:	:
10	1739.03	0.614	0.002128	10	$64.43 \cdot 10^4$	5.133	0.0114968
11	1408.36	0.614	0.002125	11	$64.82 \cdot 10^4$	5.132	0.0114965
:	:	:	:	:	:	:	:
17	452.64	0.616	0.00211923	19	$67.49 \cdot 10^4$	5.132	0.0114945
18	452.6	0.616	0.00211923	20	$67.52 \cdot 10^4$	5.132	0.0114945

final parameters set (with consistent boundary condition):

$$\mu_c = 452.6 \text{ kN/mm}^2 \text{ and } L_c = 0.616 \text{ mm} = 0.616 L.$$

Figure 6.11: Results of the parameter identification algorithm for the Cosserat model. Taken from SARHIL ET AL. [2024].

6.3.2 Full gradient of the micro-distortion field instead of its Curl

Another comparison can be conducted between the results obtained by the relaxed curvature (Curl \mathbf{P}) within the relaxed micromorphic model and the full curvature ($\nabla \mathbf{P}$) within the classical micromorphic model. The energy function of the Eringen-Mindlin micromorphic model reads (using the relaxed micromorphic model notation)

$$\begin{aligned} \psi_{\text{Eringen}}(\nabla \mathbf{u}, \mathbf{P}, \nabla \mathbf{P}) = & \frac{1}{2} \left(\text{sym}[\nabla \mathbf{u} - \mathbf{P}] : \mathbb{C}_e : \text{sym}[\nabla \mathbf{u} - \mathbf{P}] \right. \\ & + \text{sym} \mathbf{P} : \mathbb{C}_{\text{micro}} : \text{sym} \mathbf{P} \\ & + \text{skew}[\nabla \mathbf{u} - \mathbf{P}] : \mathbb{C}_c : \text{skew}[\nabla \mathbf{u} - \mathbf{P}] \\ & + (\nabla \mathbf{u} - \mathbf{P}) : \mathbb{C}_{\text{mixed}} : \text{sym} \mathbf{P} \\ & \left. + \frac{\mu L_c^2}{n^2} \nabla \mathbf{P} : \check{\mathbb{L}} : \nabla \mathbf{P} \right). \end{aligned} \quad (6.36)$$

Here, $\check{\mathbb{L}}$ is a sixth-order tensor and $\mathbb{C}_{\text{mixed}}$ is a fourth-order tensor. For the planar cubic case, the tensor $\check{\mathbb{L}}$ associated with the curvature requires already the definition of 10 independent parameters D'AGOSTINO ET AL. [2024]. Thus, we have

$$\nabla \mathbf{P} : \check{\mathbb{L}} : \nabla \mathbf{P} = \begin{pmatrix} P_{11,1} \\ P_{12,2} \\ P_{22,1} \\ P_{21,2} \\ P_{22,2} \\ P_{21,1} \\ P_{11,2} \\ P_{12,1} \end{pmatrix}^T \begin{pmatrix} L_{111111} & L_{111122} & L_{111221} & L_{111212} & 0 & 0 & 0 & 0 \\ L_{111122} & L_{122122} & L_{122221} & L_{122212} & 0 & 0 & 0 & 0 \\ L_{111221} & L_{122221} & L_{221221} & L_{221212} & 0 & 0 & 0 & 0 \\ L_{111212} & L_{122212} & L_{221212} & L_{212212} & 0 & 0 & 0 & 0 \\ 0 & 0 & 0 & 0 & L_{111111} & L_{111122} & L_{111221} & L_{111212} \\ 0 & 0 & 0 & 0 & L_{111122} & L_{122122} & L_{122221} & L_{122212} \\ 0 & 0 & 0 & 0 & L_{111221} & L_{122221} & L_{221221} & L_{221212} \\ 0 & 0 & 0 & 0 & L_{111212} & L_{122212} & L_{221212} & L_{212212} \end{pmatrix} \begin{pmatrix} P_{11,1} \\ P_{12,2} \\ P_{22,1} \\ P_{21,2} \\ P_{22,2} \\ P_{21,1} \\ P_{11,2} \\ P_{12,1} \end{pmatrix}, \quad (6.37)$$

where $L_{111111}, L_{111122}, L_{111221}, L_{111212}, L_{122122}, L_{122221}, L_{122212}, L_{221221}, L_{221212}$ and L_{212212} are to be determined. The total number of unknown parameters for the Eringen-Mindlin full micromorphic model equals 14 for the 2D case (3 for $\mathbb{C}_{\text{micro}}$, 1 for \mathbb{C}_c and 10 for \mathbb{L}) if we already exclude the mixed term $(\nabla \mathbf{u} - \mathbf{P}) : \mathbb{C}_{\text{mixed}} : \text{sym} \mathbf{P}$. Dealing with such many unknowns is not feasible for a gradient-based optimization. Therefore, for the sake of simplicity, we restrict our analysis to the most simplified curvature formulation to reduce the number of unknown parameters. Thus, the curvature will only be associated with a single scalar μL_c^2 , i.e. $\check{\mathbb{L}} : \nabla \mathbf{P} = \nabla \mathbf{P}$. However, it is clear that optimizing the coefficients of the tensor $\check{\mathbb{L}}$ (with cubic symmetries) will provide a better fit. The energy function of the simplified micromorphic model for a cubic material turns into

$$\begin{aligned}
\psi_{\text{Eringen}}(\nabla \mathbf{u}, \mathbf{P}, \nabla \mathbf{P}) &= \mu_e \left((u_{1,1} - P_{11})^2 + (u_{2,2} - P_{22})^2 \right) \\
&+ \frac{\mu_e^*}{2} (u_{1,2} + u_{2,1} - P_{12} - P_{21})^2 \\
&+ \frac{\lambda_e}{2} (u_{1,1} + u_{2,2} - P_{11} - P_{22})^2 \\
&+ \mu_{\text{micro}} (P_{11}^2 + P_{22}^2) + \frac{\mu_{\text{micro}}^*}{2} (P_{12} + P_{21})^2 \\
&+ \frac{\lambda_{\text{micro}}}{2} (P_{11} + P_{22})^2 + \frac{\mu_c}{2} (u_{1,2} - u_{2,1} - P_{12} + P_{21})^2 \\
&+ \frac{\mu L_c^2}{2n^2} \|\nabla \mathbf{P}\|^2,
\end{aligned} \tag{6.38}$$

where the parameters $\mu_{\text{micro}}, \mu_{\text{micro}}^*, \lambda_{\text{micro}}, \mu_c$ and L_c need to be defined. The optimization follows the same approach as for the relaxed micromorphic model by enforcing the consistent boundary conditions on the whole boundary. The results are displayed in Figure 6.12. The optimization gives $\mu_{\text{micro}} = 5.959 \text{ kN/mm}^2$, $\mu_{\text{micro}}^* = 80.82 \text{ kN/mm}^2$, $\lambda_{\text{micro}} = 12.06 \text{ kN/mm}^2$, $\mu_c = 1138.34 \text{ kN/mm}^2$ and $L_c = 0.695 \text{ mm}$ with an error $r^2 = 0.000612487 \text{ (kN}\cdot\text{mm)}^2$. The simplified full micromorphic model prefers an asymmetric force stress $\boldsymbol{\sigma}$, disagreeing with the relaxed micromorphic model. Moreover, $\mathbb{C}_{\text{micro}}$ for the full micromorphic model is not associated with an upper limit stiffness property, which makes the obtained tensor $\mathbb{C}_{\text{micro}}$ not physically based and, therefore, incomparable with any measurable quantity from an engineering point of view.

We can enhance the fitting by introducing a simplified isotropic curvature characterized by three independent parameters $(\alpha_1, \alpha_2, \alpha_3)$. This isotropic curvature in the full micromorphic model has the form RIZZI ET AL. [2021b]

$$\nabla \mathbf{P} : \check{\mathbb{L}} : \nabla \mathbf{P} = \sum_{i=1}^2 \left(\alpha_1 \|\text{dev sym } \mathbf{P}_{,i}\|^2 + \alpha_2 \|\text{skew } \mathbf{P}_{,i}\|^2 + \frac{2}{9} \alpha_3 \text{tr}^2(\mathbf{P}_{,i}) \right). \tag{6.39}$$

The optimization outcomes are demonstrated in Figure 6.13 assuming $L_c = 1 \text{ mm}$. The optimized parameters read $\mu_{\text{micro}} = 5.967 \text{ kN/mm}^2$, $\mu_{\text{micro}}^* = 392.15 \text{ kN/mm}^2$, $\lambda_{\text{micro}} = 10.77 \text{ kN/mm}^2$, $\mu_c = 808.94 \text{ kN/mm}^2$, $\alpha_1 = 0.187$, $\alpha_2 = 0.318$ and $\alpha_3 = 5.65$. However, the error r^2 for the isotropic curvature ($0.000528 \text{ [(kN}\cdot\text{mm)}^2]$) does not show a notable enhancement compared to the simplified curvature ($0.000612 \text{ [(kN}\cdot\text{mm)}^2]$). Note that the calculated parameters $(\mathbb{C}_{\text{micro}}, \mu_c)$ for the two formulations of curvature in the micromorphic model show a significant difference, leaving doubts about the physical interpretations.

We consider forty random modes $i_{\max} = 40$ applied on three sizes $n_{\max} = 3$

$$\bar{\mathbf{u}}_i = \mathbf{B}_i \cdot \mathbf{x} + \mathbf{C}_i \cdot \mathbf{x} \otimes \mathbf{x} \quad \text{on} \quad \partial\mathcal{B}$$

components of \mathbf{B}_i and \mathbf{C}_i are randomly generated, see Equations (6.28) and (6.29)

known from previous analysis in Equations (6.13) and (6.30):

$$\begin{aligned} \mu_{\text{macro}} &= 5.9 \text{ kN/mm}^2, & \mu_{\text{macro}}^* &= 0.627 \text{ kN/mm}^2, \\ \lambda_{\text{macro}} &= 1.748 \text{ kN/mm}^2, & \mu &= 1.537 \text{ kN/mm}^2 \end{aligned}$$

further assumptions:

$$\mathbb{C}_{\text{mixed}} = \mathbf{0}$$

set initial values:

$$\begin{aligned} \mu_{\text{micro}} &= 26.32 \text{ kN/mm}^2, & \mu_{\text{micro}}^* &= 26.32 \text{ kN/mm}^2, \\ \lambda_{\text{micro}} &= 51.08 \text{ kN/mm}^2, & \mu_c &= 1 \text{ kN/mm}^2, & L_c &= 1 \text{ mm} \end{aligned}$$

The algorithm delivers:

iteration	μ_{micro} [kN/mm ²]	μ_{micro}^* [kN/mm ²]	λ_{micro} [kN/mm ²]	μ_c [kN/mm ²]	L_c [mm]	r^2 [(kN·mm) ²]
0	26.32	26.32	51.08	1	1	0.029915
1	8.48	46.8	6.14	4.27	0.7	0.0023058
2	8.33	82.89	9.32	11.54	0.621	0.0018288
:	:	:	:	:	:	:
11	5.959	85.5	12.28	1057.11	0.688	0.000612789
12	5.959	82.99	12.16	1070.65	0.692	0.000612667
:	:	:	:	:	:	:
25	5.959	80.83	12.06	1138.32	0.695	0.000612487
26	5.959	80.82	12.06	1138.34	0.695	0.000612487

final parameters set:

$$\begin{aligned} \mu_{\text{micro}} &= 5.959 \text{ kN/mm}^2, & \mu_{\text{micro}}^* &= 80.82 \text{ kN/mm}^2, & \lambda_{\text{micro}} &= 12.06 \text{ kN/mm}^2, \\ \mu_c &= 1138.34 \text{ kN/mm}^2, & L_c &= 0.695 \text{ mm} = 0.695 L. \end{aligned}$$

Figure 6.12: Results of the parameter identification algorithm for the simplified full micromorphic model. Taken from SARHIL ET AL. [2024].

We consider forty random modes $i_{\max} = 40$ applied on three sizes $n_{\max} = 3$

$$\bar{\mathbf{u}}_i = \mathbf{B}_i \cdot \mathbf{x} + \mathbf{C}_i \cdot \mathbf{x} \otimes \mathbf{x} \quad \text{on } \partial\mathcal{B}$$

components of \mathbf{B}_i and \mathbf{C}_i are randomly generated, see (6.28) and (6.29)

known from previous analysis in Equations (6.13) and (6.30):

$$\begin{aligned} \mu_{\text{macro}} &= 5.9 \text{ kN/mm}^2, & \mu_{\text{macro}}^* &= 0.627 \text{ kN/mm}^2, \\ \lambda_{\text{macro}} &= 1.748 \text{ kN/mm}^2, & \mu &= 1.537 \text{ kN/mm}^2 \end{aligned}$$

further assumptions:

$$L_c = 1 \text{ mm}, \quad \mathbb{C}_{\text{mixed}} = \mathbf{0}$$

set initial values:

$$\begin{aligned} \mu_{\text{micro}} &= 26.32 \text{ kN/mm}^2, & \mu_{\text{micro}}^* &= 26.32 \text{ kN/mm}^2, & \lambda_{\text{micro}} &= 51.08 \text{ kN/mm}^2, \\ \mu_c &= 1 \text{ kN/mm}^2, & \alpha_1 &= \alpha_2 = \alpha_3 = 1 \end{aligned}$$

The algorithm delivers:

iteration	μ_{micro} [kN/mm ²]	μ_{micro}^* [kN/mm ²]	λ_{micro} [kN/mm ²]	μ_c [kN/mm ²]	α_1	α_2	α_3	r^2 [(kN·mm) ²]
0	26.32	26.32	51.08	1	1	1	1	0.018407
1	16.21	35.89	-0.714	1.966	0.8	0.702	2.254	0.00180853
2	11.76	62.89	3.425	4.12	0.673	0.355	3.09	0.00122141
:	:	:	:	:	:	:	:	:
13	10.33	249.7	5.974	189.27	0.398	0.212	3.69	0.000956095
14	10.2	266.56	6.24	523.67	0.373	0.212	3.77	0.000945068
:	:	:	:	:	:	:	:	:
25	5.974	430.96	11.41	773.63	0.148	0.325	5.883	0.000534085
26	5.959	406.16	11.05	784.36	0.166	0.318	5.758	0.000532797
:	:	:	:	:	:	:	:	:
49	5.966	392.15	10.77	808.91	0.187	0.318	5.65	0.000528028
50	5.967	392.15	10.77	808.94	0.187	0.318	5.65	0.000528028

final parameters set:

$$\begin{aligned} \mu_{\text{micro}} &= 5.967 \text{ kN/mm}^2, & \mu_{\text{micro}}^* &= 392.15 \text{ kN/mm}^2, & \lambda_{\text{micro}} &= 10.77 \text{ kN/mm}^2, \\ \mu_c &= 808.94 \text{ kN/mm}^2, & \alpha_1 &= 0.187, & \alpha_2 &= 0.318, & \alpha_3 &= 5.65 \end{aligned}$$

Figure 6.13: Results of the parameter identification algorithm for the full micromorphic model with isotropic curvature. Taken from SARHIL ET AL. [2024].

6.4 Comparisons and validation

The average error of the relaxed micromorphic model concerning 120 reference heterogeneous solutions equals 5.3% for parameter set 1 (not constrained) in Figure 6.8, and 7.5% for parameter set 2 in Figure 6.9 (constrained). The Cosserat case gives an average error of 13.7%. The full micromorphic model leads to an average error of 7.2% for the simplified curvature and 6.3% for the isotropic curvature. Figure 6.14 shows the results of fitting 7 deformation modes from the 40 random modes. We expand the results to encompass not just the first 3 sizes ($n = 1, 2, 3$) employed in the optimization algorithm but also the first 6 sizes ($n = 1, \dots, 6$). Further after these sizes, size-effects do not occur, and standard homogenization theory becomes valid. The relaxed micromorphic and the full micromorphic models demonstrate good agreement with the heterogeneous solutions. While the Cosserat model delivers the poorest fitting among the investigated models, no obvious superior model stands out, but the unconstrained relaxed micromorphic model (parameter set 1) illustrates the least error.

We validate the optimization procedure results in Figure 6.15 for four different deformation modes that were not considered in the optimization algorithm. Two deformation modes are first-order modes and the other are second-order modes. The models show, in general, satisfactory results. Due to the relaxed curvature expression in the relaxed micromorphic model, we do not expect to reach a perfect fitting, considering that only four unknown parameters describe the relaxed micromorphic model. The Cosserat model reproduces no size-effects for axial loading and displays good results for shear loading, which is expected. However, the relaxed micromorphic model exhibits better overall agreement with the fully resolved solution. Using the full-gradient of the micro-distortion with a single characteristic length parameter does not enhance the overall fitting (the simplified Eringen-Mindlin micromorphic model). We tested if a better fitting can be achieved using an isotropic curvature with 3 independent parameters. However, this did not lead to a significant enhancement.

Discussions

We successfully established a computational approach to define the unknown material parameters of the relaxed micromorphic model. We first conducted a short consistency check of the presented methodology for linear elasticity under affine and periodic boundary conditions. The implemented algorithm delivered the correct results of the classical homogenization theory. We expanded our approach to the relaxed micromorphic model. Due to the simplicity of the model, only the microscopic elasticity tensor $\mathbb{C}_{\text{micro}}$ and a scalar associated with curvature have to be defined via the suggested computational approach, given that the macroscopic elasticity tensor $\mathbb{C}_{\text{macro}}$ is known and \mathbb{C}_e is uniquely determined once $\mathbb{C}_{\text{micro}}$ is known.

Only four parameters were included in the algorithm for our specific unit-cell with cubic symmetry. The algorithm is based on the Hill-Mandel energy equivalence applied to various deformation modes and sizes. It employs a least squares fitting of the energies of the fully resolved metamaterial and the equivalent homogenous continuum. Thus, we have avoided the classical microscopic-macroscopic transition schemes and the identification of a representative volume element. Moreover, we eliminated the need to deal with various

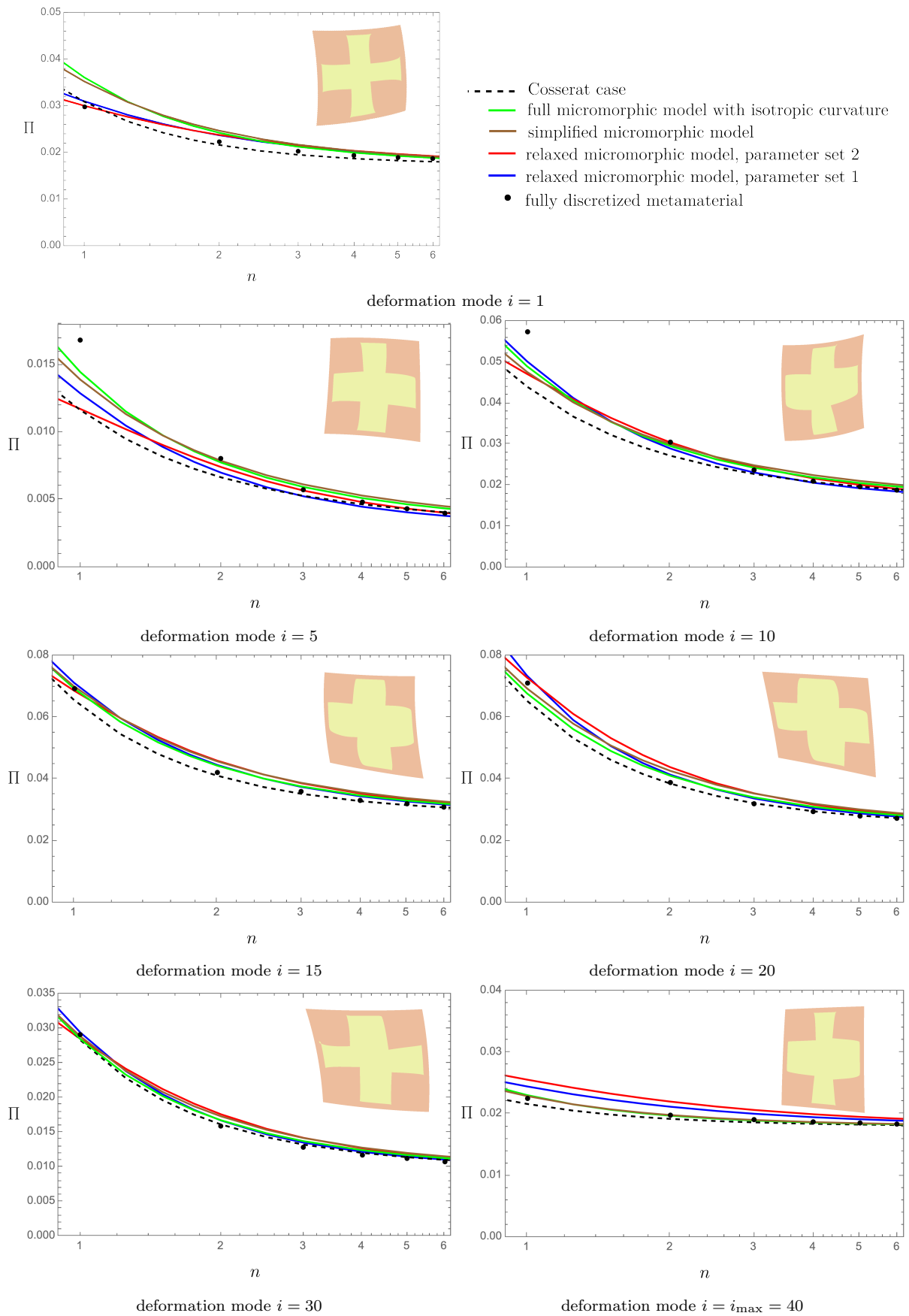


Figure 6.14: The total energy of the heterogeneous material, the relaxed micromorphic model, the Cosserat case, and the Eringen-Mindlin full micromorphic model with both the simplified and isotropic curvature. We show 7 random deformation modes with the deformed shape for $n = 1$ scaled by a factor of three. Taken from SARHIL ET AL. [2024].

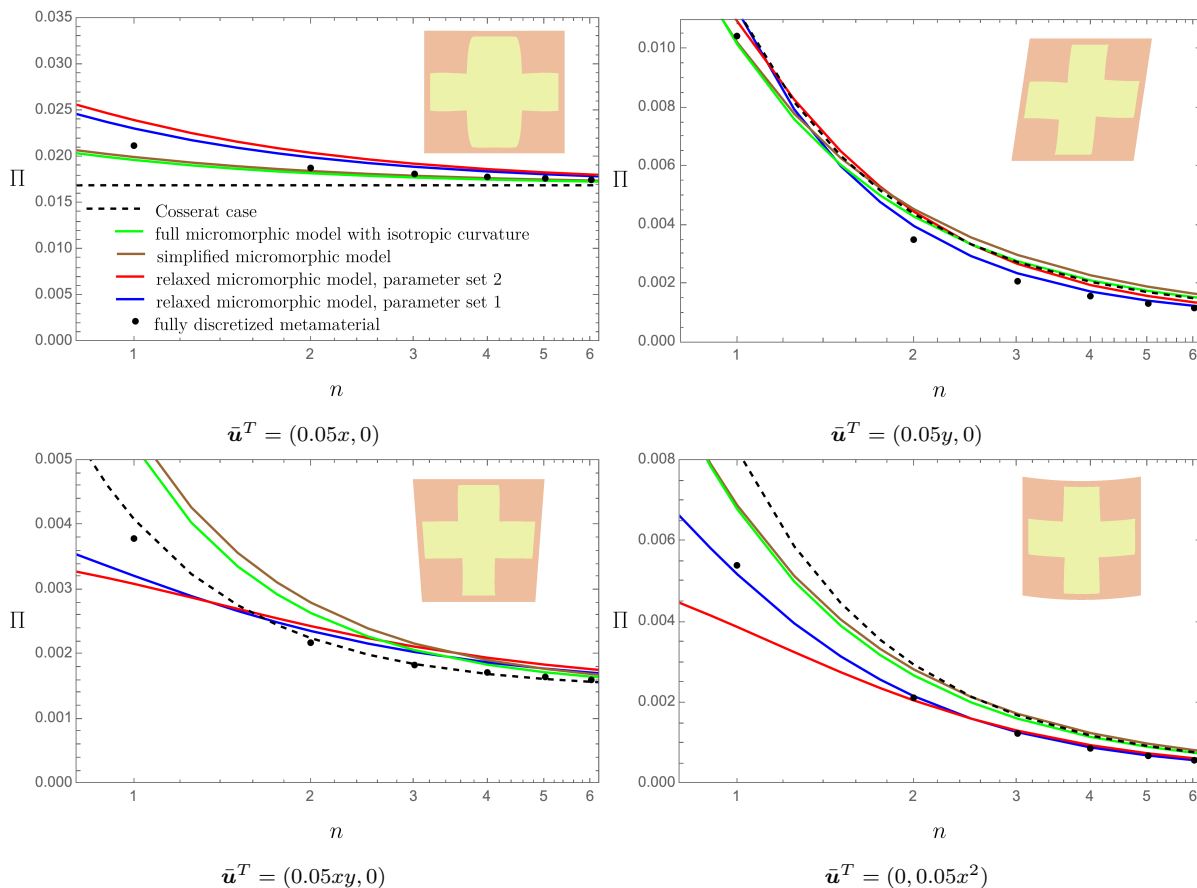


Figure 6.15: The total energy of the heterogeneous material and the homogeneous relaxed micromorphic model is examined for the two parameter sets, varying the size for four modes that were not included in the algorithm. We also show the outcomes of the Cosserat and the simplified Eringen-Mindlin micromorphic model. Dirichlet boundary conditions are set on the whole boundary $\mathbf{u} = \bar{\mathbf{u}}$ on \mathcal{B} . The deformed shape is shown for $n = 1$ enhanced by a factor of three. Taken from SARHIL ET AL. [2024].

stress quantities and their microscopic equivalents, which are unknown to us yet.

The implemented algorithm delivered a good fit, but we found it is necessary to add an additional criterion, from an engineering point of view, ensuring that the microscopic elasticity tensor cannot exceed the stiffness of the homogeneous stiff matrix for any deformation mode. We compared the obtained parameters with and without this criterion, and the results showed satisfactory agreement. Moreover, we conducted a comparison between the results of the relaxed micromorphic model and those obtained by the Cosserat model, which uses a skew-symmetric micro-distortion field, as well as the simplest case of the full Eringen-Mindlin micromorphic model. For the full Eringen-Mindlin micromorphic model, we utilized the full-gradient of the micro-distortion field for the curvature but associated with a single scalar characteristic length. We attempted to enhance the fitting of the full Eringen-Mindlin micromorphic model by employing an isotropic curvature, resulting in a slight enhancement. The relaxed and full micromorphic continuum shows a comparable fitting level to the fully resolved heterogeneous solution, while the Cosserat continuum performs the worst.

We recognize that the full Eringen-Mindlin micromorphic model can exhibit better fitting than the relaxed micromorphic model. The full Eringen-Mindlin micromorphic model

has, in the most general formulation, 903 material parameters. However, compared to the relaxed micromorphic model, no improvement is achieved for simplified forms of the full micromorphic model with a remarkably reduced number of parameters but comparable to the number of parameters of the relaxed micromorphic model. Thus, the relaxation of the curvature to consider only the Curl, as in the relaxed micromorphic model, is a reasonable simplification leveraging the strength of the very simple Cosserat model and the highly complex full micromorphic model.

7 Conclusions and outlook

Despite their potentials, the complex mathematical formulations and the high number of parameters of generalized continua theories have prevented their widespread adoption for real-life engineering problems. However, the advantageous behavior of the relaxed micromorphic model, as a true two-scale elasticity model, simplifies the physical interpretation of material parameters, which other generalized continua cannot offer.

We introduced the basic principles of continuum mechanics of solids within the framework of the Cauchy continuum, including kinematics, stress concept, balance equations and variational principles. We expanded this framework to encompass more advanced enriched continua, thus offering a more comprehensive understanding of these continua. We presented in detail the main components of the relaxed micromorphic model, including energy function, material parameters, and the variational problem that leads to the weak and strong forms with the associated boundary conditions. We analyzed the limiting cases analytically when the characteristic length parameter approaches zero or infinity, causing the model's advantageous behaviors as a two-scale elasticity model. The relaxed micromorphic model operates between a macroscopic linear elastic scale with a uniquely defined macroscopic elasticity tensor and a microscopic linear elastic scale with a to-be-defined microscopic elasticity tensor.

The **finite element formulation** of the relaxed micromorphic model must be conforming in $H(\mathcal{B}) \times H(\text{curl}, \mathcal{B})$ space. The basic principles of the finite element method and different approximation spaces were introduced in detail. We comprehensively described the construction of $H(\text{curl}, \mathcal{B})$ -conforming elements with Nédélec shape vectors. In several numerical examples, we tested the different finite elements' behavior with their convergence rates for the case of a discontinuous solution favoring $H^1(\mathcal{B}) \times H(\text{curl}, \mathcal{B})$ elements. Furthermore, we examined the different stress measures in the relaxed micromorphic model for the limiting cases of the characteristic length parameter.

We observed that the **boundary conditions** of enriched continua have not been studied meticulously in the literature. However, they play a crucial role in accurately identifying the unknown parameters since the behavior of generalized continua varies depending on the set of boundary conditions used. The consistent coupling boundary condition ensures that the intended upper bound of the relaxed micromorphic model is realized. This upper bound happens to be linear elasticity with a microscopic elasticity tensor. Thus, identifying the microscopic elasticity tensor makes sense only when the consistent boundary condition is enforced. We investigated numerically applying the consistent boundary condition for different problems (via a penalty approach when necessary), such as bending, shearing, and classical cantilever, and the microscopic elasticity tensor was always seen as an upper bound. This applies to displacement-driven and traction-driven problems. Thus, this flexibility has not been observed in other enriched continua since the consistent coupling boundary condition can always be used.

Significant efforts have been devoted to the **identification of material parameters** of enriched continua in the mechanics community. The relaxed micromorphic model, being a two-scale model, exhibits unique behavior that allows a physical interpretation to help identify the unknown parameters. The microscopic elasticity tensor is determined by the concept of the stiffest possible response of the assumed microstructure. First, the microscopic elasticity tensor was assumed to be given by the Löwner matrix supremum of elas-

ticity tensors appearing under affine Dirichlet conditions on different unit-cells, which was found to be too soft for capturing size-effects. Therefore, we introduced another approach based on calibrating the microscopic elasticity tensor via non-affine bending deformation modes. Finally, the curvature was fitted to the reference fully resolved solutions. While both approaches provided initial estimates, it is important to continue exploring and developing more accurate methods in this direction. Thus, we implemented an optimization procedure that determined the unknown material parameters for the relaxed micromorphic model after a consistency check for linear elasticity, which successfully delivered the results of classical homogenization theory. The optimization procedure is based on the least squares fitting of the energy of the equivalent homogeneous continuum with the energy of the fully resolved microstructure. Both the microscopic elasticity tensor and the characteristic length parameter in the relaxed micromorphic model were identified via the presented optimization. Two different scenarios were introduced during the optimization implementation (constrained or non-constrained by the stiff matrix from above). We compared the results of the optimization procedure of the relaxed micromorphic model, the Cosserat model, and the classical micromorphic theory with two different curvature formulations. The relaxed micromorphic model delivers the least error and best fit among them.

Future investigations are needed in the context of the higher-order homogenization theory into the relaxed micromorphic continuum. However, the microscopic-macroscopic transition relations must first be available for the relaxed micromorphic model. Further challenges are expected, such as the choice of the representative volume element and the boundary conditions on this representative volume element. It would be interesting to compare the results of the higher-order homogenization approaches to the ones from the implemented optimization and see if they can deliver better fitting.

A Nédélec shape functions

A Second-order triangular element NT2

Triangular elements are defined on a domain $\pi_e^\Delta = \{0 \leq \xi \leq 1, 0 \leq \eta \leq 1 - \xi\}$. The finite elements with the respective edge numbering are shown in Figure 4.2. The Nédélec space of a second-order triangular element (NT2) reads

$$[\mathcal{ND}^\Delta]_2^2 = \left\{ \begin{bmatrix} 1 \\ 0 \end{bmatrix}, \begin{bmatrix} \xi \\ 0 \end{bmatrix}, \begin{bmatrix} \eta \\ 0 \end{bmatrix}, \begin{bmatrix} 0 \\ 1 \end{bmatrix}, \begin{bmatrix} 0 \\ \xi \end{bmatrix}, \begin{bmatrix} 0 \\ \eta \end{bmatrix}, \begin{bmatrix} -\eta^2 \\ \xi\eta \end{bmatrix}, \begin{bmatrix} -\xi\eta \\ \xi^2 \end{bmatrix} \right\}, \quad (\text{A.1})$$

and the general form of shape functions reads

$$\mathbf{v}^2 = \begin{pmatrix} a_1 + a_2 \xi + a_3 \eta - a_7 \eta^2 - a_8 \xi \eta \\ a_4 + a_5 \xi + a_6 \eta + a_7 \xi \eta + a_8 \xi^2 \end{pmatrix}, \quad (\text{A.2})$$

where $a_i, i = 1, \dots, 8$ are coefficients yet to be defined based on the dofs. Explicit functions $r_j, j = 1, 2$ and $\mathbf{q}_i, i = 1, 2$ in Equations (4.19) and (4.20) are assumed as

$$\begin{aligned} \text{edge 1 :} & \quad r_1 = \xi, & \quad r_2 = \eta, \\ \text{edge 2 :} & \quad r_1 = \eta, & \quad r_2 = 1 - \eta, \\ \text{edge 3 :} & \quad r_1 = 1 - \xi, & \quad r_2 = \xi, \\ \text{inner :} & \quad \mathbf{q}_1 = \begin{bmatrix} 1 \\ 0 \end{bmatrix}, & \quad \mathbf{q}_2 = \begin{bmatrix} 0 \\ 1 \end{bmatrix}, \end{aligned} \quad (\text{A.3})$$

and the tangential vectors of the element edges are the same as in Equation (4.24).

The inner and outer dofs are calculated according to Equations (4.19) and (4.20) using $\xi + \eta = 1$ on the first edge, $\xi = 0$ on the second edge and $\eta = 0$ on the third edge, such as

$$\begin{aligned} m_1^{e_1} &= \frac{1}{6}(3a_1 + 2a_2 + a_3 - 3a_4 - 2a_5 - a_6 - a_7 - 2a_8), \\ m_2^{e_1} &= \frac{1}{6}(3a_1 + a_2 + 2a_3 - 3a_4 - a_5 - 2a_6 - 2a_7 - a_8), \\ m_1^{e_2} &= \frac{1}{6}(3a_4 + 2a_6), & m_2^{e_2} &= \frac{1}{6}(3a_4 + a_6), \\ m_1^{e_3} &= \frac{1}{6}(3a_1 + a_2), & m_2^{e_3} &= \frac{1}{6}(3a_1 + 2a_2), \\ m_1^{\text{inner}} &= \frac{1}{24}(12a_1 + 4a_2 + 4a_3 - 2a_7 - a_8), \\ m_2^{\text{inner}} &= \frac{1}{24}(12a_4 + 4a_5 + 4a_6 + a_7 + 2a_8), \end{aligned} \quad (\text{A.4})$$

and the resulting shape functions shown in Figure A.1 are obtained by an analogous procedure as described for NT1 element in Section 4.3.2, leading to

$$\begin{aligned}
\text{edge 1 : } \mathbf{v}_1^2 &= 2 \begin{pmatrix} -\eta + 4\eta\xi \\ 2\xi - 4\xi^2 \end{pmatrix}, & \mathbf{v}_2^2 &= 2 \begin{pmatrix} -2\eta + 4\eta^2 \\ \xi - 4\eta\xi \end{pmatrix}, \\
\text{edge 2 : } \mathbf{v}_3^2 &= 2 \begin{pmatrix} -2\eta + 4\eta^2 \\ -1 + 3\eta + \xi - 4\eta\xi \end{pmatrix}, & \mathbf{v}_4^2 &= 2 \begin{pmatrix} 3\eta - 4\eta^2 - 4\eta\xi \\ 2 - 3\eta - 6\xi + 4\eta\xi + 4\xi^2 \end{pmatrix}, \\
\text{edge 3 : } \mathbf{v}_5^2 &= 2 \begin{pmatrix} 2 - 6\eta + 4\eta^2 - 3\xi + 4\eta\xi \\ 3\xi - 4\eta\xi - 4\xi^2 \end{pmatrix}, & \mathbf{v}_6^2 &= 2 \begin{pmatrix} -1 + \eta + 3\xi - 4\eta\xi \\ -2\xi + 4\xi^2 \end{pmatrix}, \\
\text{inner : } \mathbf{v}_7^2 &= 2 \begin{pmatrix} 8\eta - 8\eta^2 - 4\eta\xi \\ -4\xi + 8\eta\xi + 4\xi^2 \end{pmatrix}, & \mathbf{v}_8^2 &= 2 \begin{pmatrix} -4\eta + 4\eta^2 + 8\eta\xi \\ 8\xi - 4\eta\xi - 8\xi^2 \end{pmatrix}.
\end{aligned} \tag{A.5}$$

B First-order quadrilateral element NQ1

Quadrilateral elements have a domain $\pi_e^\square = \{-1 \leq \xi \leq 1, -1 \leq \eta \leq 1\}$. The Nédélec space of a first-order quadrilateral element (NQ1) reads

$$[\mathcal{N}\mathcal{D}^\square]_1^2 = \left\{ \begin{bmatrix} 1 \\ 0 \end{bmatrix}, \begin{bmatrix} \eta \\ 0 \end{bmatrix}, \begin{bmatrix} 0 \\ 1 \end{bmatrix}, \begin{bmatrix} 0 \\ \xi \end{bmatrix} \right\}, \tag{A.6}$$

and the general form of shape vectors reads

$$\mathbf{v}^1 = \begin{pmatrix} a_1 + a_2 \eta \\ a_3 + a_4 \xi \end{pmatrix}, \tag{A.7}$$

where $a_i, i = 1, \dots, 4$ are coefficients yet to be defined based on the dofs. Starting from Equation (4.19), we set $r_j = 1$ for all edges. The tangential vectors for the first and third edge are $\mathbf{t}_1 = \mathbf{t}_3 = (1, 0)^T$ and for the second and fourth edge $\mathbf{t}_2 = \mathbf{t}_4 = (0, 1)^T$, see Figure 4.2 (left). We calculate edge dofs taking into consideration that $\eta = -1$ on the first edge, $\xi = 1$ on the second edge, $\eta = 1$ on the third edge and $\xi = -1$ on the fourth edge, leading to

$$m_1^{e_1} = 2(a_1 - a_2), \quad m_1^{e_2} = 2(a_3 + a_4), \quad m_1^{e_3} = 2(a_1 + a_2), \quad m_1^{e_4} = 2(a_3 - a_4). \tag{A.8}$$

We solve the system of equations obtained by an analogous procedure to the one described for NT1 element in Section 4.3.2 leading to the shape functions demonstrated in Figure B.2, which read

$$\begin{aligned}
\mathbf{v}_1^1 &= \begin{pmatrix} (-\eta + 1)/4 \\ 0 \end{pmatrix}, & \mathbf{v}_2^1 &= \begin{pmatrix} 0 \\ (\xi + 1)/4 \end{pmatrix}, \\
\mathbf{v}_3^1 &= \begin{pmatrix} (\eta + 1)/4 \\ 0 \end{pmatrix}, & \mathbf{v}_4^1 &= \begin{pmatrix} 0 \\ (-\xi + 1)/4 \end{pmatrix},
\end{aligned} \tag{A.9}$$

where \mathbf{v}_i^1 is associated with edge e_i for $i = 1, \dots, 4$.

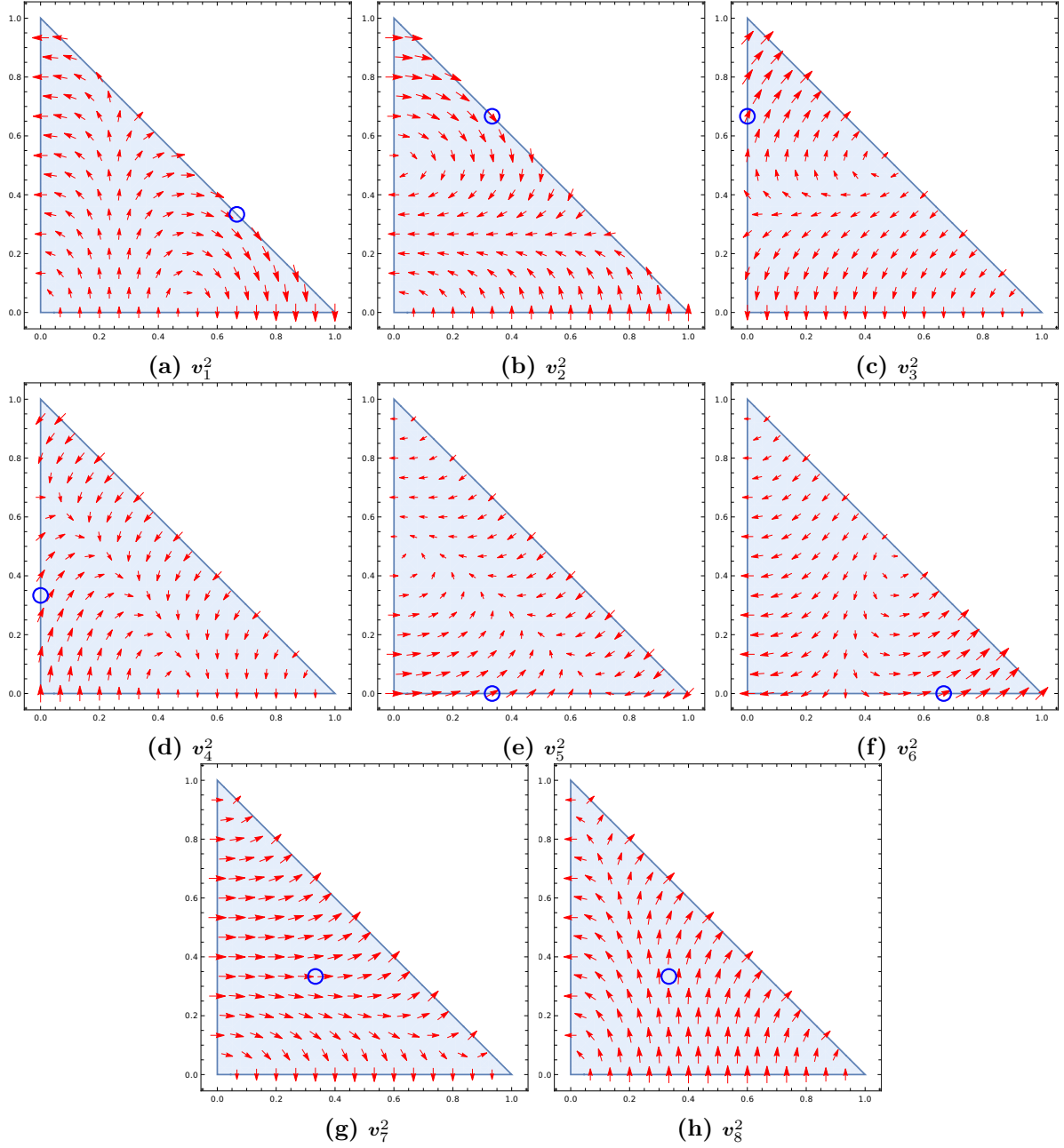


Figure A.1: Tangential-conforming vectorial shape functions of NT2 element. Blue circles indicate the position where the dofs are defined. Taken from SCHRÖDER ET AL. [2022].

C Second-order quadrilateral element NQ2

The Nédélec space of a second-order quadrilateral element (NQ2) reads

$$\begin{aligned}
 [\mathcal{ND}^{\square}]_2^2 = & \left\{ \begin{bmatrix} 1 \\ 0 \end{bmatrix}, \begin{bmatrix} \xi \\ 0 \end{bmatrix}, \begin{bmatrix} \eta \\ 0 \end{bmatrix}, \begin{bmatrix} \xi\eta \\ 0 \end{bmatrix}, \begin{bmatrix} \eta^2 \\ 0 \end{bmatrix}, \begin{bmatrix} \xi\eta^2 \\ 0 \end{bmatrix}, \right. \\
 & \left. \begin{bmatrix} 0 \\ 1 \end{bmatrix}, \begin{bmatrix} 0 \\ \xi \end{bmatrix}, \begin{bmatrix} 0 \\ \eta \end{bmatrix}, \begin{bmatrix} 0 \\ \xi\eta \end{bmatrix}, \begin{bmatrix} 0 \\ \xi^2 \end{bmatrix}, \begin{bmatrix} 0 \\ \eta\xi^2 \end{bmatrix} \right\}, \tag{A.10}
 \end{aligned}$$

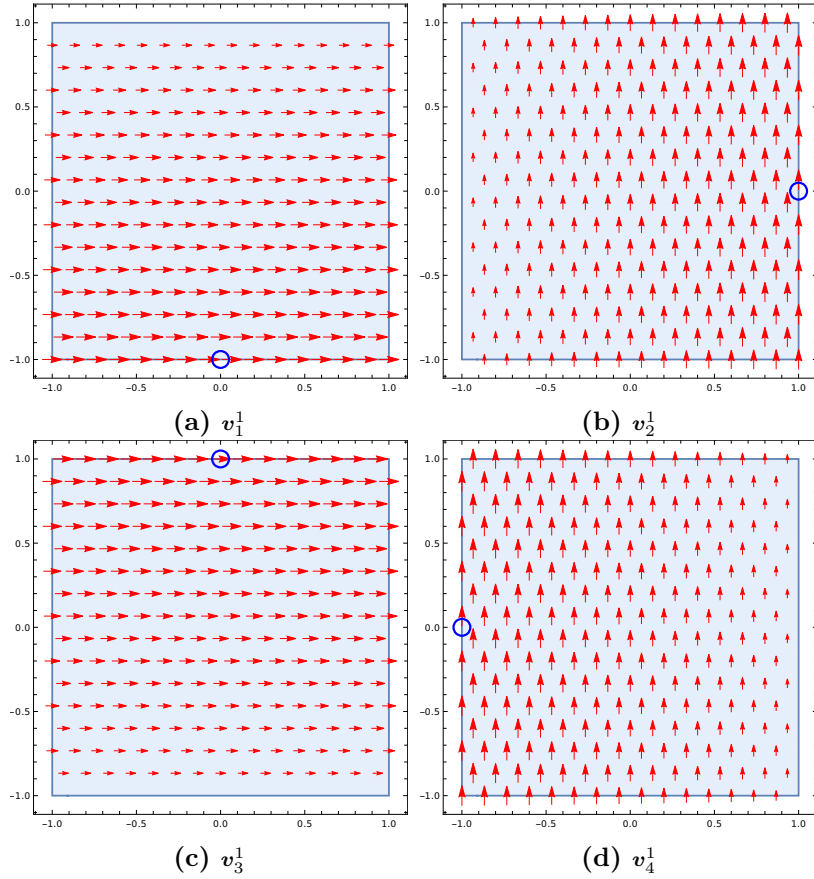


Figure B.2: Tangential-conforming vectorial shape functions of NQ1 element. Blue circles indicate the position where the dofs are defined. Taken from SCHRÖDER ET AL. [2022].

and the vectorial shape functions have the following general form

$$\mathbf{v}^2 = \begin{pmatrix} a_1 + a_2 \xi + a_3 \eta + a_4 \xi\eta + a_5 \eta^2 + a_6 \xi\eta^2 \\ a_7 + a_8 \xi + a_9 \eta + a_{10} \xi\eta + a_{11} \xi^2 + a_{12} \eta\xi^2 \end{pmatrix}, \quad (\text{A.11})$$

where $a_i, i = 1, \dots, 12$ are coefficients yet to be defined based on the dofs. Starting from Equations (4.19) and (4.21), explicit functions $r_j, j = 1, 2$ and $\mathbf{q}_i, i = 1, 2, 3, 4$ are set as

$$\begin{aligned} \text{edge 1: } r_1 &= \frac{1}{2}(1 - \xi), & r_2 &= \frac{1}{2}(1 + \xi), \\ \text{edge 2: } r_1 &= \frac{1}{2}(1 - \eta), & r_2 &= \frac{1}{2}(1 + \eta), \\ \text{edge 3: } r_1 &= \frac{1}{2}(1 + \xi), & r_2 &= \frac{1}{2}(1 - \xi), \\ \text{edge 4: } r_1 &= \frac{1}{2}(1 + \eta), & r_2 &= \frac{1}{2}(1 - \eta), \\ \text{inner : } \mathbf{q}_1 &= \begin{bmatrix} \frac{1}{2}(1 + \xi) \\ 0 \end{bmatrix}, & \mathbf{q}_2 &= \begin{bmatrix} \frac{1}{2}(1 - \xi) \\ 0 \end{bmatrix}, \\ & \mathbf{q}_3 &= \begin{bmatrix} 0 \\ \frac{1}{2}(1 + \eta) \end{bmatrix}, & \mathbf{q}_4 &= \begin{bmatrix} 0 \\ \frac{1}{2}(1 - \eta) \end{bmatrix}. \end{aligned} \quad (\text{A.12})$$

The edge and inner dofs are calculated according to Equations (4.19) and (4.21) considering that tangential vectors and coordinates coloration are identical to the NQ1 element,

such that

$$\begin{aligned}
m_1^{e_1} &= \frac{1}{3}(3a_1 - a_2 - 3a_3 + a_4 + 3a_5 - a_6), & m_2^{e_1} &= \frac{1}{3}(3a_1 + a_2 - 3a_3 - a_4 + 3a_5 + a_6), \\
m_1^{e_2} &= \frac{1}{3}(-a_{10} + 3a_{11} - a_{12} + 3a_7 + 3a_8 - a_9), & m_2^{e_2} &= \frac{1}{3}(a_{10} + 3a_{11} + a_{12} + 3a_7 + 3a_8 + a_9), \\
m_1^{e_3} &= \frac{1}{3}(3a_1 + a_2 + 3a_3 + a_4 + 3a_5 + a_6), & m_2^{e_3} &= \frac{1}{3}(3a_1 - a_2 + 3a_3 - a_4 + 3a_5 - a_6), \\
m_1^{e_4} &= \frac{1}{3}(-a_{10} + 3a_{11} + a_{12} + 3a_7 - 3a_8 + a_9), & m_2^{e_4} &= \frac{1}{3}(a_{10} + 3a_{11} - a_{12} + 3a_7 - 3a_8 - a_9), \\
m_1^{\text{inner}} &= \frac{2}{9}(9a_1 + 3a_2 + 3a_5 + a_6), & m_2^{\text{inner}} &= \frac{2}{9}(9a_1 - 3a_2 + 3a_5 - a_6), \\
m_3^{\text{inner}} &= \frac{2}{9}(3a_{11} + a_{12} + 9a_7 + 3a_9), & m_4^{\text{inner}} &= \frac{2}{9}(3a_{11} - a_{12} + 9a_7 - 3a_9).
\end{aligned} \tag{A.13}$$

Tangential-conforming shape functions demonstrated in Figure C.3 are obtained by an analogous procedure as described for NT1 element in Section 4.3.2, leading to

$$\begin{aligned}
\text{edge 1: } \mathbf{v}_1^2 &= \begin{pmatrix} -1/8 - \eta/4 + 3\eta^2/8 + 3\xi/8 + 3\eta\xi/4 - 9\eta^2\xi/8 \\ 0 \end{pmatrix}, \\
\mathbf{v}_2^2 &= \begin{pmatrix} -1/8 - \eta/4 + 3\eta^2/8 - 3\xi/8 - 3\eta\xi/4 + 9\eta^2\xi/8 \\ 0 \end{pmatrix}, \\
\text{edge 2: } \mathbf{v}_3^2 &= \begin{pmatrix} 0 \\ -1/8 + 3\eta/8 + \xi/4 - 3\eta\xi/4 + 3\xi^2/8 - 9\eta\xi^2/8 \end{pmatrix}, \\
\mathbf{v}_4^2 &= \begin{pmatrix} 0 \\ -1/8 - 3\eta/8 + \xi/4 + 3\eta\xi/4 + 3\xi^2/8 + 9\eta\xi^2/8 \end{pmatrix}, \\
\text{edge 3: } \mathbf{v}_5^2 &= \begin{pmatrix} -1/8 + \eta/4 + 3\eta^2/8 - 3\xi/8 + 3\eta\xi/4 + 9\eta^2\xi/8 \\ 0 \end{pmatrix}, \\
\mathbf{v}_6^2 &= \begin{pmatrix} -1/8 + \eta/4 + 3\eta^2/8 + 3\xi/8 - 3\eta\xi/4 - 9\eta^2\xi/8 \\ 0 \end{pmatrix}, \\
\text{edge 4: } \mathbf{v}_7^2 &= \begin{pmatrix} 0 \\ -1/8 - 3\eta/8 - \xi/4 - 3\eta\xi/4 + 3\xi^2/8 + 9\eta\xi^2/8 \end{pmatrix}, \\
\mathbf{v}_8^2 &= \begin{pmatrix} 0 \\ -1/8 + 3\eta/8 - \xi/4 + 3\eta\xi/4 + 3\xi^2/8 - 9\eta\xi^2/8 \end{pmatrix}, \\
\text{inner: } \mathbf{v}_9^2 &= \begin{pmatrix} 3/8 - 3\eta^2/8 + 9\xi/8 - 9\eta^2\xi/8 \\ 0 \end{pmatrix}, \\
\mathbf{v}_{10}^2 &= \begin{pmatrix} 3/8 - 3\eta^2/8 - 9\xi/8 + 9\eta^2\xi/8 \\ 0 \end{pmatrix}, \\
\mathbf{v}_{11}^2 &= \begin{pmatrix} 0 \\ 3/8 + 9\eta/8 - 3\xi^2/8 - 9\eta\xi^2/8 \end{pmatrix}, \\
\mathbf{v}_{12}^2 &= \begin{pmatrix} 0 \\ 3/8 - 9\eta/8 - 3\xi^2/8 + 9\eta\xi^2/8 \end{pmatrix}.
\end{aligned} \tag{A.14}$$

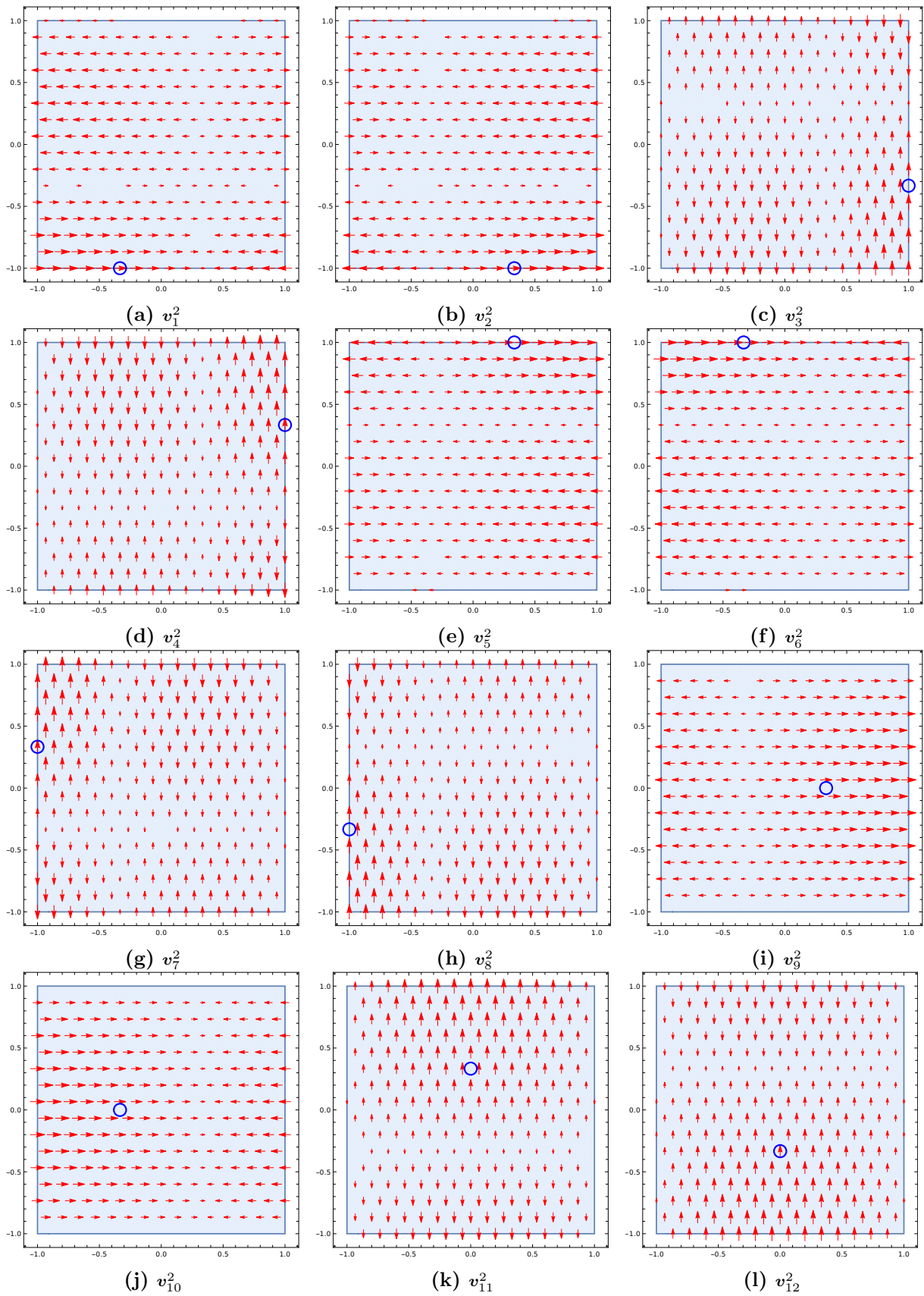


Figure C.3: Tangential-conforming vectorial shape functions of NQ2 element. Blue circles indicate the position where the dofs are defined. Taken from SCHRÖDER ET AL. [2022].

B Voigt notation

Because this thesis concentrates solely on two-dimensional case, Voigt notation will be introduced within this context. The fourth-order elasticity tensor \mathbb{C} written in 4×4 matrix notation based on the vector notation of the stresses $\hat{\boldsymbol{\sigma}} = [\sigma_{11}, \sigma_{22}, \sigma_{12}, \sigma_{21}]$ and the strains $\hat{\boldsymbol{\varepsilon}} = [\varepsilon_{11}, \varepsilon_{22}, \varepsilon_{12}, \varepsilon_{21}]$ reads

$$\hat{\mathbb{C}} = \begin{bmatrix} \mathbb{C}_{1111} & \mathbb{C}_{1122} & \mathbb{C}_{1112} & \mathbb{C}_{1121} \\ \mathbb{C}_{2211} & \mathbb{C}_{2222} & \mathbb{C}_{2212} & \mathbb{C}_{2221} \\ \mathbb{C}_{1211} & \mathbb{C}_{1222} & \mathbb{C}_{1212} & \mathbb{C}_{1221} \\ \mathbb{C}_{2111} & \mathbb{C}_{2122} & \mathbb{C}_{2112} & \mathbb{C}_{2121} \end{bmatrix}. \quad (\text{B.1})$$

For the symmetric case, i.e. $\sigma_{12} = \sigma_{21}$ and $\varepsilon_{12} = \varepsilon_{21}$, the fourth-order elasticity tensor \mathbb{C} written in 3×3 matrix notation based on the vector notation of the stresses $\tilde{\boldsymbol{\sigma}} = [\sigma_{11}, \sigma_{22}, 2\sigma_{12}]$ and the strains $\tilde{\boldsymbol{\varepsilon}} = [\varepsilon_{11}, \varepsilon_{22}, 2\varepsilon_{12}]$ reads

$$\tilde{\mathbb{C}} = \begin{bmatrix} \mathbb{C}_{1111} & \mathbb{C}_{1122} & \frac{1}{2}(\mathbb{C}_{1112} + \mathbb{C}_{1121}) \\ \mathbb{C}_{2211} & \mathbb{C}_{2222} & \frac{1}{2}(\mathbb{C}_{2212} + \mathbb{C}_{2221}) \\ \frac{1}{2}(\mathbb{C}_{1211} + \mathbb{C}_{2111}) & \frac{1}{4}(\mathbb{C}_{1222} + \mathbb{C}_{2122}) & \frac{1}{4}(\mathbb{C}_{1212} + \mathbb{C}_{2112} + \mathbb{C}_{1221} + \mathbb{C}_{2121}) \end{bmatrix}, \quad (\text{B.2})$$

which leads with the symmetries $\mathbb{C}_{ijkl} = \mathbb{C}_{klij} = \mathbb{C}_{jikl}$ to

$$\tilde{\mathbb{C}} = \begin{bmatrix} \mathbb{C}_{1111} & \mathbb{C}_{1122} & \mathbb{C}_{1112} \\ \text{sym} & \mathbb{C}_{2222} & \mathbb{C}_{2212} \\ & & \mathbb{C}_{1212} \end{bmatrix}. \quad (\text{B.3})$$

List of Figures

1.1	Annual number of peer-reviewed publications with the keyword “metamaterial” in Scopus (www.scopus.com) in the last 20 years.	1
2.1	The body in reference (material) configuration on the left and current (spatial) configuration on the right.	10
2.2	Illustration of a body detached into two parts to show the traction vector. The state of the stress can be expressed by the components of the traction vectors on three cutting planes with the normal vectors \mathbf{e}_1 , \mathbf{e}_2 , and \mathbf{e}_3 . . .	13
2.3	The micromorphic theory: the reference configuration on the left and current configuration on the right.	21
2.4	Genealogy tree of some generalized continua.	26
3.1	The stiffness of the relaxed micromorphic model (RMM) is bounded from above and below. Other generalized continua exhibit unbounded stiffness for small sizes. For large values of the characteristic length, linear elasticity with a microscopic elasticity tensor is recovered (one unit-cell) while linear elasticity with a macroscopic elasticity tensor is obtained for small values of the characteristic length (many unit-cells). Taken from SARHIL ET AL. [2024].	35
4.1	Discretization of the physical domain \mathcal{B} with the boundary $\partial\mathcal{B}$ resulting in an approximate domain \mathcal{B}_h with the boundary $\partial\mathcal{B}_h$ consisting of <i>nele</i> finite elements \mathcal{B}_e . Each finite element is formulated within the parameter space and subsequently mapped into the physical space.	40
4.2	The lowest-order ($k = 1$) Nédélec elements: triangle $[\mathcal{N}\mathcal{D}^\Delta]_1^2$ (right) and quadrilateral $[\mathcal{N}\mathcal{D}^\square]_1^2$ (left). Definition of the individual edges e_i . The red arrows indicate the orientation of tangential flux. Taken from SCHRÖDER ET AL. [2022]	43
4.3	Tangential-conforming vectorial shape functions of NT1 element. Blue circles indicate the position where the dofs are defined. Taken from SCHRÖDER ET AL. [2022]	45
4.4	Example of assembling of two neighboring elements which satisfy the orientation consistency via the orientation parameter α_I . Taken from SCHRÖDER ET AL. [2022]	46
4.5	The implemented finite elements in the parameter space. Black dots represent the displacement nodes while red squares stand for micro-distortion field nodes associated with 2×2 tensorial dofs in Lagrange formulation. Red arrows and crosses indicate the edge and inner vectorial dofs, respectively, of the micro-distortion field used in Nédélec formulation. Taken from SCHRÖDER ET AL. [2022]	48
4.6	Patch-test discretization. Taken from SCHRÖDER ET AL. [2022]	54

4.7	The error measurements $\ \mathbf{u} - \bar{\mathbf{u}}\ _{L^2}$ and $\ \mathbf{P} - \bar{\mathbf{P}}\ _{L^2}$ of the higher-order patch-test with quadratic displacement for element T2NT1 with varying number of equations in (d). Three different types of finite element meshing were chosen for the convergence study, see (a-c). Taken from SCHRÖDER ET AL. [2022]	55
4.8	The error measurements $\ \mathbf{u} - \bar{\mathbf{u}}\ _{L^2}$ and $\ \mathbf{P} - \bar{\mathbf{P}}\ _{L^2}$ of the higher-order patch-test with quadratic displacement for element Q2NQ1 with varying number of equations in (d). Three different types of finite element meshing were chosen for the convergence study, see (a-c). Taken from SCHRÖDER ET AL. [2022]	56
4.9	2D homogeneous rectangular. The inspection line, used in Figures 4.11 and 4.12, can be seen in red color. Taken from SCHRÖDER ET AL. [2022]	57
4.10	Displacement and micro-distortion field components. Taken from SCHRÖDER ET AL. [2022].	58
4.11	Illustration of P_{11} along the inspection line $y = 0.5$ using nodal elements with different mesh densities on regular structured meshes. Taken from SCHRÖDER ET AL. [2022].	59
4.12	Illustration of P_{11} along the inspection line $y = 0.5$ using $H^1(\mathcal{B}) \times H(\text{curl}, \mathcal{B})$ elements with different mesh densities on regular structured meshes. Taken from SCHRÖDER ET AL. [2022].	60
4.13	Computational convergence study (b) of first mesh depicted in (a). Taken from SCHRÖDER ET AL. [2022].	61
4.14	Computational convergence study (b) of second mesh depicted in (a). Taken from SCHRÖDER ET AL. [2022].	62
4.15	Computational convergence study (b) of third mesh depicted in (a). Taken from SCHRÖDER ET AL. [2022].	63
4.16	Boundary value problem: pure shear. Taken from SCHRÖDER ET AL. [2022].	64
4.17	Non-vanishing micro-distortion components of the second boundary problem using 3040 Q2NQ2 elements for $L_c = 5$. Taken from SCHRÖDER ET AL. [2022].	65
4.18	The non-vanishing components of \mathbf{P} along the radius for the $H^1(\mathcal{B}) \times H^1(\mathcal{B})$ elements using three mesh densities and $L_c = 5$. Taken from SCHRÖDER ET AL. [2022].	65
4.19	The non-vanishing components of \mathbf{P} along the radius for $H^1(\mathcal{B}) \times H(\text{curl}, \mathcal{B})$ elements using three mesh densities and $L_c = 5$. Taken from SCHRÖDER ET AL. [2022].	66
4.20	Elastic energy density along the radius. Taken from SCHRÖDER ET AL. [2022].	67
4.21	The non-vanishing components of \mathbf{P} and $\nabla \mathbf{u}$ along the radius. $\nabla \mathbf{u}$ is not influenced by the value of the characteristic length L_c . Taken from SCHRÖDER ET AL. [2022].	67

4.22	Total potential varying the characteristic length. Taken from SCHRÖDER ET AL. [2022].	68
4.23	Force stress shear component $\sigma_{r\theta} = \sigma_{\theta r}$ plotted along the radius. Taken from SCHRÖDER ET AL. [2022].	68
4.24	Non-zero component of moment stress m_{rz} plotted along the radius. Taken from SCHRÖDER ET AL. [2022].	69
4.25	Micro-stress shear component $(\sigma_{\text{micro}})_{r\theta} = (\sigma_{\text{micro}})_{\theta r}$ plotted along the radius. Taken from SCHRÖDER ET AL. [2022].	69
5.1	The beam models, compare Figure 5.3. Taken from SARHIL ET AL. [2023c].	73
5.2	Illustration shows the geometry of the specimens for $n = 1, 2, 3, 4, 5$ with the assumed unit-cell. The number of finite elements with degrees of freedom (dofs) are shown in parentheses. Taken from SARHIL ET AL. [2023c].	74
5.3	The boundary conditions of the fully resolved metamaterial shown exemplarily for $n = 2$ ($H \times L = 2l \times 24l$). Taken from SARHIL ET AL. [2023c].	75
5.4	The normalized bending stiffness varying the beam size $H \times L = nl \times 12nl$. Taken from SARHIL ET AL. [2023c].	76
5.5	The possible choices of the unit-cell with cubic symmetry. The edge length of the unit-cell equals to l for (1) and (2) and $\sqrt{2}l$ for (3) and (4). Taken from SARHIL ET AL. [2023c].	77
5.6	The normalized bending stiffness varying the beam size $H \times L = nl \times 12nl$ compared to the ones obtained by linear elasticity with different elasticity tensors shown in Section 5.2.2. Taken from SARHIL ET AL. [2023c].	79
5.7	Illustration shows the procedure used to calculate β_i . Taken from SARHIL ET AL. [2023c].	80
5.8	The values of the parameter β_i calculated for different unit-cells. Unit-cell (a) provides the stiffest flexural stiffness with $\beta^* = \beta_1 = 1.64$. Taken from SARHIL ET AL. [2023c].	81
5.9	The parameter β converges to the value one when increasing the size of a cluster of unit cells ($n \times n$) shown exemplarily for type (a) in Figure 5.8. We also show the extrapolated value $\beta = 1.75$. Taken from SARHIL ET AL. [2023c].	81
5.10	The normalized bending stiffness varying the beam size $H \times L = nl \times 12nl$ compared to the ones obtained by linear elasticity with different elasticity tensors shown in Section 5.2.3. Taken from SARHIL ET AL. [2023c].	82
5.11	The boundary value problems of the homogeneous relaxed micromorphic model for both loading cases. These boundary value problems are equivalent to the two cases of the heterogeneous metamaterial shown in Figure 5.3. The upper and lower edges are traction-free. Taken from SARHIL ET AL. [2023c].	83

5.12	The normalized bending stiffness obtained by the relaxed micromorphic model for both loading cases for the symmetric force stress scenario $\mathbb{C}_c = \mathbf{0}$ while varying the characteristic length L_c . Sufficient BCs indicate applying the consistent coupling condition on the left and right edges, see Figure 5.11. Removing the consistent coupling condition on left or right edge is considered as insufficient and leads to no size-effect. Taken from SARHIL ET AL. [2023c].	84
5.13	The normalized bending stiffness obtained by the relaxed micromorphic model for both loading cases with non-symmetric force stress and with varying the characteristic length L_c . Different scenarios are investigated for the boundary conditions of the micro-distortion field. Enforcing the consistent coupling condition on both left and right edges (c) reproduces the results of the symmetric force stress case in Figure 5.11 and Cosserat modulus has no effect. Taken from SARHIL ET AL. [2023c].	85
5.14	The deformed beams for the case $\mathbb{C}_{\text{micro}} = 1000 \mathbb{C}_{\text{macro}}$ "Cosserat type" with $L_c = 1000 m$ and $\mu_c = 2 \mu_{\text{macro}}$. The classical bending deformation can only be induced when the consistent coupling condition is applied on both its left and right ends (d). Taken from SARHIL ET AL. [2023c].	86
5.15	The relative total energy obtained by the relaxed micromorphic model for both loading cases with non-symmetric force stress ($\mu_c \neq 0$) and with varying the characteristic length L_c . Here, we assume $\mathbb{C}_{\text{micro}} = 1000 \mathbb{C}_{\text{macro}}$ leading to a skew-symmetric micro-distortion field which retrieves the Cosserat model since the curvature expression is then equivalent with the Cosserat framework, see GHIBA ET AL. [2023]. Different scenarios are investigated for the boundary conditions of the micro-distortion field. Taken from SARHIL ET AL. [2023c].	87
5.16	The normalized bending stiffness varying the beam size $H \times L = n l \times 12 n l$ obtained by the fully discretized metamaterial and the relaxed micromorphic model. We analyze here different choices for $\mathbb{C}_{\text{micro}}$ with varying L_c and fixing $\mu = \mu_{\text{macro}}$. The results are equivalent for both loading cases. Taken from SARHIL ET AL. [2023c].	90
5.17	The normalized bending stiffness varying the beam size $H \times L = n l \times 12 n l$ obtained by the fully discretized metamaterial and the relaxed micromorphic model. We analyze here different choices for $\mathbb{C}_{\text{micro}}$ with varying μ and fixing $L_c = l$. The results are equivalent for both loading cases. Taken from SARHIL ET AL. [2023c].	91
5.18	Boundary value problem: pure shear, shown exemplarily for $n = 2$, for the fully discretized metamaterial and the homogeneous relaxed micromorphic continuum. Taken from SARHIL ET AL. [2023c].	92
5.19	The normalized shear force varying the specimen's size $H \times L$ for different choices of $\mathbb{C}_{\text{micro}}$. Taken from SARHIL ET AL. [2023c].	94
5.20	Boundary value problem: cantilever, shown exemplarily for $n = 2$, for the fully discretized metamaterial and the homogeneous relaxed micromorphic continuum. Taken from SARHIL ET AL. [2023c].	95

5.21	The beam model of the cantilever and the deformed shape for $n = 2$. Taken from SARHIL ET AL. [2023c].	95
5.22	The inverse of the normalized deflection at the free end of the cantilever ($x = 0$) for varying the specimen's size $H \times L$ for different choices of $\mathbb{C}_{\text{micro}}$. Taken from SARHIL ET AL. [2023c].	96
6.1	Unit-cell with the material and geometrical parameters. Taken from SARHIL ET AL. [2024].	100
6.2	Illustration of the homogenization algorithm used to identify the parameters of an equivalent linear elastic medium under affine kinematic boundary condition. Taken from SARHIL ET AL. [2024].	101
6.3	Results of the parameter identification algorithm for an equivalent linear elasticity continuum under affine boundary conditions. Taken from SARHIL ET AL. [2024].	105
6.4	Periodicity condition of the fluctuation field is enforced on both heterogeneous and homogeneous equivalent continua. Taken from SARHIL ET AL. [2024].	106
6.5	Results of the parameter identification algorithm for an equivalent linear elasticity continuum under periodic boundary conditions. Taken from SARHIL ET AL. [2024].	107
6.6	Illustration of the scaling L_c/n delivering the intended “smaller is stiffer” effect for computations on a domain of fixed size and constant L_c . Taken from SARHIL ET AL. [2024].	108
6.7	Illustration of the minimization problem to obtain the material parameters in the RMM. The consistent coupling condition is enforced on the whole boundary. Taken from SARHIL ET AL. [2024].	110
6.8	Results of the parameter identification algorithm for the relaxed micromorphic model. We refer to the obtained final parameters set here as parameter set 1 . Taken from SARHIL ET AL. [2024].	114
6.9	Results of the parameter identification algorithm for the relaxed micromorphic model. Here, we impose a constraint on the microscopic elasticity tensor $\mathbb{C}_{\text{micro}}$ to ensure it is not stiffer than the stiff matrix. We refer to the obtained final parameters set here as parameter set 2 . Taken from SARHIL ET AL. [2024].	117
6.10	Results of the parameter identification algorithm for the relaxed micromorphic model. Here, we impose a constraint on the microscopic elasticity tensor $\mathbb{C}_{\text{micro}}$ to ensure it is not stiffer than the stiff matrix. We start with different initial values and the algorithm delivers the same values as in Figure 6.9. Taken from SARHIL ET AL. [2024].	118
6.11	Results of the parameter identification algorithm for the Cosserat model. Taken from SARHIL ET AL. [2024].	119
6.12	Results of the parameter identification algorithm for the simplified full micromorphic model. Taken from SARHIL ET AL. [2024].	122

6.13	Results of the parameter identification algorithm for the full micromorphic model with isotropic curvature. Taken from SARHIL ET AL. [2024].	123
6.14	The total energy of the heterogeneous material, the relaxed micromorphic model, the Cosserat case, and the Eringen-Mindlin full micromorphic model with both the simplified and isotropic curvature. We show 7 random deformation modes with the deformed shape for $n = 1$ scaled by a factor of three. Taken from SARHIL ET AL. [2024].	125
6.15	The total energy of the heterogeneous material and the homogeneous relaxed micromorphic model is examined for the two parameter sets, varying the size for four modes that were not included in the algorithm. We also show the outcomes of the Cosserat and the simplified Eringen-Mindlin micromorphic model. Dirichlet boundary conditions are set on the whole boundary $\mathbf{u} = \bar{\mathbf{u}}$ on \mathcal{B} . The deformed shape is shown for $n = 1$ enhanced by a factor of three. Taken from SARHIL ET AL. [2024].	126
A.1	Tangential-conforming vectorial shape functions of NT2 element. Blue circles indicate the position where the dofs are defined. Taken from SCHRÖDER ET AL. [2022].	133
B.2	Tangential-conforming vectorial shape functions of NQ1 element. Blue circles indicate the position where the dofs are defined. Taken from SCHRÖDER ET AL. [2022].	134
C.3	Tangential-conforming vectorial shape functions of NQ2 element. Blue circles indicate the position where the dofs are defined. Taken from SCHRÖDER ET AL. [2022].	136

List of Tables

4.1	The parametric $H^1(\mathcal{B})$ -conforming elements with the shape functions. . . .	42
4.2	Material parameters of the third boundary problem, see Figure 4.16. Taken from SCHRÖDER ET AL. [2022]	64
5.1	Material parameters of the assumed metamaterial. Taken from SARHIL ET AL. [2023c].	73
5.2	The elasticity parameters of the unit-cells shown in Figure 5.5 under affine Dirichlet boundary conditions. The elasticity parameters define elasticity tensors which exhibit cubic symmetry similar to $\mathbb{C}_{\text{macro}}$. Taken from SARHIL ET AL. [2023c].	78

References

- B. E. Abali. Revealing the physical insight of a length-scale parameter in metamaterials by exploiting the variational formulation. *Continuum Mechanics and Thermodynamics*, 31:885–894, 2019.
- B. E. Abali and E. Barchiesi. Additive manufacturing introduced substructure and computational determination of metamaterials parameters by means of the asymptotic homogenization. *Continuum Mechanics and Thermodynamics*, 33:993–1009, 2021.
- B. E. Abali, H. Yang, and P. Papadopoulos. A computational approach for determination of parameters in generalized mechanics. In H. Altenbach, W. H. Müller, and B. E. Abali, editors, *Higher Gradient Materials and Related Generalized Continua*, pages 1–18. Springer International Publishing, Cham, 2019.
- B. E. Abali, B. Vazic, and P. Newell. Influence of microstructure on size effect for metamaterials applied in composite structures. *Mechanics Research Communications*, 122:103877, 2022.
- S. Abdullah, G. Xiao, and R. Amaya. A review on the history and current literature of metamaterials and its applications to antennas & radio frequency identification (RFID) devices. *IEEE Journal of Radio Frequency Identification*, 5(4):427–445, 2021.
- E. Aifantis. On the role of gradients in the localization of deformation and fracture. *International Journal of Engineering Science*, 30(10):1279–1299, 1992.
- E. Aifantis. On the gradient approach - Relation to Eringen’s nonlocal theory. *International Journal of Engineering Science*, 49(12):1367–1377, 2011.
- A. Aivaliotis, D. Tallarico, M. V. d’Agostino, A. Daouadji, P. Neff, and A. Madeo. Frequency- and angle-dependent scattering of a finite-sized meta-structure via the relaxed micromorphic model. *Archive of Applied Mechanics*, 90:1073–1096, 2020.
- K. S. Al-Basyouni, A. Tounsi, and S. R. Mahmoud. Size dependent bending and vibration analysis of functionally graded micro beams based on modified couple stress theory and neutral surface position. *Composite Structures*, 125:621–630, 2015.
- S. Alavi, J.-F. Ganghoffer, H. Reda, and M. Sadighi. Construction of micromorphic continua by homogenization based on variational principles. *Journal of the Mechanics and Physics of Solids*, 153:104278, 2021a.
- S. Alavi, M. Nasimsobhan, J. Ganghoffer, A. Sinoimeri, and M. Sadighi. Chiral Cosserat model for architected materials constructed by homogenization. *Meccanica*, 56(10):2547–2574, 2021b.
- S. Alavi, J. Ganghoffer, M. Sadighi, M. Nasimsobhan, and A. Akbarzadeh. Continualization method of lattice materials and analysis of size effects revisited based on Cosserat models. *International Journal of Solids and Structures*, 254-255:111894, 2022a.
- S. Alavi, J.-F. Ganghoffer, and M. Sadighi. Chiral Cosserat homogenized constitutive models of architected media based on micromorphic homogenization. *Mathematics and Mechanics of Solids*, 27(10):2287–2313, 2022b.

- S. Alavi, J. F. Ganghoffer, H. Reda, and M. Sadighi. Hierarchy of generalized continua issued from micromorphic medium constructed by homogenization. *Continuum Mechanics and Thermodynamics*, 35(6):2163–2192, 2023.
- B. Altan and E. C. Aifantis. On some aspects in the special theory of gradient elasticity. *Journal of the Mechanical Behavior of Materials*, 8(3):231–282, 1997.
- S. Altan and E. Aifantis. On the structure of the mode iii crack-tip in gradient elasticity. *Scripta Metallurgica et Materialia*, 26(2):319–324, 1992.
- A. Ascenzi, P. Baschieri, and A. Benvenuti. The torsional properties of single selected osteons. *Journal of Biomechanics*, 27(7):875–884, 1994.
- H. Askes and E. C. Aifantis. Gradient elasticity in statics and dynamics: An overview of formulations, length scale identification procedures, finite element implementations and new results. *International Journal of Solids and Structures*, 48(13):1962–1990, 2011.
- H. Askes, A. V. Metrikine, A. V. Pichugin, and T. Bennett. Four simplified gradient elasticity models for the simulation of dispersive wave propagation. *Philosophical Magazine*, 88(28-29):3415–3443, 2008.
- N. Auffray, R. Bouchet, and Y. Bréchet. Strain gradient elastic homogenization of bidimensional cellular media. *International Journal of Solids and Structures*, 47(13):1698–1710, 2010.
- A. Bacigalupo and L. Gambarotta. Second-order computational homogenization of heterogeneous materials with periodic microstructure. *Journal of Applied Mathematics and Mechanics*, 90(10-11):796–811, 2010a.
- A. Bacigalupo and L. Gambarotta. Second-order computational homogenization of heterogeneous materials with periodic microstructure. *Zeitschrift für Angewandte Mathematik und Mechanik*, 90(10-11):796–811, 2010b.
- A. Bacigalupo, M. Paggi, F. Dal Corso, and D. Bigoni. Identification of higher-order continua equivalent to a Cauchy elastic composite. *Mechanics Research Communications*, 93:11–22, 2018. Mechanics from the 20th to the 21st Century: The Legacy of Gérard A. Maugin.
- D. Balzani. *Polyconvex Anisotropic Energies and Modeling of Damage Applied to Arterial Walls*. PhD thesis, University of Duisburg-Essen, 2006.
- G. Barbagallo. *Modeling fibrous composite reinforcements and metamaterials: theoretical development and engineering applications*. PhD thesis, INSA–Lyon, 2017.
- G. Barbagallo, A. Madeo, M. V. d’Agostino, R. Abreu, I.-D. Ghiba, and P. Neff. Transparent anisotropy for the relaxed micromorphic model: Macroscopic consistency conditions and long wave length asymptotics. *International Journal of Solids and Structures*, 120: 7–30, 2017.
- G. Barbagallo, D. Tallarico, M. V. d’Agostino, A. Aivaliotis, P. Neff, and A. Madeo. Relaxed micromorphic model of transient wave propagation in anisotropic band-gap metastructures. *International Journal of Solids and Structures*, 162:148–163, 2019.

- E. Barchiesi, M. Spagnuolo, and L. Placidi. Mechanical metamaterials: a state of the art. *Mathematics and Mechanics of Solids*, 24(1):212–234, 2019.
- K.-J. Bathe. *Finite element procedures*. Prentice Hall, New Jersey, 2006.
- K. Berkache, S. Deogekar, I. Goda, R. Picu, and J.-F. Ganghoffer. Construction of second gradient continuum models for random fibrous networks and analysis of size effects. *Composite Structures*, 181:347–357, 2017.
- D. Besdo. A numerical Cosserat-approach predicting the statical stability of a plane frictionless block-structure, and its boundary conditions. In O. Brüller, V. Mannl, and J. Najar, editors, *Advances in Continuum Mechanics: 39 Papers from International Experts Dedicated to Horst Lippmann*, pages 122–142. Springer Berlin Heidelberg, Berlin, Heidelberg, 1991.
- R. Biswas and L. H. Poh. A micromorphic computational homogenization framework for heterogeneous materials. *Journal of the Mechanics and Physics of Solids*, 102:187–208, 2017.
- T. Blesgen and P. Neff. Simple shear in nonlinear Cosserat micropolar elasticity: Existence of minimizers, numerical simulations, and occurrence of microstructure. *Mathematics and Mechanics of Solids*, 28(7):1576–1602, 2023.
- D. Boffi, F. Brezzi, and M. Fortin. *Mixed Finite Element Methods and Applications*, volume 44 of *Springer Series in Computational Mathematics*. Springer, Berlin, Heidelberg, 2014.
- C. Boutin. Microstructural effects in elastic composites. *International Journal of Solids and Structures*, 33(7):1023–1053, 1996.
- D. Brands. *Geometrical Modeling and Numerical Simulation of Heterogeneous Materials*. PhD thesis, University of Duisburg-Essen, 2012.
- S. Brenner and L. Scott. *The mathematical theory of finite element methods*. Springer, 2008.
- F. Brezzi and M. Fortin. *Mixed and Hybrid Finite Element Methods*. Springer, 1991.
- F. Brezzi, J. Douglas, and L. D. Marini. Two families of mixed finite elements for second order elliptic problems. *Numerische Mathematik*, 47:217–235, 1985.
- S. Brinkhues. *Modeling and simulation of arterial walls with focus on damage and residual stresses*. PhD thesis, University of Duisburg-Essen, 2012.
- A. Carcaterra, F. dell’Isola, R. Esposito, and M. Pulvirenti. Macroscopic description of microscopically strongly inhomogeneous systems: A mathematical basis for the synthesis of higher gradients metamaterials. *Archive for Rational Mechanics and Analysis*, 218: 1239–1262, 2015.
- Y. Chen and J. Lee. Connecting molecular dynamics to micromorphic theory. (i). instantaneous and averaged mechanical variables. *Physica A: Statistical Mechanics and its Applications*, 322:359–376, 2003a.

- Y. Chen and J. Lee. Determining material constants in micromorphic theory through phonon dispersion relations. *International Journal of Engineering Science*, 41(8):871–886, 2003b.
- E. Cosserat and F. Cosserat. *Théorie des corps déformable*, 1909. Librairie Scientifique A. Hermann et Fils, engl. translation by D. H. Delphenich, pdf available at (<http://www.mathematik.tu-darmstadt.de/fbereiche/analysis/pde/staff/neff/patrizio/Cosserat.html>), reprint 2009 by Hermann Librairie Scientifique, ISBN 978 27056 6920 1, Paris.
- C. W. Crowley, P. P. Silvester, and H. Hurwitz. Covariant projection elements for 3D vector field problems. *IEEE Transactions on Magnetics*, 24(1):397–400, 1988.
- M. d’Agostino, G. Rizzi, H. Khan, P. Lewintan, A. Madeo, and P. Neff. The consistent coupling boundary condition for the classical micromorphic model: existence, uniqueness and interpretation of parameters. *Continuum Mechanics and Thermodynamics*, 34(6):1393–1431, 2022a.
- M. V. d’Agostino, G. Barbagallo, I.-D. Ghiba, B. Eidel, P. Neff, and A. Madeo. Effective description of anisotropic wave dispersion in mechanical band-gap metamaterials via the relaxed micromorphic model. *Journal of Elasticity*, 139:299–329, 2020.
- M. V. d’Agostino, G. Rizzi, H. Khan, P. Lewintan, A. Madeo, and P. Neff. The consistent coupling boundary condition for the classical micromorphic model: existence, uniqueness and interpretation of the parameters. *Continuum Mechanics and Thermodynamics*, 2022b. doi: 10.1007/s00161-022-01126-3.
- M. V. d’Agostino, R. J. Martin, P. Lewintan, D. Bernardini, A. Danescu, and P. Neff. On the representation of fourth and higher order anisotropic elasticity tensors in generalized continuum models, 2024. URL <https://arxiv.org/abs/2401.08670>. To appear in *Mathematics and Mechanics of Solids*.
- D. Del Vesco and I. Giorgio. Dynamic problems for metamaterials: Review of existing models and ideas for further research. *International Journal of Engineering Science*, 80:153–172, 2014.
- F. Demore, G. Rizzi, M. Collet, P. Neff, and A. Madeo. Unfolding engineering metamaterials design: Relaxed micromorphic modeling of large-scale acoustic meta-structures. *Journal of the Mechanics and Physics of Solids*, 168:104995, 2022.
- C. Drapaca and S. Sivaloganathan. *Brief Review of Continuum Mechanics Theories*, pages 5–37. Springer New York, New York, NY, 2019.
- A. R. El Dhaba. Reduced micromorphic model in orthogonal curvilinear coordinates and its application to a metamaterial hemisphere. *Scientific Reports*, 10, 2020.
- W. Elmadih, D. Chronopoulos, and J. Zhu. Metamaterials for simultaneous acoustic and elastic bandgaps. *Scientific Reports*, 11(1):14635, 2021.
- V. A. Eremeyev, A. Cazzani, and F. dell’Isola. On nonlinear dilatational strain gradient elasticity. *Continuum Mechanics and Thermodynamics*, 33:1429–1463, 2021.

- A. Eringen. *Mechanics of Continua*. John Wiley & Sons, 1967.
- A. Eringen. Mechanics of micromorphic continua. In *Mechanics of Generalized Continua*, pages 18–35. Springer, Berlin, Heidelberg., 1968.
- A. Eringen. Linear theory of nonlocal elasticity and dispersion of plane waves. *International Journal of Engineering Science*, 10(5):425–435, 1972.
- A. Eringen. On differential equations of nonlocal elasticity and solutions of screw dislocation and surface waves. *Journal of Applied Physics*, 54(9):4703–4710, 09 1983.
- A. Eringen and E. S. Suhubi. Nonlinear theory of simple micro-elastic solids-I. *International Journal of Engineering Science*, 2(2):189–203, 1964.
- P. Fischer, M. Klassen, J. Mergheim, P. Steinmann, and R. Müller. Isogeometric analysis of 2D gradient elasticity. *Computational Mechanics*, 47:1432–0924, 2011.
- S. C. L. Fischer, L. Hillen, and C. Eberl. Mechanical metamaterials on the way from laboratory scale to industrial applications: Challenges for characterization and scalability. *Materials*, 13(16), 2020.
- S. Forest. Homogenization methods and mechanics of generalized continua - part 2. *Theoretical and Applied Mechanics*, 28-29:113–144, 2002.
- S. Forest. Micromorphic media. In H. Altenbach and V. A. Eremeyev, editors, *Generalized Continua from the Theory to Engineering Applications*, pages 249–300. Springer Vienna, Vienna, 2013.
- S. Forest. Nonlinear regularization operators as derived from the micromorphic approach to gradient elasticity, viscoplasticity and damage. *Proceedings of the Royal Society*, 472(2188):20150755, 2016.
- S. Forest. Strain gradient elasticity from capillarity to the mechanics of nano-objects. In A. Bertram and S. Forest, editors, *Mechanics of Strain Gradient Materials*, pages 37–70. Springer International Publishing, Cham, 2020.
- S. Forest and K. Sab. Cosserat overall modeling of heterogeneous materials. *Mechanics Research Communications*, 25(4):449–454, 1998.
- S. Forest and K. Sab. Stress gradient continuum theory. *Mechanics Research Communications*, 40:16–25, 2012.
- S. Forest and D. Trinh. Generalized continua and non-homogeneous boundary conditions in homogenisation methods. *Journal of Applied Mathematics and Mechanics*, 91(2): 90–109, 2011.
- J.-F. Ganghoffer and H. Reda. A variational approach of homogenization of heterogeneous materials towards second gradient continua. *Mechanics of Materials*, 158:103743, 2021. ISSN 0167-6636. doi: <https://doi.org/10.1016/j.mechmat.2021.103743>. URL <https://www.sciencedirect.com/science/article/pii/S0167663621000028>.

- J.-F. Ganghoffer, A. Wazne, and H. Reda. Frontiers in homogenization methods towards generalized continua for architected materials. *Mechanics Research Communications*, 130:104114, 2023.
- I.-D. Ghiba and P. Neff. Linear constrained Cosserat-shell models including terms up to $\mathcal{O}(h^5)$: conditional and unconditional existence and uniqueness. *Zeitschrift für angewandte Mathematik und Physik*, 74(2):47, 2023.
- I.-D. Ghiba, P. Neff, A. Madeo, L. Placidi, and G. Rosi. The relaxed linear micromorphic continuum: existence, uniqueness and continuous dependence in dynamics. *Mathematics and Mechanics of Solids*, 20(10):1171–1197, 2015.
- I.-D. Ghiba, P. Neff, and S. Owczarek. Existence results for non-homogeneous boundary conditions in the relaxed micromorphic model. *Mathematical Methods in the Applied Sciences*, 44(2):2040–2049, 2021.
- I.-D. Ghiba, G. Rizzi, A. Madeo, and P. Neff. Cosserat micropolar elasticity: Classical Eringen vs. dislocation form. *Journal of Mechanics of Materials and Structures*, 18(1): 93–123, 2023.
- R. N. Glaesener, J.-H. Bastek, F. Gonon, V. Kannan, B. Telgen, B. Spöttling, S. Steiner, and D. M. Kochmann. Viscoelastic truss metamaterials as time-dependent generalized continua. *Journal of the Mechanics and Physics of Solids*, 156:104569, 2021.
- F. Gmeineder, P. Lewintan, and P. Neff. Optimal incompatible Korn-Maxwell-Sobolev inequalities in all dimensions. *Calculus of Variations and Partial Differential Equations*, 62(6):182, 2023.
- F. Gmeineder, P. Lewintan, and P. Neff. Korn-Maxwell-Sobolev Inequalities for General Incompatibilities. *Mathematical Models and Methods in Applied Sciences*, 2024.
- I. Goda and J.-F. Ganghoffer. Construction of first and second order grade anisotropic continuum media for 3D porous and textile composite structures. *Composite Structures*, 141:292–327, 2016.
- M. Godio, I. Stefanou, K. Sab, J. Sulem, and S. Sakji. A limit analysis approach based on Cosserat continuum for the evaluation of the in-plane strength of discrete media: Application to masonry. *European Journal of Mechanics - A/Solids*, 66:168–192, 2017.
- P. Gourgiotis, G. Rizzi, P. Lewintan, D. Bernardini, A. Sky, A. Madeo, and P. Neff. Green’s functions for the isotropic planar relaxed micromorphic model - concentrated force and concentrated couple. *International Journal of Solids and Structures*, 292: 112700, 2024.
- M. Hoegen. *Modeling the passive mechanical response of soft tissues: constitutive modeling approaches, efficient parameter selection and subsequent adjustments due to residual stresses*. PhD thesis, University of Duisburg-Essen, 2019.
- S. B. Hosseini and J. Niiranen. 3D strain gradient elasticity: Variational formulations, isogeometric analysis and model peculiarities. *Computer Methods in Applied Mechanics and Engineering*, 389:114324, 2022.

-
- G. Hütter. Homogenization of a Cauchy continuum towards a micromorphic continuum. *Journal of the Mechanics and Physics of Solids*, 99:394–408, 2017.
- G. Hütter. On the micro-macro relation for the microdeformation in the homogenization towards micromorphic and micropolar continua. *Journal of the Mechanics and Physics of Solids*, 127:62–79, 2019.
- G. Hütter. Interpretation of micromorphic constitutive relations for porous materials at the microscale via harmonic decomposition. *Journal of the Mechanics and Physics of Solids*, page 105135, 2022.
- M. Igelbüscher. *Mixed and Hybrid Least-Squares FEM in Nonlinear Solid Mechanics*. PhD thesis, University of Duisburg-Essen, 2021.
- A. Iyer, A. Alù, and A. Epstein. Metamaterials and metasurfaces—historical context, recent advances, and future directions. *IEEE Transactions on Antennas and Propagation*, 68(3):1223–1231, 2020.
- R. Jänicke and H. Steeb. Minimal loading conditions for higher-order numerical homogenization schemes. *Archive of Applied Mechanics*, 82(8):1075–1088, 2012.
- J. Jeong and P. Neff. Existence, uniqueness and stability in linear Cosserat elasticity for weakest curvature conditions. *Mathematics and Mechanics of Solids*, 15(1):78–95, 2010.
- J. Jeong, H. Ramézani, I. Münch, and P. Neff. A numerical study for linear isotropic Cosserat elasticity with conformally invariant curvature. *Zeitschrift für Angewandte Mathematik und Mechanik*, 89(7):552–569, 2009.
- Y. Jiang and Y. Li. 3D printed auxetic mechanical metamaterial with chiral cells and re-entrant cores. *Scientific reports*, 8(1):2397, 2018.
- N. Jiménez, W. Huang, V. Romero-García, V. Pagneux, and J.-P. Groby. Ultra-thin metamaterial for perfect and quasi-omnidirectional sound absorption. *Applied Physics Letters*, 109(12):121902, 09 2016.
- X. Ju, R. Mahnken, L. Liang, and Y. Xu. Goal-oriented mesh adaptivity for inverse problems in linear micromorphic elasticity. *Computers and Structures*, 257:106671, 2021.
- M. Kadic, G. Milton, M. van Hecke, and M. Wegener. 3D metamaterials. *Nature Reviews Physics*, 1(3):198–210, 2019.
- M.-A. Keip. *Modeling of Electro-Mechanically Coupled Materials on Multiple Scales*. PhD thesis, University of Duisburg-Essen, 2012.
- S. Khakalo and J. Niiranen. Lattice structures as thermoelastic strain gradient metamaterials: Evidence from full-field simulations and applications to functionally step-wise-graded beams. *Composites Part B: Engineering*, 177:107224, 2019.
- S. Khakalo and J. Niiranen. Anisotropic strain gradient thermoelasticity for cellular structures: Plate models, homogenization and isogeometric analysis. *Journal of the Mechanics and Physics of Solids*, 134:103728, 2020.

- S. Khakalo, V. Balabanov, and J. Niiranen. Modelling size-dependent bending, buckling and vibrations of 2D triangular lattices by strain gradient elasticity models: Applications to sandwich beams and auxetics. *International Journal of Engineering Science*, 127:33–52, 2018.
- H. Khan, I.-D. Ghiba, A. Madeo, and P. Neff. Existence and uniqueness of Rayleigh waves in isotropic elastic Cosserat materials and algorithmic aspects. *Wave Motion*, 110:102898, 2022.
- R. C. Kirby, A. Logg, M. E. Rognes, and A. R. Terrel. Common and unusual finite elements. In *Automated Solution of Differential Equations by the Finite Element Method: The FEniCS Book*, pages 95–119. Springer Berlin Heidelberg, Berlin, Heidelberg, 2012.
- S. Kirchhof, A. Ams, and G. Hütter. On the question of the sign of size effects in the elastic behavior of foams. *Journal of Elasticity*, 2023.
- D. Knees, S. Owczarek, and P. Neff. A local regularity result for the relaxed micromorphic model based on inner variations. *Journal of Mathematical Analysis and Applications*, 519(2):126806, 2023.
- D. Knees, S. Owczarek, and P. Neff. Global regularity for a physically nonlinear version of the relaxed micromorphic model on lipschitz domains, 2024. URL <https://arxiv.org/abs/2403.17451>. To appear in Proceedings of the Royal Society of Edinburgh Section A: Mathematics.
- J. Korelc. Automatic generation of finite-element code by simultaneous optimization of expressions. *Theoretical Computer Science*, 187(1):231–248, 1997.
- J. Korelc and P. Wriggers. *Automation of Finite Element Methods*. Springer International Publishing, 2016.
- V. Kouznetsova, M. Geers, and W. Brekelmans. Multi-scale constitutive modelling of heterogeneous materials with a gradient-enhanced computational homogenization scheme. *International Journal for Numerical Methods in Engineering*, 54:1235–1260, 2002.
- V. Kouznetsova, M. Geers, and W. Brekelmans. Multi-scale second-order computational homogenization of multi-phase materials: a nested finite element solution strategy. *Computer Methods in Applied Mechanics and Engineering*, 193:5525–5550, 2004.
- R. Kumar, M. Kumar, J. Chohan, and S. Kumar. Overview on metamaterial: History, types and applications. *Materials Today: Proceedings*, 56:3016–3024, 2022. 3rd International Conference on Contemporary Advances in Mechanical Engineering.
- M. Labusch. *A two-scale homogenization scheme for the prediction of magneto-electric product properties*. PhD thesis, University of Duisburg-Essen, 2018.
- A. Lahbazi, I. Goda, and J.-F. Ganghoffer. Size-independent strain gradient effective models based on homogenization methods: Applications to 3D composite materials, pantograph and thin walled lattices. *Composite Structures*, 284:115065, 2022.
- R. Lakes. On the torsional properties of single osteons. *Journal of Biomechanics*, 28(11):1409–1410, 1995.

- R. Lakes. Cosserat shape effects in the bending of foams. *Mechanics of Advanced Materials and Structures*, 2022. doi: 10.1080/15376494.2022.2086328.
- M. Lazar. On gradient field theories: gradient magnetostatics and gradient elasticity. *Philosophical Magazine*, 94(25):2840–2874, 2014.
- M. Lazar, G. A. Maugin, and E. C. Aifantis. Dislocations in second strain gradient elasticity. *International Journal of Solids and Structures*, 43(6):1787–1817, 2006.
- J. Lee and A. Eringen. Continuum theory of smectic liquid crystals. *The Journal of Chemical Physics*, 58(10):4203–4211, 08 2003.
- J.-H. Lee, J. P. Singer, and E. L. Thomas. Micro-/nanostructured mechanical metamaterials. *Advanced Materials*, 24(36):4782–4810, 2012.
- M. Lei, W. Hong, Z. Zhao, C. Hamel, M. Chen, H. Lu, and H. . Qi. 3D printing of auxetic metamaterials with digitally reprogrammable shape. *ACS Applied Materials & Interfaces*, 11(25):22768–22776, 2019.
- P. Lewintan and P. Neff. L^p -trace-free generalized Korn inequalities for incompatible tensor fields in three space dimensions. *Proceedings of the Royal Society of Edinburgh: Section A Mathematics*, pages 1–32, 2021. ISSN 0308-2105.
- P. Lewintan, S. Müller, and P. Neff. Korn inequalities for incompatible tensor fields in three space dimensions with conformally invariant dislocation energy. *Calc. Var.*, 60(4):150, 2021. ISSN 1432-0835.
- A. Li, Q. Wang, M. Song, J. Chen, W. Su, S. Zhou, and L. Wang. On strain gradient theory and its application in bending of beam. *Coatings*, 12(9), 2022.
- J. Li and X.-B. Zhang. A numerical approach for the establishment of strain gradient constitutive relations in periodic heterogeneous materials. *European Journal of Mechanics - A/Solids*, 41:70–85, 2013.
- C. Liebold and W. H. Müller. Comparison of gradient elasticity models for the bending of micromaterials. *Computational Materials Science*, 116:52–61, 2016.
- C. Lu, M. Hsieh, Z. Huang, C. Zhang, Y. Lin, Q. Shen, F. Chen, and L. Zhang. Architectural design and additive manufacturing of mechanical metamaterials: A review. *Engineering*, 17:44–63, 2022.
- A. Madeo, P. Neff, I.-D. Ghiba, L. Placidi, and G. Rosi. Band gaps in the relaxed linear micromorphic continuum. *Zeitschrift für angewandte Mathematik und Mechanik*, 95(9): 880–887, 2015.
- A. Madeo, P. Neff, M. V. d’Agostino, and G. Barbagallo. Complete band gaps including non-local effects occur only in the relaxed micromorphic model. *Comptes Rendus Mécanique*, 344(11-12):784–796, 2016a.
- A. Madeo, P. Neff, I.-D. Ghiba, and G. Rosi. Reflection and transmission of elastic waves in non-local band-gap metamaterials: a comprehensive study via the relaxed micromorphic model. *Journal of the Mechanics and Physics of Solids*, 95:441–479, 2016b.

- A. Madeo, P. Neff, G. Barbagallo, M. V. d'Agostino, and I.-D. Ghiba. A review on wave propagation modeling in band-gap metamaterials via enriched continuum models. In *Mathematical Modelling in Solid Mechanics*, volume 69 of *Advanced Structured Materials*, pages 89–105. Springer, Singapore, 2017.
- M. Madeo, A. and Collet, M. Miniaci, K. Billon, M. Ouisse, and P. Neff. Modeling phononic crystals via the weighted relaxed micromorphic model with free and gradient micro-inertia. *Journal of Elasticity*, 130(1):59–83, 2018.
- R. D. Mindlin. Micro-structure in linear elasticity. *Archive for Rational Mechanics and Analysis*, 16:51–78, 1964.
- R. D. Mindlin. Second gradient of strain and surface-tension in linear elasticity. *International Journal of Solids and Structures*, 1(4):417–438, 1965.
- R. D. Mindlin and N. N. Eshel. On first strain-gradient theories in linear elasticity. *International Journal of Solids and Structures*, 4(1):109–124, 1968.
- L. Mohan, P. Nott, and K. Rao. A frictional Cosserat model for the flow of granular materials through a vertical channel. *Acta Mechanica*, 138(1):75–96, 1999.
- V. Monchiet, N. Auffray, and J. Yvonne. Strain-gradient homogenization: A bridge between the asymptotic expansion and quadratic boundary condition methods. *Mechanics of Materials*, 143:103309, 2020.
- P. Monk. An analysis of Nédélec's method for the spatial discretization of Maxwell's equations. *Journal of Computational and Applied Mathematics*, 47(1):101–121, 1993.
- S. M. Montgomery, X. Kuang, C. D. Armstrong, and H. J. Qi. Recent advances in additive manufacturing of active mechanical metamaterials. *Current Opinion in Solid State and Materials Science*, 24(5):100869, 2020.
- H. B. Mühlhaus. Shearband analysis in granular material by Cosserat-theory (in german). *Ingenieur-Archiv*, 56(5):389–399, 1986.
- J. C. Nédélec. Mixed finite elements in \mathbb{R}^3 . *Numerische Mathematik*, 35(3):315–341, 1980.
- J. C. Nédélec. A new family of mixed finite elements in \mathbb{R}^3 . *Numerische Mathematik*, 50:57–81, 1986.
- P. Neff. The Cosserat couple modulus for continuous solids is zero viz the linearized Cauchy-stress tensor is symmetric. *Zeitschrift für Angewandte Mathematik und Mechanik*, 86(11):892–912, 2006.
- P. Neff and S. Forest. A geometrically exact micromorphic model for elastic metallic foams accounting for affine microstructure. modelling, existence of minimizers, identification of moduli and computational results. *Journal of Elasticity*, 87(2):239–276, 2007.
- P. Neff and J. Jeong. A new paradigm: the linear isotropic Cosserat model with conformally invariant curvature energy. *Zeitschrift für Angewandte Mathematik und Mechanik*, 89(2):107–122, 2009.

- P. Neff, J. Jeong, and A. Fischle. Stable identification of linear isotropic Cosserat parameters: bounded stiffness in bending and torsion implies conformal invariance of curvature. *Acta Mechanica*, 211(3):237–249, 2010a.
- P. Neff, J. Jeong, I. Münch, and H. Ramézani. Linear Cosserat elasticity, conformal curvature and bounded stiffness. In *Mechanics of Generalized Continua: One Hundred Years After the Cosserats*, pages 55–63. Springer New York, 2010b.
- P. Neff, I.-D. Ghiba, A. Madeo, L. Placidi, and G. Rosi. A unifying perspective: the relaxed linear micromorphic continuum. *Continuum Mechanics and Thermodynamics*, 26(5):639–681, 2014a.
- P. Neff, J. Lankeit, and A. Madeo. On Grioli’s minimum property and its relation to Cauchy’s polar decomposition. *International Journal of Engineering Science*, 80:209–217, 2014b.
- P. Neff, I. D. Ghiba, M. Lazar, and A. Madeo. The relaxed linear micromorphic continuum: well-posedness of the static problem and relations to the gauge theory of dislocations. *The Quarterly Journal of Mechanics and Applied Mathematics*, 68(1):53–84, 2015.
- P. Neff, I. Münch, I.-D. Ghiba, and A. Madeo. On some fundamental misunderstandings in the indeterminate couple stress model. a comment on recent papers of A.R. Hadjesfandiari and G.F. Dargush. *International Journal of Solids and Structures*, 81:233–243, 2016.
- P. Neff, B. Eidel, M. V. d’Agostino, and A. Madeo. Identification of scale-independent material parameters in the relaxed micromorphic model through model-adapted first order homogenization. *Journal of Elasticity*, 139:269–298, 2020.
- A. N. Norris. The isotropic material closest to a given anisotropic material. *Journal of Mechanics of Materials and Structures*, 1(2):223–238, 2006.
- J. Nye. Some geometrical relations in dislocated crystals. *Acta Metallurgica*, 1(2):153–162, 1953.
- M. Olm, S. Badia, and A. F. Martín. On a general implementation of h- and p-adaptive curl-conforming finite elements. *Advances in Engineering Software*, 132:74–91, 2019.
- P. R. Onck. Cosserat modeling of cellular solids. *Comptes Rendus Mécanique*, 330(11):717–722, 2002.
- S. Owczarek, I.-D. Ghiba, M. V. d’Agostino, and P. Neff. Nonstandard micro-inertia terms in the relaxed micromorphic model: well-posedness for dynamics. *Mathematics and Mechanics of Solids*, 24(10):3200–3215, 2019.
- H. C. Park and R. S. Lakes. Cosserat micromechanics of human bone: Strain redistribution by a hydration sensitive constituent. *Journal of Biomechanics*, 19(5):385–397, 1986.
- L. Placidi, E. Barchiesi, and A. Battista. An inverse method to get further analytical solutions for a class of metamaterials aimed to validate numerical integrations. In F. dell’Isola, M. Sofonea, and D. Steigmann, editors, *Mathematical Modelling in Solid Mechanics*, pages 193–210. Springer Singapore, Singapore, 2017.

- J. Plocher and A. Panesar. Review on design and structural optimisation in additive manufacturing: Towards next-generation lightweight structures. *Materials & Design*, 183:108164, 2019.
- J. Qi, Z. Chen, P. Jiang, W. Hu, Y. Wang, Z. Zhao, X. Cao, S. Zhang, R. Tao, Y. Li, and D. Fang. Recent progress in active mechanical metamaterials and construction principles. *Advanced Science*, 9(1):2102662, 2022.
- P. A. Raviart and J. M. Thomas. A mixed finite element method for 2-nd order elliptic problems. In I. Galligani and E. Magenes, editors, *Mathematical Aspects of Finite Element Methods*, pages 292–315, Berlin, Heidelberg, 1977. Springer Berlin Heidelberg.
- H. Reda, S. E. Alavi, M. Nasimsobhan, and J.-F. Ganghoffer. Homogenization towards chiral Cosserat continua and applications to enhanced Timoshenko beam theories. *Mechanics of Materials*, 155:103728, 2021.
- G. Rizzi, G. Hütter, A. Madeo, and P. Neff. Analytical solutions of the simple shear problem for micromorphic models and other generalized continua. *Archive of Applied Mechanics*, 91:2237–2254, 2021a.
- G. Rizzi, G. Hütter, A. Madeo, and P. Neff. Analytical solutions of the cylindrical bending problem for the relaxed micromorphic continuum and other generalized continua. *Continuum Mechanics and Thermodynamics*, 33:1505–1539, 2021b.
- G. Rizzi, H. Khan, I.-D. Ghiba, A. Madeo, and P. Neff. Analytical solution of the uniaxial extension problem for the relaxed micromorphic continuum and other generalized continua (including full derivations). *Archive of Applied Mechanics*, 2021c. doi: 10.1007/s00419-021-02064-3.
- G. Rizzi, M. V. d’Agostino, P. Neff, and A. Madeo. Boundary and interface conditions in the relaxed micromorphic model: Exploring finite-size metastructures for elastic wave control. *Mathematics and Mechanics of Solids*, 27(6):1053–1068, 2022a.
- G. Rizzi, G. Hütter, H. Khan, I.-D. Ghiba, A. Madeo, and P. Neff. Analytical solution of the cylindrical torsion problem for the relaxed micromorphic continuum and other generalized continua (including full derivations). *Mathematics and Mechanics of Solids*, 27(3):507–553, 2022b.
- G. Rizzi, P. Neff, and A. Madeo. Metamaterial for inner protection and outer tuning through a relaxed micromorphic approach. *Philosophical Transactions of the Royal Society A: Mathematical, Physical and Engineering Sciences*, 380(2231):20210400, 2022c.
- G. Rizzi, D. Tallarico, P. Neff, and A. Madeo. Towards the conception of complex engineering meta-structures: Relaxed-micromorphic modelling of low-frequency mechanical diodes/high-frequency screens. *Wave Motion*, 113:102920, 2022d.
- G. Rizzi, M. V. d’Agostino, J. Voss, D. Bernardini, P. Neff, and A. Madeo. From frequency-dependent models to frequency-independent enriched continua for mechanical metamaterials. *European Journal of Mechanics - A/Solids*, 106:105269, 2024.

- M. E. Rognes, R. C. Kirby, and A. Logg. Efficient assembly of $H(\text{div})$ and $H(\text{curl})$ conforming finite elements. *SIAM Journal on Scientific Computing*, 31(9):4130–4151, 2009.
- O. Rokoš, M. M. Ameen, R. H. J. Peerlings, and M. G. D. Geers. Micromorphic computational homogenization for mechanical metamaterials with patterning fluctuation fields. *Journal of the Mechanics and Physics of Solids*, 123:119–137, 2019.
- O. Rokoš, M. M. Ameen, R. H. J. Peerlings, and M. G. D. Geers. Extended micromorphic computational homogenization for mechanical metamaterials exhibiting multiple geometric pattern transformations. *Extreme Mechanics Letters*, 37:100708, 2020a.
- O. Rokoš, J. Zeman, M. Doškář, and P. Krysl. Reduced integration schemes in micromorphic computational homogenization of elastomeric mechanical metamaterials. *Advanced Modeling and Simulation in Engineering Sciences*, 7, 2020b.
- Z. Rueger, C. S. Ha, and R. S. Lakes. Cosserat elastic lattices. *Meccanica*, 54:1983–1999, 2019.
- M. M. Saem, I.-D. Ghiba, and P. Neff. A geometrically nonlinear Cosserat (micropolar) curvy shell model via gamma convergence. *Journal of Nonlinear Science*, 33(5):70, 2023.
- B. C. Sarar, M. E. Yildizdag, and B. E. Abali. Comparison of homogenization techniques in strain gradient elasticity for determining material parameters. In H. Altenbach, A. Berezovski, F. dell’Isola, and A. Porubov, editors, *Sixty Shades of Generalized Continua: Dedicated to the 60th Birthday of Prof. Victor A. Eremeyev*, pages 631–644. Springer International Publishing, 2023.
- M. Sarhil, L. Scheunemann, P. Neff, and J. Schröder. On a tangential-conforming finite element formulation for the relaxed micromorphic model in 2D. *Proceedings in Applied Mathematics and Mechanics*, 21(1):e202100187, 2021.
- M. Sarhil, L. Scheunemann, J. Schröder, and P. Neff. Modeling the size-effect of metamaterial beams under bending via the relaxed micromorphic continuum. *Proceedings of Applied Mathematics and Mechanics*, 22(1):e202200033, 2023a.
- M. Sarhil, L. Scheunemann, J. Schröder, and P. Neff. On the identification of material parameters in the relaxed micromorphic continuum. *Proceedings of Applied Mathematics and Mechanics*, 23(3):e202300056, 2023b.
- M. Sarhil, L. Scheunemann, J. Schröder, and P. Neff. Size-effects of metamaterial beams subjected to pure bending: on boundary conditions and parameter identification in the relaxed micromorphic model. *Computational Mechanics*, 72(5):1091–1113, 2023c.
- M. Sarhil, L. Scheunemann, P. Lewintan, J. Schröder, and P. Neff. A computational approach to identify the material parameters of the relaxed micromorphic model. *Computer Methods in Applied Mechanics and Engineering*, 425:116944, 2024. doi: <https://doi.org/10.1016/j.cma.2024.116944>.

- T. A. Schaedler, A. J. Jacobsen, A. Torrents, A. E. Sorensen, J. Lian, J. R. Greer, L. Valdevit, and W. B. Carter. Ultralight metallic microlattices. *Science*, 334(6058):962–965, 2011.
- L. Scheunemann. *Scale-bridging of Elasto-Plastic Microstructures using Statistically Similar Representative Volume Elements*. PhD thesis, University of Duisburg-Essen, 2017.
- F. Schmidt, M. Krüger, M.-A. Keip, and C. Hesch. Computational homogenization of higher-order continua. *International Journal for Numerical Methods in Engineering*, 123(11):2499–2529, 2022.
- J. Schöberl and S. Zaglmayr. High order Nédélec elements with local complete sequence properties. *The international journal for computation and mathematics in electrical and electronic engineering*, 24(2):374–384, 2005.
- J. Schröder, M. Sarhil, L. Scheunemann, and P. Neff. Lagrange and $H(\text{curl}, \mathcal{B})$ based Finite Element formulations for the relaxed micromorphic model. *Computational Mechanics*, 70(6):1309–1333, 2022. doi: 10.1007/s00466-022-02198-3.
- J. Schröder, R. de Boer, and J. Bluhm. Tensor calculus for engineers: with applications to continuum and computational mechanics. Lecture series, 2013.
- N. Shekarchizadeh, B. E. Abali, E. Barchiesi, and A. M. Bersani. Inverse analysis of metamaterials and parameter determination by means of an automatized optimization problem. *Zeitschrift für Angewandte Mathematik und Mechanik*, 101(8):e202000277, 2021.
- N. Shekarchizadeh, B. E. Abali, and A. M. Bersani. A benchmark strain gradient elasticity solution in two-dimensions for verifying computational approaches by means of the finite element method. *Mathematics and Mechanics of Solids*, 27(10):2218–2238, 2022.
- F. Shi, N. Fantuzzi, P. Trovalusci, Y. Li, and Z. Wei. Stress field evaluation in orthotropic microstructured composites with holes as Cosserat continuum. *Materials*, 15(18), 2022.
- A. Skrzat and V. A. Eremeyev. On the effective properties of foams in the framework of the couple stress theory. *Continuum Mechanics and Thermodynamics*, 32:1779–1801, 2020.
- A. Sky. *Higher Order Finite Elements for Relaxed Micromorphic Continua*. PhD thesis, TU Dortmund, 2022.
- A. Sky, M. Neunteufel, I. Münch, J. Schöberl, and P. Neff. A hybrid $H^1 \times H(\text{curl})$ finite element formulation for a relaxed micromorphic continuum model of antiplane shear. *Computational Mechanics*, 68:1–24, 2021.
- A. Sky, M. Neunteufel, I. Münch, J. Schöberl, and P. Neff. Primal and mixed finite element formulations for the relaxed micromorphic model. *Computer Methods in Applied Mechanics and Engineering*, 399:115298, 2022.
- A. Sky, I. Münch, G. Rizzi, and P. Neff. Higher order Bernstein-Bézier and Nédélec finite elements for the relaxed micromorphic model. *Journal of Computational and Applied Mathematics*, 438:115568, 2024a.

- A. Sky, M. Neunteufel, P. Lewintan, A. Zilian, and P. Neff. Novel H(symCurl)-conforming finite elements for the relaxed micromorphic sequence. *Computer Methods in Applied Mechanics and Engineering*, 418:116494, 2024b.
- A. Sridhar, V. G. Kouznetsova, and M. G. D. Geers. Homogenization of locally resonant acoustic metamaterials towards an emergent enriched continuum. *Computational Mechanics*, 57:423–435, 2016.
- A. Sridhar, L. Liu, V. G. Kouznetsova, and M. G. D. Geers. Homogenized enriched continuum analysis of acoustic metamaterials with negative stiffness and double negative effects. *Journal of the Mechanics and Physics of Solids*, 119:104–117, 2018.
- E. S. Suhubi and A. C. Eringen. Nonlinear theory of micro-elastic solids-II. *International Journal of Engineering Science*, 2(4):389–404, 1964.
- J. U. Surjadi, L. Gao, H. Du, X. Li, X. Xiong, N. X. Fang, and Y. Lu. Mechanical metamaterials and their engineering applications. *Advanced Engineering Materials*, 21(3):1800864, 2019.
- T.-H. Tran, V. Monchiet, and G. Bonnet. A micromechanics-based approach for the derivation of constitutive elastic coefficients of strain-gradient media. *International Journal of Solids and Structures*, 49(5):783–792, 2012.
- D. Trinh, R. Janicke, N. Auffray, S. Diebels, and S. Forest. Evaluation of generalized continuum substitution models for heterogeneous materials. *International Journal for Multiscale Computational Engineering*, 10(6):527–549, 2012. ISSN 1543-1649.
- P. Trovalusci and A. Pau. Derivation of microstructured continua from lattice systems via principle of virtual works: the case of masonry-like materials as micropolar, second gradient and classical continua. *Acta Mechanica*, 225:157–177, 2014. doi: 10.1007/s00707-013-0936-9.
- C. Truesdell. *Rational Thermodynamics*. McGraw-Hill, New York, 1969.
- C. Truesdell. Cauchy and the modern mechanics of continua. *Revue d'histoire Des Sciences*, 45(1):5–24, 1992.
- C. Truesdell and W. Noll. The nonlinear field theories of mechanics. In *Encyclopedia of Physics*, chapter The nonlinear field theories of mechanics. Springer, 1965.
- C. Truesdell and R. Toupin. The classical field theories. In S. Flügge, editor, *Principles of Classical Mechanics and Field Theory / Prinzipien der Klassischen Mechanik und Feldtheorie*, pages 226–858. Springer Berlin Heidelberg, Berlin, Heidelberg, 1960a.
- C. Truesdell and R. Toupin. The classical field theories. In S. Flügge, editor, *Encyclopedia of Physics*, volume III/1. Springer, 1960b.
- N. Viebahn. *A Contribution to Stress-Displacement Based Mixed Galerkin Finite Elements for Hyperelasticity*. PhD thesis, University of Duisburg-Essen, 2019.
- A. Waseem, T. Heuzé, L. Stainier, M. Geers, and V. Kouznetsova. Enriched continuum for multi-scale transient diffusion coupled to mechanics. *Advanced Modeling and Simulation in Engineering Sciences*, 7:1–32, 2020.

- O. Weeger. Numerical homogenization of second gradient, linear elastic constitutive models for cubic 3D beam-lattice metamaterials. *International Journal of Solids and Structures*, 224:111037, 2021.
- M. Wheel, J. Frame, and P. Riches. Is smaller always stiffer? On size effects in supposedly generalised continua. *International Journal of Solids and Structures*, 67-68:84–92, 2015. ISSN 0020-7683.
- P. Wriggers. *Nonlinear Finite Element Methods*. Springer, Berlin, Heidelberg, 2008.
- W. Wu, W. Hu, G. Qian, H. Liao, X. Xu, and F. Berto. Mechanical design and multifunctional applications of chiral mechanical metamaterials: A review. *Materials & Design*, 180:107950, 2019.
- H. Yang and W. H. Müller. Size effects of mechanical metamaterials: a computational study based on a second-order asymptotic homogenization method. *Archive of Applied Mechanics*, 91:1037–1053, 2021.
- H. Yang, B. E. Abali, D. Timofeev, and W. H. Müller. Determination of metamaterial parameters by means of a homogenization approach based on asymptotic analysis. *Continuum Mechanics and Thermodynamics*, 32:1251–1270, 2020.
- H. Yang, D. Timofeev, B. E. Abali, B. Li, and W. H. Müller. Verification of strain gradient elasticity computation by analytical solutions. *Zeitschrift für Angewandte Mathematik und Mechanik*, 101(12):e202100023, 2021.
- H. Yang, B. E. Abali, W. H. Müller, S. Barboura, and J. Li. Verification of asymptotic homogenization method developed for periodic architected materials in strain gradient continuum. *International Journal of Solids and Structures*, 238:111386, 2022.
- S. Yin, Z. Xiao, Y. Deng, G. Zhang, J. Liu, and S. Gu. Isogeometric analysis of size-dependent Bernoulli-Euler beam based on a reformulated strain gradient elasticity theory. *Computers and Structures*, 253:106577, 2021.
- X. Yu, J. Zhou, H. Liang, Z. Jiang, and L. Wu. Mechanical metamaterials associated with stiffness, rigidity and compressibility: A brief review. *Progress in Materials Science*, 94: 114–173, 2018.
- J. Yvonnet, N. Auffray, and V. Monchiet. Computational second-order homogenization of materials with effective anisotropic strain-gradient behavior. *International Journal of Solids and Structures*, 191-192:434–448, 2020.
- A. A. Zadpoor. Mechanical meta-materials. *Materials Horizons*, 3:371–381, 2016.
- J. Zhi, L. H. Poh, T.-E. Tay, and V. B. C. Tan. Direct FE2 modeling of heterogeneous materials with a micromorphic computational homogenization framework. *Computer Methods in Applied Mechanics and Engineering*, 393:114837, 2022.
- O. Zienkiewicz and R. Taylor. The finite element patch test revisited a computer test for convergence, validation and error estimates. *Computer Methods in Applied Mechanics and Engineering*, 149(1):223–254, 1997.

-
- O. Zienkiewicz, R. Taylor, and J. Zhu, editors. *The Finite Element Method: its Basis and Fundamentals (Seventh Edition)*. Butterworth-Heinemann, Oxford, seventh edition edition, 2013.
- T. Zohdi. *Homogenization Methods and Multiscale Modeling*, chapter 12. John Wiley & Sons, Ltd, 2004.
- T. Zohdi and P. Wriggers. *An Introduction to Computational Micromechanics*. Springer Berlin, Heidelberg, 2005.

Der Lebenslauf ist in der Online-Version aus Gründen des Datenschutzes nicht enthalten.

In dieser Schriftenreihe bisher erschienene Berichte:

- Nr. 1 (2004) *Ein Modell zur Beschreibung finiter anisotroper elastoplastischer Deformationen unter Berücksichtigung diskreter Rissausbreitung*, J. Löblein, Dissertation, 2004.
- Nr. 2 (2006) *Polyconvex Anisotropic Energies and Modeling of Damage applied to Arterial Walls*, D. Balzani, Dissertation, 2006.
- Nr. 3 (2006) *Kontinuumsmechanische Modellierung ferroelektrischer Materialien im Rahmen der Invariantentheorie*, H. Romanowski, Dissertation, 2006.
- Nr. 4 (2007) *Mehrskaligen-Modellierung polykristalliner Ferroelektrika basierend auf diskreten Orientierungsverteilungsfunktionen*, I. Kurzhöfer, Dissertation, 2007.
- Nr. 5 (2007) *Proceedings of the First Seminar on the Mechanics of Multifunctional Materials*, J. Schröder, D.C. Lupascu, D. Balzani (Ed.), Tagungsband, 2007.
- Nr. 6 (2008) *Zur Modellierung und Simulation diskreter Rissausbreitungsvorgänge*, O. Hilgert, Dissertation, 2008.
- Nr. 7 (2009) *Least-Squares Mixed Finite Elements for Solid Mechanics*, A. Schwarz, Dissertation, 2009.
- Nr. 8 (2010) *Design of Polyconvex Energy Functions for All Anisotropy Classes*, V. Ebbing, Dissertation, 2010.
- Nr. 9 (2012) *Modeling of Electro-Mechanically Coupled Materials on Multiple Scales*, M.-A. Keip, Dissertation, 2012.
- Nr. 10 (2012) *Geometrical Modeling and Numerical Simulation of Heterogeneous Materials*, D. Brands, Dissertation, 2012.
- Nr. 11 (2012) *Modeling and simulation of arterial walls with focus on damage and residual stresses*, S. Brinkhues, Dissertation, 2012.
- Nr. 12 (2014) *Proceedings of the Second Seminar on the Mechanics of Multifunctional Materials*, J. Schröder, D.C. Lupascu, M.-A. Keip, D. Brands (Ed.), Tagungsband, 2014.
- Nr. 13 (2016) *Mixed least squares finite element methods based on inverse stress-strain relations in hyperelasticity*, B. Müller, Dissertation, 2016.
- Nr. 14 (2016) *Electromechanical Modeling and Simulation of Thin Cardiac Tissue Constructs*, R. Frotscher, Dissertation, 2016.
- Nr. 15 (2017) *Least-squares mixed finite elements for geometrically nonlinear solid mechanics*, K. Steeger, Dissertation, 2017.

- Nr. 16 (2017) *Scale-Bridging of Elasto-Plastic Microstructures using Statistically Similar Representative Volume Elements*, L. Scheunemann, Dissertation, 2017.
- Nr. 17 (2018) *Modeling of Self-healing Polymers and Polymeric Composite Systems*, S. Specht, Dissertation, 2017.
- Nr. 18 (2018) *Proceedings of the Third Seminar on the Mechanics of Multifunctional Materials*, J. Schröder, D.C. Lupascu, H. Wende, D. Brands (Ed.), Tagungsband, 2018.
- Nr. 19 (2018) *Least-squares finite element methods with applications in fluid and solid mechanics*, C. Nisters, Dissertation, 2018.
- Nr. 20 (2018) *A two-scale homogenization scheme for the prediction of magneto-electric product properties*, M. Labusch, Dissertation, 2018.
- Nr. 21 (2019) *Modeling the passive mechanical response of soft tissues: constitutive modeling approaches, efficient parameter selection and subsequent adjustments due to residual stresses*, M. von Hoegen, Dissertation, 2019.
- Nr. 22 (2019) *Constitutive modeling of female pelvic floor dysfunctions and reconstructive surgeries using prosthetic mesh implants*, A. Bhattarai, Dissertation, 2019.
- Nr. 23 (2019) *A contribution to stress-displacement based mixed galerkin finite elements for hyperelasticity*, N. Viebahn, Dissertation, 2019.
- Nr. 24 (2020) *Gefrier- und Auftauprozesse in gesättigten porösen Materialien - ein Modellierungskonzept im Rahmen der Theorie poröser Medien*, W.M. Bloßfeld, Dissertation, 2020.
- Nr. 25 (2021) *Electromechanical modelling and simulation of hiPSC-derived cardiac cell cultures*, A. Jung, Dissertation, 2021.
- Nr. 26 (2021) *Mixed and Hybrid Least-Squares FEM in Nonlinear Solid Mechanics*, M. Igelbüscher, Dissertation, 2021.
- Nr. 27 (2023) *The Material Point Method for dynamic Metal Processing*, S. Maassen, Dissertation, 2023.
- Nr. 28 (2023) *Modeling of Fluid-Structure Interactions with the Least-Squares FEM*, S. Averweg, Dissertation, 2023.
- Nr. 29 (2023) *Numerical simulation of microstructural residual stresses of hot bulk forming parts with targeted cooling*, S. Hellebrand, Dissertation, 2023.
- Nr. 30 (2023) *The Theory of Porous Media in the Framework of the Mesh-in-Element Method*, S. Maike, Dissertation, 2023.
- Nr. 31 (2024) *Numerical analysis of magneto-mechanically coupled mesostructures*, M. Reichel, Dissertation, 2024.